Magnetic Properties of Ultrathin Films, Coupled Trilayers and *3d/5d* Multilayers
studied by
X-ray Magnetic Circular Dichroism

im Fachbereich Physik
der Freien Universität Berlin
eingereichte Dissertation

vorgelegt von
Fabrice Wilhelm

April 2000

| 1. Gutachter: | Prof. Dr. K. Baberschke |
| 2. Gutachter: | Prof. Dr. N. Schwentner |

| Tag der Disputation: | 6. Juni 2000 |

To my Parents

In our work, we are doing nothing more but studying the same trivial elements that since a few centuries have been investigated in Science. It is, however, their combination in new forms and the application of new techniques and ideas that gives us the eternal sense of freshness. Even now, that this Dissertation has been terminated, there is the same feeling as in the beginning, that all starts just now. Because, simply, a poem is never finished; it is only abandoned.

Contents

Introduction

The research in magnetism and magnetic materials is actually experiencing a renaissance. This is mostly due to the discovery of magnetic multilayers and their technological relevance for magnetic storage and recording industry [1]. Actually, the longitudinal magnetic recording devices have a density storage capacity of about 5 Gbits/in^2. A limit of 40 Gbits/in^2 is predicted where the thermal effect becomes more important and induces spontaneous magnetization reversal processes. Higher density storage capacity for longitudinal or perpendicular magneto-optic recording media could be achieved using materials with higher anisotropy and coercivity [2]. Multilayers or alloys based on $3d$ and $5d$ transition metals are the most promising candidates since they exhibit strong uniaxial anisotropy and resistance against oxidation and corrosion. Research on thin film magnetism is strongly stimulated by this major technological impact. A precise understanding of the mechanisms governing the magnetic multilayers goes through the study of their basic constituents, that are thin films in the range of a few monolayers. Only few years ago, the advances of ultra-high vacuum compatible growth techniques allowed us to control thin film growth at an atomic level in order to form epitaxial and heteroepitaxial structures. In association with the improvement of the sensitivity of many experimental techniques, the fundamental magnetic observables, i.e. magnetic moment per atom, magnetization, Curie temperature and magnetic anisotropy, can be probed in the monolayer limit [3].

Techniques based on synchrotron radiation, such as spin resolved photoemission, x-ray magnetic circular dichroism, x-ray magnetic scattering and latest x-ray magnetic microscopy have been shown to provide unique capabilities for the study of the magnetic phenomena and magnetic materials. X-ray magnetic circular dichroism (XMCD) spectroscopy in photoabsorption, since its first experimental observation by Schütz *et al.* in 1987 [4], has become a powerful technique to investigate the magnetic properties of matter. Over the last ten years, this technique has been developed both experimentally and theoretically into a quantitative magnetometer.

The XMCD is defined as the difference between the absorption cross section for left

1

and right circularly polarized x-rays. The magnetic properties of transition metals are mainly due to the d-states. Since, the $L_{3,2}$-edges of the d transition metals correspond to $2p \rightarrow d$ transitions, the XMCD signal is directly sensitive to the spin-imbalance of unoccupied final d-states. Then, the XMCD signal is related to the local magnetic properties of the absorbing atom via spin-orbit coupling and exchange interactions. One of the advantages of the XMCD compared to other classical magnetometry techniques, is its element specificity. Different elements which compose a magnetic system can be probed separately. By taking advantage of the selection rules, it is even possible to separate the contribution to the total magnetic moment of the individual electronic shells (s, p, d, f). Moreover, since the derivation of sum rules, a quantitative separation and determination of the spin and orbital magnetic moments and their anisotropies is possible. Taking also into account its submonolayer sensitivity, XMCD is now a tool which forms by itself a unique class of magnetometers.

The subject of this thesis is to study the magnetic properties of ultrathin films, coupled trilayers and finally $3d/5d$ multilayer systems. This work is mainly focussed on the spin and orbital magnetism separately and the temperature dependent magnetization. The x-ray magnetic circular dichroism is an adequate technique.

The reduced symmetry and coordination number of low dimensional magnetic systems leads to modifications in a variety of phenomena such as magnetic ordering, magnetic anisotropy, and localized electronic states. Band structure calculations involving both spin-orbit coupling and orbital magnetism have shown that, as compared to bulk values, the orbital moment of Co and Ni deposited on Cu(001) is enhanced at the surface. With the exception of Ni on Cu(001), the spin moment also shows the same trend [5]. The enhanced orbital moment of Co/Cu(001) has also been confirmed experimentally [6]. However, the spin and orbital magnetic moment for ultra thin Co and Ni films on Cu(001) have never been examined separately. We will show that it is possible to determine separately with high accuracy the spin and orbital magnetic moments. Are the theoretically predicted results in accordance with the experimental ones? The spin and orbital magnetic moment were found to be enhanced for Co ultrathin films compared to the bulk values. However, a strong reduction of the spin and orbital magnetic moment are observed for ultrathin Ni films. The surface and interface with the substrate play here an important role to explain such observations.

Often, in literature, ultrathin films grown *in situ* are capped with non-magnetic protective layers in order to be prevented from oxidation for *ex situ* magnetic characterization. In the case of thick films, the influence of the interfaces and surface on the magnetic observables like the magnetic moments and Curie temperature is negligible. We will show that this is not the case for ultrathin films. By Cu-capping the ultrathin Co and Ni/Cu(001)

films, a decrease of the total magnetic moment is observed which will be determined. By performing, temperature-dependent XMCD measurements, the Curie temperature compared to the bare films is reduced. We will show that these two observables are correlated within the framework of a mean-field model.

Moreover, we will show that it is possible to shift towards higher temperatures the Curie temperature of the bilayer Cu/Ni/Cu(001). This can be done by evaporating on the top another ferromagnetic layer like Co. This system is a prototype system, since it constitutes the unit cell of multilayer systems. The two ferromagnetic layers interact then through the Cu-spacers via the interlayer exchange coupling. Does this coupled trilayer present a separate or one single (common) Curie temperature? How does the interlayer exchange coupling affect the temperature-dependent sublayer magnetizations? To solve these questions, we will perform temperature dependent element-specific magnetization measurements using the XMCD technique. Up to now, very few work has been devoted to this subject. We will show that the origin of the oscillatory positive shift of the lowest ordering temperature is the suppression of the spin fluctuations due to the oscillatory interlayer exchange coupling. Moreover, it is possible by tuning the thickness of the ferromagnetic Co top layer to observe crossing sublayer magnetizations.

Non-magnetic transition metals in contact with a ferromagnetic one acquire an induced magnetic moment. To study fully these interface effects, it is essential to know what are the magnetic moments of both constituents. Up to now, no complete work has been reported on such effects. In the case of Ni/Pt multilayer systems, are the Ni magnetic layers influenced by the presence of Pt layers at the interfaces? How large will be the induced magnetic moment of Pt, if any? We will construct a full magnetic moment profile for Ni and Pt and show that Pt acquires an induced magnetic moment, whereas, Ni magnetic moment is reduced at the interfaces. A separation in spin and orbital magnetic moment will also be performed. Recently, great attention has been paid on the orbital magnetism, which is the origin of the magnetic anisotropy. We will determine the anisotropy of the orbital magnetic moment of Ni in Ni/Pt and this will be related to the magnetic anisotropy energy (MAE). Finally, we will present first measurements of W and Ir induced magnetic moments in Fe/T(T=W,Ir) multilayer systems.

This study is organized in the following way: In chapter one, we will give a theoretical description of the XMCD technique and a detailed data analysis in order to extract the spin and orbital magnetic moment from the XMCD integrated signal. In chapter two, we will present the experimental setup at different synchrotron facilities and we will demonstrate the importance of the saturation effect corrections. The magnetic properties of Co and Ni ultrathin films will be compared to bulk films in chapter three. The capping and interlayer exchange coupling effect on bilayer and trilayer systems, respectively, will

be described in chapter four. Chapter five is focussing on the anisotropy of the Ni orbital magnetic moment in Ni/Pt and finally, in chapter six, the induced magnetic moment of Pt in Ni/Pt and W, Ir in Fe/T (T=W,Ir) will be determined. A full magnetic moment profile will be given for Ni/Pt multilayers.

Chapter 1

The X-ray Magnetic Circular Dichroism

The pioneer work done by Michael Faraday in 1846 on the rotation of the polarisation vector of linearly polarized light upon transmission through a magnetic material opened the door for the investigation of magnetic materials using electromagnetic radiation [7]. The same phenomenon was observed by Kerr for reflected light 30 years later [8]. Since then, many other magneto-opical effects, as for example the Zeeman, Voigt and Moutton-Cotton effects [9] have been found. Today, laser-based methods are used to investigate magnetic properties. One of the primary techniques used is the Magneto Optic Kerr Effect (MOKE). Typical laser light has photon energies in the 1-4eV range. Thus, the Faraday and Kerr effects involve electronic transitions from filled to unfilled electronic valence states. Based on the same principle with MOKE, one of the first experiments trying to investigate the influence of magnetism on x-ray absorption spectra were performed by Chapman [10] and Forman [11]. The first realistic approach to this problem was done by Erskine and Stern [12] in 1975 who predicted the X-ray Magnetic Circular Dichroism (XMCD) at the $M_{3,2}$-edges in Ni metal. The XMCD is the difference between the absorption spectrum for left and right circularly polarized x-rays. This paper constitutes the birth of the XMCD spectroscopy. The calculation was based on a band- structure formalism involving transitions from localized core states (Ni $3p$) to "delocalized" final $3d$ valence states including the $3p$ core spin-orbit splitting. Later, Thole et $al.$ predicted an X-ray Magnetic Linear Dichroism (XMLD) at $M_{5,4}$-edges of magnetic rare-earths involving transitions in highly "localised" final $4f$ valence states using atomic multiplet theory [13]. The XMLD is the difference between the absorption spectrum by changing the direction of the magnetization relative to the $\vec{E}$ vector for linearly polarized x-rays. The XMLD spectroscopy provides complementary information compared to the XMCD spec-

troscopy. The first proof for XMLD was given by van der Laan *et al.* by investigating the $M_{5,4}$-edges of Tb in $Tb_3Fe_5O_{12}$ [14]. Later, Schütz *et al.* measured the first XMCD signal at the K-edge of Fe metal [4]. In the last decade, the progress and development of the x-ray optics and synchrotron radiation facilities allowed the observation of the Faraday [15] and Kerr [16] effects in the x-ray regime, the magnetic dichroism in fluorescence [17], the magnetic scattering [18], the x-ray natural circular dichroism [19], as well as many other related phenomena [20].

1.1   Theoretical Aspects

The so-called X-ray Magnetic Circular Dichroism is per definition the difference between the absorption spectrum for left and right circularly polarized x-ray light for a magnetic static field applied along the incident photon axis. Following the optic convention, x-ray light emitted are left circularly polarized when the charges seem to turn left (counter-clockwise) from the point of view of the sample [21]. Left circularly polarized x-ray light corresponds to a $+\hbar$ helicity.

1.1.1   General aspects

The fundamental processes occurring during the interaction between the x-ray light and matter are the scattering processes, the photoelectric absorption and the production of electron-positron pairs. For the energy range we consider here (10eV-100keV), the production of the electron-positron pairs is not possible. The most important processes are the scattering processes and the photoelectric absorption. In Fig. 1.1, the cross-sections as a function of the energy for Cu are shown.   The scattering processes involved are essentially the Thomson scattering (elastic), the Compton and Raman scattering (inelastic). The photoelectric absorption corresponds to the excitation of a core electron to a bound state or the continuum. Following the absorption event, a photoelectron is emitted.

In the energy range 10eV-30keV, the photoelectric absorption process is larger than the scattering processes by two to three orders of magnitude. Then, the intensity $I(E,d)$ transmitted through a material of thickness d is related to the absorption coefficient μ via the Beer's law:

$$I(E,d) = I_0(E) \cdot e^{-\mu d} \tag{1.1}$$

$I_0(E)$ is the incident photon intensity. Usually one deals with the normalized intensity $I(E,d)/I_0(E)$.

In a simplified picture, the x-ray absorption can be modelled by means of independent processes: creation of a core hole, departure of the photoelectron experiencing a potential (perturbed or not by the core hole) and finally electronic rearrangements to go back into the ground state. Near the edge, the adiabatic approximation (screened core hole) is used to simulate the photoelectron evolution and the photoelectron "sees" the other electrons completely rearranged. In the EXAFS region, the sudden approximation is used which means the core hole is not screened and that the potential where the photoelectron moves corresponds to the passive electrons frozen in their ground-state. The filling of the hole by an electron coming from external level can done via a radiative decay (Fluorescence yield) or via a non-radiative decay (Auger yield) (see Fig. 1.2).

The total transition probability between the initial state $\mid i\rangle$ and all the other states is proportional to the width of the initial state (inverse of the lifetime of the core hole). The total probability varies smoothly with the atomic number Z (see Fig. 1.2).

The transition or absorption probability $\Gamma_{i,f}$ between the initial state $\mid i\rangle$ and a final state $\mid f\rangle$ is given by the Fermi golden rule:

$$\Gamma_{i,f} = \frac{2\pi}{\hbar} \mid \langle f \mid H_{inter} \mid i\rangle \mid^2 \cdot \delta(E_f - E_i - \hbar\omega)$$

(1.2)

where the interaction Hamiltonian operator between the photon and the atom (neglect the scattering process) is given by:

$$H_{inter} = \frac{e}{mc}\vec{A} \cdot \vec{p}$$

(1.3)
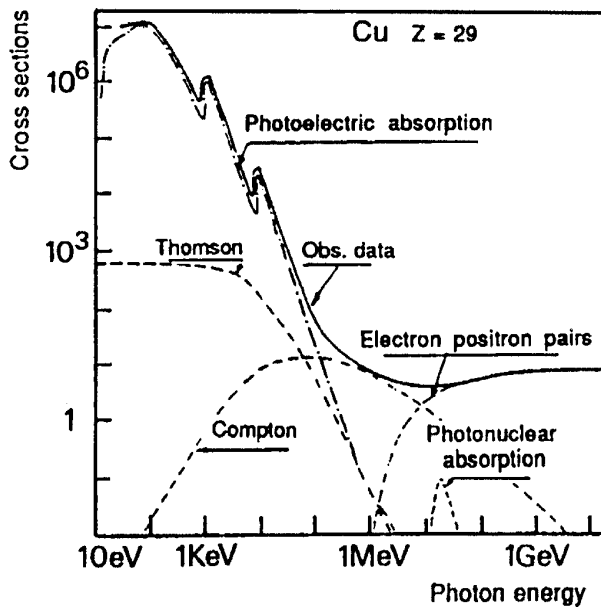
Figure 1.1: Variation of cross sections with energy for the copper atom [22].

where $\vec{A}$ is the vector potential which is written in the form of a plane electromagnetic wave of unit vector $\vec{\epsilon}$. In the electric dipole approximation, $|\text{k.r}| \ll 1$, the Hamiltonian is then written:

$$H_{inter} = \frac{e}{mc} A_0 e^{-i\omega t} \vec{\epsilon} \cdot \vec{p} \tag{1.4}$$

For circularly polarized photons, the Wigner-Eckart theorem, which contains the composition rules for spherical harmonics, leads to the following selection rules:

$$\Delta s = 0 \qquad \Delta \ell = \pm 1 \qquad \Delta j = 0, \pm 1 \qquad \Delta m = \pm 1 \tag{1.5}$$

$\Delta s = 0$ means that during the transition of the electron, a spin-flip is not allowed. The electron cannot go into the final state which has an opposite spin-polarization. We see here that x-ray absorption is orbital selective.

The X-ray absorption cross-section is the ratio between the absorbed energy and the incident photon flux. The photon flux F_{ph} is given by the energy flux of the electromagnetic field divided by the photon energy:

$$F_{ph} = \frac{E_0^2 c}{2\pi\hbar\omega} = \frac{A_0^2 \omega}{2\pi\hbar c} \tag{1.6}$$

The total absorption cross-section in the dipole approximation is given by the sum, of all the initial and final states:

$$\sigma(\hbar\omega) = \frac{4\pi^2 e^2}{cm^2\omega} \sum_{i,f} | \langle f | \vec{\epsilon} \cdot \vec{p} | i \rangle |^2 \cdot \delta(E_f - E_i - \hbar\omega) \tag{1.7}$$

Figure 1.2: Fluorescence yield and auger yield for the K shell excitation. For shallower excitations, L and M shells, the fluorescence decay is the most important [23].

and finally:

$$\sigma(\hbar\omega) = 4\pi^2 \alpha \hbar\omega \sum_{i,f} \mid \langle f \mid \vec{\epsilon} \cdot \vec{r} \mid i \rangle \mid^2 \cdot \delta(E_f - E_i - \hbar\omega) \tag{1.8}$$

where α is the fine structure constant (α=1/137)The last term express the energy conservation.By tuning the incident photon energy $\hbar\omega$ ($=E$), we can select the appropriate element.
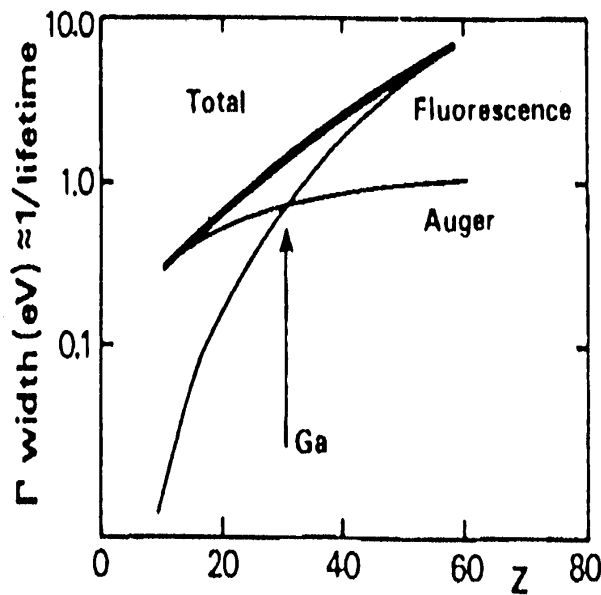
1.1.2 The two step-model

The origin of the XMCD effect can be simply explained in a so-called "two step model". Let us consider the dichroic effect at the L_3 and L_2-edges for *3d* transition metals.

In the first step, a circulary polarized photon excites and polarizes a core-electron from the p shells. The core shell can be viewed as an atomic-specific source of spin-polarized electrons. Let us assume only transitions from $p \rightarrow d$. The core state is split into $2p_{3/2}$ and $2p_{1/2}$ (the L_3 and L_2−edges, respectively) by the spin-orbit interaction ξ_c. The energy separation of these two initial states is a few eV for the *3d* transitions metals. Due to this interaction, the substates are not any more pure spin states, but are coupled to the orbital moment. At the L_3 and L_2-edges, $\vec{\ell}$ and $\vec{s}$ are coupled parallel and antiparallel, respectively. As a consequence, it is possible to spin-polarize the photoelectrons even if the spin does not interact directly with the electric field (the dipole-operator does not act on the spin). Left and right circularly polarized photons possess an angular momentum $+\hbar$ and $-\hbar$, respectively. The photon angular momentum is transferred into both the orbital and spin degrees of freedom of the excited photoelectron. At the L_3-edge, the absorption of left circularly polarized photons will mostly excite spin-up photoelectrons because the transition probability is maximum when $\vec{\ell}, \vec{s}$ and $+\hbar$ are parallel. At the L_2-edge, mostly spin-down photoelectrons will be excited, because $\vec{s}$ and $+\hbar$ are antiparallel. The absorption of right circularly polarized photons will excite the same amount of photoelectrons but of opposite spin. Spin-up and spin-down are defined relative to the vector wave $\vec{k}$ of the incident photons (parallel and antiparallel). In an atomistic model, which neglects the spin-orbit splitting in the d band, for the L_3-edge (L_2-edge), left circularly polarized photons excite 62.5% (25%) spin-up and 37.5% (75%) spin-down electrons, and right circularly polarized photons do the opposite (see Fig. 1.3).

In the second step, the d valence band can be considered as a spin-detector which means that a spin-down photoelectron will be excited into the spin-down unoccupied state above the Fermi-energy (spin-up unoccupied state for a spin-up photoelectron). If the metal is ferromagnetic, there exists an imbalance in unoccupied spin-un and spin-down due to the exchange coupling (Stoner model). The dichroism effect will be proportional
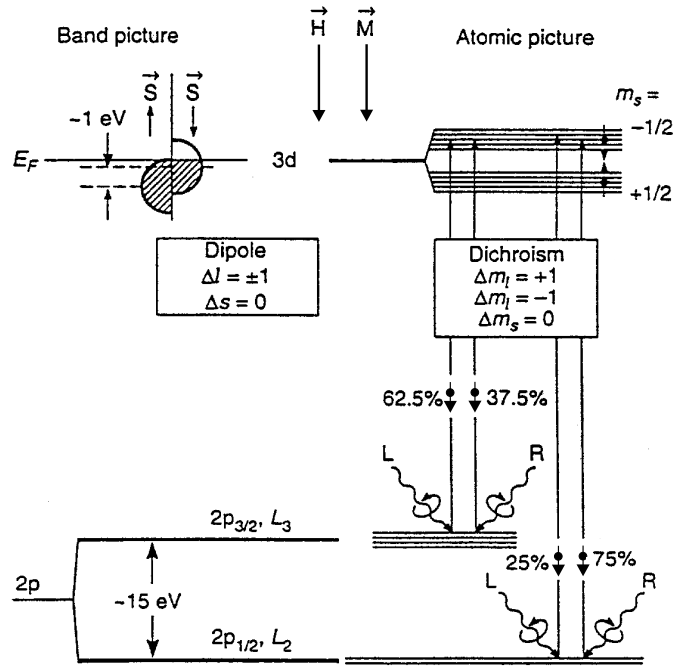
Figure 1.3: Schematic representation of the two-step model for the *L*-edges. In a first step, the absorption of polarized photons by the *p* core shell leads to the excitation of spin-polarized photoelectrons. The spin polarization of the photoelectrons is then analyzed by the valence shell (right). Transition probability and selection rules are also given. In a second step (left), in a Stoner model, the valence shell for a magnetic material has a spin imbalance. The dichroism is then proportional to this imbalance [24].

to the difference in the unoccupied spin-down and spin-up states (the holes), i.e. to the spin-magnetic moment.

In summary, the existence of a dichroic effect at the $L_{3,2}$-edges is mostly due to spin-orbit interaction in the core state and the exchange coupling in the valence band.

At the K or L_1-edge, since the initial states at these edges have s symmetry (zero angular momentum) and there is no spin-orbit splitting, a dichroic effect exists only if the p valence shell exhibits an orbital moment.

1.1.3   The sum rules

Here, we will give a brief description of the sum rules for the x-ray magnetic circular dichroism and a discussion about their theoretical limitations.

The first and second sum rules

In 1992, B. T. Thole *et al.* derived a new magneto-optic sum rule that could be applied for circular dichroism in the x-ray regime [25]. They show that it is possible to measure directly the expectation average value of the ground-state of the orbital angular momentum operator L_Z acting on the shell that receives the photoelectron in the final state. This is achieved by considering the difference between the integrated absorption intensity for right and left circularly polarized photons. This integral has to be taken over the complete spin-orbit split core level edges. The importance of the integrated XMCD is that it measures directly the ground-state property. One year later, P. Carra *et al.* derived a second sum rule which relates the integrated dichroic signal to the ground-state expectation average value of the spin momentum operator S_Z and magnetic dipole operator T_Z acting on the shell that receives the photoelectron in the final state [26]. These rules were extended by Carra *et al.* to include the electric quadrupole transitions and the magnetic linear dichroism [27]. In 1998, Van der Laan derived the sum rules for jj-coupled operators by including the cross terms between the ground-state levels, so that the sum rules are not longer restricted to jj-coupling but valid in intermediate coupling [28].

For a transition between a core level c towards a valence level l with n electrons in the ground state, the two sum rules, the so-called orbital and spin sum rules, read:

$$\frac{\int(I^{-1}_{c+1/2} - I^{+1}_{c+1/2})d\omega + \int(I^{-1}_{c-1/2} - I^{+1}_{c-1/2})d\omega}{\int(I^{-1}_{c+1/2} + I^{+1}_{c+1/2} + I^{0}_{c+1/2})d\omega + \int(I^{-1}_{c-1/2} + I^{+1}_{c-1/2} + I^{0}_{c-1/2})d\omega} = A(c,\ell,n)\langle L_z \rangle \quad (1.9)$$

with

$$A(c,\ell,n) = \frac{\ell(\ell+1) - c(c+1) + 2}{2\ell(\ell+1)[2(2\ell+1) - n]}$$

and

$$\frac{\int(I^{-1}_{c+1/2} - I^{+1}_{c+1/2})d\omega - \frac{c+1}{c}\int(I^{-1}_{c-1/2} - I^{+1}_{c-1/2})d\omega}{\int(I^{-1}_{c+1/2} + I^{+1}_{c+1/2} + I^{0}_{c+1/2})d\omega + \int(I^{-1}_{c-1/2} + I^{+1}_{c-1/2} + I^{0}_{c-1/2})d\omega} =$$

$$B(c,\ell,n)\langle S_z \rangle + C(c,\ell,n)\langle T_z \rangle \quad (1.10)$$

with

$$B(c, \ell, n) = \frac{\ell(\ell+1) - c(c+1) - 2}{3c[2(2\ell+1) - n]}$$

$$C(c, \ell, n) = \frac{\ell(\ell+1)[\ell(\ell+1) + 2c(c+1) + 4] - 3(c-1)^2(c+2)^2}{6c\ell(\ell+1)[(2(2\ell+1) - n]}$$

The $I_{c\pm1/2}^q$ are normalised absorption cross sections (equivalent to the absorption cross sections divided by the photon energy) for polarisation q, q=-1,1,0 corresponding to left, right circularly and linear polarized photons, respectively. The indices $c\pm1/2$ correspond to the two spin-orbit split core level edges. The $I_{c\pm1/2}^q$ integrals are proportional to the sum of transitions matrix elements squared. The integrals are performed on $\hbar\omega$ from $-\infty$ to $+\infty$. From these sum rules, the following magnetic moments are determined:

i) the orbital magnetic moment: $m_L = -\frac{\mu_B}{\hbar}\langle L_z \rangle$

ii) the spin magnetic moment: $m_S = -\frac{2\mu_B}{\hbar}\langle S_z \rangle$

iii) the magnetic dipole moment: $m_T = +\frac{\mu_B}{\hbar}\langle T_z \rangle$

According to the dipole selection rules, there are two possible transitions from the core state c. The conservation of the orbital angular momentum implies transitions to the state $\ell = c + 1$ and $\ell = c - 1$. The sum rules for these two different channels are different. The x-ray absorption spectra contain these two contributions which cannot be easily localised. This makes the simultaneous application of the sum-rules for these two channels impossible. However, for the $L_{3,2}$-edges of $3d$ transitions metals, the ratio of the radial dipole matrix elements for $\ell = c - 1$ transitions and $\ell = c + 1$ transitions is approximately equal to [29]:

$$\frac{|\langle 4s \parallel r \parallel 2p \rangle|^2}{|\langle 3d \parallel r \parallel 2p \rangle|^2} \approx \frac{1}{50} \tag{1.11}$$

Then, the $p \longrightarrow s$ transitions are negligible as $p \longrightarrow d$ transitions are favoured by a factor of 50. Calculations using the FEFF7 code indeed show that the $p \longrightarrow s$ contribution can be neglected [30]. The sum rules given by the upper equations will be:

$$\frac{\int_{j^++j^-}(I^{-1} - I^{+1})d\omega}{\int_{j^++j^-}(I^{-1} + I^{+1} + I^0)d\omega} = \frac{\langle L_z \rangle}{\ell n_h} \qquad n_h = 2(2\ell+1) - n \tag{1.12}$$

$$\frac{\int_{j^+}(I^{-1} - I^{+1})d\omega - \frac{\ell}{\ell-1}\int_{j^-}(I^{-1} - I^{+1})d\omega}{\int_{j^++j^-}(I^{-1} + I^{+1} + I^0)d\omega} = \frac{2}{3n_h}\left(\langle S_z \rangle + \frac{2\ell+3}{\ell}\langle T_z \rangle\right) \tag{1.13}$$

where $j^{\pm} = c \pm 1/2$. The magnetic dipole operator $\overrightarrow{T}$ is per definition equal to

$$\overrightarrow{T} = \overrightarrow{S} - 3\hat{r}(\hat{r} \cdot \overrightarrow{S}) \tag{1.14}$$

The term $\langle T_z \rangle$ measures the asphericity of the spin-magnetization. More details about this term will be given in a next paragraph.

The theoretical limitations

The derivation of the two sum rules was carried out only for electric dipole transitions in a localized model, considering a single ion in an arbitrary crystal-field symmetry with the valence shell only partly filled. Moreover, only transitions between a pure $c^{4c+2}\ell^n$ initial configuration and a pure $c^{4c+1}\ell^{n+1}$ final configuration have been considered. In other words, the other shells do not involve in the absorption process. Thole *et al.* showed that the presence of an extra shell has no effect on the integrated XMCD, as well as hybridization, which is not clear. In the original derivation, all the radial matrix elements are constant for all the transitions. On the other hand, the many-body effects are included.

An other approximation is that the energy dependence of the radial parts of the matrix elements and the intershell hybridization are neglected in the derivation of the sum rules. Wu *et al.* showed that this affects more the spin sum rule than the orbital sum rule [31, 32]. The radial part of the matrix elements R_d of the d band ($|\langle 3d \| r \| 2p \rangle|^2$) varies linearly with the photoelectron energy and is proportional to the spin-orbit coupling energy ξ_{3d}. The orbital magnetic moment L_z is proportional to ξ_{3d} and the dichroic signal is proportional to R_d. Therefore L_z is strictly proportional to the dichroic. For the spin magnetic moment, this proportionality is holding only approximately. Such effects are usually absent in the strongly localized f shell of the rare earths which have narrow band widths.

The most important source of errors by applying the sum rules comes directly from the evaluation of the denominators in the left parts of Eq.s 1.10 and 1.11. They are directly affected by the s and p contributions. The denominator corresponds to the isotropic absorption cross-section which is proportional to the number of holes n_h in the shell ℓ. To eliminate the contribution from the high lying s and p states (called continuum states), a double step function is fitted below the absorption cross-section and subtracted. This procedure ensures the validity of the sum rules. This adds some arbitrariness in the determination of the number of holes in the final state. By using highly precise local density approach, the calculations show that the orbital sum rule is found to be valid to within 5-10%, the error being due to sd hybridization. For the spin sum-rule, the error due to hybridization can be 40-50% for Ni, 20% for Co and 15% for Fe systems. Again, it is the

denominator that causes the largest error in the spin sum-rule. Actually, a new procedure is developed for quantitative applications of the XMCD sum-rules. This approach, based on theoretical calculations, overcomes the difficulties of background subtraction [33].

Finally, a possible intermixing between the two absorption edges $j^{\pm}$ is neglected. This means that it is possible to integrate the signal of a core level assuming that it is a good quantum numbers, such as the total angular momentum j. This assumption is reasonable if the separation in energy of the core split edges which is equal to $(2c+1)\xi_c/2$ is large enough to prevent their mixing, caused by the Coulomb interactions in the final state. Using a fully relativistic model, Schwitalla and Ebert demonstrate that the electron core-hole interaction and especially the Coulomb part leads to a coupling of the two absorption $L_{3,2}$-edges [34]. This effects directly the so-called branching ratio, for the $L_{3,2}$-edge, i.e. the ratio of the jumps of the absorption coefficient at the L_3- and L_2-edges, which will deviate from the ideal ratio 2 : 1. The application of the sum-rule will be in this case problematic. However, as expected, they show that the influence of the electron core-hole interaction decreases along the 3d-series, while the spin orbit splitting of the 2p-levels increases. As a consequence, the application of the sum-rules seems to be problematic for the middle of the 3d-transition metals but is reasonably well justified for the late 3d-transition metals Fe, Co and Ni.

The magnetic dipole moment

The second sum rule (Eq. 1.8) allows us to determine the sum of the spin magnetic moment m_S and the magnetic dipole moment m_T, which is called an effective spin magnetic moment m_S^{eff} ($m_S^{eff} = m_S - (4\ell + 6)m_T/\ell$). Per definition, the magnetic moment of a magnetic material is only the sum of the spin and orbital magnetic moment. There is no other contribution like the dipole magnetic moment. The expectation value of the magnetic dipole operator $\langle T_z \rangle$ provides a measure of the anisotropy of the field of the spins when the atomic cloud is distorted either by the spin-orbit interaction or by the crystal field [35]. In general, we can rewrite the Eq. 1.12 for $\vec{k}, \vec{H}_{ext} \| \alpha$ where the index $\alpha = x, y, z$ denotes the Cartesian frame as following:

$$\langle T_\alpha \rangle = \langle \sum_\beta Q_{\alpha\beta} S_\beta \rangle \tag{1.15}$$

indicating the coupled charge Q and spin $\vec{S}$ components of $\vec{T}$. Q is the quadrupole operator of the charge where $Q_{\alpha\beta} = \delta_{\alpha\beta} - 3r_\alpha r_\beta/r^2$ is a second rank tensor with the symmetry properties $Q_{\alpha\beta} = Q_{\beta\alpha}$ and $\sum_\alpha Q_{\alpha\alpha} = 0$. For 3$d$ transition metals, the spin-orbit interaction $\xi_{3d} \vec{L} \cdot \vec{S}$ ($\xi_{3d} \leq 0.1eV$) is much smaller than the exchange interaction (band splitting $\Delta_{ex} \approx 1eV$) and the crystal field potential (characteristic splitting $\Delta_{cf} \approx 1eV$).

Stöhr and König demonstrated that a perturbative calculation of $\langle T_\alpha \rangle$ yields a decoupling of the charge Q and spin S for high symmetry:

$$\langle T_\alpha \rangle \approx \sum_i Q_\alpha^i s^i \tag{1.16}$$

where $\langle S_\alpha \rangle = \sum_i s^i$. This result is exact in the case when there is no spin-orbit coupling. This implies, then, that the $\langle T_\alpha \rangle$ depends only on the crystallographic symmetry. In $3d$ transition metals, since the higher correction terms are negligible (order of $(\xi_{3d}/\Delta_{ex})^2 < 0.01$), $\langle T_\alpha \rangle$ originates from a lower than cubic site symmetry only, and the effect of the spin-orbit coupling can be neglected. From these properties, a new sum rule was then deduced [36]:

$$\sum_\alpha \langle T_\alpha \rangle \approx \sum_i s^i \sum_\alpha Q_\alpha^i = 0 \tag{1.17}$$

From this, we see that we can directly determine the spin magnetic moment $\langle S \rangle$ by averaging the dichroism measurements along the x, y and z axis. For ultrathin films, this correction is expected to be large, due to the breaking of the symmetry. The charge density and spin density are not any more spherically symmetric. Effectively, by performing atomic multiplet calculations, Stöhr and König found that upon angle averaging, the dipolar contribution is cancelled for tetragonal crystal field splitting larger than the spin-orbit splitting. Also, the angle averaged dipolar contribution is smaller in tetragonal than in cubic symmetry. However, as expected, along each axis, the dipolar contribution increases when the tetragonal distortion (tetragonal crystal field splitting) increases [36]. Wu and Freeman confirmed this last statement by performing first principles calculations [31]. The $\langle T_z \rangle$ term is negligible for atoms with cubic symmetry but not in noncubic environment such as surfaces or interfaces. At the surface of Fe(001), Co(0001) and Ni(001) the magnitude of $7\langle T_z \rangle$ is $0.23\mu_B$, $0.24\mu_B$ and $-0.082\mu_B$ respectively compared to the bulklike layers (atoms with cubic symmetry) where the magnitude is $0.028\mu_B$, $0.014\mu_B$ and $-0.027\mu_B$.

The orbital-spin ratio

The determination of the absolute orbital and spin magnetic moment seems to be difficult mostly because of the determination of the denominators. One simple way to avoid this difficulty is to apply the sum rules by taking the ratio of the orbital-to-spin, for the $L_{3,2}$-edges as follows:

$$\frac{\int_{j_+ + j_-} (I^{-1} - I^{+1})d\omega}{\int_{j_+} (I^{-1} - I^{+1})d\omega - \frac{\ell}{\ell-1}\int_{j_-}(I^{-1} - I^{+1})d\omega} = \frac{3}{2\ell}\frac{\langle L_z \rangle}{\langle S_z \rangle + \frac{2\ell+3}{\ell}\langle T_z \rangle} \tag{1.18}$$

In this case, the number of holes and the isotropic absorption cross-section minus the contributions originating from the continuum states are cancelled. The only difficulty which remains is the knowledge of the magnetic dipole contribution. For bulklike atoms in a cubic symmetry, this term can be neglect. Unfortunately, the Eq. 1.16 cannot provide $\langle L_z \rangle$ and $\langle S_z \rangle$ separately, but only their ratio.

1.1.4 Validity of the sum rules

The XMCD sum rule which relates the energy integrated XMCD signals for a given spin-orbit split absorption edge to the local spin and orbital magnetic moments shows clearly that XMCD is a powerful probe of magnetism in solids. Nevertheless, this sum rule was derived based on a single ion-atomic model with several approximations. Using Multiplet Theory, Sainctavit *et al.* showed that at the $L_{3,2}$-edges for cations of transition metals, the sum rules are rigorously verified [37]. Using FP-LAPW electronic band structure calculations, Wu *et al.* showed that the orbital spin sum-rule is valid within an error of 10%, whereas the errors of the spin sum rule are 40% for bulk Ni(001) (up to 50% for the surface), 20% for Co(0001) and 15% for Fe(001). This is essentially due to the difficulty to determine properly the number of holes from the isotropic absorption cross-section which is strongly affected by the intershell hybridization and the energy dependence of the radial matrix elements [31, 32]. Ankudinov and Rehr rederived the sum rules based on the independent electron approximation and the dipole approximation for transitions rates [38]. No assumption is made that the radial matrix elements are constant for all the transitions. Using a fully relativistic multiple-scattering formalism for spin polarized solids, Ebert showed that the estimation of the spin and orbital magnetic moment deduced from the sum rules for the corresponding calculated XMCD spectra is about 15% and 21% smaller respectively, compared to the directly calculated one [39]. Since this deviation seems to be systematic, it could be corrected by using a correction factor or by using the magnetic properties of a well studied reference system. In our case, we choose to apply the sum rules by using a reference sample. In 1998, Guo has rederived the XMCD sum rules within an itinerant model such as spin-polarized relativistic multiple-scattering theory with similar approximations as in the initial derivation [40]. So, the sum rules should not have particular fundamental problems for metallic systems simply because they were originally obtained from a localized ion model.

Experimentally, the XMCD sum rules were confirmed for Fe and Co bulk. The magnetic moments determined from XMCD spectra were found to be in excellent agreement for the orbital-to-spin ratio within 3% and in good agreement for the spin and orbital moments separately within 7% with those obtained from Einstein-de Haas gyromagnetic

ratio measurements [41]. The accuracy for the ratio is better mainly because the number of holes drops out. Finally, despite the theoretical limitations, the sum-rules are still a powerful tool to determine orbital and spin magnetic moment which are the fundamental quantities for understanding the macroscopic magnetic properties of matter. No other experimental technique can provide so directly these quantities.

1.2 Data analysis

In this section, we will present a detailed discussion of the analysis of experimental data and the application of the sum rules in order to determine the spin and orbital magnetic moment. As examples, we will determine the spin and orbital magnetic moment by applying the sum rules to the absorption and XMCD spectrum measured at the $L_{3,2}$-edges of a thick bulklike Co/Cu(001) and a 15ML Ni/Cu(001) films. We will give details of the analysis and present the different sources of errors and uncertainties[1].

1.2.1 Normalization of the absorption spectra

The XMCD signal can be obtained by taking the difference of the absorption spectra for left and right circularly polarized x-ray light with a fixed magnetization direction. Also, it is equivalent to take the difference of the absorption spectra by inverting the magnetization direction for a fixed polarisation [42]. Figure 1.4 represents the quasi total electron yield spectrum for a bulklike Co film. The spectra were recorded at 300K which is far away from the Curie temperature (1390K). It is known that the total electron yield $Y(\omega)$ is related to the absorption coefficient $\sigma(\omega)$ through the relationship $Y(\omega) \propto \hbar\omega\sigma(\omega)$. For the $L_{3,2}$-edges for the $3d$ transition metals, since the spin-orbit interaction ξ_c is much smaller compared to the threshold energy of the edges, it is not necessary to normalize the yield with the energy.

The first step is to match the two experimental spectra recorded with left and right circularly polarized light (or parallel and antiparallel magnetic fields) before and after the absorption edges. In the ideal case, the two spectra match directly without any correction. Indeed no magnetic signal is expected far before and after the absorption edges[2] There is some arbitrariness in the choice of the matching energy range. To get rid of this, it is strongly recommended to record spectra from 30eV before the L_3-edge until 40eV after the

---

[1]In order to perform comparisons, all the spectra presented in the figures have to be corrected for the polarisation degree and the incident angle.

[2]The corresponding Magnetic EXAFS signal after the $L_{3,2}$ absorption edges is 100 times smaller and so its influence is negligible.
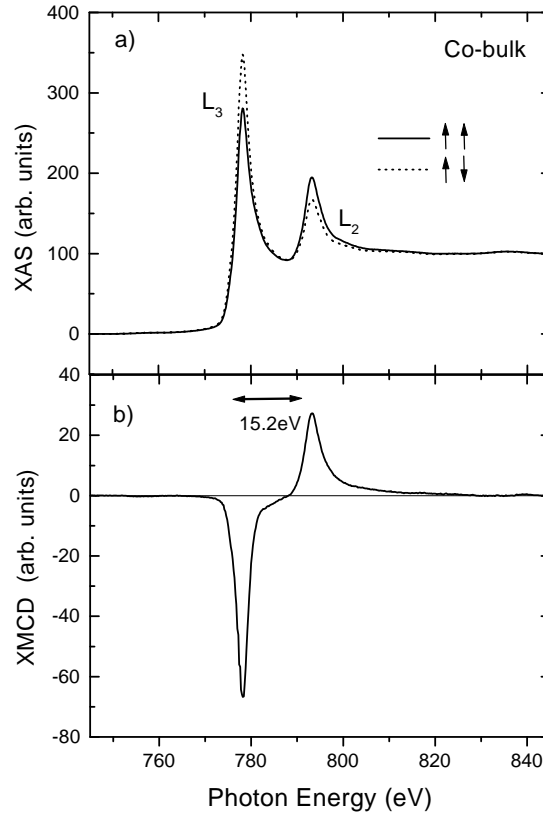
Figure 1.4: a)Absorption spectra for parallel and antiparallel magnetization direction with respect to the incident photon vector and b) XMCD spectra at the Co $L_{3,2}$-edges. The spectra are not corrected for saturation effects and polarisation degree. The spectra were recorded at 300K and at grazing incidence (70°).

L_2-edge. The number of the energy points per eV should be high enough (in our case, 6-10 points per eV). An integral value could depend on the density of the points. However, the main sources of errors upon collecting x-ray absorption spectra come from the detection mode (charging effect, dark current, electric and magnetic isolation, sensitivity, etc...), the instability of the x-ray beam, and of the optics (monochromator, mirrors, stepped motors). These have as a consequence to increase the noise and to modify the background and efficiency factors of the collected spectra. In our detection configuration (see §2.1), no charging effect exists since the sample is grounded. The instability of the x-ray beam and optics can be easily averaged out by taking at least 5 XMCD spectra. There are three different ways of normalisation which will be compared:

   i) The first method is to multiply by a correcting factor which should be near unity

in order to match the two absorption spectra taken with inverted polarizations or opposite magnetic field directions before the edges (30eV). The XMCD signal is then obtained by subtracting these two experimental spectra. If the two spectra are not matching after the edges, a slope need to be subtracted from the XMCD signal. The slope should be linear. The division of the two absorption spectra together allows to see directly if the shape of the slope is linear or not. If it is the case, the slope can be subtracted from the XMCD signal and from one of the two spectra.

ii) The second method is to subtract directly the two absorption spectra in order to
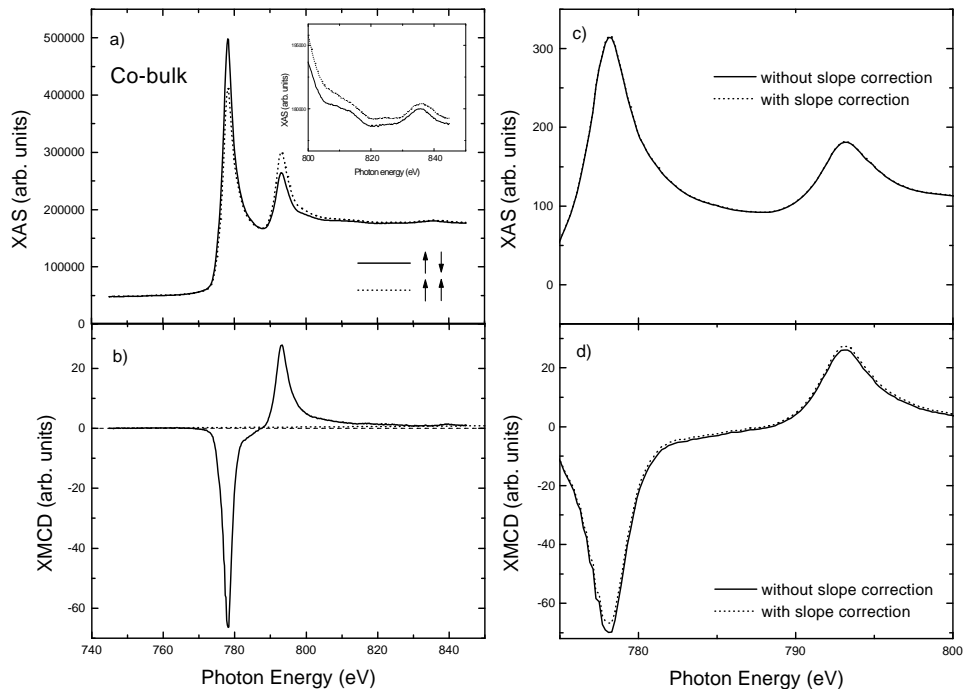
Figure 1.5: Influence of the slope correction in the absorption spectra and the XMCD signal. A Co bulk film is chosen as an example. a) Experimental absorption spectra for parallel and antiparallel magnetization direction with respect to the incident photons vector. b) the XMCD spectra after normalizing with the same factor the two absorption spectra. Note the non-vanishing XMCD signal at higher energy . c) No difference is observed in the isotropic absorption spectra with slope correction (first method) or without slope correction (third method). d) XMCD signal obtained by correcting the slope (first method) and without slope correcting (third method). A clear difference is observed. An incorrect normalization results in a wrong spin and orbital magnetic moment.

get the XMCD signal. Again, the division of the two absorption spectra allows for investigating directly the shape of the slope of the XMCD signal, if it is linear or not. If linear, the slope can be subtracted from the XMCD signal and from one of the two spectra.

iii) The two absorption spectra are each directly normalized from 0 to 100. The difference gives then directly the XMCD signal.

Thus, we found that the energy range of the measurement must be large enough to judge whether the shape of the slope is linear or not. If not, the spectra can not be corrected in a reliable way. In all the cases, to normalize directly the two absorption spectra from 0 to 100 and after to make the difference to obtain the XMCD signal gives erroneous results since this method skips "without solving" the problem the slope as we will show in Fig. 1.5. The two first methods presented above are in principle the same if the correcting factor is within 5% unity. From the Fig. 1.5, for a slope of 4%, the
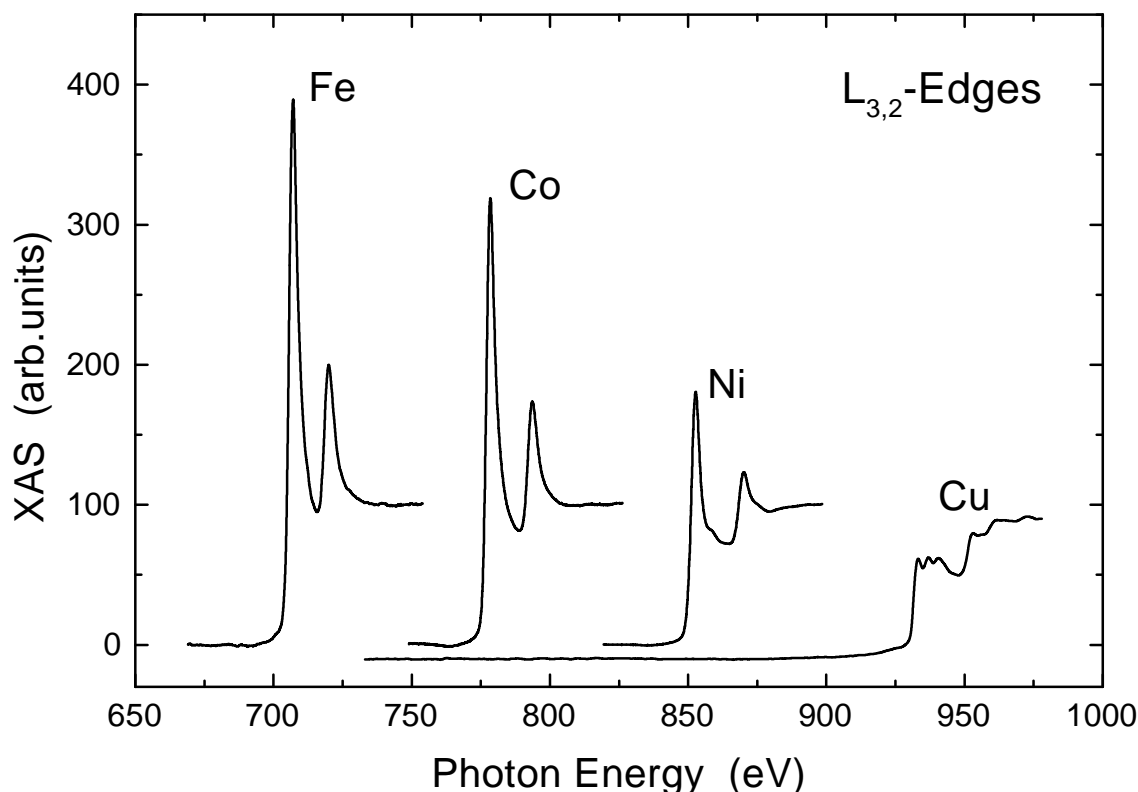
Figure 1.6: Isotropic absorption spectra of Fe, Co Ni and Cu measured at the $L_{3,2}$-edges. The spectra were normalized from 0 to 100. The Cu spectra was artificially shifted down in order to see clearly the linear background.

difference of the total integrated area of the XMCD signal is less than 1%. This difference will increase for larger slopes. We have used in our case the first method. This kind of effect occurs mostly for submonolayer coverages where the signal to background is not so important (less than 50%). The incident photon intensity plays also an important role. The higher the photon intensity, the lower the noise to signal ratio. The stability of the x-ray beam is much better controlled for synchrotron sources of 3rd generation. We will show in chapter 5, that with synchrotron sources of last generation, it is possible to probe small effects out of the error bars.

In the second step, we have to subtract the background slope from the two spectra. This background slope comes from the absorption decay with the photon energy. For thick films, the intensity of the background is small compared to the intensity of Co absorption spectrum. Since a line which has the same slope to the absorption signal before the edge (the first 15eV) can simulate easily this background. Since the Cu absorption spectra

Figure 1.7: Absorption spectra taken at the $L_{3,2}$-edges for parallel (dotted line) and antiparallel (solid line) magnetization direction with respect to the incident photon vector for a) Co bulk and b) 15ML Ni/Cu(001). The spectra are recorded at 50K.

before the $L_{3,2}$-edges, as depicted in Fig. 1.6, is linear and flat in the energy range (680-900eV), the same procedure can be applied for thinner Co films (in the monolayer range) grown on Cu(001). For films thinner than 1ML, this procedure could tilt slightly the spectra. By subtracting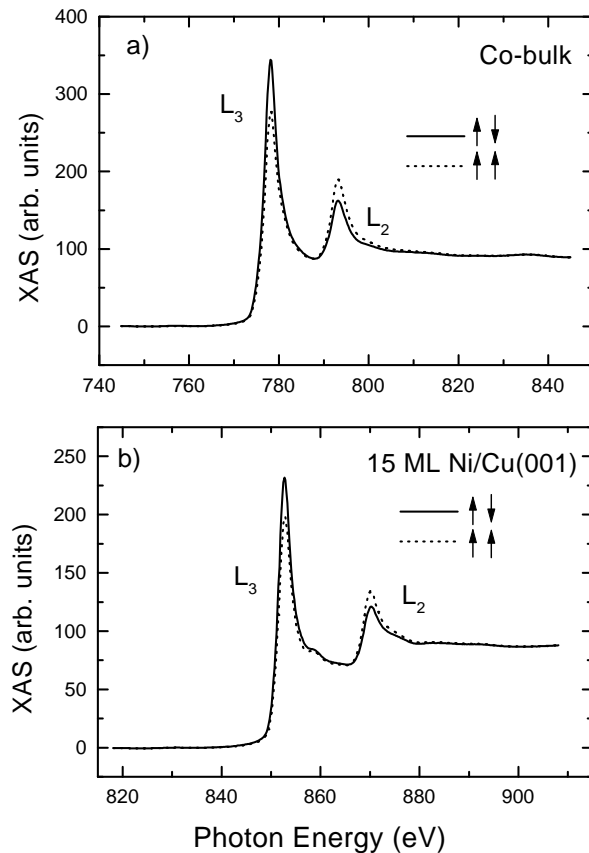 the same background from the two absorption spectra, the XMCD signal remains the same. This way of proceeding does not introduce any artefacts. The most important is always to extract first the XMCD signal which is independent of any background. In order to compare easily the spectra with literature, it is helpful to normalize the spectra by taking the top of the first EXAFS wiggle to be 1 or 100 arbitrary units (the same normalisation factor for the XMCD signal). The normalized absorption spectra for different magnetization direction for a thick Co (>50ML) and Ni (15ML) film on Cu(001) are illustrated in Fig. 1.7.

The isotropic normalized absorption cross-section for linear polarized light I^0 which we need to know for applying the sum rules is rarely measured. Instead, it is approximately equal to the average of the normalized absorption cross-section for left and right circularly polarized photons, so $I^0 \approx (I^{+1} + I^{-1})/2$ [38]. Only, for a polycrystalline sample, this relation is valid.

1.2.2   Correction for saturation effects

After a proper normalisation of the spectra, we need to correct them for the saturation effects. Saturation effects occur if the electron yield sampling is larger than or comparable to the absorption depth of the incident x-rays. They are strongly thickness- and angular-dependent. The saturation effects will be described in detail in §2.3. In Fig. 1.8, the normalized XMCD intensity for the thick Co/Cu(001) is presented before and after corrections of saturation effects . The easy magnetization direction is in the plane of the film and the measurements have been performed at an incident photon angle of $\theta = 70^o$ (with respect to the normal). The inset of Fig. 1.8 shows clearly that the saturation effects cannot be neglected. For the Ni film, since the easy magnetization axis is out of plane and the measurements were performed at normal incidence, there exists no saturation effect. Figures 1.9 and 1.10 show the isotropic absorption and the XMCD signal and their integral for a thick Co film and a 15ML Ni/Cu(001).

1.2.3   Determination of the ratio m_L/m_S^{eff}

For the determination of the ratio m_L/m_S^{eff} ($m_S^{eff} = m_S - 7m_T$), only the different areas of the XMCD signal are requested (see Eq. 1.16). The orbital-to-spin ratio is with the
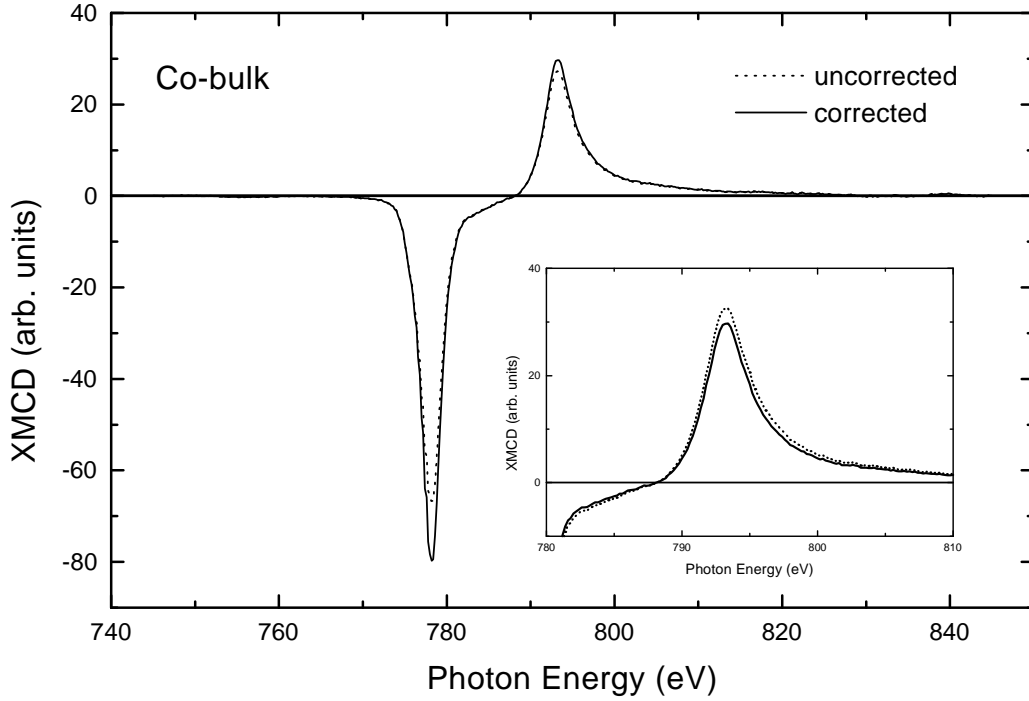
Figure 1.8: XMCD spectra for Co-bulk taken at 50K and under a grazing incidence of 20°. The uncorrected (dotted line) and corrected (solid line) spectra for saturation effects are shown. In the inset is presented an enlargement of the L_2-edges for the two spectra normalized at the same L_3 peak height.

following indices (see figure 1.9 and 1.10):

$$\frac{m_L}{m_S^{eff}} = \frac{2}{3}\frac{R+1}{R-2} \qquad (1.19)$$

with

$$R = \frac{\Delta A_3}{\Delta A_2} \qquad \Delta A_3 < 0, \quad \Delta A_2 > 2$$

The integration limits before the L_3- and after the L_2-edges are not critical if they are far away from the edges, i.e. 30-40eV before and 45-55eV after. The difficulty is to define the integration limit between the edge, since the edges are only separated by few eV (13.1eV for Fe, 15.2eV for Co and 17.3eV for Ni). The limit between the integrated areas of the L_3 and L_2 XMCD spectra is taken just below the onset of the XMCD L_2 edge where the signal is zero. Several difficulties have first to be eliminated as the *sp* magnetism and the magnetic dipole contributions.

Figure 1.9: Left, the isotropic absorption spectra (a) taken at the $L_{3,2}$-edges and its integral (b) for a Co bulk film. Right, the corresponding XMCD corrected for saturation effects (a) and its integral (b). The integration areas and their limit are also represented. The spectra were taken at 50K and at grazing incidence (70°).

The influence of the saturation effects

Often in the literature, the spectra are not corrected for the saturation effects. However, this effect has first to be corrected. In the case of Ni, there is no saturation effects for spectra measured at normal incidence. For Co, the saturation effects influence the ratio m_L/m_S^{eff} and in the same way the determination of the magnetic moments. For the thick bulk-like Co/Cu(001) measured under an incident angle of ($\theta = 70°$), we obtain a ratio:

$$uncorrected \quad Co \quad data: \quad m_L/m_S^{eff} \quad = \quad 0.084$$
$$corrected \quad Co \quad data: \quad m_L/m_S^{eff} \quad = \quad 0.095$$

The error due to the saturation effects is around 12% for this angle. Without this correction, the orbital moment determined by application of the sum rules will be underestimated, since the saturation effects have a larger influence on the orbital moment (see §2.3.).
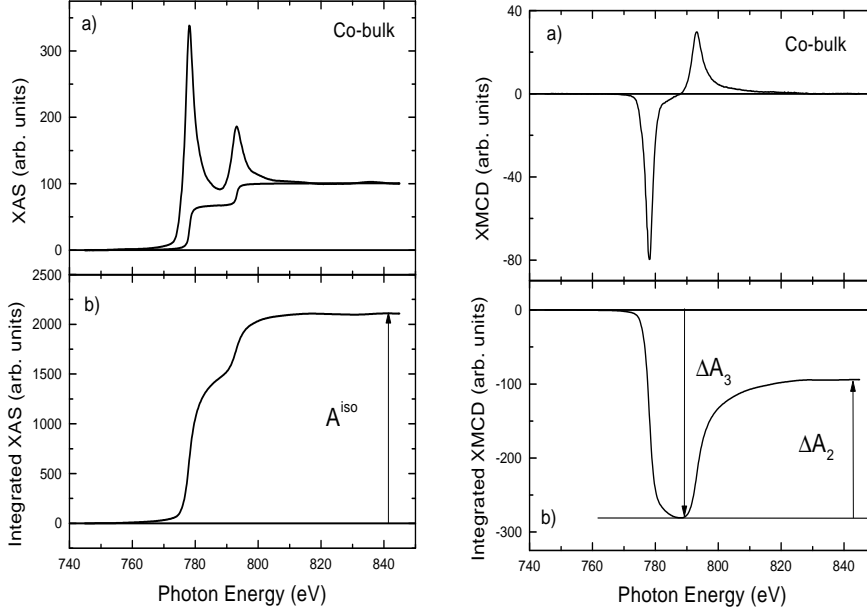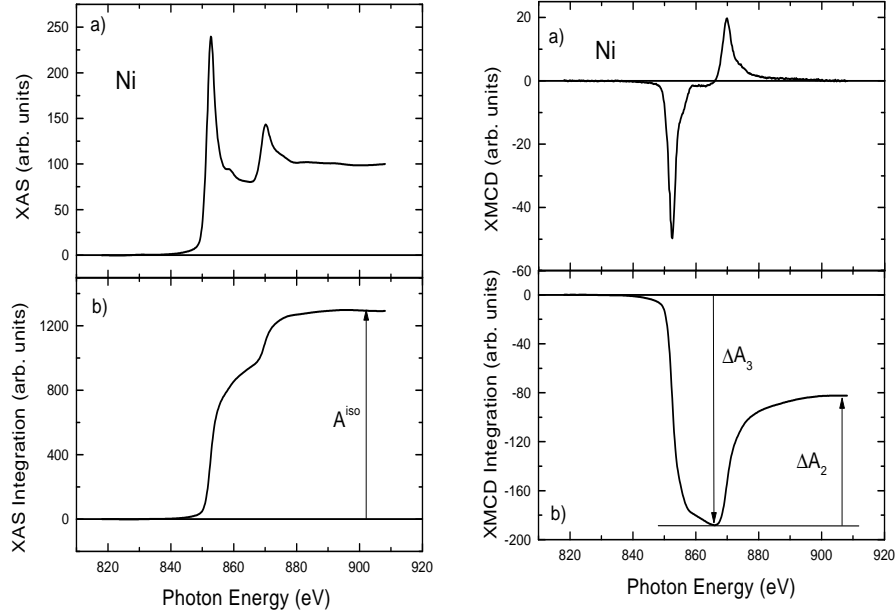
Figure 1.10: Left, the isotropic absorption spectra (a) taken at the $L_{3,2}$-edges and its integral (b) for a 15ML Ni/Cu(001) film. Right, the corresponding XMCD corrected for saturation effects (a) and its integral (b). The areas and their integration limit are also represented. The spectra were taken at 50K and at normal incidence.

For the 15ML Ni/Cu(001) film, the ratio is:

$$Ni \quad data: \quad m_L/m_S^{eff} \quad = \quad 0.137$$

This result for Ni does not need to be corrected.

The contribution of the sp magnetism

We can observe from Fig. 1.11 that for the $3d$ transition metals, the inter-edge XMCD signal is strongly positive for V and progressively decreases along the $3d$-series and becomes negative for Ni [43]. The XMCD signal between the L_3- and L_2-edges for Fe, Co and Ni does not disappear completely. The signal is positive for Fe, slightly negative for Co and negative for Ni. Since the spin-orbit splitting ξ_c is larger at the end of the $3d$-series, this inter-edge XMCD signal is easier sizeable. Controlled adsorption and gradual annealing of O_2 on Ni thin films revealed that the absorption intensity at the $L_{3,2}$-edges increases monotonously from pure Ni to NiO. The transfer of the electrons to the $2p$-

oxygen state leads to an increase of the Ni $L_{3,2}$ white line which is a direct measure of the density of the empty d states. Contrary to this, the absorption intensity between the two edges and above the L_2-edge (20eV) decreases. This is due to the strong hybridization between the $2p$-oxygen and the $4sp$-nickel states [44]. Indeed, the core-valence Coulomb interaction pulls down final states with localized $3d$-character compared to those with an s-character. The latter will be at higher photon energies. Recent experiments of Ni on Co/Cu(001) showed that the negative remaining Ni dichroism between the edge is ascribed to transitions into empty s states which are strongly polarized [45].

The spin contributions to the magnetic moments can be separated into $3d$ contribution and diffuse contribution, which is the sum of the sp magnetism and the interstitial moment. This latter part of the moment is mainly located at the interstitial region of the crystal atoms. The "diffuse magnetism" is, for instance, believed to be the reason why the moments measured by polarized scattering experiments differ from those measured
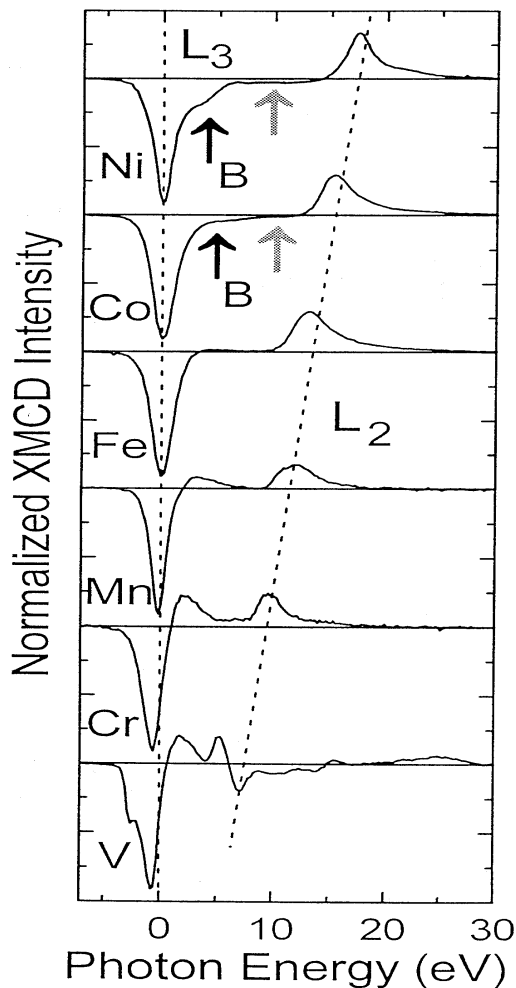

Figure 1.11: V, Cr, Mn, Fe, Co and Ni XMCD spectra at the $L_{3,2}$-edges shown normalized to constant L_3 peak height. The shoulder labelled B are due to multiple initial state configurations. The constant negative intensity features between B and L_2, gray arrows, is attributed to diffuse magnetic moments.

by magnetization measurements [46].

The sum rules treat only the $2p \longrightarrow 3d$ transitions and therefore do not take into account effects in the solid phase coming from the *spd*-wave mixing or from the overlap of the *sp* band and the *d* band. In the $3d$ transition metals, the $4s$- and $2p$-levels are hybridized to an $4sp$-band which is partially filled until the Fermi level. So, since transition into the *s*-states are possible from the dipole selection rules, and that the *s*-states are polarized, it will give some contribution to the XMCD signal even if the probability for $2p \longrightarrow 4s$ transitions is 50 times smaller than $2p \longrightarrow 3d$ transitions. The extraction of the $4s$-like contribution from the XMCD signal is not clear yet.

Because of the *s*-like character, we can assume that the $4sp$ orbital moment is $m_L^{4sp} = 0$. For $2p \longrightarrow 4s$ transitions, the sum rules indeed predict only a *s* spin moment which is of opposite sign to that of the *d*-spin moment. This means that the XMCD signal coming from the *sp* contribution should have equal intensity at the L_3- and L_2-edges but with opposite sign (same sign to the *d*-contribution), since the integrated intensity over both edges should vanish because the *s*-states have no orbital moment. Using this argument, a first method was proposed to describe the *s*-like contribution to the XMCD signal for Ni far above the L_3-edge by a triangle with height $2h$ and with a baseline of $\Delta E \approx 10eV$ and far above the L_2-edge by a triangle with height h and with a baseline of $\Delta E \approx 20eV$ as sketched in Fig. 1.12 [47]. Band structure calculations for Fe, Co and Ni predict negative diffuse magnetism due to the *sp*-projected and interstitial moments too [48]. The diffuse moment m_S^{diff} and the ratio of the diffuse moment to the *d* spin moment are summarized in table 1.1.

Under strong assumption $(m_S^s \approx m^{diff}/2)$, the height should be $h \approx 1\%$ for Ni ($\approx 0.6\%$ for Co, negligible for Fe) of the maximum L_3 XMCD intensity which is in the same order of magnitude with the XMCD intensity above the $L_{3,2}$-edges. So, the XMCD integrated intensity above the $L_{3,2}$-edges which corresponds to *sp* magnetism has to be eliminated in order to apply the sum rules. The second method based on the same principle was applied by O'Brien and Tonner only between the edges of Co and Ni/Cu(001) [49]. They

	Fe	Co	Ni
m_S^d ($\mu_B/atom$)	2.20	1.62	0.57
m^{diff} (μ_B/atom)	-0.04	-0.07	-0.04
m^{diff}/μ_S^d (%)	-2	-4	-7

Table 1.1: *Calculated d spin and diffuse moments in units of $\mu_B/atom$ and their ratio in % for bulk bcc Fe, hcp Co and fcc Ni [48].*
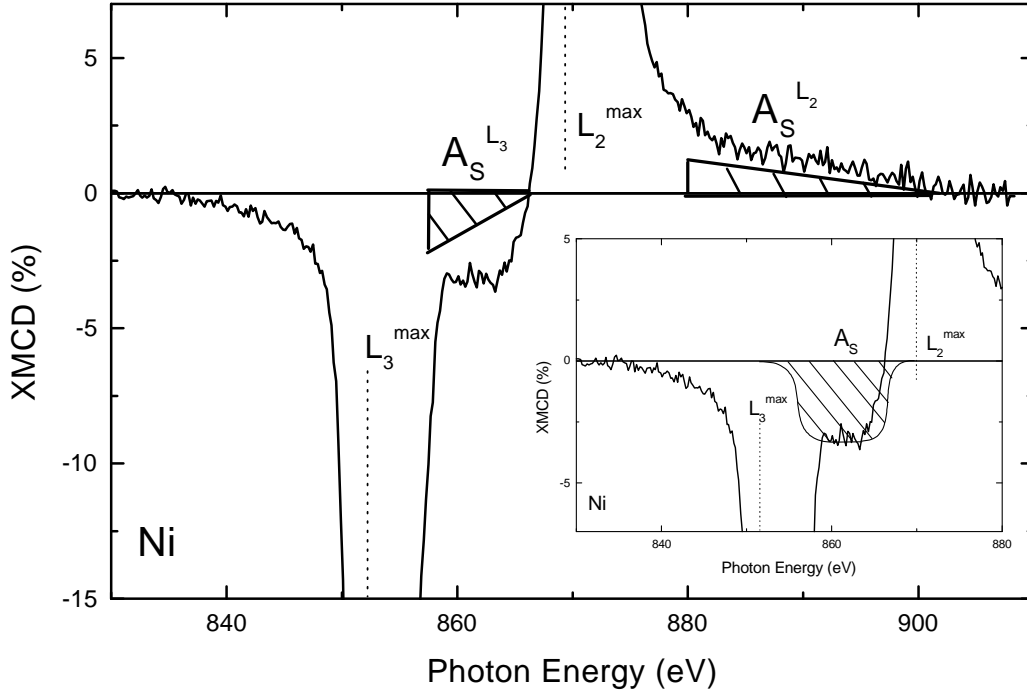
Figure 1.12: XMCD spectra of Ni taken at the $L_{3,2}$-edges. Schematic representation of the s-like contributions (noted by the triangles $A_S^{L_3}$ and $A_S^{L_2}$ which have the same areas). In the inset, we consider the s-like character only between the $L_{3,2}$-edges following Ref. [49].

subtracted the s-like contributions by taking out a quasi-quadratic area only between the edges as it is shown in the inset of Fig. 1.12. They simply argue without reasons that these s-like contributions are absent above the L_2-edge.

This argument was later apparently confirmed by Dhesi et $al.$ [45]. By decreasing the coverage of Ni on Co/Cu(001), the dichroic signal increases above the L_3-edge but not above the L_2-edge. This increase of the dichroism can only come from the s-like contribution since the satellite structure decreases for thinner coverage (less than 2ML). Above the L_2-edge, the dichroism decreases like the satellite structure for lower coverage. This is in contradiction to the argument that the s-like contribution should exist above the two edges. One possible explanation given by the authors is that the s and d states are strongly mixed, which becomes possible in lower than cubic symmetry, as for thin films. By following the two different methods , the corrected ratio after subtracting the

	Fe	Co	Ni
m_S (in $\mu_B/atom$)	2.25	1.63	0.58
m_L (in $\mu_B/atom$)	0.082	0.123	0.058
m_L/m_S	0.036	0.075	0.100

Table 1.2: *Calculated spin and orbital moments in units of $\mu_B/atom$ including the spin-orbit coupling as well as the orbital polarization for bulk bcc Fe, hcp Co and fcc Ni [5].*

s-contribution the Co-bulk are:

$$Co \quad ratio \quad (L_3 \quad and \quad L_2 \quad contributions) \quad m_L/m_S^{eff} \; = \; 0.098$$
$$Co \quad ratio \quad (inter-edge \quad contributions) \quad m_L/m_S^{eff} \; = \; 0.090$$

and for the 15ML/Cu(001):

$$Ni \quad ratio \quad (L_3 \quad and \quad L_2 \quad contributions) \quad m_L/m_S^{eff} \; = \; 0.142$$
$$Ni \quad ratio \quad (inter-edge \quad contributions) \quad m_L/m_S^{eff} \; = \; 0.120$$

Since for the first method, the orbital moment is not affected but only the spin moment is reduced, an increase of the ratio is observed. Concerning the second method, the spin moment and mostly the orbital moment are reduced which leads to a reduction of this ratio too. It seems that even if the first method is physically more realistic, the ratio differs from the theoretical calculated one as summarized in table 1.2 [5]. We will proceed using the same way proposed by O'Brien and Tonner who have taken into account only the contribution between the $L_{3,2}$-edges [49].

The $\langle T_z \rangle$ contribution

Usually, the dipole magnetic term $\langle T_z \rangle$ is neglected in the application of the sum rules on experimental data. As seen in §1.1.3, the dipole magnetic term can be important at the surfaces or interfaces where the symmetry is broken. One method proposed by Stöhr and König is to measure and to average the XMCD signal using an external magnetic field (large enough to magnetically saturate the sample) parallel to the incident photons along three orthogonal directions [36] or to measure directly at the "magic angle", 54.7° from the z axis. In this case, since $\sum_\alpha \langle T_\alpha \rangle \approx 0$, the effective magnetic spin $m_S^{eff} = m_S$. The spin moment is *a priori* isotropic (it is not angular-dependent). In this case, we know directly the magnetic spin moment. Another possibility is to perform fully angular-dependent measurements of the XMCD signal between the hard- and easy-axis for uniaxial systems

		m_S	$7m_T$
Fe	Surface layer	2.71	0.230
	Bulklike layers	2.10	0.028
Co	Surface layer	1.61	0.240
	Bulklike layers	1.52	0.014
Ni	Surface layer	0.67	-0.082
	Bulklike layers	0.62	-0.027

Table 1.3: *Calculated values of $7m_T$ in units of $\mu_B/atom$ for fcc Ni(001), hcp Co(0001) and bcc Fe(001) [32].*

(see §5.2). However for this task, measurements in an applied field are necessary. The calculated values of $7\langle T_\alpha \rangle$ are given in table 1.3.

For a thick bulklike Co film, the theoretical correction of the term $7m_T = 0.014\mu_B$, is indeed very small. For a 2ML Co/Cu(001) ultrathin film, we will consider that the interface layer is equivalent to a bulklike layer[3]. So, the theoretical correction will be $7m_T = 0.127\mu_B$. By performing high-field angle- dependent XMCD measurements on a Au/Co-staircase/Au, Weller *et al.* found for a thickness of $t_{Co} =$4AL, by using the approximate symmetry relation (Eq. 1.13), that $7m_T^{\parallel} = 0.112\mu_B$ and $7m_T^{\perp} = -0.224\mu_B$. Since the data follow a simple m_T/t_{Co} dilution law, they expect for a $t_{Co} =$2AL, a correction $7m_T^{\parallel} = 0.224\mu_B$ for the in-plane component [50]. Grange *et al.* found that for an fcc (111) $CoPt_3$, chemically ordered, an in-plane correction $7m_T^{\parallel} = 0.063\mu_B$ which is smaller compared to the precedent value [51]. This is due to the lattice distortion. Indeed, this correction increases as a function of the tetragonal distortion [36]. Since at the $L_{3,2}$-edges, $m_S^{eff} = m_S - 7m_T$, the m_S^{eff} needs to be corrected by $+1\%$ for Co bulk and by -4.1% for Ni bulk (we will consider that 15ML Ni/Cu(001) are bulk-like). The ratio will decrease for Co and increase for Ni by very few %.

Addition of the $4s$ and $4p$ magnetic moments

In order to have finally the spin magnetic moment, the $4s$ and $4p$ contributions have to be added. It was shown that the $4s$ and $4p$ have no contribution to the orbital moments, but they do have small negative contributions to the spin moments. The calculated $4s$ and $4p$ contributions to the spin moments in units of $\mu_B/atom$ for bulk and surface layers are summarized in table 1.4.

---

[3]This is realistic since they have the same coordination number.

		m_S^s	m_S^p	m_S^d	m_S^{tot}
Ni	bulk	-0.005	-0.017	0.570	0.548
	surface	-0.002	-0.012	0.600	0.586
Co	bulk	-0.008	-0.035	1.625	1.582
	surface	-0.008	-0.030	1.784	1.746
Fe	bulk	-0.006	-0.020	2.205	2.179
	surface	0.009	0.008	2.851	2.868

Table 1.4: *Calculated spd projected moments in units of μ_B/atom for fcc Ni(001), hcp Co(0001) and bcc Fe(001) [48].*

Using the calculated $4s/4p$ to $3d$ spin moment ratio, in order to have the total spin magnetic moment, the spin moment m_S^{3d} needs to be corrected by -2.6% for Co bulk and by -3.9% for Ni bulk.

The ratio m_L/m_S and the error bars

Now, we are able to determine more accurately the ratio m_L/m_S for our Co on Cu(001) bulklike and for the 15ML Ni/Cu(001) films. By using the calculated corrections for the m_T term and the $4s/4p$ contribution, we need to correct the above $m_S^{3d,eff}$ XMCD spin moment by only -1.6% for Co bulk and -8% for Ni bulk-like 15ML. After using these minor corrections, the ratio will finally be:

$$m_L/m_S = 0.0915 \pm 0.004 \quad for \quad Co$$
$$m_L/m_S = 0.130 \pm 0.006 \quad for \quad Ni$$

Finally, we are able to determine the orbital-to-spin magnetic moment ratio. Minor corrections have been used to correct these values. The Co ratio is in good agreement with experimental and theoretical and previous XMCD measurements [41]. Concerning the 15ML Ni/Cu(001), the ratio is higher than the 0.10 found experimentally and theoretically [26]. This higher value for Ni thin films comes from the strong perpendicular magnetic anisotropy. The error bars are typically 5%. The same ratios have been determined independently with XMCD and with FMR [52] (more details will be given in §5.1).

1.2.4 Evaluation of the number of n_h^d holes

To determine the spin and orbital moments separately, we need to know the number of holes n_h^d and the isotropic absorption cross-section $I^{iso} = (I^{+1} + I^0 + I^{-1})/3$ with

$I^0 \approx (I^{+1} + I^{-1})/2$. Experimentally, the latter is the factor which gives the most of the uncertainties. First, the continuum modelled by a two step-function has to be removed from the isotropic absorption spectrum. This procedure serves to eliminate the contribution from the continuum states. The height of the $L_3(L_2)$ step was set to $2/3(1/3)$ of the average intensity of the last 15eV of the isotropic absorption spectrum. The ratio $2 : 1$ is according to its quantum degeneracy, $2j + 1$. The calculated branching ratio is nearly equal to $1.75 : 1$ for Fe, Co and Ni , so lower than the ideal ratio $2 : 1$ [34]. Experimental data showed that the branching ratio is $2.4 : 1$ for Ni, $2.25 : 1$ for Co and $2 : 1$ for Fe [53]. In the initial derivation of the sum rule, j was assumed to be a good quantum number, that is an integer. So, if one uses a branching ratio different from the ideal one, the sum rules are not valid any more even if the coefficients are changed in the numerator. One of the other points that was discussed is the position of the thresholds for the two-step function. We will set the inflection point of the two-step function to the peak positions of the L_3 and L_2 white lines. A variation of the position for ± 1eV changes the integrated area of the absorption spectra by $\pm 5\%$ for Co. The two-step like functions and the integration of the isotropic absorption spectrum after continuum removal ($A^{iso} = I^{iso}-$continuum), are shown for Co and Ni in Fig. 1.9 and 1.10. For the number of holes n_h^d, we used the value 2.43 for bulk Co and 1.45 for Ni [54].

1.2.5   Application of the sum rules

To determine the absolute values of the spin and orbital magnetic moment, we have to follow the same method as used for determining the ratio of orbital-to-spin moment. First, we have to normalize properly the spectra, to correct for the saturation effects and then to eliminate the contribution for the *sp* magnetism. Then, we can apply the sum rule for the spin and orbital magnetic moment with the following indices (see figure 1.9 and 1.10). The obtained values have to be corrected by the incident angle of photons θ and the incomplete degree of polarisation P_C:

$$m_S^{eff} = -\frac{2n_h}{P_C cos\theta} \cdot \frac{\Delta A_3 - 2\Delta A_2}{2A^{iso}} \qquad (1.20)$$

$$m_L = -\frac{4n_h}{3P_C cos\theta} \cdot \frac{\Delta A_3 + \Delta A_2}{2A^{iso}} \qquad (1.21)$$

By taking into account the m_T term and the $4s/4p$ contributions by correcting the m_S^{eff} with -1.6% for bulk Co, we are able to determine the spin moment. The degree of polarisation can be evaluated with high precision experimentally. For this, we fixed the spin magnetic moment to be $m_S = 1.55(\mu_B)$, taken from Chen *et al.* which was determined

	m_S	m_L	m_{tot}	m_L/m_S
Co-bulk	1.55	0.142 ± 0.01	1.69 ± 0.01	0.092 ± 0.01
Ni-15ML	0.61 ± 0.08	0.075 ± 0.01	0.69 ± 0.1	0.130 ± 0.03

Table 1.5: *Experimentally determined spin and orbital magnetic moments in μ_B/atom for bulk Co and 15ML Ni films on Cu(001).*

with high precision XMCD experiments [41]. By comparing with our value, we found that the degree of polarisation is $P_C = 0.73 \pm 0.05$ which agrees with the calculated one ($P_C = 0.65$ for $\pm$ 0.3mrad [55]). Later, it was determined experimentally with polarimetry which confirmed very well our value [56]. Since the Co data were measured along the [100]-axis in plane, and that the easy axis of magnetization is along [110], we need to correct by multiplying by $\sqrt{2}$. We obtain the spin and orbital magnetic moment shown in table 1.5.

These experimental results are in good agreement with the ones given in the literature [57]. Thus, it appears that the sum rules have a reliability of 10% for an absolute moment determination and even more for moments determination relative to a standard, measured under the same conditions.

1.3 Conclusion

We described here the basic principles of the XMCD spectroscopy technique. The power of this technique is its ability to determine element-specific spin and orbital magnetic moments using magneto-optic sum rules. So, the XMCD has become of great importance to probe the macroscopic magnetic properties of matter. In association with EXAFS (MEX-AFS), and by performing temperature-dependent measurements, it is possible to probe local spin fluctuations [58]. In conjunction with a small oscillatory field, it is possible to perform element-specific *ac*-susceptibility XMCD measurements to determine element-specific Curie temperatures [59]. Today, the explosion of new techniques like the x-ray resonance magnetic scattering allows to identify the presence of antiferromagnetic and ferromagnetic exchange coupling [60], and further to quantify magnetic-domain structures [61]. Recent development in the x-ray magnetic spectrometry allows us to image ferromagnetic [62] and even antiferromagnetic domains [63]. One should not forget, that the development of all these new spectroscopic techniques are essentially possible due to development of third-generation x-ray synchrotron sources.

Chapter 2

Experimental details

In this chapter, we will describe the experiments performed at BESSY-I and at the ESRF. These concern, respectively, the measurements on ultrathin, trilayer (chapter 3, 4) and multilayer systems (chapter 5,6). In the last section, we will discuss the saturation effects which occur in the electron yield measurements. They are strongly thickness-and angle-dependent. The saturation effect corrections are not negligible in the case of multilayers. By not taking them into account in the data analysis, erroneous conclusions can be drawn.

2.1   Measurements at BESSY

The measurements using single crystals as substrate were performed at the *Berliner Elektronenspeicherring-Gesellschaft für Synchrotronstrahlung* (BESSY-I)[1]. These concern the measurements presented in Chapters 3 and 4. BESSY-I was a second generation type synchrotron radiation source. BESSY-I was operated at 800MeV. Since 1998, BESSY-II is operating.

In this work, the XMCD measurements were carried out at the Co, Ni $L_{3,2}$-edges located in the soft X-ray regime at (778.1, 793.3eV) and (852.7, 870.0eV), respectively. For XMCD measurements elliptically polarized x-rays were used which were provided by the SX-700/III (PM3) plane-grating monochromator at BESSY-I [55]. A schematic view of the SX-700/III beamline at BESSY-I is given in Fig. 2.1. The unique feature of this beamline was the mirror system (before the monochromator). It was designed to extract the elliptically polarized light out of the electron-orbit plane (angle ψ) and to redirect it into the monochromator. Two different setups for the out-of-plane angle ψ were used. The out-of-plane angle could be adjusted to $\psi = \pm 0.3$mrad or $\psi = \pm 0.6$mrad. This corresponds to a degree of polarisation of about $P_c = 0.73 \pm 0.05$ and $P_c = 0.84 \pm 0.05$,

---

[1]The last official electron in BESSY-I was circulating the 15 December 1999.
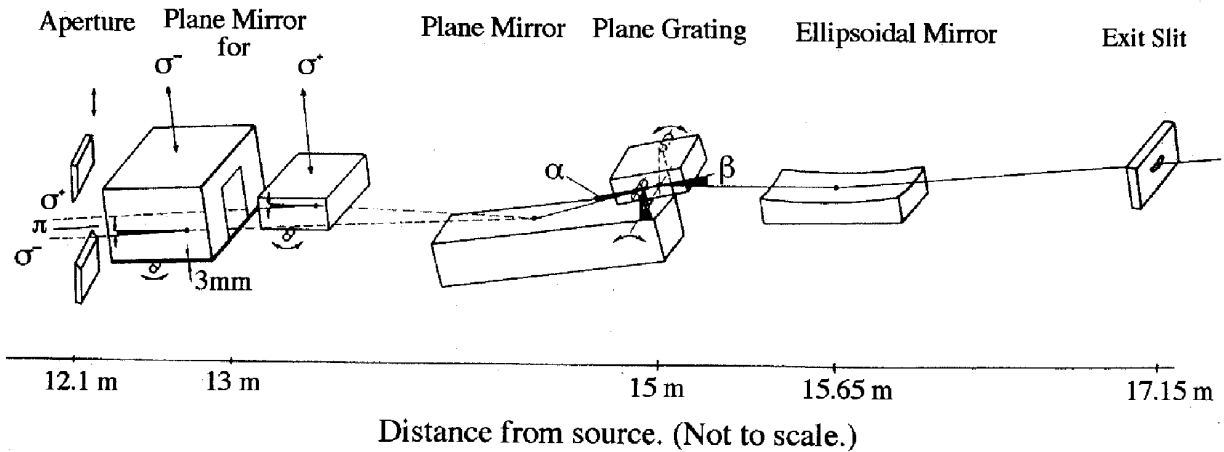
Figure 2.1: Schematic illustration of the SX-700/III monochromator at BESSY-I.

respectively. The degree of polarisation was determined experimentally by using a thick Co sample considered as bulk (see §1.2.). Mostly, we were working with a fixed helicity and reversing the applied external magnetic field. By keeping the helicity constant, the stray light contribution remains the same for all the spectra. Then, the background is identical and the data can be compared to each other. Changes could result only from beam and optical instabilities, but their contributions are negligible since a set of same samples showed the good reproducibility of the data.

All the data were measured with a $50\mu m$ exit slit and with 1200lines/mm grating. The energy resolution was evaluated via the La $M_{4,5}$-edges of a $LaAl_2$ sample for every beamtime. The energy resolution ΔE was found to range from 1.51eV for Fe to 1.7 for Ni $L_{3,2}$-edges [64].

All the samples were prepared *in situ* in an ultra-high vacuum (UHV) chamber [47, 66]. The UHV chamber is equipped with various surface characterization techniques, such as low and medium energy electron diffraction (LEED and MEED) and Auger electron spectroscopy (AES). The base pressure of the chamber is $2 \cdot 10^{-10}$ mbar. The sample can be cooled with liquid helium down to ~30K using a commercial cryostat. The temperature was measured directly at the sample using a thermocouple. The cromel/alumel thermocouple was calibrated with an absolute uncertainty smaller than 1K in the non-linear regime. Concerning temperature-dependent XMCD measurements, the temperature in the range of 35-300K was stabilized down to ±0.25K using a commercial feedback heating system mounted at the tip of the helium transfer tube. This does not introduce any electrical perturbation which could distort our detection system.

The samples were magnetised *in situ* by a pulse driven coil (details can be found in Ref. [67]). A current pulse (FWHM of ~5ms) of maximum intensity 340A applied to
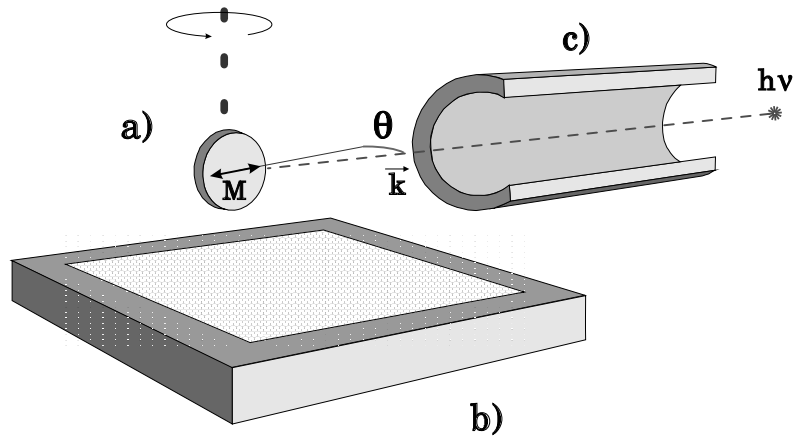
Figure 2.2: Schematic illustration of the experimental setup used at BESSY-I. The synchrotron radiation passes through the coil (c) and hits the sample (a) under a variable incidence angle θ. The microchannel plate which measures the quasi total electron yield is mounted below the sample. The direction of the magnetization was reversed using the coil. The distance between the sample and the coil is 2cm.

the coil leads to a maximum field of 3.7kG at the sample position. This field is largely sufficient to magnetise and to reverse the magnetisation of ultrathin films like Fe, Co and Ni. The XMCD intensity signal was not changing by applying different field amplitude. A schematic view of the experimental setup used in Bessy-I is shown in Fig. 2.2.

The x-ray absorption measurements were carried out with quasi total electron yield (also called partial electron yield) using a microchannel plate detector (chevron model). A retarding voltage was used to discriminate low kinetic electrons. The electron yield signal is composed of photoelectrons, Auger electrons and secondary electrons generated from the inelastic cascade process of the high energy primary electrons. The high-energy Auger electrons created in the core hole decay are predominantly responsible for the secondary electron signal which dominates the total electron yield [68]. The total electron yield is known to be proportional to the absorption coefficient [65, 69, 70]. More details about the detector characteristics and setup can be found in Ref. [71]. The electron yield signal was then normalized to the incident photon intensity measured via a gold grid placed before the coil. The noise-to-signal ratio is typically 10^{-3} for an background signal normalized to unity. The advantage of such detection mode is its high surface sensitivity but it suffers from saturation effects which will be discussed in §2.3.

2.1.1 Film preparation

The ultrathin films and trilayer systems (chapter 3 and 4) were evaporated on a Cu single crystal. The Cu single crystal was cleaned by means of Ar-sputtering ($E = 1 - 3$keV and $p_{Ar} = 2 - 3 \cdot 10^{-6}$mbar) and annealing (up to 900K) cycles. This crystal preparation needs between 30-50 cycles in order to obtain a surface free of impurities. The surface was then examined by LEED and AES. The sample was heated to temperatures above room temperature (300-1000K) by electron bombardment at the back of the sample. The same procedure with fewer cycles is used to remove an evaporated film.

The ultrathin films were prepared *in situ* using commercial e-beam evaporators. The evaporation materials consisted of Co, Ni and Cu wires (2mm diameter) with a purity higher than 99.998%. During evaporation, the base pressure stayed below $7 \cdot 10^{-10}$mbar. The evaporation rates are controlled via a flux monitor. Typically, the evaporation rates were 0.4-0.8ML/min for Co and Ni and 0.2ML/min for Cu. The films were evaporated at room temperature.

2.1.2 Film characterisation

The relative thickness d of the film can be determined using the so-called jump ratio $J_R(d)$, which is given by the ratio signal/background at the minimum between the $L_{3,2}$-edges. The absorption spectra were measured with linearly polarized light and with an incident angle normal to the surface. The calibration in absolute thickness was done using
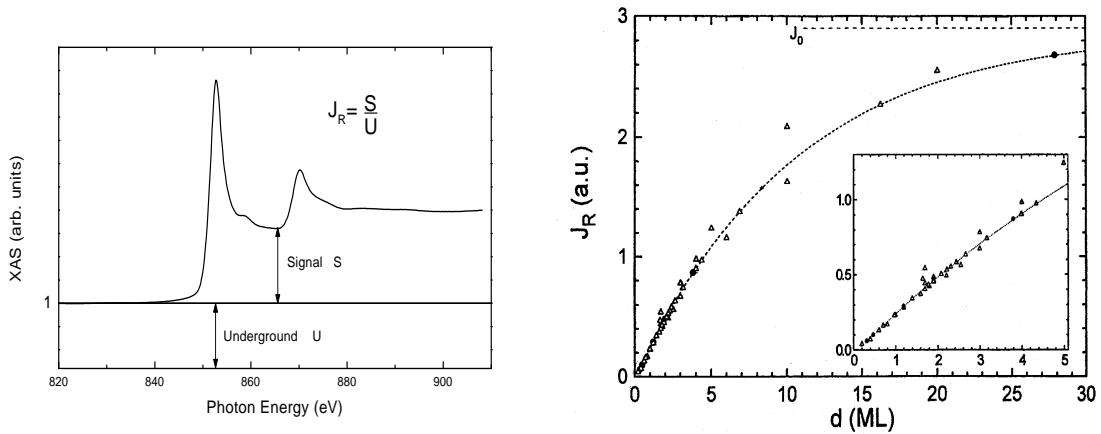

Figure 2.3: Edge jump ratio definition (left) and edge jump ratio as a function of the film thickness for Co and Ni film on Cu(001) [47]. From the edge jump ratio using the Eq. 2.1, the electron escape depth was estimated to be 17Å. The inset shows an enlargement of the edge jump ratio for film thicknesses below 5ML.

an accurate quartz crystal balance, MEED oscillations and Auger intensities [47]. Figure 2.3 shows the edge jump ratio as a function of the absolute thickness for Co and Ni. For films thinner than 4ML, the edge jump increases quasilinearly and is constant for very thick films. The saturation of the edge jump comes from the finite electron escape depth. The accuracy of the thickness for films thinner than 3ML is 0.1ML. For thicker films, the accuracy is 0.25ML. Above 30ML, a thickness determination using the edge jump is not possible. The edge jump ratio is then given:

$$J_R(d) = J_0 \cdot \left(1 - e^{-dn/\lambda_e}\right) \tag{2.1}$$

where d is the thickness of the film in ML, n the interlayer distance and λ_e the electron escape depth. For fcc-Co and fcc-Ni bulk the interlayer distance n is 1.77Å/ML and 1.76Å/ML, respectively. However, Ni and Co grow with an fct phase on Cu(001) and a contraction of only $\sim$2% is observed for the interlayer distance which can be considered as negligible. The edge jump saturation was estimated via a bulk film and the Cu crystal to be $J_0 = 2.90(3)$. Using Eq. 2.1 and the above parameter, an electron escape depth for Co and Ni was found to be $\lambda_e =$17Å with an experimental error of $\sim 10\%$ [47]. The electron depth depends essentially on the crystallographic and electronic structure.

2.2 Measurements at the ESRF

The measurements of the multilayers Ni/Pt, Fe/T(T= W, Ir) (chapter 5 and 6) were carried out at the hard x-ray beamline ID12A (W, Ir and Pt $L_{3,2}$-edges) [75] and the soft x-ray beamline ID12B (Ni $L_{3,2}$-edges) [76] at the *European Synchrotron Radiation Facility* (ESRF) located at Grenoble, France. The ESRF is a third generation synchrotron operating with electrons of 6GeV. The straight section ID12 of the machine is currently equipped with two helical undulators units: Helios-I (0.5-8 keV)and Helios-II(3-20 keV). The Helios type of helical undulator has one magnet array that produces a vertical modulated field, as in a normal undulator. The other array is specially designed to produce a horizontal modulated field, that introduces a vertical polarisation component in the light. By longitudinal phasing of the magnetic arrays, the polarisation of the undulator emission can be changed from linear to elliptical and circular. Asymmetric variations of the undulator half gaps allow the user to select the ellipticity and the azimuthal angle for elliptically polarised radiation. Helios-I is used by the grating optics beamline ID12B and Helios-II by the crystal optics beamline ID12A. The photon flux at the sample is typically 10^{10}-10^{12}ph/s/100 mA (depending on the resolution).

The monochromator on the beamline ID12A is a double-crystal monochromator with fixed exit whereas for ID12B it is a spherical grating monochromator Dragon type. Typ-

ically, the resolution is $\Delta E/E \sim 10^{-4}$. The degree of polarisation was $P_c = 0.84$ (Pt, Ir and W $L_{3,2}$edges) for ID12A and $P_c = 0.85$ (Ni $L_{3,2}$-edges) for ID12B, respectively.

The samples were measured *in situ* in high vacuum (10^{-8}mbar). The advantage of the beamlines is first the ability to reverse the helicity of the x-rays light routinely and to apply a constant external magnetic field up to 7T. The samples can be cooled in the temperature range from 10 to 300K. The detection mode used at ID12A is the fluorescence yield and in ID12B the total electron yield. The advantage of the fluorescence yield is its bulk sensitivity contrary to the total electron yield which is surface sensitive. However, the fluorescence yield can suffer from self-absorption effects. More details about the experimental setup may be found in Ref. [77].

2.3   Electron yield saturation effect corrections

The saturation effects, also called self-absorption effects, are discussed in conjunction with fluorescence [72] or electron yield [49, 64] detection in x-ray absorption spectroscopy. Saturation effects lead to a recorded signal no longer proportional to the photoabsorption cross-section as the photon energy is varied. The saturation effects arise if the electron yield escape depth is larger or comparable to the x-ray penetration depth. This is the case for measurements done at grazing incidence depending on the sample thickness. These effects in the case of $3d$ transition metals have been discussed by several authors [47, 73]. Although the saturation effects are well known, they are not always taken into account in the data analysis yet. We will show that they can affect dramatically the determination of the orbital and also the spin magnetic moment. All the models developed consider the case of a single film on a substrate. Unfortunately, no model has been extended for the case of multilayers. This will be presented here.

The absorption coefficient μ is defined as the inverse of the x-ray penetration length (or x-ray attenuation length $\lambda_x = 1/\mu$). The x-ray penetration depth is then defined by $\lambda_x\cos\theta$ as depicted in Fig. 2.4 [73]. In a simple picture, the saturation effects can be illustrated as following: if we assume that the x-ray penetration is much shorter than the electron escape depth ($\lambda_x\cos\theta \ll \lambda_e$), all the incident photons will be converted into photoelectrons. Therefore, the photoelectron signal will be proportional to the incident photon intensity I_0 and not to the absorption coefficient μ. This illustrates the saturation effects very well.

Let us now describe in detail the saturation effects. First, the number of electrons (mostly Auger electrons), which reach the surface $dY_e(z)$, decay exponentially as a func-

tion of depth [65]:

$$dY_e(z) = dY_{e,0}(z)e^{-z/\lambda_e} \tag{2.2}$$

where z is the depth from the surface in Å and $dY_{e,0}(z)$ the number of electrons produced in a thickness dz at the depth z which itself is given by [65]:

$$dY_{e,0}(z) = I_0 e^{-\mu z/cos\theta} \frac{\mu dz}{cos\theta} \tag{2.3}$$

where I_0 is the number of incident photons and θ the angle from the normal. We will then obtain the electron yield intensity $Y_e(E)$ by combining Eqs. 2.1 and 2.2 (i denotes the element):

$$Y_e(E) \sim \int_0^d \frac{\mu_i(E,z)}{cos\theta} e^{-\int_0^z \left(\frac{\mu_i(E,z')}{cos\theta} + \frac{1}{\lambda_e(z')} \right) dz'} dz \tag{2.4}$$
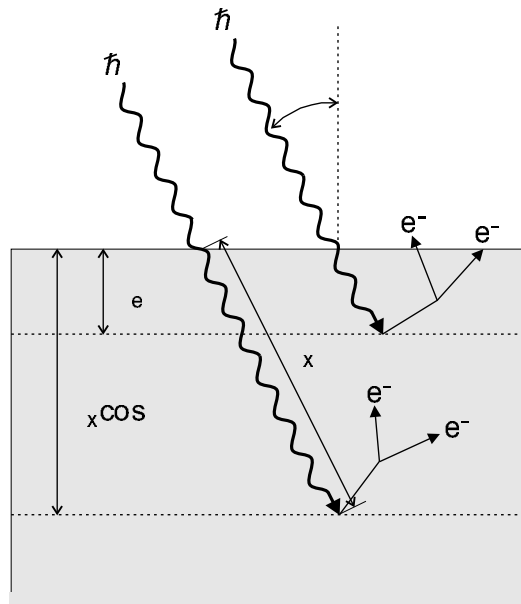

Figure 2.4: Qualitative description of electron yield method for x-ray for absorption [73].

2.3.1   Semi infinite thick film

For a semi infinite thick film, by integrating over the depth z from $z = 0$ to $z = \infty$, the measured yield $Y_e(E)$ intensity for the total electron yield[2] detection is then:

$$Y_e(E) \sim \frac{\mu(E)}{\mu(E) + \frac{1}{\lambda_e} cos\theta} \tag{2.5}$$

where $\mu(E)$ is the absorption coefficient, λ_e the electron escape depth[3] and θ the x-ray incidence angle from the surface normal.

The x-ray attenuation length for the two different elements Ni and Co before the L_3-(pre-edge) and after the L_2-edge (post-edge) studied here are summarized in table 2.1 [74]. We see that the x-ray attenuation length is larger than the electron escape depth which was estimated to be around 17Å for Co and Ni using the edge jump as a function of the thickness (this value concerns the measurements done with our Bessy setup). Directly at the white line, the x-ray attenuation length is strongly reduced and for small angle θ it is not more negligible compared to $cos\theta/\lambda_e$.

	λ_x in (Å) before L_3 [energy]	λ_x in (Å) after L_2 [energy]
Co	5344 [745eV]	850 [835eV]
Ni	5791 [820eV]	909 [910eV]

Table 2.1: Calculated x-ray attenuation length (in Å) for Co and Ni before their L_3-edge and after their L_2-edge, respectively [74].

From Eq. 2.4, we see clearly that for normal incidence ($\theta=0^0$), $\mu \ll cos\theta/\lambda_e$, the electron yield intensity is proportional to the absorption coefficient, $Y_e(E) \sim \mu(E)$. In the case of very small incident angle ($\theta \sim 90^0$), $\mu \gg cos\theta/\lambda_e$, the electron yield intensity $Y_e(E)$ becomes constant, regardless of the absorption coefficient.

The method to correct the spectra from saturation effects has been reported by Hunter Dunn *et al.* [64]. The spectra measured with left and right circularly polarized x-rays have to be corrected separately and to be normalized from 0 to 100. Then the spectra measured under an incident angle θ need to be stretched linearly to the corresponding theoretical values $Y_e(\mu_{pre-edge,\theta})$ and $Y_e(\mu_{post-edge,\theta})$. Each absorption coefficient $\mu(E)$ corresponding

---

[2]It is also valid for partial electron yield. The only difference lies in the evaluation of the electron escape depth due to the retarding voltage.

[3]The electron escape depth is also energy dependent. However, for the L-edges of Fe, Co and Ni, we can consider it to be constant.

to the experimental yield spectra $Y_e(\mu(E), \theta)$ will then be calculated. Using Eq. 2.4, the corresponding yield $Y_e(\mu(E), 0)$ for $\theta=0^o$ can be deduced and stretched linearly again in order to obtain the normalized corrected experimental spectra:

$$data(E, \theta) \times k_{11} + k_{22} = Y_e(\mu(E), \theta) \tag{2.6}$$

$$data_{corr}(E, 0) = k_1 + k_2 \times Y_e(\mu(E), 0) \tag{2.7}$$

where $data(E, \theta)$ are the experimental spectra and $data_{corr}(E, 0)$ the spectra corrected for the saturation effects. This procedure has to be done numerically.

2.3.2 Film of finite thickness

The above description for semi-infinite thick samples can be extended to samples of finite thickness d on a bulk substrate. The electron yield signal contains two different contributions, the intensity of the absorption edges of the film and the background signal of the substrate, which are described by the absorption coefficient $\mu_f(E)$ and $\mu_s(E)$ respectively [47]. Assuming that the electron escape depth is the same for the film and substrate, the electron yield is then given by Eq. 2.4 with different integration range (0 to d for the film and d to ∞ for the substrate):

$$Y_e(E) \sim \frac{\mu_f}{cos\theta} \cdot \frac{1 - e^{-(\frac{1}{\lambda_e} + \frac{\mu_f}{cos\theta})d}}{\frac{1}{\lambda_e} + \frac{\mu_f}{cos\theta}} \quad + \quad \frac{\mu_s}{cos\theta} \cdot \frac{e^{-(\frac{1}{\lambda_e} + \frac{\mu_f}{cos\theta})d}}{\frac{1}{\lambda_e} + \frac{\mu_s}{cos\theta}} \tag{2.8}$$

where μ_s will be assumed to be constant in the energy range considered. Indeed, the x-ray attenuation length of Cu in the energy range of Co and Ni L-edges (745-910eV) increases from 3901Å to 6363Å. The decrease of the absorption coefficient is by a factor 5 less important than the absorption jump of Co or Ni. For Pt, in the same range (745-910eV), the x-ray attenuation length is almost constant: it changes only from 676Å to 814Å. From this value, we see that Cu is almost transparent in this energy range which is not the case for Pt.

In Fig. 2.5 the fraction of the values for the spin (left) and orbital (right) magnetic moment are plotted. The values are obtained by using the sum rules for uncorrected electron yield data relative to the ideal modelled unsaturated data as a function of the thickness of Ni bulk for grazing incidence (70° from the normal). We model the unsaturated data by using Eq. 2.6. We have taken an electron escape depth of 25Å. The change in the number of d-holes were taken into account. The Ni bulk spectra used for this modelling were measured at the ESRF at the ID12B soft x-ray beamline. We have chosen for μ_{Ni}(pre-edge) (inverse of the attenuation length) and μ_{Ni}(post-edge) the values given in table 2.1. Concerning the substrate, we have assumed an average value for the absorption
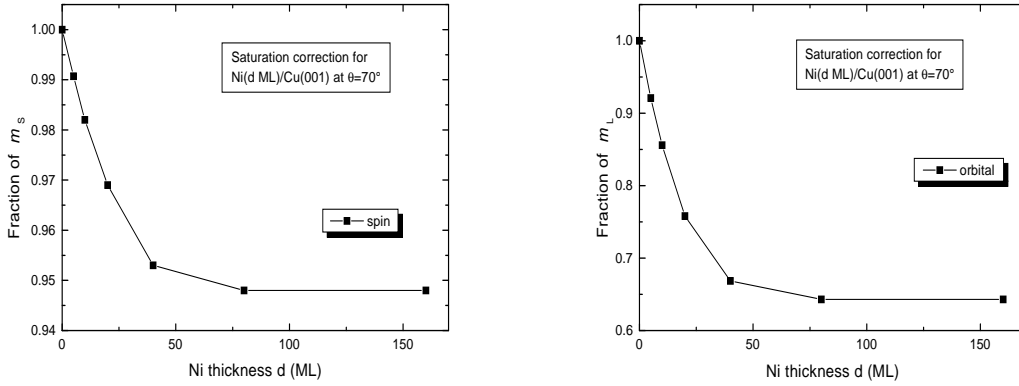
Figure 2.5: Saturation effects modelling in electron yield for bulk Ni as a function of the thickness of grazing incidence (70° from the normal). The fraction of the values for the spin (left) and orbital (right) magnetic moment is obtained by the sum rule analysis of electron yield data with respect to the ideal modelled unsaturated data. The escape electron depth is 25Å.

coefficient which is considered to be constant in the Ni energy range μ_{Cu} =17400cm^{-1}. We see that for low coverage of Ni on Cu(001)(lower than 5ML), the saturation effects are negligible, since the spin and orbital magnetic moment are only affected by less than 5%. By increasing the Ni coverage, the orbital magnetic moments is more affected by the saturation effects. This results from the fact that the saturation effects are larger for the L_3 than the L_2-edges. This is more reflected on the difference between the absolute dichroic intensities at the two edges (orbital moment) than on the sum of the two areas (spin moment). The saturation effects are maximum when the film thickness exceeds three times the electron escape depth. The orbital magnetic moment is artificially reduced by 35% whereas the spin magnetic moment by only 5% for 70° grazing incidence. We see clearly that the saturation effects are not negligible for thicker Ni films. For lower grazing incident angles (smaller than $\theta <70^o$), the saturation effects decrease, but they are not negligible. The saturation effects scale with the white line intensity, so they are more important for Co and even more for Fe (the white line is directly proportional with to the number of d-holes). Indeed, for Fe, the orbital moment can appear to be negative due to electron yield saturation for grazing angle of incidence larger than 70° [73]. It was also found that the saturation effects depend linearly on the degree of circular polarisation. Therefore, if one corrects first for saturation effects and after for incomplete circular polarisation the data or vice versa, this does not influence the final results.

2.3.3 Multilayer system

Sine we have measured in this work magnetic multilayers, we had to extend the above model to layered structure. The saturation correction for multilayer systems are often assumed to be negligible. We will show here that the assumption is not always correct. It depends strongly on the total thickness and the thickness of the layers in one repetition. Here, we will restrict our discussion to the Ni/Pt multilayer system. In chapter 5, we will study essentially the anisotropy of the orbital magnetic moment of Ni in Ni/Pt, so it is important to correct our data for saturation effects in order to determine the true orbital contribution.

The above description for samples of finite thicknesses can be easily transferred to multilayers. We consider the exact structure of the multilayers that were measured. We consider the Pt substrate were the multilayers are grown, the number n of multilayer periods, the thickness d_1 of Ni and d_2 of Pt and the thickness d of the Pt cap layer. The electron yield signal is composed of four different contributions, the signal coming from the cap layer, the intensity of the absorption in the Ni and Pt layers in the multilayers and the background signal of the substrate (then d Pt/d_1 Ni/$[d_2$ Pt/d_1 Ni$]_n$ / Pt substrate). Assuming that the electron escape depth is the same for the film and substrate, the electron yield is then given by Eq. 2.4 with different integration range (0 to d for the cap, d to $d + d_1$ for the first layer of Ni, etc...), :

$$
\begin{aligned}
Y_e(E) \sim\ & \frac{\mu_{Pt}}{cos\theta} \cdot \frac{1 - e^{-(\frac{1}{\lambda_e} + \frac{\mu_{Pt}}{cos\theta})d}}{\frac{1}{\lambda_e} + \frac{\mu_{Pt}}{cos\theta}} + \\
& \frac{\mu_{Pt}}{cos\theta} \cdot \frac{1 - e^{-(\frac{1}{\lambda_e} + \frac{\mu_{Pt}}{cos\theta})d_2}}{\frac{1}{\lambda_e} + \frac{\mu_{Pt}}{cos\theta}} \cdot \left(\sum_1^n e^{-\left(\frac{d + nd_1 + (n-1)d_2}{\lambda_e} + \frac{\mu_{Ni} nd_1}{cos\theta} + \frac{\mu_{Pt}(d + (n-1)d_2)}{cos\theta} \right)} \right) + \\
& \frac{\mu_{Ni}}{cos\theta} \cdot \frac{1 - e^{-(\frac{1}{\lambda_e} + \frac{\mu_{Ni}}{cos\theta})d_1}}{\frac{1}{\lambda_e} + \frac{\mu_{Ni}}{cos\theta}} \cdot \left(\sum_1^n e^{-\left(\frac{d + nd_1 + nd_2}{\lambda_e} + \frac{\mu_{Pt}(d + nd_2)}{cos\theta} + \frac{\mu_{Ni} nd_1}{cos\theta} \right)} \right) + \\
& \frac{\mu_{Pt}}{cos\theta} \cdot \frac{e^{-\left(\frac{d + (n+1)d_1 + nd_2}{\lambda_e} + \frac{\mu_{Ni}(n+1)d_1}{cos\theta} \right) + \frac{\mu_{Pt}(d + nd_2)}{cos\theta}}}{\frac{1}{\lambda_e} + \frac{\mu_{Pt}}{cos\theta}} \quad (2.9)
\end{aligned}
$$

First, we see that the formula for the multilayers is more complicated. If we assume now $n = 0$, and no cap layer, i.e. $d = 0$, the first and second term in Eq. 2.9 are then zero and we find again the same equation as in the case of a sample with finite thickness (Eq. 2.7).

In Fig. 2.6 the uncorrected XMCD spectra for Ni_2/Pt_2 multilayer (the indices represent the thickness in monolayers) measured at grazing incidence ($\theta = 60^o$)(solid line) are shown. For the correction of saturation effects, we used an electron escape depth of 25Å and assumed an average value of the absorption coefficient of the Pt substrate
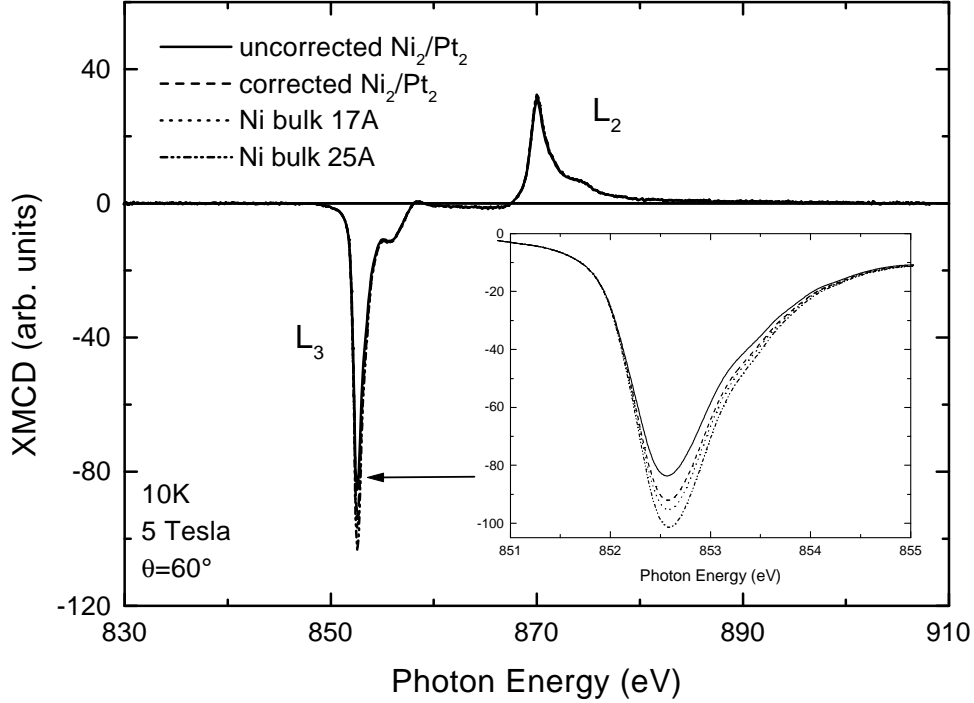
Figure 2.6: XMCD spectra at the Ni $L_{3,2}$-edges of Ni_2/Pt_2 before (solid line) and after correction of the saturation effects (dashed line) (the electron escape depth is 25Å). For comparison, the correction by assuming the multilayer to be Ni bulk with different electron escape depth in Å units. The uncorrected XMCD spectra of the multilayer were recorded at grazing incidence ($\theta = 60^o$) at 10K and under an applied magnetic field of 5 Tesla. In the inset an enlargement of the L_3-edge of Ni is presented for better view.

which is practically constant in the Ni energy range, $\mu_{Pt} = 128300 cm^{-1}$. After correcting for the saturation effects (dashed line), we see a clear increase of the XMCD intensity at the L_3-edges. In comparison, by assuming the same multilayer to be Ni bulk, the corrections are more important (short dashed line). We see that the XMCD spectra of the corrected multilayer lies just between the uncorrected and the bulk one. It is shown, also, the correction for Ni bulk with an electron escape depth of 17Å. The corrections are very sensitive to the electron escape depth which has to be determined accurately. We have seen before that the electron escape depth may be determined from the edge jump. It can also be determined by measuring a bulk sample at different grazing angles and applying the saturation effect corrections in order to obtain the bulk value given by the measurements performed normal to the surface (the anisotropy of the orbital moment in

	m_S in (%)	m_L in (%)	m_L/m_S in (%)
Ni$_2$/Pt$_2$	1	10.5	9.6
Ni bulk	2	20.2	18.6

Table 2.2: Calculated saturation effect corrections for a Ni$_2$/Pt$_2$ multilayer and the same multilayer considered as Ni bulk for a grazing incidence angle of 60° with respect to the corrected value.

bulk $3d$ transition metals is very small, see chapter 5, and thus a change in the spectra for different angles is not expected). The saturation effects are obviously larger for the bulk than for the multilayer.

The saturation corrections obtained after applying the sum rules with respect to the corrected value for Ni$_2$/Pt$_2$ multilayer and the same multilayer considered as Ni bulk are shown in table 2.2. We see that for an angle of incidence of 60° the saturation effect corrections are larger for the multilayer considered as Ni bulk. We see here, that the orbital magnetic moment has to be corrected by 10.5% with respect to the corrected value for the Ni$_2$/Pt$_2$ multilayer. This is almost the half compared to the same multilayer considered as Ni bulk. This is not negligible at all even for 60°. In the case of Ni/Cu, these corrections should be slightly larger due to a smaller absorption coefficient. For Co/Pt or Fe/Pt, these corrections should be much larger than in the case of Ni/Pt. In a first approximation, for thick multilayers, the saturation effect corrections at a constant angle seem to be proportional to the ratio $d_1/(d_1 + d_2)$.

In summary, we have demonstrated the necessity of correcting for satuartion effects the spectra of samples of finite thickness and also multilayer systems. Saturation effects have a strong influence on the estimation of the orbital magnetic moment and, to a less extent, of the spin moment. Erroneous conclusions can be drawn if the saturation effects are not taken into account.

Chapter 3

Magnetic properties of ultrathin films

The reduced dimensionality at solid surfaces can provide a variety of unusual electronic and magnetic properties absent in bulk materials. For $3d$ transition metals it is even more attractive since the electronic and magnetic properties are strongly sensitive to the structural and chemical environment of the atoms. The XMCD technique has demonstrated its ability to investigate the spin and orbital magnetism separately [41, 50]. By combining ultra-high vacuum experiments with XMCD, our group has been pioneer in investigating the orbital magnetism in ultrathin Co/Cu(001) films [47]. However previously, only the ratio m_L/m_S was determined to avoid the complication arising through some parameters like the number of d-holes or the polarisation degree. Our recent work enables us to use a realistic value for the number of d-holes [78] and a more sophisticated data analysis, hence making the separate determination of the spin and orbital moment possible.

In this chapter, the spin and orbital moment of ultrathin Co and Ni on Cu(001) and ultrathin Co on Cu(1 1 21) substrate in comparison to a Co bulk reference sample will be determined separately. We will show that the quenching of the orbital moment is partly lifted on the surface and at surface steps. We will show that the total magnetic moment are enhanced for 2ML Co on Cu(001) and on Cu(1 1 21) compared to Co bulk film. On the other hand, 4ML Ni on Cu(001) have reduced magnetic moments compared to Ni bulk-like film.

3.1   Ultrathin Co films on Cu(001)

Co/Cu(001) is the most studied system in the literature due to its layer-by-layer growth at room temperature in the 2-20ML thickness range and the small lattice mismatch between

Co and Cu. Previous experiments with XMCD have revealed an enhancement of the orbital magnetism at the surface of Co/Cu(001) [6] and Co/Cu(1 1 13) [79]. However, unfortunately, no direct determination of the spin and the orbital magnetic moment was carried out. Here, we will study the magnetic moments and separate the spin and orbital contributions, of 2ML Co on Cu(001) and Cu(1 1 21) in comparison to bulk Co by using the XMCD. The influence of stepped surfaces on the magnetic moments of Co will be discussed.

3.1.1   Growth and Structure

Co grows on Cu(001) substrate at room temperature in a perfect layer-by-layer mode above 2ML until 30ML [80]. Below 2ML, STM experiments at room temperature have reported a bilayer island growth depending on the deposition rate [81]. Density-functional theory calculations suggested indeed a bilayer Co island covered by copper as the lowest energy configuration [82]. However, kinetics plays an important role and, therefore, metastable structures may exist at surfaces. Recent experimental and theoretical studies focus on the initial stage of growth. Due to atomic exchange process between Co adatoms and Cu atoms on the surface, a bimodal initial growth mode has been identified [83]. Substitutional adsorption during the initial deposition of Co on Cu(001) gives rise to formation of large Co-decorated Cu islands and a high density of small Co islands. For Co/Cu(001), an ideal fcc structure is not observed, but a tetragonally distorted fct structure coming from the lateral lattice mismatch of two materials. EXAFS experiments have revealed a pseudomorphic growth from 2 to 15ML [84]. The lattice constant of (magnetic, fcc) Co is 2% smaller than of (non magnetic, fcc with $a_p = 2.56$Å at room temperature) Cu. The spacing between the layers will be 1.73Å as confirmed by LEED experiment [85]. For higher coverage, Co grows in mixed fcc and hcp structures [58].

Co on Cu(1 1 21) substrate grows at room temperature pseudomorphically and layer-by-layer independent of the thickness as a recent STM-study has shown [86]. The lateral size of the terraces (average lateral size of ~27Å) are conserved until 9ML Co.

3.1.2   Electronic structure

All the Co films grown on Cu(001) and Cu(1 1 21) were evaporated at room temperature. The films have their easy magnetization direction in-plane along the [110]-axis. Figure 3.1 shows the Co $L_{3,2}$-edges absorption spectra for linear light for 2.1ML Co on Cu(001), on Cu(1 1 21) and bulk Co(50ML) on Cu(001) after subtracting the continuum. The continuum was fitted by a double step function with a ratio of 2:1. All the spectra were

corrected for the saturation effects. The thick Co film on Cu(001) is used as a reference for all the measurements. All measurements were performed at grazing incidence (70°). In Figure 3.1, we observe clearly that the white line intensity decreases with the Co thickness. Previous experiments revealed the same behaviour [88]. The integrated white line is a measure of the number of unoccupied states in the valence band above the Fermi energy, i.e. it is proportional to the number of d-holes (n_h^{3d}). We set the number of d-holes equal to 2.43 as explained in §1.2 [54] to the integrated white line of the 50ML Co/Cu(001). The inset shows that the number of d-holes decreases with the Co thickness for the Cu(001) and Cu(1 1 21) substrates. For 2.1ML Co, n_h^{3d} is equal to 2.30 ± 0.1 on Cu(001) and 2.20 ± 0.1 on Cu(1 1 21) (see table 3.1). This difference could be attributed to the stepped Cu surface. These results do not support those obtained for ultrathin Co on Cu(1 1 13). Dürr *et al.* found an increase in the number of d holes by 0.7 ± 0.2 compared to the 2.4 holes for fcc Co bulk [79]. This could be attributed to the lateral
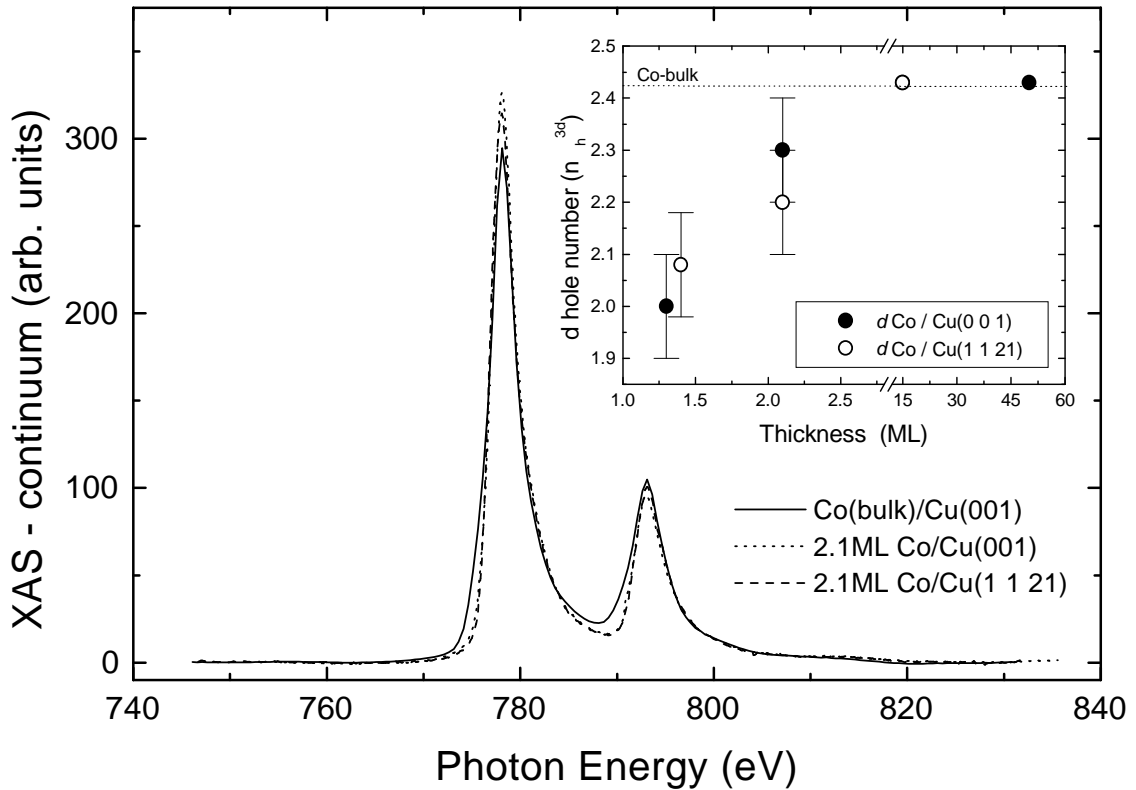

Figure 3.1: Co $L_{2,3}$-edge absorption spectra for linear light after subtraction of the continuum for 2.1ML Co on Cu(001) and Cu(1 1 21) and for 50ML Co/Cu(001). All the spectra were taken at grazing incidence. The inset shows the number of d-holes as a function of the Co coverage. The largest value is taken as 2.43 (see text).

Experimental	n_h^{3d}
2.1ML Co/Cu(1 1 21)	2.20±0.1
2.1ML Co/Cu(001)	2.30±0.1
15ML Co/Cu(1 1 21)	2.43
50ML Co/Cu(001)[1]	2.43

[1] Reference [88]

Table 3.1: Experimentally determined number of d-holes n_h^{3d} for Co on Cu(001) and Cu(1 1 21).

terrace size which is smaller (~ 17Å).

In the determination of the magnetic moments, the reduction of the number of d-holes has to be taken into account. The very small reduction of the number of d-holes for ultrathin films could be explained from two different mechanism:

i) At the surface, the hybridization of the Cu and Co d bands resulting in a charge transfer from Cu to Co d-orbitals reduces the number of Co d-holes for ultrathin films compared to thicker films [89].

ii) Contrary to that, the narrowing of the d-bands at the surface due to the reduction of the coordination number increases the number of d-holes.

The reduction of the number of d-holes is only 5% and 9% for 2ML Co on Cu(001) and Cu(1 1 21), respectively. This is less than the 21% reduction of the d-holes for 2ML Ni on Cu(001)[78]. This comes from the fact that the Co bands at the surface are narrower than those of Ni [5].

In summary, a small decrease in the number of d-holes is found for ultrathin Co films on Cu(001) and is mostly attributed to hybridization of the Cu and Co d-bands. This change of the electronic structure has to be taken into account in the determination of the magnetic moments.

3.1.3   Magnetic moments

Figure 3.2 shows the XMCD spectra (left scale) and the integrated XMCD signal (right scale) of the 2.1ML and 50ML Co/Cu(001) measured at 40K. The remanent magnetization M_r direction is in-plane and along the [110]-axis for all the Co films. From the Fig. 3.2, we see clearly that the XMCD signal for the ultrathin Co/Cu(001) film is higher at the

L_3-edge compared to the 50 ML Co/Cu(001). The same effect is observed for 2.1ML Co on Cu(1 1 21).

The Curie temperatures of the 2.1ML Co on Cu(001) and on Cu(1 1 21) are around 350K. So, in a reduced temperature scale ($t = T/T_c$), the temperature of 40K may considered nearly 0 ($t = 0.1$). The data were taken at 40K for an incident photon beam parallel to the [100]-axis which means along a hard direction in-plane. The same measurements have also been done along the in-plane [110]-axis. No difference after correcting the projection was found. All the data has been corrected for saturation effects. The degree of circular polarisation $P_c = 0.73$ was determined by using the thick bulklike Co/Cu(001). The reliability of the data normalization can been seen from the flatness at higher energy of the integrated XMCD signal.

The spin m_S and orbital m_L magnetic moments determined through the sum rules are tabulated in table 3.2. Since the same system was measured in several beamlines
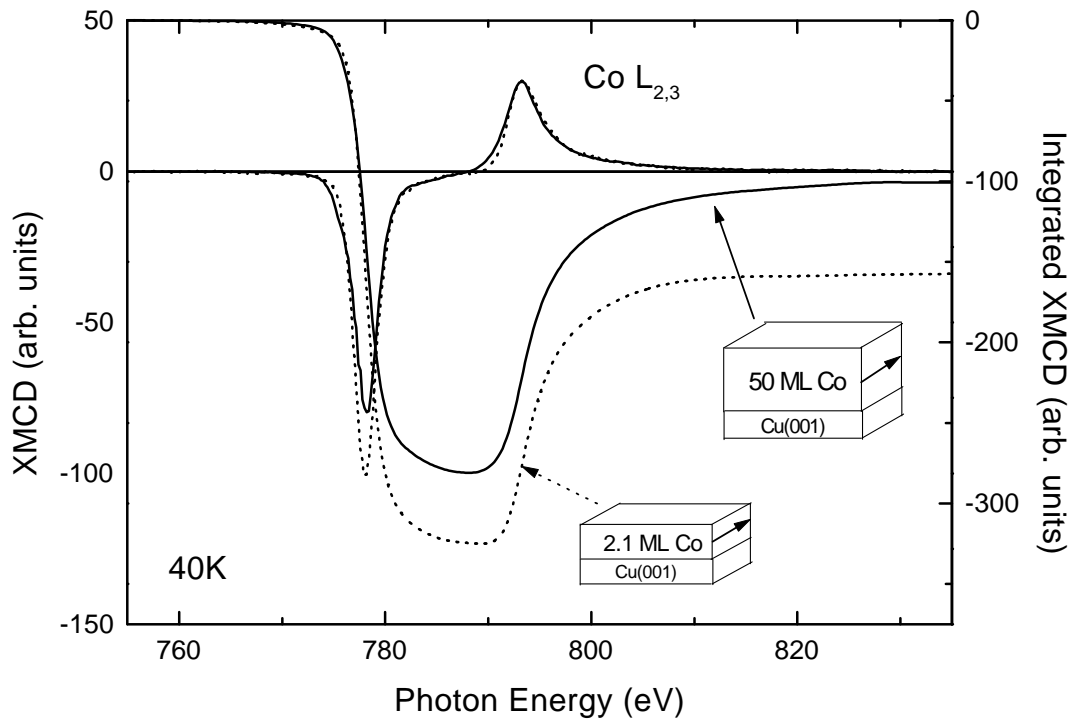

Figure 3.2: XMCD (left scale) and integrated XMCD (right scale) signal of 2.1ML and 50ML Co/Cu(001). The easy direction of magnetization for each sample is also shown. All the absorption spectra have been normalized to the same signal-to-background ratio, which is set to 100 arbitrary units.

with different polarisation, the moments given in this table are the average values. These average values are consistent with our previous publication [78, 90]. The process of the analysis described in §1.2 is used for the magnetic moment determination. The value of m_S was determined after subtracting the spin magnetic dipole contribution (m_T) and adding the $4s$ and $4p$ contributions (the "diffuse magnetism") to the spin moment (for the orbital moment, the last contributions can be neglected). This corrections have been done by assuming that the Co/Cu(001) films can be decomposed in one surface layer and all the other layers including the interface as bulklike equivalent layers. Since no other data is available to take into account any distortion of the Co lattice, theoretically predicted values of bulk and bulk surfaces were used for the 2ML Co on Cu(001) and Cu(1 1 21) and for the 50ML Co on Cu(001). This is a reasonable assumption since these contributions are localized mostly at the surface. These corrections (both T_Z and addition of $4s$, $4p$ contributions) in m_S were found to be +5.5% for 2ML and -1.6% for 50ML Co. We have

Experimental	$m_S(\mu_B/\text{atom})$	$m_L(\mu_B/\text{atom})$	$m_{tot}(\mu_B/\text{atom})$	m_L/m_S
2.1ML Co/Cu(1121)	1.96±0.1	0.26±0.05	2.22±0.1	0.132±0.01
2.1ML Co/Cu(001)	1.76±0.1	0.22±0.05	1.98±0.15	0.125±0.01
50ML Co/Cu(001)	1.55	0.142±0.01	1.69±0.01	0.092±0.01
2.0ML Co/Cu(001)[1]	-	-	-	0.105±0.01
Theory				
OPB + FP-LMTO				
1ML Co/Cu(001)[2]	1.85	0.261	2.11	0.141
2ML Co/Cu(001)[2]	1.73	0.188	1.91	0.107
FP-LAPW				
2ML Co/Cu(001)[3]	1.589	-	-	-
LDA+U				
2ML Co/Cu(001)[4]	1.783	0.142	1.925	0.080
hcp Co bulk[2]	1.63	0.123	1.753	0.075
fcc Co bulk[2]	-	-	-	0.078

[1] Reference [6]

[2] Reference [5]

[3] Reference [82]

[4] Reference [91]

Table 3.2: Experimentally determined and calculated values of m_S, m_L and their ratio m_S/m_L for Co on Cu substrate.

taken for $7m_T = +0.127\mu_B$/atom and $m_S^s + m_S^p = -0.04\mu_B$/atom for the 2.1ML Co on Cu(001) and Cu(1 1 21).

First, from table 3.2, we notice that the theoretical value of m_L for Co bulk is in good agreement ($\leq 15\%$) with experiments. By comparing the experimental values for 2.1ML on Cu(001) and on Cu(1 1 21) with the one for the Co bulk, we found clearly that both m_S and m_L are enhanced compared to the bulk values. The orbital moment m_L is enhanced by 55% and by 85% for 2.1ML Co on Cu(001) and on Cu(1 1 21) respectively. The spin moment m_S is less enhanced by 13% and 26%, respectively, after correcting of the T_z term. As a consequence, the ratio m_L/m_S is enhanced by 36% compared to the bulk value confirming the outcome of our earlier study [6]. The ratio 0.105 published earlier is lower than the actual determination, because the experimental value has been scaled to match the theoretical ratio for bulk Co 0.078. Compared to the bulk ratio, m_L/m_S is enhanced by 34% which is in very good agreement with our findings . The enhancement of the orbital moment for ultrathin films can be explained as following [6]:

i) The hybridization of the Cu and Co d-bands resulting in a charge transfer from Cu and Co d-orbitals at the interface reduces the spin moment and in the same way the orbital moment.

ii) Contrary to this, the narrowing of the d-bands at the surface due to the reduction of the coordination number causes a larger spin moment which, due to the spin-orbit coupling, produces an enhanced orbital moments.

iii) The lower symmetry at the surface and the distorted fct structure modifies the crystal field and lifts partially the quenching of the orbital moment.

iv) The value of the DOS at the Fermi level is larger than in bulk and favours more the ferromagnetism from a simple Stoner argument.

It is interesting to observe that the number of d-holes does not follow the same trends. The increase of the orbital and spin moment have been predicted theoretically for 2ML Co/Cu(001) using different theoretical approaches. The small differences of the spin moment come rather from the use of the experimental lattice constant of copper and/or the lack of considering the interlayer relaxation as suggested by Pentcheva *et al.* [82]. By using a local density approximation + U method framework, Shick *et al.* have shown that the orbital and spin moment depend strongly on the Coulomb interaction (U) [91]. Contrary to this the orbital correction of Brooks acts only on the orbital moment and not on the spin moment [5]. We notice that the orbital moment at the stepped surface Cu(1 1 21) is slightly higher than on the flat Cu(001) surface. This larger orbital moment

could be assigned to a large uniaxial magnetic anisotropy as observed for Co/Cu(1 1 13) [79, 92]. A strongly anisotropic electronic structure localized at the step-edges [93] can be ruled out due to the low density of these sites (average lateral size is of $\sim$27Å). Dürr *et al.* have observed an increase of the orbital moment near the surface of 200% for Co/Cu(1 1 13) [79]. They attribute this huge increase to the nano-structured surface morphology which plays a dominant role. Such an enhancement is not observed for Co on Cu(001) or Cu(1 1 21). The interface Co/Cu can play an important role since electronic surface states can be confined on the terraces.

3.2 Ultrathin Ni films on Cu(001)

Most of the studies on Ni/Cu(001) have been focused on the spin reorientation transition and on the thickness and temperature dependence [52]. Very few attention has been paid on the determination of the magnetic moments in the ML-range thickness of films grown *in-situ* [45]. Here, we will study the magnetism of 4-5ML Ni/Cu(001) and compare it to a 15ML Ni/Cu(001). For thicknesses lower than 7ML, an unexpected, strong reduction of the magnetic moments is observed. For the first time, a separation into spin and orbital contributions is presented and several possibilities will be discussed to explain such a reduction.

3.2.1 Growth and Structure

In the last years, the growth and structure of Ni on Cu(001) have been studied extensively. Ni grows on Cu(001) at room temperature in a layer-by-layer mode with increasing roughness. Scanning tunneling microscopy (STM) has shown that for a 5ML mass-equivalent Ni on Cu(001), the peak-to-peak roughness is $\pm$1ML. This roughness has a pyramidal morphology with a lateral size of 60Å [86, 87]. The height and the lateral size of the pyramids increase up to $\pm$4ML and 110Å for 30ML mass-equivalent Ni film. Concerning the structure, a well defined pseudomorphic growth on Cu(001) up to eleven monolayers has been observed. The films are distorted tetragonally (fct structure). The lattice constant is expanded compared to bulk fcc Ni by 2.5% in the plane ($a_p = 2.56$Å for Cu at room temperature) and compressed by 3.2% ($a_n = 1.70$Å) along the surface normal. The latest have been measured via IV-LEED for all the spacings until 11ML [94]. No relaxation is found in this thickness range. At the interface, recent room temperature STM studies have demonstrated the existence of atomic exchange processes between Cu- and Ni-atoms. This intermixing is essentially limited to the interface between Ni and Cu [95].

3.2.2   Electronic structure

The Ni films were grown on Cu(001) at room temperature. The 15ML Ni onCu(001) as presented in the §1.2 has its easy magnetization axis perpendicular to the film plane. In comparison, the easy magnetization axis for 4ML Ni/Cu(001) is in-plane and along the [100]-axis. The perpendicular magnetization is explained by competition of a magnetoelastic volume anisotropy due to the pseudomorphic growth which favours out-of-plane easy magnetization axis, the shape anisotropy and the sum of surface plus interface anisotropies which all favour an in-plane easy magnetization axis [96]. Figure 3.3 shows the Ni $L_{3,2}$-edges absorption spectra for linear light for 15 ML (solid line) and 4ML (dotted line) after subtracting the double step function. The 15ML Ni/Cu(001) spectra was taken at normal incidence and the 4ML Ni/Cu(001) at grazing incidence (20°). The L_3-to-L_2 edge jump ratio was taken as 2:1.   As reported by Srivastava *et al.*, a reduction of the white
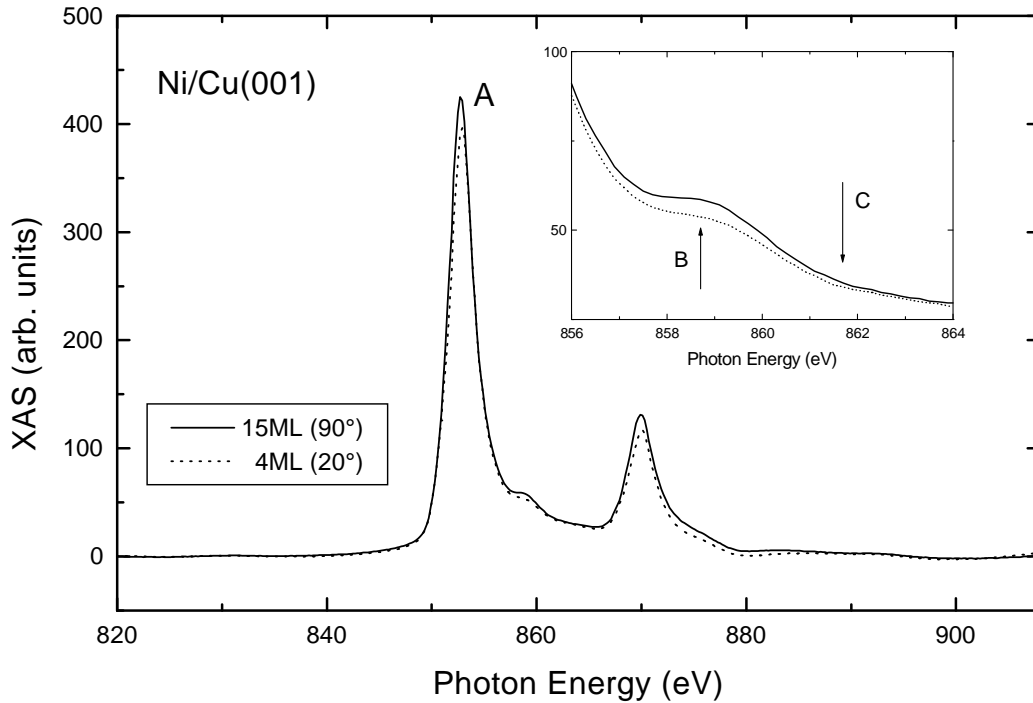

Figure 3.3: Ni $L_{2,3}$-edge absorption spectra for linear light after subtraction of the background for 4ML Ni/Cu(001) (grazing incidence) and for 15ML Ni/Cu(001) (normal incidence). Features marked as A, B and C are discussed in the text. An enlarged picture of the satellite is shown in the inset.

line intensity is found with decreasing Ni thickness [78]. Corrections for saturation effects for electron yield have been taken into account for the 4ML Ni/Cu(001) (less than 3%). The integrated intensity of the absorption spectra, after corrections for transitions into continuum, is a measure of the number of unoccupied states in the valence band (the n_h^{3d} number of d-holes). The number of s-holes is much smaller than the number of d-holes, so its contribution is negligible. It is of primary importance to know the number of d-holes with a high precision before applying the sum rules. The reduction in the number of d-holes in our case has three origins:

i) The charge density is anisotropic in ultrathin Ni/Cu(001) films due to the distorted tetragonally structure. More d-holes have in-plane character which means that the DOS above the Fermi level (E_F) have more $d_{x^2-y^2}$, d_{xy} character as compared to $d_{3z^2-r^2}$, d_{xz} and d_{yz} [78]. So, a partial reduction comes from this anisotropic charge density.

ii) As for Co, the hybridization of the Cu and Ni d-bands, resulting in a charge transfer from Cu and Ni d orbitals at the interface, reduces the number of d-holes for ultrathin films compared to thicker films [89].

iii) Again, the narrowing of the d bands due to the lower coordination number at the surface which favours an increase of the d-holes is not sufficient to overcome the hybridization effect coming from the interface.

For thicker films, the number of d-holes saturates after 5ML since the effects coming from the interface and surface will contribute less. By taking as a reference the 15ML Ni/Cu(001) for the bulk number of d-holes $n_h^{3d} = 1.45$, we obtain for the 4ML Ni/Cu(001) by integrating either until the L_3-edge maximum (A) or all the spectra, a number of d-holes $n_h^{3d} = 1.25 \pm 0.05$. This corresponds to 14% reduction which is larger than for 2ML Co/Cu(001). We clearly see here that the hybridization is stronger than in the case of 2ML Co or 3ML Fe on Cu(001) [97] due to a higher overlap of the Ni and Cu d bands as predicted theoretically [5]. This value is in excellent agreement with our previous publications [44, 78]. So, a reduction of 14% in the number of d-holes is observed for 4ML Ni/Cu(001) compared to bulklike Ni (see table 3.3). Different features can be distinguished above the L_3-edge main line (A), a satellite at $\sim$6eV (B) and a continuum (C). The inset of Fig. 3.3 shows more details in the region around the satellite structure. Such structures and their change with the thickness have been already observed [78, 45]. The origin of the satellite can be interpreted in two different ways:

i) According to a Configuration Interaction (CI) approach, the satellite intensity is ascribed to a$2p^5 3d^9$ final state (reached from a $3d^8$ initial state) ([45]).

Experimental	n_h^{3d}
4.0ML Ni/Cu(001)	1.25±0.05
4.3ML Ni/Cu(001)	1.25±0.08
15ML Ni/Cu(001)[1]	1.45

[1] Reference [78]

Table 3.3: Experimentally determined number of d-holes n_h^{3d} for Ni on Cu(001).

ii) According to one-electron band structure theory, the satellite intensity is attributed to states of d character hybridized with the unoccupied sp band [39].

We can observe a small decrease in the intensity of the satellite which is explained by a reduced Ni-Cu hybridization (proportional to the square root of the number of neighbours) with decreasing the thickness. In the CI approach, the $3d^8$ weight in the ground state diminishes and implies that the $2p^5 3d^9$ final state is not longer reached. Concerning the continuum (C), which provides information about the number of unoccupated d and $s - d$ hybridized states, the difference is very small.

In summary, a decrease of the number of d-holes is found for ultrathin Ni/Cu(001) and is attributed to hybridization of the Cu and Ni d bands. This electronic structure reflects directly the changes of the density of states near and above the Fermi level and will affect the total magnetic moments too.

3.2.3 Magnetic properties

Figure 3.4 shows the XMCD spectra (left scale) and the integrated XMCD signal (right scale) of the 4ML and 15ML Ni/Cu(001) measured at 40K. The remanent magnetization M_r is out-of-plane for the 15ML Ni and and in-plane along the [100]-axis for the 4ML Ni. From Fig. 3.4, we clearly see that the XMCD signal for the ultrathin Ni/Cu(001) film is strongly reduced compared to the 15 ML Ni/Cu(001). This effect is not due to the temperature since the Curie temperature of the 4ML is around 250K (bulk is 627K). In a reduced temperature scale, the temperature of 40K may be considered nearly to be 0 ($t = 0.16$). The data for 4ML were corrected for saturation effects and for the incident photon angle (20°). The degree of circular polarisation $P_c = 0.73$ was determined by using a thick bulklike Co/Cu(001) ($\sim$50ML). The reliability of the data normalisation may been seen from the flatness of the integrated XMCD signal at higher energy. The spin m_S and orbital m_L magnetic moments from the spectra using the sum rules are presented in table 3.4. The same analysis as described in §1.2 is used for the magnetic
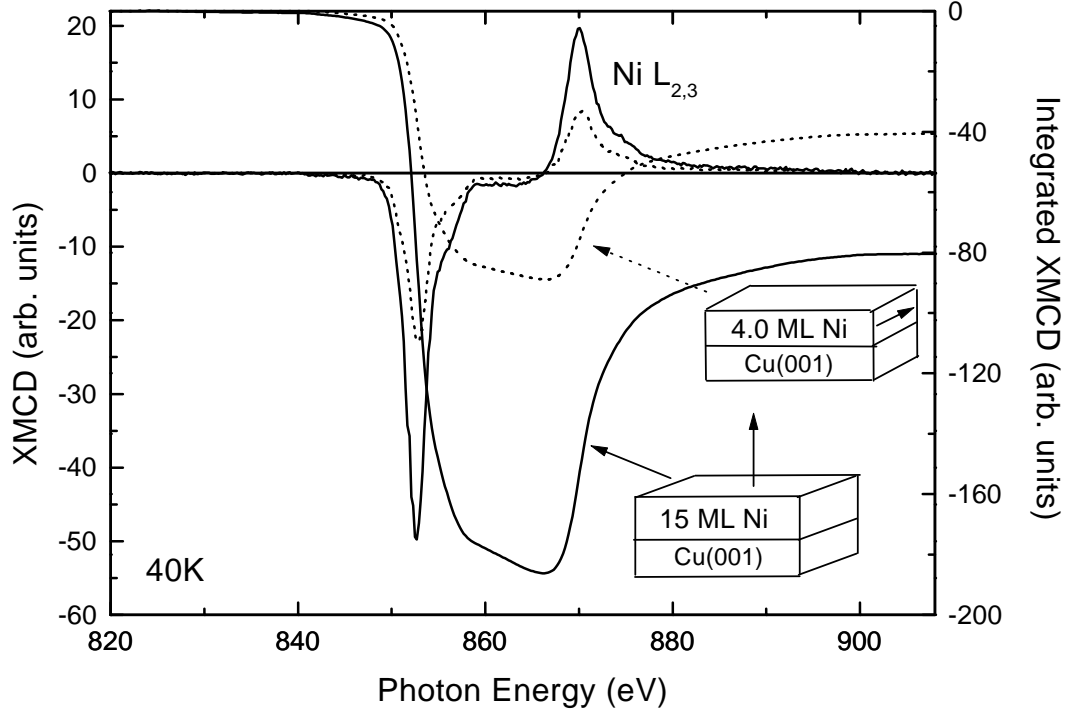
Figure 3.4: XMCD (left scale) and integrated XMCD (right scale) signal of 4.0ML and 15ML Ni/Cu(001). The easy direction of magnetization for each sample is also shown. All the absorption spectra have been normalized to the same signal-to-background ratio, which is set to 100 arbitrary units.

moment determination. Concerning the corrections (both T_Z and addition of $4s$, $4p$ contributions) in m_S were found to be -10% for 4ML and -8% for 15ML Ni. We have taken for $7m_T = -0.04\mu_B$/atom and $m_S^s + m_S^p = -0.02\mu_B$/atom for the 4ML Ni on Cu(001). Contrary to Co, the correction for T_Z is negative.

For the 4.3 ML Ni/Cu(001), the spectra were recorded at 160K. The m_S and m_L given in table 3.4 were obtained by extrapolating the data to T= 0 by using the temperature dependence of the XMCD difference of a 4ML Ni/Cu(001) [98]. We can first notice that both m_S and m_L are comparable for the two Ni/Cu(001) films showing the reliability of the data analysis. The calculation for 1ML Ni/Cu(001) has been performed using a full-potential linear muffin-tin orbital method in a slab geometry [5]. The Ni overlayer is assumed to have the same crystal structure and lattice constant as the Cu(001) substrate. The experimental value for the ratio m_L/m_S for the 4ML and 4.3ML Ni/Cu(001) films are enhanced by 45% compared to the bulk value 0.100 (see §5.1) and reduced by 25%

Experimental	$m_S(\mu_B/\text{atom})$	$m_L(\mu_B/\text{atom})$	$m_{tot}(\mu_B/\text{atom})$	m_L/m_S
4.0ML Ni/Cu(001)	0.24±0.08	0.035±0.01	0.275±0.1	0.145±0.03
4.3ML Ni/Cu(001)	0.25±0.08	0.036±0.01	0.29±0.1	0.144±0.03
15ML Ni/Cu(001)	0.61±0.08	0.075±0.01	0.69±0.1	0.130±0.03
Theory				
1ML Ni/Cu(001)[1]	0.45	0.087	0.537	0.193
fcc Ni bulk[1]	0.58	0.058	0.638	0.100

[1] Reference [5]

Table 3.4: Experimentally determined and calculated values of m_S, m_L and their ratio m_L/m_S for Ni on Cu(001).

compared to the theoretical value for 1ML Ni/Cu(001). Even for 15ML Ni/Cu(001), the ratio is enhanced compared to bulk value. By examining the value of m_L and m_S separately, we see that for the 4ML and 4.3ML Ni/Cu(001) both are reduced by a factor ~ 2 in comparison to the Ni bulk. Such a large reduction in the magnetic moment can not be explained by the existence of magnetically dead Ni layers since, a ferromagnetic response ($T_c \approx 45$K) has been found down to 1.6ML Ni/Cu(001) [98]. An other explanation could be the intermixing effect at the interface Ni/Cu since it is well known that the onset of ferromagnetism in CuNi alloys is about 42at.%-Ni and that CuNi alloys have small magnetic moments [99]. In order to investigate a possible alloying effect which could be the origin of the reduced magnetic moments, 4-5ML Ni/Cu(001) were grown and measured at 60K in order to compare with the film growth at room temperature. At this temperature growth (60K), no intermixing effect between Cu and Ni is expected [100]. The magnetic moment found for the 4ML Ni/Cu(001) grown at low temperature is about 0.3 μ_B/atom which is within the error bars the same as for the 4ML Ni/Cu(001) film grown at room temperature. Moreover, the influence of a soft annealing (5 min. at 400K) has negligible influence on the magnetic moments for the 4-5ML Ni/Cu(001) since a decrease less than 5% is found. So, intermixing is essentially limited to the interface and has a very small influence on the magnetic moments for 4-5ML Ni/Cu(001) [95] and is not responsible for the reduced magnetic moments in ultrathin 4-5ML Ni/Cu(001) films. A reduction of the spin magnetic moment for 1ML Ni/Cu(001) as compared to the bulk has been predicted by theory [5]. A similar reduction ($m_{tot} = 0.42\mu_B$/atom) is also observed for 1ML Ni on magnetic substrate Co/Cu(001) [45].

The Ni-d-Cu-d hybridization which is the dominant effect, as compared to the Ni d band narrowing, is responsible for the reduced moment of the Ni atoms on the Cu sub-

strate. The hybridization with the Cu state also tends to reduce the magnetic moments of the Co overlayer, but in this case the narrowing of the bands is sufficient to produce larger moments. As a consequence of the hybridization which is an overlap of the orbitals of Ni and Cu, the exchange splitting of the Ni d band is reduced. Thus, the hybridization reduces the spin magnetic moment and in the same way the orbital moment, but the reduced crystal field interaction at the surface enhances again the orbital magnetic moment. The hybridization seems to influence more than the interface layers. This explains the reduction of the spin and orbital moment compared to the bulk and the enhanced orbital-to-spin ratio.

Contrary to the 4ML Ni/Cu(001), the spin magnetic moment m_S for the 15ML Ni/Cu(001) is bulk-like and the orbital magnetic moment m_L is enhanced compared to the Ni bulk. For this thickness, effects coming rather from hybridization at the interface or from the reduced crystal-field interaction at the surface are more or less negligible. The enhancement of the orbital moment is due to the tetragonal distortion in the 15ML Ni/Cu(001) film. With calculations based on linear muffin tin orbitals, Hjortstam *et al.* have shown that the magnetic anisotropy energy and the orbital moment in fct Ni vary as a function of strain [101]. For the experimental ratio $c/a = 0.945$ (c is the side length parallel to the z axis and a the side length in the xy plane), an increase in the orbital moment of 6% is calculated ($m_L = 0.068\mu_B$/atom) which is lower than our experimental value, but the same trends are observed. So, for thinner films than about 50ML Ni/Cu(001), where a gradual transition back to in-plane occurs due to strain relaxation, an enhanced orbital moment should be observed compared to the bulk.

Chapter 4

The Co/Cu/Ni/Cu(001) trilayer systems: element-specific magnetizations

In the following chapter, the power of element-specific and temperature-dependent XMCD measurements in the investigation of Co/Cu/Ni trilayers on Cu(001) will be demonstrated. Using this technique not only the magnetic moments but also the Curie temperature T_c, the critical exponent, the magnetization and essentially its correlation with the interlayer exchange coupling J_{inter} can be determined via temperature dependent characterization. The interlayer exchange coupling has been extensively studied but its effect on the basic magnetic observables has received very few attention. However, this is very important in order to understand the magnetic properties of metallic multilayers. The element-specificity of the XMCD allowed us to record separately the magnetization of the two ferromagnetic sublayers. The aim of this chapter is to address and elucidate the following questions: i) do coupled magnetic layers present a separate or a common single T_c and ii) how does J_{inter} affect the temperature-dependent sublayer magnetizations?

In a first section, we will briefly describe the magnetic phase transition for thin films and the important parameters which affect this phase transition. After, we will show that nonmagnetic overlayers such as Cu have a very strong influence on the properties of thin magnetic films. A direct consequence of this is that measurements of coated thin films, for example performed on systems transported *ex-situ*, may not be comparable to uncapped thin films characterized *in-situ*. Finally, the Co/Cu/Ni/Cu(001) trilayer systems will be investigated.

4.1 The magnetic phase transition

From theoretical point of view, the itinerant magnetism at finite temperatures is very complex [102]. Simple statistical models of localized spins are in general sufficient to give a useful physical insight on the behaviour of magnetic films at finite temperatures. These models are justified since the critical behaviour close to T_c depends essentially on the dimensionality D, the dimensionality of the order parameter n and the range of the interaction between the spins [103], the latter confirmed by the renormalization group theory [104].

4.1.1 The statistical models and critical behaviour

The simplest Hamiltonian which includes spins alignment is:

$$H = -\sum_{i,j} J_{ij}\sigma_i \cdot \sigma_j \tag{4.1}$$

where J_{ij} is the direct exchange interaction coupling and σ_i the Pauli matrix. This is the *quantum Heisenberg Model* Hamiltonian. However, the quantum effects near T_c are negligible; they are important only near $T = 0K$. So, the Pauli matrix can be replaced by $\vec{S}$. For magnetic systems, the possible values of D are $D = 1, 2, 3$. The dimensions of the order parameter n are $n = 1$ (Ising model), $n = 2$ (XY model) and $n = 3$ (Heisenberg model). Since the correlation length diverges at $T = T_c$, the system is then invariant by expansion at $T = T_c$. An important consequence is the homogeneity of the Gibbs function. It leads to a singular behaviour of thermodynamical quantities near T_c which can be described with power laws:

$$\text{correlation} \quad \text{length} \quad \xi \;=\; \xi_0 \cdot t^{-\nu} \tag{4.2}$$

$$\text{susceptibility} \quad \chi \;=\; \chi_0 \cdot t^{-\gamma} \tag{4.3}$$

$$\text{spontaneous} \quad \text{magnetization} \quad M_s \;=\; M_0 \cdot t^{+\beta} \tag{4.4}$$

with an universal equation:

$$D\nu = 2\beta + \gamma \tag{4.5}$$

where $t = (T - T_c)/T_c$ for $T > T_c$ and $t = (T_c - T)/T_c$ for $T < T_c$. The values of the critical exponents β and γ for Ising, XY and Heisenberg model with short interactions are given in table 4.1. The case $D > 4$ corresponds to the mean field theory. For a given value of n, the stability increases and the thermal fluctuations decrease with higher dimensionality. Following, the Mermin-Wagner theorem, a $2D$-ferromagnet with short range interactions doesn't show a long range order (LRO) at finite temperatures for $n = 2$ and 3 [105].

	$D = 1$	$D = 2$	$D = 3$	$D > 4$
$n = 1$	X	$\beta = 1/8$	$\beta = 0.325$	$\beta = 1/2$
	X	$\gamma = 7/4$	$\gamma = 1.2402$	
$n = 2$	X	$\gamma = \infty$	$\beta = 0.346$	
		no LRO	$\gamma = 1.316$	
$n = 3$	X	X	$\beta = 0.3647$	
			$\gamma = 1.3866$	$\gamma = 1$

Table 4.1: *Values of the critical exponents β and γ for different dimensionality D and n. The symbol X means that no long range order at $T \neq 0$ exists.*

The Curie temperature of thin films

Within the Ginzburg-Landau theory, for thermodynamic phase transitions of second order, the order parameter is non-zero below T_c and zero above. The order parameter is the spontaneous magnetization. The susceptibility $\chi(T) = \partial M(T)/\partial H$ is diverging at T_c. For bulk 3D ferromagnets, the Curie temperature is 1043K for Fe , 1388K for Co and 627K for Ni. In the mean field theory, the Curie temperature of a $3D$-ferromagnet with spin S is directly correlated to the direct exchange interaction with:

$$T_c = \frac{2zS(S+1)J}{3k_B} \tag{4.6}$$

where z is the coordination number.

For thinner films, the Curie temperature decreases as a function of the thickness [106, 107]. This can be explained qualitatively from the reduction of the magnetic coordination number (finite-size effect). In the mean-field model, the reduction of $T_c(d)$ can be quantitatively described by including the reduction of the coordination number as following:

$$\frac{T_c(d)}{T_c(\infty)} = 1 - \left(\frac{d}{d_0}\right)^{-1/\nu} \tag{4.7}$$

where $T_c(\infty)$ is the Curie temperature of the bulk. The exponent ν corresponds to the one of the $3D$ case ($\nu = 0.705$). The critical thickness d_0, which is a free parameter, is 3.2ML for Ni/Cu(001)[108]. This relation is only valid in the $3D$-regime. A film behaves like a $2D$-film (ultrathin film) when the perpendicular component of the spin-waves vector is zero (uniform saturation magnetization across the film thickness). For Fe and Co, this corresponds to a thickness around 4-8ML. From the critical exponent β as a function of

the thickness for Ni(111)/W(111), a dimensional transition from $3D$ to $2D$ Ising occurs around $d = 6 \pm 1 ML$ [109]. However, the Mermin-Wagner theorem tell us that a $2D$-ferromagnet does not have a long range ferromagnetic order at finite temperatures if the only interaction between the spins is the isotropic exchange interaction. At finite temperatures, the very large amplitude of spin fluctuations of long wavelength break up the long-range order. However, the existence of a magnetic anisotropy is very important since it suppresses these fluctuations efficiently and stabilise again a ferromagnetic order at finite temperatures. The Curie temperature $T_c(1ML)$ in a $2D$-Heisenberg-Model with uniaxial anisotropy is then [110]:

$$T_c(1ML) = \frac{2T_c(\infty)}{ln(\pi^2 J/ \mid K \mid)} \tag{4.8}$$

where J is the direct exchange interaction and K the magnetic anisotropy. The transition temperature indeed vanishes in the limit of vanishing anisotropy. It is clear that the anisotropy plays a crucial role in ultrathin films.

4.1.2   The spontaneous magnetization

The spontaneous magnetization given by the Eq. 4.4 is only valid near the Curie temperature. The temperature-dependence of the magnetization far away from the T_c can be described with the spin-wave model. Unfortunately, the spin-waves model (Bloch 1930), neglects thermal fluctuations. But at low temperature, this assumption is valid. From the dispersion relation of a $3D$-solid ($\hbar\omega = D_s\mathbf{k}^2$ for long wavelenght, $D_s = 2J_{intra}Sa^2$), the magnetization will decrease with a power law $T^{3/2}$:

$$M(T) = M_0(0)(1 - b_3 \cdot T^{3/2}) \tag{4.9}$$

with the spin-waves constant

$$b_3 = \frac{0.0587}{Sq}\left(\frac{k_B}{D_s}\right)^{3/2} \tag{4.10}$$

where D_s is the spin wave coefficient (281meV.Å^2 at 295K for Fe) and S the ground state magnetization (q is the number of atoms in the unit cell).

In the case of ultrathin films at low temperatures, only the spin-waves with a perpendicular wave vector component will be excited. As discussed above, this should not give a spontaneous magnetization. On the other hand, by taking into account the anisotropy, the magnetization will decrease linearly with the temperature [111]:

$$M(T) = M_0(0)(1 - b_2 \cdot T) \tag{4.11}$$

with the spin-wave constant

$$b_2 = \frac{a_0^2 k_B}{8\pi D_s S} \cdot ln\left(\frac{k_B T}{\sqrt{K_{//} K_\perp}}\right) \tag{4.12}$$

where a_0 is the lattice constant of the crystal and $K_{//}, K_\perp$ the in-plane and out-of-plane anisotropy constant, respectively. Only at very low temperatures, the influence of the logarithmic temperature dependence of b_2 will hold. If the anisotropy is very large, the magnetization will be practically constant. For Fe on W(110), from torsion oscillation magnetometry, the spin-wave constants which are determined from thickness dependent magnetization measurements are typically $b_3 = 5.2 \times 10^{-6} K^{-3/2}$ (bulk value) and $b_2 = 5.6 \times 10^{-5} K^{-3/2}$ (one monolayer value) [112].

4.2 The effects of Cu-capping on ultrathin films

The capping procedure on thin films and multilayers is very common and widely used in order to prevent the film from oxidation and to allow for *ex-situ* measurements. The main difference is that the top layer surface (film/vacuum) is changed into an interface (film/capping layer). In general, for thick films, the surface and interfaces have negligible contributions. For thinner films (in the monolayer range), surfaces and interfaces directly affect the magnetic observables like the Curie temperature, magnetic moments and anisotropy. In this section, we will investigate the influence of Cu-capping on ultrathin Co and Ni films grown on Cu(001). We will show that the Cu-capping will modify the electronic structure and reduce the Curie temperature and the magnetic moments. The result will be interpreted in the framework of a mean field model.

4.2.1 Ultrathin Co films

Here, we will compare the electronic structure and magnetic moments of Co/Cu(001) with $d_{Co} \sim 2ML$ before and after capping with $d_{Cu} \sim$ 2-6ML of Cu. The Co films were evaporated at room temperature. However, different samples were prepared by changing the growth temperature of the Cu-capping film (100K and 300K). No change in the magnetic properties were observed for Cu growth at 100K and 300K. So, 2ML of Cu seems to grow layer-by-layer on the Co/Cu(001) films. A reduction of the edge jump of Co was observed by capping with Cu which excludes a possible intermixing between Co and the 2ML Cu. A simple thermodynamical argument is that the surface energy of a clean Cu(001)-surface ($E^f = 0.79eV/(1\times1)$-cell) is lower compared to the surface energy of Co(001) with the lattice constant of copper and relaxed interlayer distances

$(E_F^f M = 1.11\text{eV}/\ (1 \times 1)\text{-cell})$ [82]. This means that Co will not segregate on the surface. Figure 4.1 shows the magnetization of a 1.9ML Co/Cu(001) before and after capping with a 6.8ML Cu. Such magnetization curves are obtained by measuring the XMCD spectra at different temperatures. Since the isotropic absorption spectrum is not temperature dependent, the XMCD spectra can be directly compared each other. The y-scale was calibrated by determining the magnetic moments using the sum rules for the spectra taken at the lowest temperature. The y-scale was then converted in Gauss units. The T_c of 1.9ML Co is about 290K. After Cu-capping the T_c is reduced by 120K. The magnetization curve is shifted towards lower temperatures, but the shape still remains the same which means that the critical exponent does not change with capping. A strong reduction of 75K is also observed for 1.8ML Co/Cu(001) by capping with 4.8ML Cu (see table 4.2). Similar observations have been earlier reported for Co/Cu(001) films [113, 114]. So, the T_c of 2ML Co/Cu(001) is reduced by $\approx$100K with capping which corresponds to 30%.
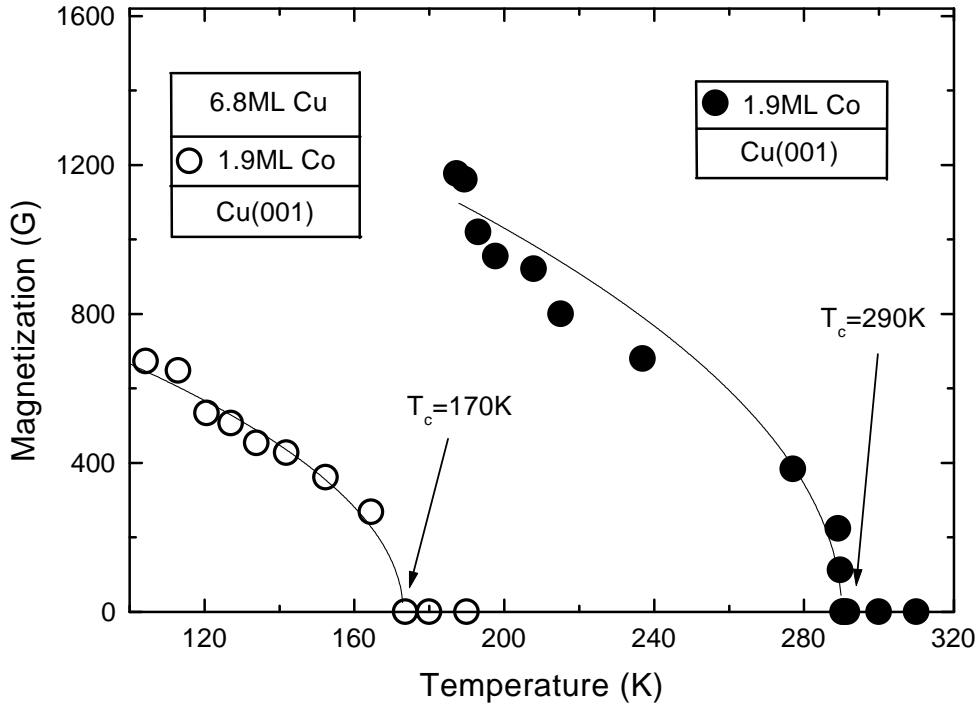

Figure 4.1: Magnetisation curves taken at remanence for 1.9ML Co/Cu(001) before (solid circles) and after capping (open circles) with Cu. The temperature where the XMCD signal vanishes is the Curie temperature T_c. A clear reduction in T_c can be seen on capping. A power law function $M_o \cdot t^{-\beta}$ was used to improve the guide to the eye line.

d_{Co}(ML)	T_c(K)	d_{Cu}(ML)	ΔT_c(K)
1.9	290	6.8	-120
1.8	280	4.8	-75

Table 4.2: *T_c of various ultrathin Co on Cu(001) films before capping with Cu. The capping layer thickness d_{Cu} and the decrease ΔT_c after capping are noted.*

The reduction could be attributed to an interface effect.

Now, let us analyse the isotropic absorption spectra at the $L_{3,2}$-edges of 2.1ML Co on Cu(001) before and after capping with a 2ML Cu (see Fig. 4.2a). After normalization, we see that the white line is strongly reduced at the L_3-edge, and less at the L_2-edge. No sizeable changes are observed between the edges. This may be related to the decrease of the number of 3d-holes. This change of the white line intensity at the edges suggests that a modification of the electronic structure occurs after capping which influences the number of 3d-holes and certainly the total magnetic moments. The relative change after subtraction of the continuum is $\approx$10% if we take into account all the area under the spectrum and $\approx$14% if we integrate only up to the maximum of the L_3-edges. This corresponds to 2.20 and 2.10 number of 3d-holes respectively in comparison with 2.43 of the bulk value. It is very important to know the number of holes to determine the magnetic moments of Co before and after Cu-capping.

In Fig. 4.2b, we plot the XMCD spectra at the $L_{3,2}$-edges of the 2.1ML Co/Cu(001) measured before and after capping with 2ML of Cu. The measurements were done at a temperature of 35K. It is obvious that the XMCD signal is strongly decreased. Taking into account that the T_c of the Co capped film is about 200K (table 4.2), the temperature of 35K may be considered to be nearly 0 in a reduced temperature scale. This is the reason, why it is possible to compare directly the magnetic moments of Co before and after capping with Cu without facing the problems coming from a change in the reduced temperature. By applying the sum rules to the spectra, we find that the total magnetic moment for 2.1ML Co/Cu(001) is 1.98±0.10$\mu_B/atom$ before and 1.41±0.10 $\mu_B/atom$ after capping. For comparison, the total magnetic moment of a bulk sample is 1.69± 0.10$\mu_B/atom$. So, the Cu-capping reduces the Co total magnetic moments compared to the uncapped or bulk film by 30% or 16% respectively. The same reduction was observed for different Cu-capping deposition temperatures. This reduction of the magnetic moments is attributed to the interface to Cu which reduces the magnetic moments through hybridization effects. Also, one may not exclude that structural changes could occur due to atomic exchange process. The hybridisation leads to a broadening of the Co bands, an increased overlap
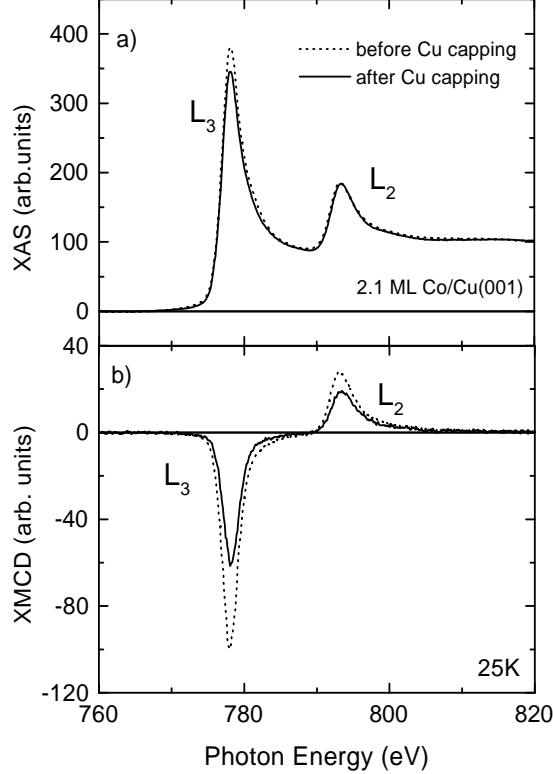
Figure 4.2: Isotropic absorption spectra (upper) and XMCD signal (lower) for 2.1ML Co/Cu(001) before (dotted line) and after (solid line) 2ML Cu capping. These spectra were taken at 25K and at grazing incidence (70°). A clear difference is visible between the isotropic and XMCD spectra.

between the spin-up and spin-down states and a decreased exchange splitting (see chapter 1). Hybridization is also responsible for the reduction of the T_c since it is related to the magnetic moments (see Eq. 2.12). The T_c is proportional to the square of the magnetic moments. Effectively, the ratio of the T_c's and magnetic moments are comparable:

$$\frac{T_c^{capped}}{T_c^{uncapped}} = \frac{170}{290} \approx 0.65$$

$$\frac{m_{capped}^2}{m_{uncapped}^2} = \frac{1.41^2}{1.98^2} \approx 0.50$$

In a simple mean-field theory, the reduction of the magnetic moment enters in the prefactor T_c of Eq. 2.13 and through this the reduction of $T_c(ML)$ after capping may be justified by considering the intralayer exchange coupling constant (J_{intra}). More rigorous calculations by Jensen *et al.* have been carried out within an improved mean-field theory. They provide a detailed picture of the T_c variation as a function of the film thickness and the magnetic moment at the interface/surface [115]. In that model, the thermal fluctuations due to low dimensionality are partly taken into account. They show that 20% reduction

of the bulk magnetic moment at the interface/surface reduces the Curie temperature by 30% for a 2ML ferromagnetic film on Cu(001). The predicted T_c reductions for 2ML films with the interface moment as a parameter in the calculations are in excellent agreement with our present measurements for Cu-capped Co films.

To summarize, we showed that Cu-capping decreases the Curie temperature and the magnetic moments of ultrathin Co/Cu(001) films and that these magnetic observables are correlated.

4.2.2 Ultrathin Ni films

Here, we will compare in the same way as for 2ML Co/Cu(001) the electronic structure and magnetic moments of 4ML Ni films on Cu(001) before and after capping with a 2-6ML Cu. The Ni films were evaporated at room temperature. Ni grows on Cu(001) quasi layer-by-layer. Islands appear after 5ML to 7ML [116, 86]. By annealing, the height of these islands can be reduced [117]. Figure 4.3 shows the magnetization of a 4.3ML Ni/Cu(001) before and after capping with a 2.3ML Cu. Such magnetization curves are again obtained by measuring the XMCD spectra at different temperatures. The y-scale was calibrated in the same way as for Co/Cu(001). The T_c of 4.3ML Ni is about 306K and after Cu-capping the T_c is reduced by 34K. As for Co/Cu(001), the magnetization curve is shifted towards lower temperatures but the shape still remains the same which means that the critical exponent does not change with capping. This reduction of around 35±15K is also observed for different Ni thicknesses (see table 4.3).

From Fig. 4.4, we see that by decreasing the Ni thickness, the ratio $|\Delta T_c|/T_c^{uncapped}$ increases. This shows clearly that the reduction is essentially an interface Ni/Cu effect. In the inset is shown that the reduction as a function of the Cu-capping

d_{Ni}(ML)	T_c(K)	d_{Cu}(ML)	ΔT_c(K)
3.6	168	2.0	-31
4.0	217	2.5	-37
4.0	210	3.5	-50
5.0	275	2.0	-25
5.1	278	0.5	-23
5.1	268	7.0	-32

Table 4.3: *T_c of various ultrathin Ni on Cu(001) films before capping with Cu. The capping layer thickness d_{Cu} and the decrease ΔT_c after capping are noted.*

thickness is constant and it saturates after one monolayer. For a 4ML Ni/Cu(001) film, the Curie temperature is reduced by 43K by capping which corresponds to 20% reduction.

In Fig. 4.5a, one may see the isotropic absorption spectrum at the $L_{3,2}$-edges of 4ML Ni/Cu(001) before and after capping with 2ML Cu. After normalisation, the white line is reduced at the L_3-edge and at the L_2-edge. Compared to the Co case, the reduction is less pronounced. No sizeable changes are again observed between the edges. As seen before, these changes of the white line intensity at the edges suggest that a modification of the electronic structure occurs after capping which influences the number of $3d$-holes and certainly the total magnetic moments. The relative change after subtraction of the continuum is ≈-2.5% if we take into account all the area under the spectrum and ≈-2% if we integrate only up to the maximum of the L_3-edges. This corresponds to 1.22 number of $3d$-holes compared to 1.45 for the bulk. In Fig. 4.5b, we plot the XMCD spectra at the
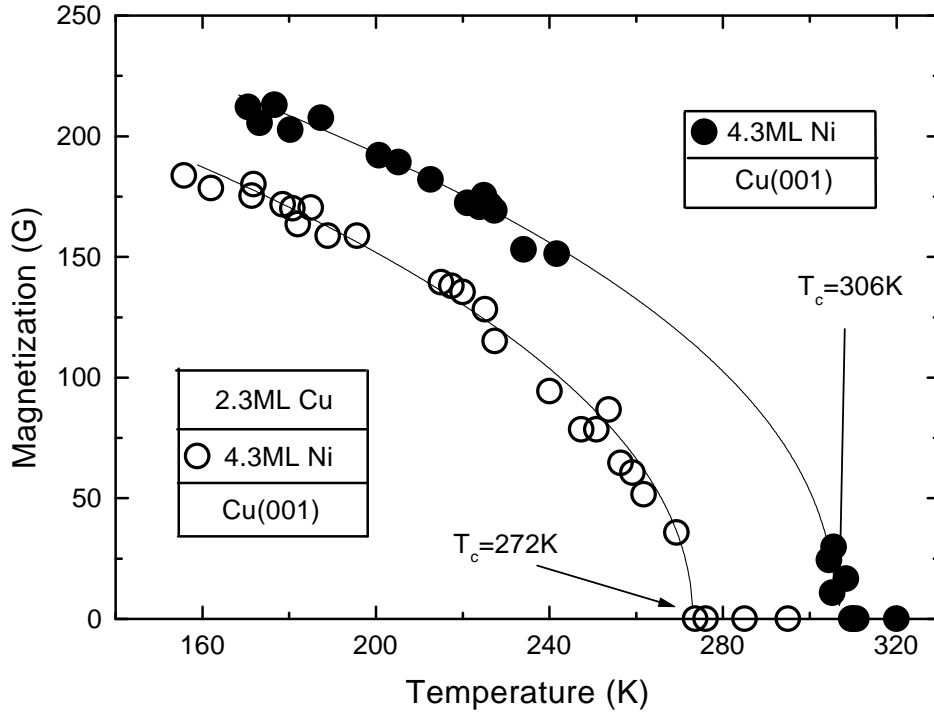
Figure 4.3: Magnetisation curves taken at remanence for 4.3ML Ni/Cu(001) before (solid circles) and after capping (open circles) with Cu. The temperature where the XMCD signal vanishes is the Curie temperature T_c. A clear reduction in T_c can be seen on capping. A power law function $M_o \cdot t^{-\beta}$ was used to improve the guide to the eye line.

$L_{3,2}$-edges of the 4ML Ni/Cu(001) measured before and after capping with 2ML of Cu. The measurements were again done at a temperature of 35K. It is clear that the XMCD signal is strongly decreased. Since the measurements are done far from the T_c, we can compare directly the Ni magnetic moment before and after capping with Cu.

By applying the sum rules to the spectra, we find that the total magnetic moment for 4ML Ni on Cu(001) is $0.275\pm0.08\mu_B/atom$ before and 0.20 ± 0.08 $\mu_B/atom$ after capping. For comparison, the total magnetic moment of a bulk sample is $0.66\pm$ $0.08\mu_B/atom$. So, the Cu-capping reduces by 27% or 70% the Ni total magnetic moments compared respectively to the uncapped or bulk film. This reduction of the magnetic moments is attributed to the interface with Cu which reduces the magnetic moments through hybridization effects. These hybridization effects are comparable to those of Co/Cu. The hybridization effects are also responsible for the reduction of T_c since it is correlated with the magnetic moments (see Eq. 2.12). The T_c is proportional to the square of the magnetic
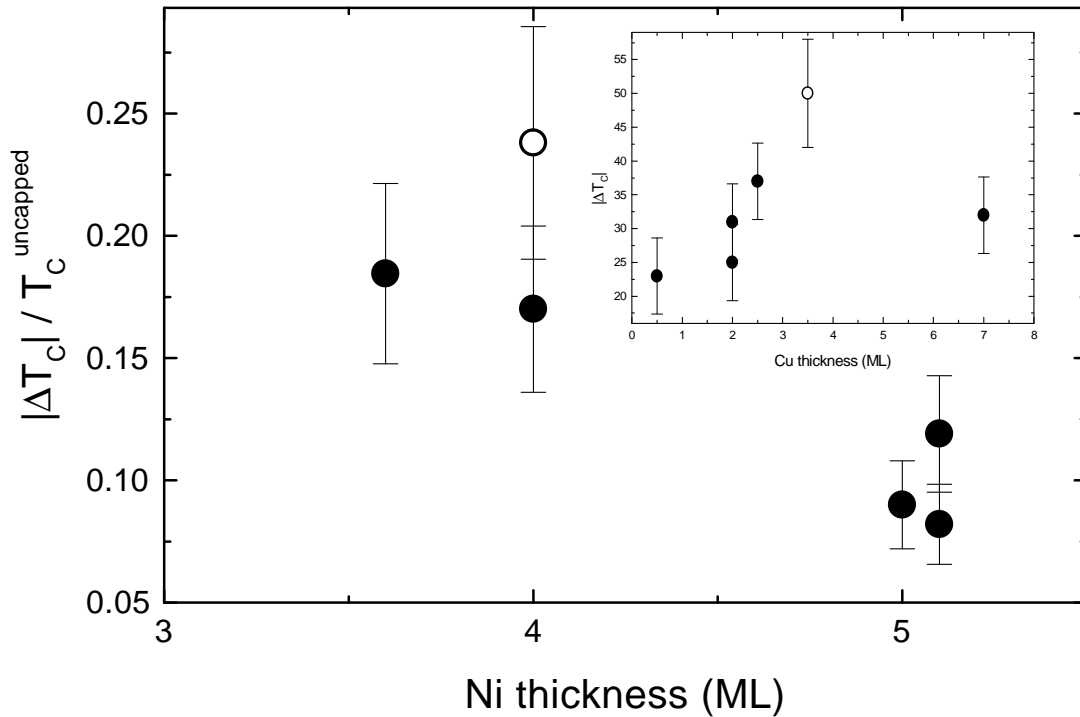

Figure 4.4: Ratio $|\Delta T_c|/T_c^{uncapped}$ as a function of the Ni thickness in ML. The solid circles are susceptibility measurements and the open circle is a XMCD measurements. We see that the ratio decreases with increasing Ni thickness. In inset is shown the difference $|\Delta T_c|$ as a function of Cu thickness. This difference is constant within the error bars.

moments. Effectively, the ratio of the T_c's and magnetic moments are comparable:

$$\frac{T_c^{capped}}{T_c^{uncapped}} = \frac{170}{214} \approx 0.70 \qquad \frac{m_{capped}^2}{m_{uncapped}^2} = \frac{0.20^2}{0.275^2} \approx 0.53$$

Compared to the Co case, we see that the ratio of the Curie temperatures is higher due to a less pronounced reduction of the T_c due to capping. Again the T_c ratio is higher than the magnetic moment ratio. This discrepancy comes from the assumption that the direct exchange coupling J_{intra} is constant and that the anisotropy does not play any role. However from the Eq. 4.8, the curie temperature for thin films depends on the anisotropy. In the coherent growth regime ($d < d_c$), FMR measurements show that a second Cu/Ni interface roughly doubles $|K_2^S|$ and modifies K_2^V by 10% only. If one assumes that the Ni on Cu interface is the same as Cu on Ni, one estimates that the Vac/Ni(001) interface anisotropy is negligible. No change of the easy magnetization direction was found in this thickness regime [119].

To summarize, we see here again that the reduction of the magnetic moments and the Curie temperature are correlated. A 27% reduction of the magnetic moment reduces the
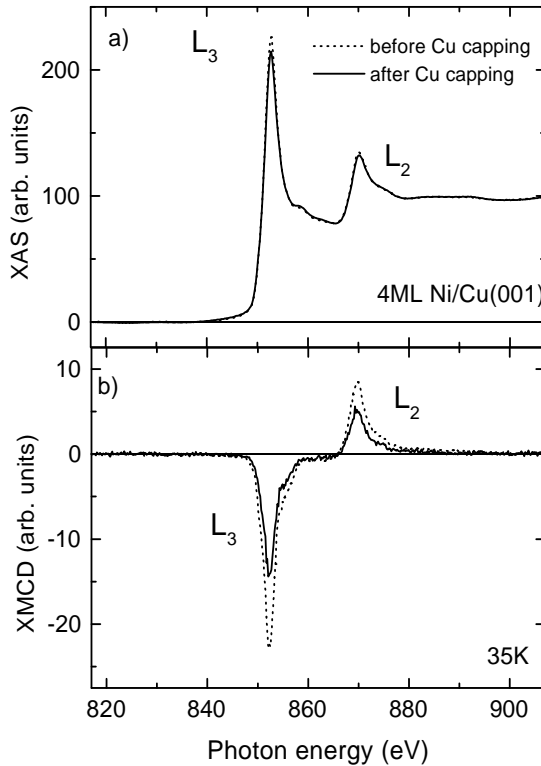

Figure 4.5: Isotropic absorption spectra (upper) and XMCD signal (lower) for 4ML Ni/Cu(001) before (dotted line) and after (solid line) 2ML Cu capping. These spectra were taken at 25K and at grazing incidence (70°). A clear difference is visible betwenn the isotropic and XMCD spectra.

Curie temperature by 20% for a 4ML Ni on Cu(001) film. From the theory using, for a 4ML ferromagnetic film on Cu(001), a reduction of 20% of the magnetic moment at the surface reduces only the Curie temperature by 10% [115].

4.3   The Co/Cu/Ni trilayer systems

At the ultrathin film limit, the two different ferromagnetic components of a bilayer system, i.e. Co/Ni/Cu(001)[120], always undergo under one phase transition at the same Curie temperature. In this case, the direct interlayer exchange coupling is responsible for the appearence of one single Curie temperature T_c. Will one observe a single phase transition for an indirect exchange interlayer coupling, this is to say when two ferromagnetic layers are separated with a nonmagnetic layer?

4.3.1   Element-specific magnetizations

The trilayers were grown at room temperature on Cu(001) substrate in ultra-high vacuum (UHV) conditions and characterized by LEED. A precise thickness determination of the films have been achieved by a precalibrated quartz microbalance, MEED-oscillations, and by using the Ni, Co and Cu $L_{3,2}$-edge jump ratios (see §2.1). The measurements were performed at the monochromator SX700-II and -III at Bessy I. The XMCD spectra were taken by keeping the helicity constant of the incident light fixed and reversing the direction of the remanent magnetization. All the spectra were taken under 70° grazing incidence to the photon spin since the easy magnetization directions of Co and Ni are in the film plane. The easy direction of magnetization of Ni in the bilayer is along the in-plane [100] and for Ni and Co in the trilayer along the [110] if the Curie temperature for Co is higher compared to Ni. The projection was corrected when the measurements were done along the easy axis. The films first were cooled down to 30-50K in order to measure magnetization curves with increasing temperature (the stability of the temperature during recording the spectra was ±0.25K). Figure 4.6 shows the XMCD signals at the $L_{3,2}$ edges of Co and Ni recorded at two different temperatures in a Co/Cu/Ni/Cu(001) trilayer. The dotted spectra were recorded at 290K. At this temperature, for the given thickness the Co and the Ni elements show a clear magnetic signal implying that they are in a ferromagnetic state. By increasing the temperature up to 336K (solid spectrum), the Ni signal disappears within our experimental accuracy showing that it has enter in a paramagnetic phase. Co still remains in a ferromagnetic state. Its signal is strongly reduced due to the fact that Co approaches its Curie temperature. A rotation of the Ni easy axis magnetization is ruled out since, even at higher temperatures, no Ni XMCD

signal is observed.

Here we demonstrate the beauty of this technique which is its element-specificity. Associated with temperature-dependent measurements, it makes XMCD a powerful tool to characterize such prototype trilayer systems [121]. Figure 4.7 shows the temperature dependence of the remanent magnetization curves of Ni and Co for two different trilayers. The y-axis which represents the magnetization has been calibrated in Gauss units following the same procedure explained in the precedent section. The arrows represent the easy axis of the magnetization direction. For all the trilayers, the easy magnetization axis is in the plane of the films. First, we can see that there are two different remanent magnetizations, one for Co and one for Ni, which disappear at two separated temperatures. For the trilayer with a Cu spacer of 3.4ML, we can first observe that the Co and Ni are coupled antiferromagnetically. It is clear that Ni shows no ferromagnetism above $T*^{Ni}$ =213K. The T_c of Co was found to be about 360K. For the trilayer with even a thinner Cu spacer of 2.8ML, for which Co and Ni are coupled ferromagnetically, the same behaviours have
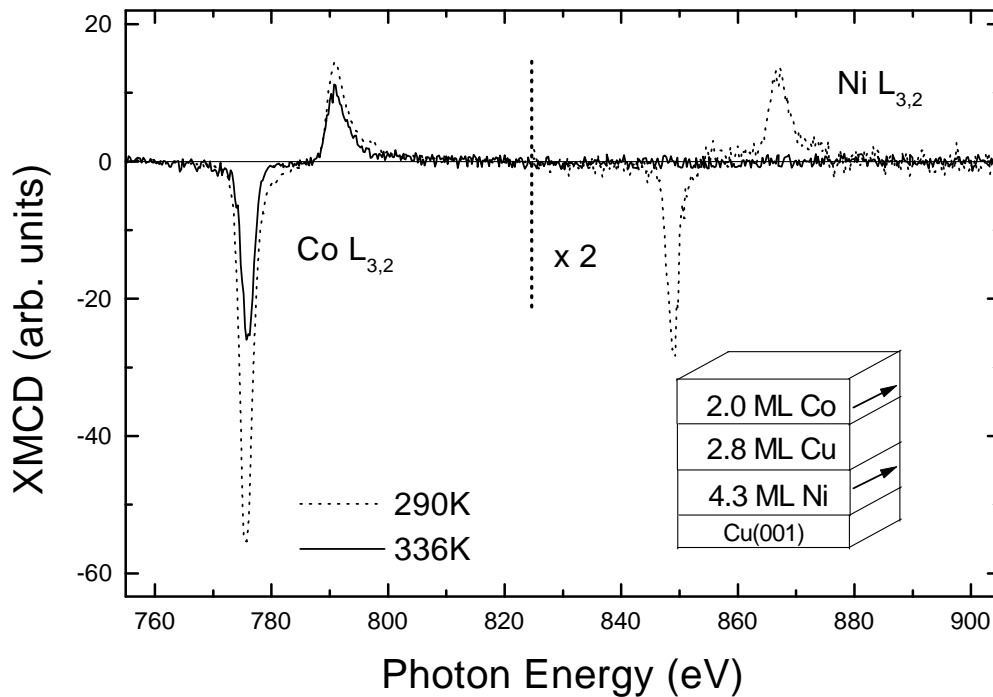

Figure 4.6: XMCD signal of Co and Ni at the $L_{3,2}$-edges in a trilayer at two different temperatures. At $T = 290$K (dotted spectra), both Co and Ni are in ferromagnetic phase state, whereas at $T = 336$K (solid spectra) Ni becomes paramagnetic.

been recorded.

These measurements show that, despite the very thin Cu spacers allowing a strong interlayer coupling between Co and Ni, the two layers enter the paramagnetic phase at different temperatures. For these two trilayers, it is possible to give an estimate for the critical exponent β from the magnetization curves (Eq. 4.4). For Ni/Cu(001) films, a transition from $3D$ to $2D$ behaviour occurs around 5ML. The critical exponent β as a function of the Ni thickness has been estimated via XMCD magnetization measurements. For 4ML Ni/Cu(001), a $\beta = 0.31 \pm 0.10$ has been evaluated [98]. This value is smaller compared to the 0.36 predicted in the $3D$-Heisenberg model. As seen from the previous section, the value should not be affected by Cu-capping. In the case of the trilayers, the analysis shows that this value is enhanced up to $\beta = 0.55 \pm 0.10$ for Ni which is much higher compared to the theoretical $3D$-Heisenberg model. This could be an indication that the temperature where the Ni magnetization disappears is not a true Curie temperature.
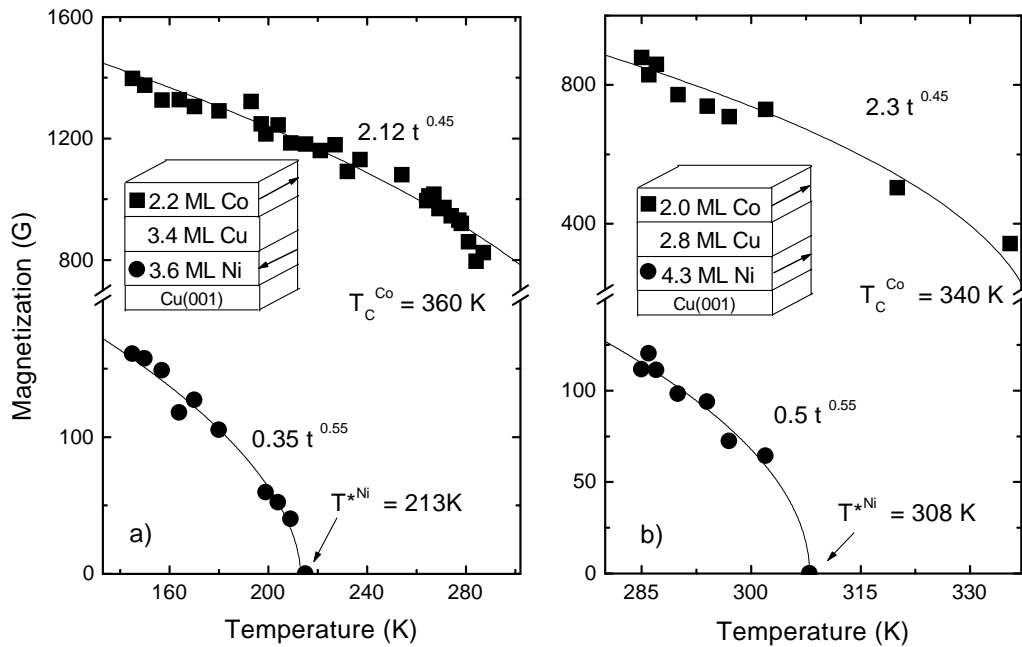

Figure 4.7: Magnetisation curves at remanence of Ni and Co for two trilayers. In both cases, two magnetization curves vanishing at different temperatures were obtained. An asterik (*) has been used for the temperature at which the magnetization of Ni vanishes. The power law $M_o \cdot t^{-\beta}$ was used to fit the magnetization curves.

By shifting the vanishing temperature of Ni by ±1K, the critical exponent is the same within the error bars.

Concerning Co, the same observation can be made in the Ni temperature range. The critical exponent in this case is $\beta = 0.45 \pm 0.10$ which is smaller compared to Ni but still higher than the expected $2D$ critical exponent. This anomalous high critical exponent
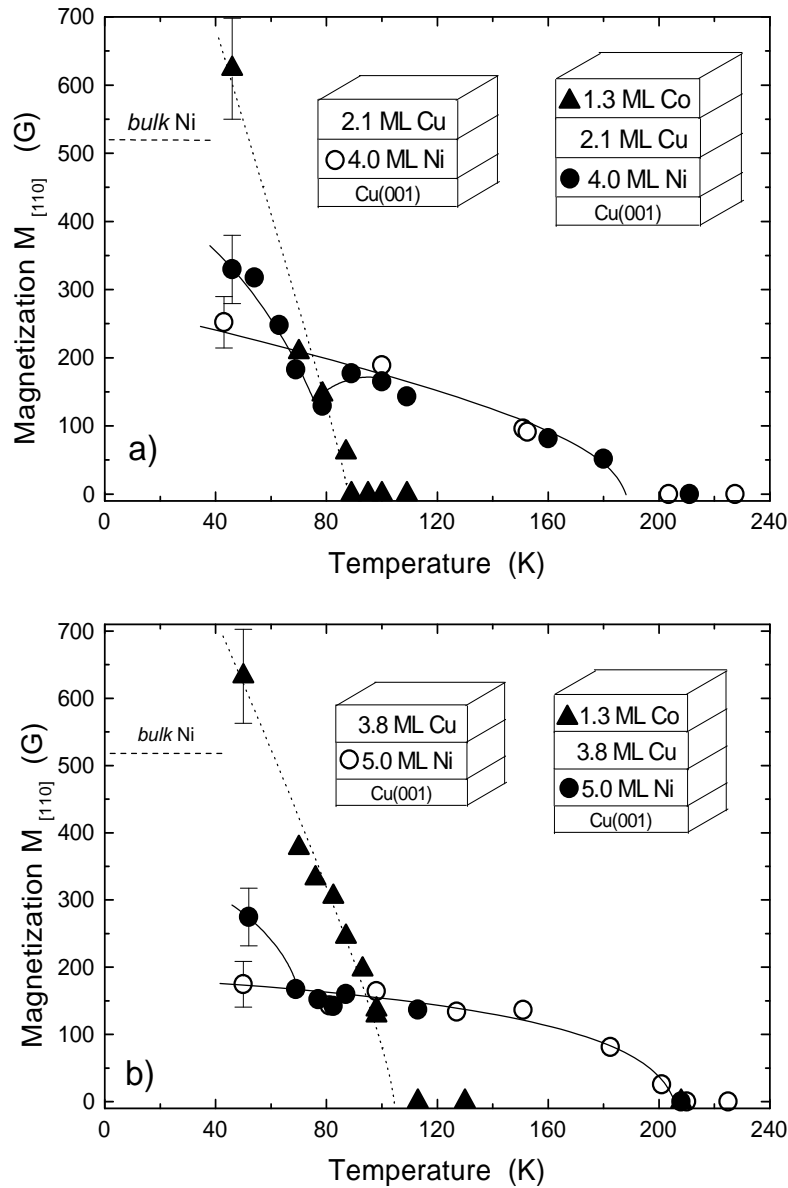

Figure 4.8: Element-specific remanent magnetization curves for two different trilayers. Note that the higher ordering temperature is the one of Ni. At lower temperature the Ni magnetization is increased compared to the bilayer one. The lines are guide to the eyes.
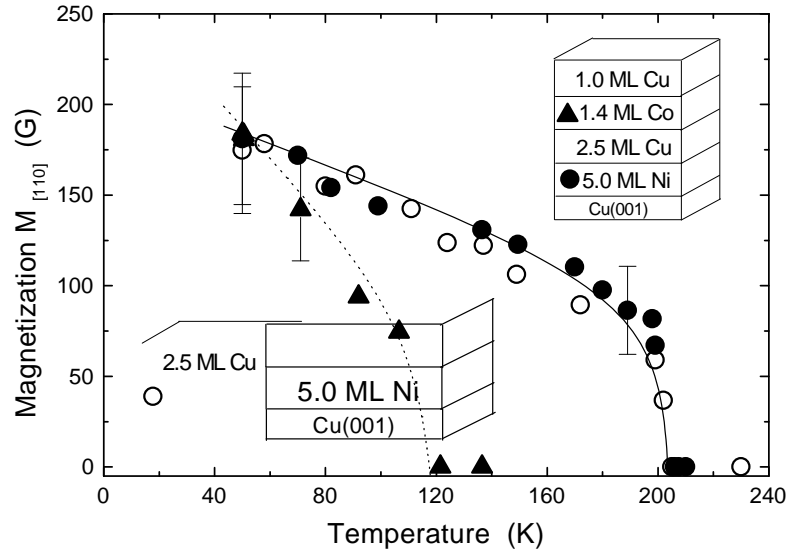
Figure 4.9: Element-specific remanent magnetization curves for a trilayers. At low temperature, no increase of the Ni magnetization is observed as much as the Co magnetization is lower.

could be explained by the presence of an indirect interlayer exchange coupling. No data were collected above 340K in order to avoid intermixing between Cu and Co.

One interesting aspect would be to see if the remanent magnetization of Co directly affects the shape of the magnetization curve of Ni. For this, we have to reduce artificially the ordering temperature of Co so that the ordering temperature of Co is lower than the one of Ni in Cu/Ni/Cu(001) bilayer system. This means contrary to the previous case that a crossing of the remanent magnetization will take place [67]. The Co ordering temperature can be reduced either by decreasing the Co thickness or by capping Co with Cu as seen in §4.2.1.

Figure 4.8 and 4.9 show the element-specific remanent magnetization curves for Co and Ni in the trilayer and in the corresponding bilayer system. All the measurements have been performed along the easy in-plane magnetization of Co [110]. The measurements have been performed along the easy in-plane magnetization axis of Co, i.e. the [110]. In this case, the ordering temperature of Co and Ni are again separated clearly. The remanent magnetizations for the 1.3ML Co and 1.4ML Co capped with Cu vanish around 100-120K. Above this temperature no signal is detected. The ordering temperature of Ni in Cu(2.5-3.8ML)/Ni(5ML)/Cu(001) is approximately 210K. A clear difference of about 90-110K is observed. Concerning the shape of the Ni $M_r(t)$, above the ordering temperature of Co, no changes of the Ni magnetization are observed between the trilayer and bilayer system. The two $M_r(t)$ of Ni in the trilayer and bilayer are exactly superimposed which

is expected since Co is in the paramagnetic phase. This shows the reproductibility of the measurement. Below $T*^{Co}$, the Co $M_r(t)$ increases continuous by decreasing the temperature. Concerning the Ni $M_r(t)$, a change of the magnetization is observed at lower temperatures compared to the bilayer one. This increase of the Ni magnetization at 50K is around 36% and 56% compared to the bilayer one.

In summary, for coupled trilayers Co/Cu/Ni/Cu(001), two different magnetization curves $M_r(t)$ vanishing a two different temperatures are observed. In this case, the Ni and Co $M_r(t)$ are well separated.

4.3.2   Ordering temperature of Ni and Co

Figure 4.10 show $M_r(t)$ curves for both Ni and Co for two different trilayers with respect to the Ni bilayers. $M_r(t)$ of the Ni bilayer was first measured and after evaporating successively Co on the same bilayer. So, the bilayer can be compared directly with the trilayer without introducing any error due to the thickness calibration. Two observations may be done: (i) at low temperatures as observed for thinner Co overlayer, the Ni magnetization in the trilayer is enhanced by 85% compared to the bilayer (Fig. 4.10b [122] and (ii) it is obvious that the $M_r(t)$ of Ni in the trilayer is shifted towards higher temperatures compared to the bilayer one.

The temperature where $M_r(t)$ of Ni vanishes is shifted by $\Delta T = 36$K and $\Delta T = 37$K to $T^{*Ni} = 308$K and $T^{*Ni} = 312$K, respectively. Above T^{*Ni} no XMCD signal of Ni is detected. Since J_{inter} was not acting in the capped Ni bilayer film, the positive ΔT arises from an additional coupling energy in the trilayer. In this temperature range Co is still magnetic. Ni and Co in both trilayers enter the paramagnetic phase at different temperatures. A quantitative analysis of the critical exponent β implies that the vanishing temperature of the Ni magnetization is not a Curie temperature.

Measurements of the thermal-expansion coefficient of antiferromagnetic multilayers $(FeF_2)_m/(CoF_2)_n$ reported by Ramos *at al.* display either one or two maxima depending on the composition m/n [123]. The specific heat of similar systems was studied theoretically [124] and experimentally [125] showing the same behaviour. In order to explain the results of Ramos *at al.*, Wang and Mills [126] studied the onset of long-range order in a model superlattice within the Ginzburg-Landau theory that consists of two materials directly coupled, each of them presenting a different Curie temperature in bulk form (T_c^{low} and T_c^{high}). The calculation of the magnetic susceptibility reveals the existence of two maxima, one "true singularity" at the thermodynamic phase transition near T_c^{high} and a resonant-like anomaly near T_c^{low} (finite maxima). The order parameters, that is the magnetization of the two materials are also calculated. The two magnetizations vanished at

the "true singularity" transition temperature and were non-zero between the two susceptibility maxima. The authors also expect the presence of this effect in indirectly coupled ferromagnetic layers. Our trilayers offer the opportunity to tune the interlayer exchange coupling J_{inter} by changing the thickness of the non-magnetic Cu spacer. Thus, strongly or weakly indirectly coupled trilayers can be studied. Mutual inductance ac-susceptibility measurements for weakly indirect coupled trilayers (25 ML Cu spacer) reveal indeed the
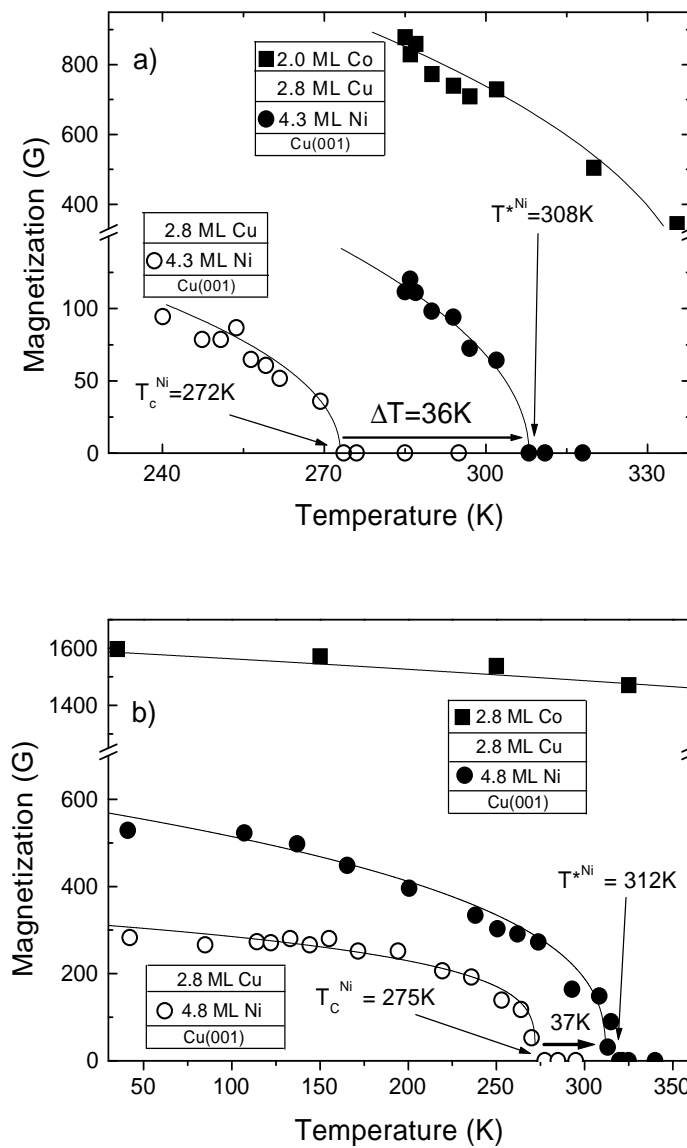

Figure 4.10: Element-specific remanent magnetization curves for two different trilayers. The power law function $M_o \cdot t^{-\beta}$ was used to improve the guide to the eye line.

existence of two signals, corresponding to the "true singularity" at the phase transition of the whole trilayer T_c^{Co} and a resonant-like anomaly at the lower transition T^{*Ni}. The second does not correspond to a phase transition. At this temperature, there is a resonant fluctuation of Ni spins where the Co are still ferromagnetically aligned. In the case of strongly indirectly coupled trilayers, that is with thinner Cu spacer, only one susceptibility maximum is observed [127, 128]. These results support the theoretical analysis of Wang and Mills [126]. From an amplitude analysis of the susceptibility maxima, it was deduced that the indirect interlayer coupling between Ni and Co can be interpreted in terms of an exchange field H_{exch}.

Recently, Jensen *et al.* have shown theoretically by taking into account magnetic fluctuations (Green's-function method) in the Ni film, that the interlayer coupling induces a strong magnetization for $T \geq T_c^{Ni}$ in the Ni film [129, 130]. This was also shown theoretically by Wu *et al.* [131]. Indeed, a resonancelike peak of the Ni susceptibility $\chi_{Ni}(T)$ is obtained for $T \geq T_c^{Ni}$ (Fig. 4.11) . By increasing the interlayer coupling J_{inter}, the
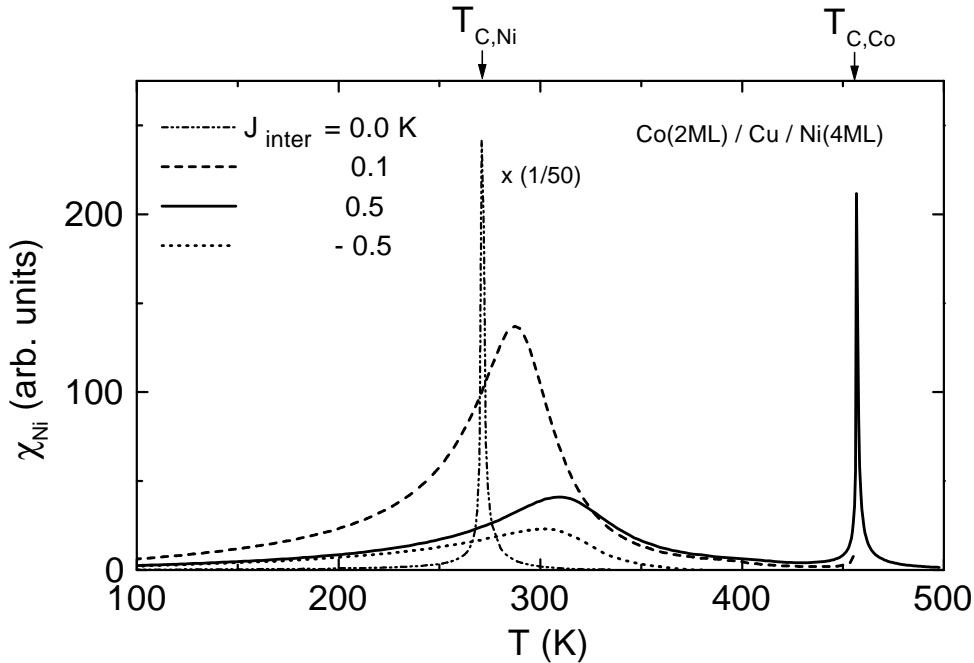

Figure 4.11: Calculated Ni susceptibility in Co(2ML)/Cu/Ni(4ML)/Cu(001) as a function of the interlayer coupling. The susceptibility amplitude field is 2G. The two cases were the interlayer coupling is ferro- and antiferromagnetic is also considered. In the uncoupled case, the susceptibility is scaled by a factor 0.02 [130].

susceptibility peak is shifted to higher temperatures but this maximum value is strongly decreased compared to the uncoupled case (by a factor of 50). The same effect is observed for ferro- and antiferromagnetic coupling. A singularity of the Ni susceptibility occurs at the Co ordering temperature. Thus, the true phase transition is is the Curie temperature of Co (the high temperature ordering) in the case of the coupled Co/Cu/Ni/Cu(001) trilayer systems.

In presence of the interlayer coupling which acts as an external field, the $M_r(t)$ of Ni should qualitatively follow the calculated temperature dependence as shown in Fig. 4.12. We see that the induced Ni magnetization which present a tail, although very small, vanishes at the Co Curie temperature. This explains the unusual high value of the critical exponent β discussed above. The calculated tail which results from J_{inter} at higher temperature cannot be ruled out within our experimental sensitivity (20G). Another explanation of this discrepancy could come from the temperature dependence of the interlayer coupling [132] which was taken as a constant [129]. Very near the ordering
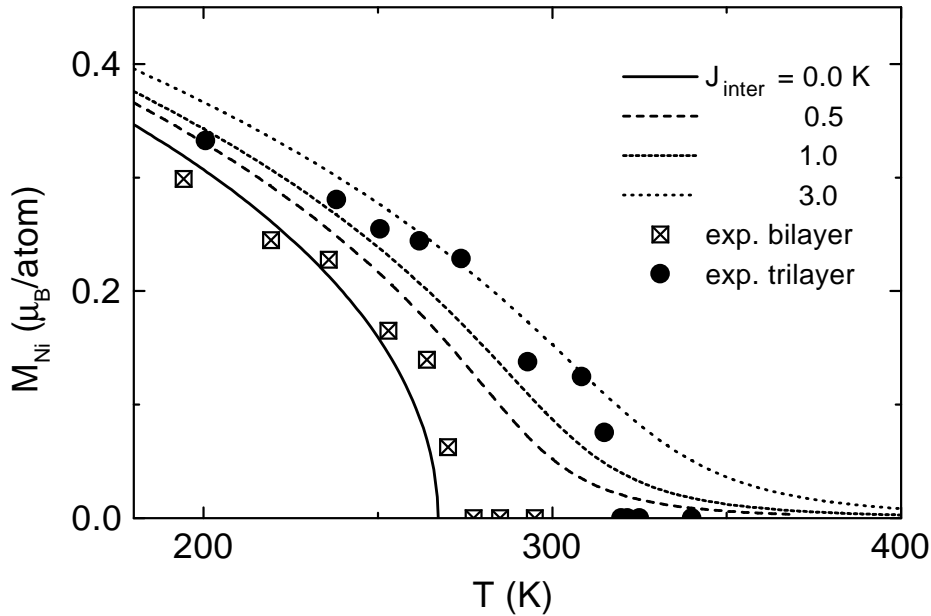

Figure 4.12: Theoretical Ni magnetization for a Co(3ML)/Cu/Ni(5ML) using different interlayer couplings J_{inter}. The T_c of the uncoupled case ($J_{inter} = 0$) is 267K for Ni. The experimental results of the Ni magnetization for the bilayer and trilayer from Fig. 4.10b are also indicated [129].
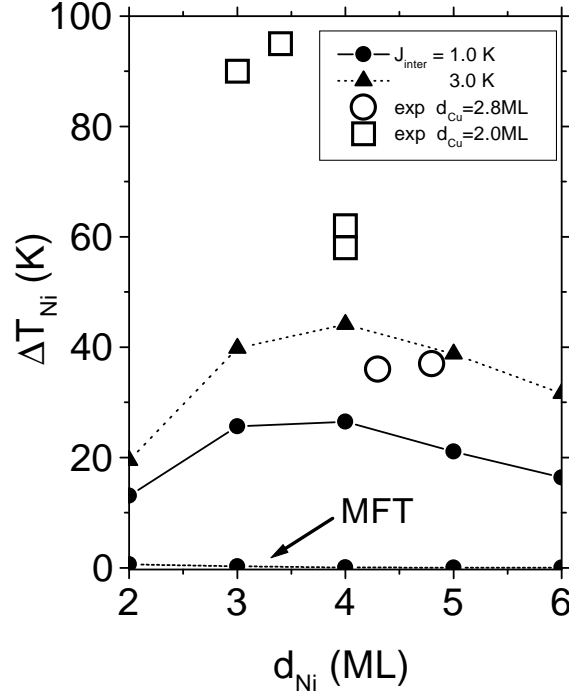
Figure 4.13: Experimental measured ΔT shift of the Ni magnetization as a function of the Ni thickness for Cu-spacer thicknesses d_{Cu} =2.0ML (open squares) and d_{Cu} =2.8ML (open circles) in Co/Cu/Ni/Cu(001) trilayers. Theoretically ΔT shift of the Ni magnetization as a function of the Ni thickness and interlayer coupling (connected solid symbols) is also shown . For comparison is plotted the ΔT shift for strong interlyer coupling (3K) using a mean-field theory (MFT) approach [129].

temperature T^{*Ni}, the coupling strength would be less strong and such a tail would be even less pronounced. The inflection point T_{infl} of the $M_r(t)$ of Ni (which is approximately the calculated maximum of $\chi_{Ni}(T)$) is taken as a measure for the corresponding temperature shift ΔT_{Ni}. One may observe that already a small value of the interlayer coupling J_{inter} (1K) produces a large ΔT_{Ni} ($\approx$30K). By using a mean-filed theory (which neglects the spin fluctuations), for the same value of J_{inter}, the calculated shift ΔT_{Ni} is about ten times smaller than by taking into account the spin fluctuations. Generally, spin fluctuations diminish the magnetization of a two-dimensional (2D) magnetic system more strongly than for a bulk magnet. The interlayer coupling which acts as an external magnetic field suppresses the spin fluctuations, resulting in a larger shift of the 2D Ni magnetization

compared to the 3D.

Furthermore, it could be interesting to see what are the influence of the spin fluctuations on the ΔT shift for different Ni film thicknesses. The Ni magnetization should be more influenced since it has the lower ordering temperature. In Fig. 4.13 is plotted the experimentally measured shift ΔT of the Ni magnetization in Co/Cu/Ni/Cu(001) trilayers (open symbols) as a function of the Ni thickness for two different Cu-spacer thicknesses. The Co thickness was 2.5ML±0.5ML. We see that for 2.8ML, the ΔT shift is constant for 4 and 5ML thick Ni films. The shift is $\simeq 40K$. In the limit case were the Cu-spacer is 2ML thin, the ΔT shift depends on the Ni thickness. For 4ML Ni, the shift is about 60K and for thinner Ni film (3ML), the shift is even around 90K. The Curie temperature of Ni in Cu/Ni(3ML)/Cu(001) bilayer is only around 100K. In comparison, Jensen *et al.* have shown that the ΔT shift between the inflection point of the Ni magnetization is maximum for 4ML Ni films. The maximum calculated shift is 44K. By increasing the thickness of the Ni film, this shift is found to be decreasing. For Ni film thinner than 4ML, contrary to the experiment, the shift decreases again. It is interesting to notice, that using a simple mean-field theory, even if the ΔT is much smaller for a same interlayer coupling, a small increase is observed for 1 and 2 ML Ni film. We see also that a mean-field theory which neglects the spin fluctuations gives much more smaller ΔT shift than those observed experimentally. The difference between the experimental observation and theory could come from proximity effects in addition to the interlayer coupling. Also, pinholes (direct contact between Ni and Co) can not be excluded. In this case, the Ni and Co magnetization should vanish at the same temperature which was not observed.

A similar effect should be observed in the case where the Curie temperature T_c^{high} of the system is the T_c^{Ni}. The measured ordering temperatures T^{*Co} are slightly higher compared to the Curie temperatures of the corresponding Co/Cu(001) [47] (see table 4.4).

System(ML)/Cu(001)	T_c(K)	T^{*Co}(K)	T/T^{*Co}
Co(1.4)/Cu(2.4)/Ni(3.7)		140±5	0.36
Co(1.3)/Cu(3.8)/Ni(5)		105±5	0.55
Co(1.3)/Cu(2.1)/Ni(4)		90±5	0.56
Cu(1)/Co(1.4)/Cu(2.5)/Ni(5)		115±8	0.51
Co(1.3)	80		
Co(1.4)	110		
Co(1.5)	135		

Table 4.4: *Ordering temperature T^{*Co} of Co in Co/Cu/Ni/Cu(001) trilayer systems .*

Strictly speaking, a precise determination of the enhancement of T^{*Co} is difficult since the roughness at the Cu interface is certainly not the same as for Co on Cu(001). In order to avoid such additional effects, it would be better to compare with a Co/Cu/Cu(001) bilayer system.

In summary, indirectly coupled trilayers exhibit only one true phase transition at the temperature where the higher T_c element is placed. Only for thicker Cu spacers, where J_{inter} is very small, a second maximum is observed at T^* which corresponds to a susceptibility resonance.

4.3.3   The indirect interlayer exchange coupling

In a simple mean-field model, the enhancement of the ordering temperature of Ni ΔT originates from an additional coupling energy which comes from the indirect interlayer exchange coupling J_{inter}. In a ferromagnet, the interaction responsible for the T_c is the intralayer exchange energy E_{intra} between two neighbouring spins $\vec{S}_i$ and $\vec{S}_j$:

$$E_{intra} = -2J_{intra}\vec{S}_i \cdot \vec{S}_j \tag{4.13}$$

In a trilayer, the interlayer exchange energy E_{inter} is given by:

$$E_{inter} = -J_{inter}\frac{\vec{M}_{Ni} \cdot \vec{M}_{Co}}{M_{Ni}M_{Co}} \tag{4.14}$$

So, in a first approximation, we can calculate T^{*Ni} by

$$T^{*Ni} = \frac{1}{k_B}\left(\frac{2}{3}J_{intra}zS(S+1) + J_{inter}\frac{\vec{M}_{Ni} \cdot \vec{M}_{Co}}{M_{Ni}M_{Co}}\right) \tag{4.15}$$

where z is the number of nearest neighbours. We have to notice, that even if the coupling J_{inter} changes its sign from plus (ferromagnetic) to minus (antiferromagnetic) the enhancement ΔT will stay positive, since the magnetizations change their direction too (Eq. 4.14). According to Eq. 4.15, an enhancement of $\Delta T = 36K$ should correspond to $k_B\Delta T = J_{inter} \approx 3$meV which is, some how, an overestimated value [133]. It is still much smaller than the typical values for $J_{intra} \approx 100$meV. In the previous paragraph, we showed that within spin waves theory, smaller values of J_{inter} may produce a ΔT of about 40K [129]. Figure 4.14 shows two different trilayers with different Cu spacer thickness. In the first case (Fig. 4.14a), Co and Ni are coupled ferromagnetically since the $L_{3,2}$-edges of Co and Ni have the same sign. For this, the spectrum of Co and Ni were recorded together in one long scan. In order to compare easily the intensity of the XMCD signal, the edge jump of Co and Ni is normalized to 100 each (this procedure blows up the Ni noise).
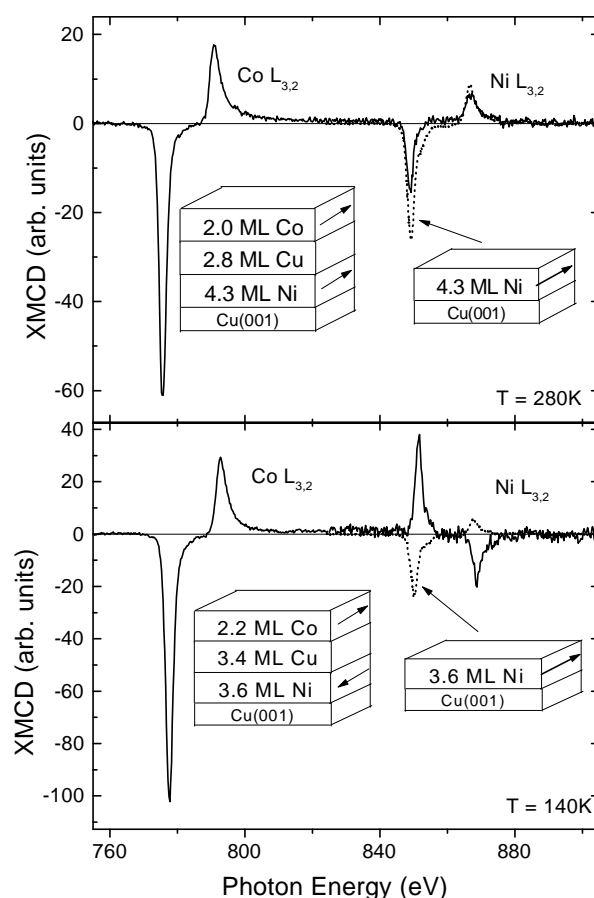
Figure 4.14: XMCD signals of Co and Ni in two trilayers. a) Co and Ni are coupled ferromag-
netically and in b) antiferromagnetically. The spectra shown in a) and b) were recorded at 280K
and 140K, respectively which explains the difference in the XMCD intensity. The corresponding
Ni single layer is shown as a reference.

In the second case (Fig. 4.14b), Co and Ni are coupled antiferromagnetically, since
the $L_{3,2}$-edges have opposite sign. By comparing to a Ni single film taken with same
conditions, we observe that it is the direction of the Ni magnetization which has been
changed and not the one of Co. This is directly linked to the in-plane anisotropy which is
smaller for Ni than for Co. The difference of the Co XMCD signal comes from the different
temperature scanning. The Ni XMCD signal for the single film has been recorded at low
temperatures ($\approx$ 50K). In the first case, the Ni XMCD signal intensity is lower, since
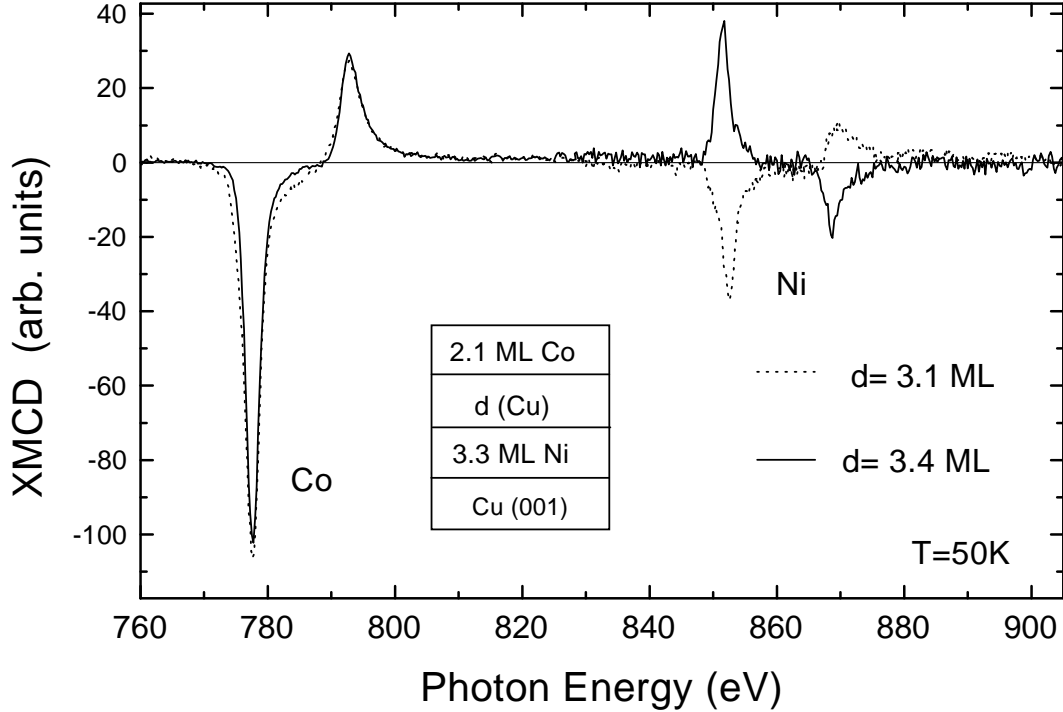
Figure 4.15: XMCD signals of Co and Ni in Co/Cu/Ni/Cu(001) trilayers with different Cu spacer thickness d.

we approach the ordering temperature T^{*Ni}. In the second case, the Ni XMCD signal intensity is larger than the one of single film. As we will show in the next section, the Ni magnetic moment in the trilayer is larger than in the Ni single film on Cu(001). Figure 4.15 again shows the difference of the sign of Ni spectra in trilayers with Cu spacer of different thicknesses.

No difference of the XMCD signal intensity between these two configurations is found. At a first glance, the interlayer coupling depends only on the Cu spacer thickness [134]. For the first time, an antiferromagnetic coupling is observed in trilayers with such a thin Cu spacer [135]. In this configuration, the sign of the coupling remains the same at all the temperatures in agreement with theoretical predictions and previous experiments [136, 137]. The determination of the coupling from the remanent element-specific magnetizations is acceptable for trilayers with small in-plane magnetic anisotropy energy (fourth order) and large J_{inter}. However for larger uniaxial anisotropies and smaller J_{inter}, a parallel alignment of the magnetizations was found in spite of an antiferromagnetic interlayer coupling [137]. Concerning the quality of the trilayer, even for a 2.2ML Cu-spacer, an

antiferromagnetic coupling has been observed which means that the presence of pinholes is negligible. Moreover, pinholes favour a direct exchange coupling between the ferromagnetic layers which are coupled ferromagnetically and then a common phase transition should be observed as it the case in the ultrathin ferromagnetic bilayer system [44].

Theoretical description

Since the first observation of an antiferromagnetic coupling of Fe films separated by a Cr spacer by Grünberg *et al.* in 1986 [1], the interlayer exchange interaction between ferromagnetic layers separated by a nonmagnetic spacer has been a subject of intense research in the last several years [138]. The discovery of oscillations of the interlayer exchange coupling in Fe/Cr/Fe and in Co/Ru/Co multilayers as a function of the spacer thickness [139] and later with any transition metal as a spacer layer [133] has attracted a lot of interest.

To treat the oscillatory character of the coupling theoretically, two different approaches were made: total energy calculations and model calculations. The first approach calculates the total energy of the system for configurations of parallel and antiparallel alignment of the magnetizations and then relates the energy difference to the interlayer exchange coupling. This approach is very difficult since the energy difference between parallel and antiparallel configurations is of the order of 1meV whereas the total energy is larger (for a review see Ref. [140]). For the second approach, various models have been derived (i) the Ruderman-Kittel-Kasuya-Yosida (RKKY) model in which the magnetic layers are described as arrays of localized spins interacting with conduction electrons by a contact potential, (ii) the free electron model, (iii) the hole confinement model, which is essentially a tight-binding model with spin-dependent potential steps and (iv) the Anderson (or *sd*-mixing) model. All these models are unified today into one general approach based on quantum interferences (for a review see Ref. [141]). It describes the interlayer coupling in terms of quantum interferences due to the (spin-dependent) reflection coefficients of electrons at the interfaces between the non-magnetic spacer and the ferromagnetic layers. In a layered structure, all reflected and transmitted electron waves will interfere. Under certain conditions for the electron wavelengths, layer thickness, and phase shift upon reflection, the interference will be constructive or destructive giving rise to oscillations of the density of states as a function of the layer thickness (in analogy with the reflection oscillations in an optical Fabry-Perot cavity), and in many cases to oscillations of related properties, e.g. magnetic anisotropy [142]. In addition to the well-established correlation between the periods of oscillations and the Fermi surface of the interlayer spacer, an oscillatory dependence of the coupling strength on the thickness of the ferromagnetic

layers is expected in this framework. This was confirmed experimentally by Bloemen *et al.* in Co/Cu/Co(001) [143] and by Okuno and Inomata in Fe/Cr/Fe(001) [144].

The exchange coupling energy per unit area between two ferromagnetic films F_A and F_B separated by a non-magnetic spacer is expressed as:

$$E_{A,B} = -J_{inter} cos\theta \tag{4.16}$$

where θ is the angle between the magnetizations in F_A and F_B. The positive (resp. negative) sign of J_{inter} corresponds to a ferromagnetic (resp. antiferromagnetic) coupling. Based on the RKKY model, and taking into account the topology of the spacer Fermi surface of the (001) surface, the interlayer exchange coupling J_{inter} is a superposition of two sine waves:

$$J_{inter}(d) = \frac{1}{d^2}\{A_1 \ sin(2\pi d/\Lambda_1 + \Phi_1) + A_2 \ sin(2\pi d/\Lambda_2 + \Phi_2)\} \tag{4.17}$$

where d is the spacer thickness. For the case of Cu(001) spacer, the short and long periods are predicted to be $\Lambda_1 = 2.56$ ML and $\Lambda_2 = 5.88$ ML (1ML=0.18nm) and with the corresponding phases $\Phi_1 = 0.5\pi$ and $\Phi_2 = \pi$ [134]. The ratio of amplitudes A_1/A_2 have been found to depend critically on the sample quality and ferromagnetic layer thickness. Spin-polarized scanning electron microscopy (spin-SEM) study on M/Cu/Co/Cu(001) trilayers (M=Fe,Co,Ni) has revealed both short- and long- period oscillations in good agreement with theoretical values. For Ni/Cu/Co/Cu(001) trilayers, an amplitude ratio of $A_1/A_2 = 1.3 \pm 0.5$ was observed [145].

The effect of J_{inter} on T^{*Ni}

Very little work has been done on the influence which the quantum size effects might have on the Curie temperature of the ferromagnetic layer. As pointed out before, in a simple mean-field picture, the Curie temperature is proportional to the total exchange energy per atom which is the sum of interlayer and intralayer coupling energy (Eq. 4.15). Then the T_C should oscillate as a function of the spacer layer thickness and with a period of oscillation half of the period of J_{inter}. Evidence for this was found experimentally in polycrystalline Ni/Au multilayers [146]. But the uncertainty reported in the magnetic layer thickness could lead to T_C variations due to finite-size effects similar in magnitude to the observed T_C oscillation amplitude. In order to avoid such effects, epitaxial trilayers with two different ferromagnetic layers, e.g. Ni and Co, having separate ordering temperatures are ideal prototype systems for illustrating the relation between J_{inter} and T_C [135]. Epitaxial trilayers Co(2-2.8ML)/Cu(2.2-4.5ML)/Ni(3-4.8ML)/Cu(001) were characterized via the XMCD technique between 30K and 300K. For Cu-spacer thinner than 3ML, the thickness
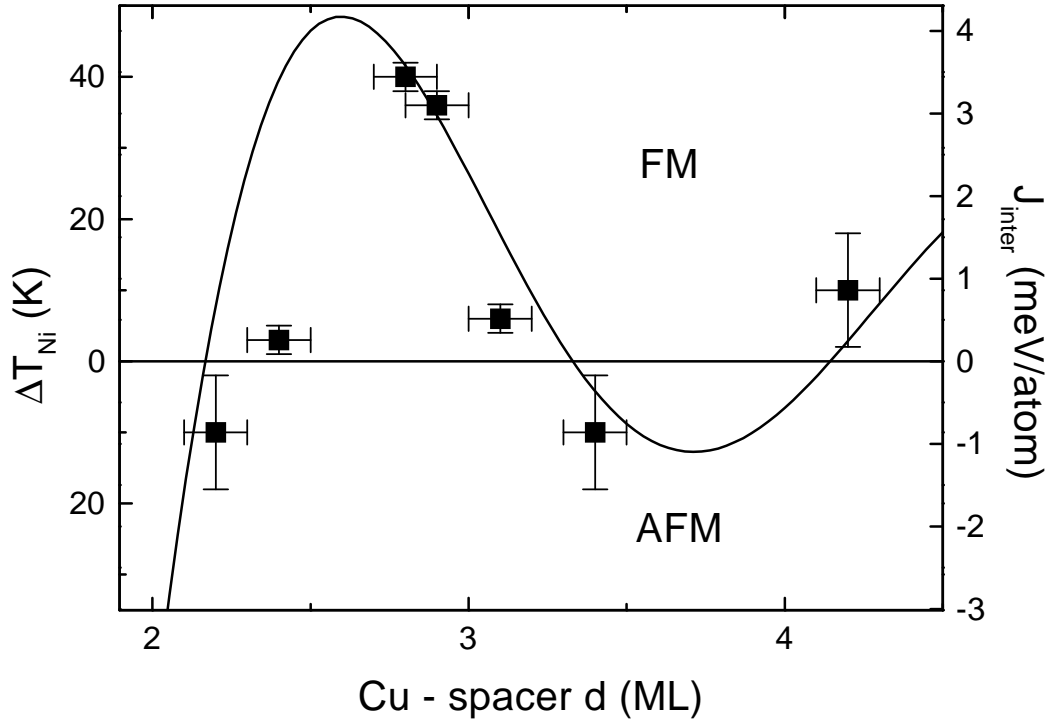
Figure 4.16: Shift of the ordering temperature of Ni ΔT_{Ni} as a function of the Cu spacer thickness for various Co/Cu/Ni/Cu(001) trilayers. The left axis is in temperature units whereas the right axis is in coupling units.

of Ni was kept constant to 4±0.2ML. Element-specific remanent magnetization curves for Ni before and after evaporation of the Co layer were recorded.

Figure 4.16 shows the shift $\Delta T_{Ni} = T^{*Ni} - T_C^{Ni}$ (left scale) as a function of the Cu spacer thickness d (solid symbols). This shift is always positive irrespective of the sign of the coupling. Since the sign of the coupling can be determined unambiguously from XMCD, the positive shift for FM coupling is plotted upwards on the y axis and the positive shift for AFM coupling downwards. As stressed before, existence of AFM interlayer coupling in trilayers with Cu(001) spacers thinner than 5 ML is observed. This enhancement of the ordering temperature is found to oscillate. The maximum variation is about 40K which is for a 2.8ML Cu spacer. High resolution photoemission study of quantum well states in Cu/Co(001) have observed exactly the 2 clear quantum well states for 2.8ML Cu [147]. This is directly correlated to our maxima shift of the ordering temperature. Moreover, a short-wavelength (2.6M± 0.3ML) and a long-wavelenght (5.7± 0.2ML) quantum well state was observed. These correspond very well to the predicted either in the RKKY-like

model or in the QW theory for magnetic coupling. In the simplest mean-field model, ΔT_{Ni} is due to J_{inter} [146, 127]. In this picture, the magnitude of J_{inter} can be derived from the simple relation:

$$z^* \, J_{inter} = k_B \, \Delta T_{Ni} \tag{4.18}$$

Its sign is determined by the XMCD spectra. The values of J_{inter} are given in meV/atom on the right axis of Fig. 4.14. These values given by a mean-field theory are ten times larger than the expected values calculated by taken into account the spin fluctuations. Indeed to observe the same ΔT shift, the interlayer coupling using mean-field theory has to be ten times larger. The "effective coordination number" z^* is set to 1 since the magnetizations contribute as a whole to the interlayer coupling [127]. The solid line in Fig. 4.14 is calculated according to Eq. 4.17 with the theoretical parameters $\Lambda_1 = 2.56ML$, $\Lambda_2 = 5.88ML$, $\Phi_1 = \pi/2$ and $\Phi_2 = \pi$ [134]. The experimental amplitude ratio $A_1/A_2 = 1.3$ is used [145]. No adjustable parameter was used in this calculation. A perfect agreement between the ΔT_{Ni} and J_{inter} is found, which shows clearly that the enhancement of the ordering temperature ΔT_{Ni} is a measure for J_{inter} and it oscillates with double its periodicity. Several remarks have to be made here [141]:

i) The RKKY-model is only valid for integer number of the layers of the spacer. This comes from the discreteness of the spacer layer. In the quantum interferences approach, the spacer thickness is a continuous variable.

ii) In the quantum interference approach, only the out-of-plane wavevector $q_\perp$ ($\vec{q}$ is the difference of the wavevectors of the electron coming from the right $\vec{k^+}$ and reflected $\vec{k^-}$ to the left) which propagates perpendicular trougth the spacer layer is responsible for the interference.

iii) Since only the *sp* band intersect the Fermi level, the Fermi surface is rather simple, and does not depart very much from a free-electron Fermi sphere.

The thickness of the Cu spacer given in Fig. 4.14 is a mass equivalent thickness. In reality, for the 2.8ML thickness spacer, the spacer thickness is an average of 2ML and 3ML of Cu. The coupling strength for 2.8ML Cu spacer is not a simple addition of the coupling strength for 2ML and 3ML Cu spacer. First, Ni grows on Cu(001) almost perfectly layer-by-layer until 4 ML. A difference peak to peak of steps are found to be 1ML. The Cu evaporated on the top of Ni keeps the decoration of the Ni surface. No intermixing between Cu and Ni is found. Cu grows on Ni layer-by-layer too, which is confirmed by the saturated reduction of the Ni T_C after the first monolayer (see §4.2.2).

The maximum roughness is about ± 0.5ML. The lateral size of the island for non integer number of Cu spacer layer is about 50Å or less. Since the band width of localized d- and s-electrons is about 5eV and 50eV respectively, the corresponding mean free path would be about 5-10Å and 50Å. Since the sp-electrons are responsible for the coupling and since their propagation length is larger than the Cu island size, they see an average Cu spacer thickness which corresponds to the mass equivalent (the size spot of the beam is 5x1mm^2). An other argument is that we measure near the ordering temperature, and thus, the fluctuations are of white noise type so composed of low and high frequency fluctuations. The long range order fluctuations are at least about 0.4μm (lower limit for the lateral size of a magnetically homogeneous regime [128]). This means again, that a lateral averaging of the Cu spacer thickness is observed. So, the origin of the enhancement of the ordering temperature of Ni is essentially the exchange interlayer coupling J_{inter}. The probability that proximity effects can play a role can be ruled out since for 2.2ML Cu spacers, an antiferromagnetic coupling is observed.

4.3.4 The magnetic moments

As it was noticed before, from Fig. 4.8 and 4.10b, an increase of the Ni magnetization was observed compared to the bilayer in both cases where the Curie temperature of the trilayer is the one of Co or Ni. Several remarks have to be made before some conclusions.

i) The easy magnetization direction for Ni/Cu(001) for thicknesses below 5ML is in-plane and along the [100]-axis and after until 8ML the easy axis of magnetization is along the [110]-axis (see §3.3.1). By capping the Ni with Cu, no change of the easy axis of magnetization was observed so far.

ii) The easy magnetization direction of fcc Co/Cu(001) is in-plane and along the [110]-axis irrespective of the thickness.

Since it is not possible with our setup to rotate the crystal in the azimuth plane, the measurements were done only along one direction. Depending on the measurement in-plane axis (along either the [100] or [110]-axis), we had to correct for the projection.

For coupled trilayer where T_c^{Co} is the Curie temperature of the system (Fig. 4.8), the easy axis of magnetization for Ni and Co due to the interlayer coupling is along the in-plane [110]. Since the measurements were done along the [100], we corrected the magnetization of Ni and Co in the trilayers by a factor of $\sqrt{2}$. The easy magnetization direction of Ni in the bilayer should be along the [100]-axis. Since the in-plane reorientation occurs around 5ML, the possibility that the easy axis is along the [110] can not be excluded. Even by correcting with $\sqrt{2}$, the Ni magnetization at low temperature would either be

$\approx 282 \pm 70G$ or $\approx 400 \pm 70G$ for an easy magnetization direction along the [100]- or [110]-axis, respectively. This is in all the cases lower than the magnetization of Ni in the trilayer which is$\approx 520 \pm 70G$ and this for all the temperatures. Using the sum-rules at low temperatures, the total magnetic moment of Ni in the trilayer (since the ordering temperature is far away from the lowest temperature) is estimated to be $m_{tot}^{Ni} = 0.63 \pm 0.08 \mu_B$ compared to the $m_{tot}^{Ni} = 0.33 \pm 0.08 \mu_B$ or $m_{tot}^{Ni} = 0.47 \pm 0.08 \mu_B$ total magnetic moment of Ni in the bilayer (depending on the easy axis). There is, therefore, an increase of the moment by a factor of 1.4-2 for a 4.8ML Ni in the trilayer. A similar effect has be observed in Ni/Au multilayers for the coupled case compared to the uncoupled case ($0.42 \mu_B$ compared to $0.36 \mu_B$ for 0.73nm Ni thickness) and in Ni/Pt (see §6.1.3).

As pointed out by Bruno [141], the density of states of the system is modified by the quantum interference since the wavefunction of the reflected electron are modified due to the electron confinement. In fact, the effect of interlayer coupling on the ground state moments has been studied theoretically using a tight binding scheme for the Fe/Cr system [148]. Indeed a correlation between the coupling and the magnetic moments was found. So, apparently a ferromagnetic or even antiferromagnetic interlayer coupling not only stabilizes the magnetic order at finite temperatures, but also enhances the ground state moments in the itinerant ferromagnet compared to the bilayer system. In our case, since for the 2.8ML of Cu-spacer, quantum well states are observed, it is reasonable to expect that an increase of the Ni magnetization takes place. In Fig. 4.12, such an effect is not observed since the magnetic moment is a fixed parameter. In the case of Co, an enhanced total magnetic moment $m_{tot}^{Co} = 1.9 \pm 0.1 \mu_B$ is found, as expected, for 2ML Co/Cu(001).

For coupled trilayers where T_c^{Ni} is the Curie temperature for the whole system (Fig. 4.8), an increase of the Ni magnetization at low temperatures in the trilayer is found too. Contrary to the previous case, the measurements were done along the in-plane [110] since the ordering temperature of Co is lower. This increase is of the order of 36% and 56%, respectively compared to the bilayer. It could have two origins:

i) A reorientation occurs in the plane. Following the same argument as before, it could be that the easy magnetization direction is along the [110]- or[100]-axis (since 5ML of Ni is the transition thickness). If it is along the [100]-axis, a rotation of 45° would have taken place. If it is the last case, then as before, the magnetization has to be corrected by $\sqrt{2}$, and this could correspond approximately to the observed enhancement. However, from the shape of the Ni magnetization, it seems that the Ni magnetization is not saturated at low temperatures, since the slope is very abrupt (which is an indication of temperature-dependent interlayer coupling).

ii) Another explanation could be the formation of domains near the T^{*Co} ordering

temperature. By decreasing the temperature, the interlayer coupling acts as an external field and restores the film fully in a single-domain.

The second argument is the less plausible scenario since the formation of domains is essentially observed for system with perpendicular anisotropy (in this case a multidomain state with perpendicular magnetization could be stabilized [137]).

From Fig. 4.9, no enhancement of the Ni magnetization in trilayers is found for low temperatures. This can come from the temperature dependence of the interlayer coupling. Indeed, we can observe from the Fig. 4.8 that for a Co magnetization lower than 300G, no change in the Ni magnetization is observed. Only up to this value, an increase of the Ni magnetization occurs. This explains why no increase of the Ni magnetization is observed in Fig. 4.9. In order to determine the magnetic moments, the magnetization has to be extrapolated to 0K. Since the reduced temperature of Co is only $t = 0.6$, no extrapolation is feasible in order to deduce magnetic moments.

Chapter 5

Magnetic anisotropy of Ni in Ni/Pt multilayers

The orbital magnetism of $3d$ transition metals has become a topic of major interest. We have shown in the third chapter that transition metal ultrathin films as Co on Cu(001) or on Cu(1 1 21) or even Ni on Cu(001) exhibit either enhanced spin and/or orbital moments, and large magnetic anisotropies, e.g. perpendicular magnetic anisotropy (PMA). Their microscopic origin was attributed to the reduced symmetry experienced by magnetic atoms near the interfaces or surfaces. Of particular interest for technological application are systems with large PMA which are highly desired for magneto-optical recording, for example. Earlier, perpendicular magnetized Co layers have been considered as promising materials [149], but the undesirable high Curie temperature T_c has stimulated a search for alternative solutions. Recently, Pt-Ni multilayers have shown perpendicular anisotropy and good magneto-optical features at room temperature for technological applications [150]. Interestingly, and contrary to the Co/Pt multilayers, the perpendicular anisotropy in Ni/Pt multilayers develops not only for very thin magnetic layer thickness in the multilayer period but also for thicker ones (1.5 nm) when the Pt layers become extremely thin (0.3-0.4 nm). Thus, in this multilayered system, we have a unique type of spin reorientation phase transition depending on the thickness of the non-ferromagnetic element. However, Ni/Pt multilayers with very thin Ni and Pt layers ($\approx$2 monolayers in the multilayer period) are the only Ni-based perpendicular magnetized multilayers with relatively large values of magnetic anisotropy energy (MAE) [151]. For comparison, in ultrathin Ni/Cu(001) films, large values of MAE have also been reported. For 20ML fct Ni/Cu(001) measured at room temperature, ferromagnetic resonance measurements done at room temperature have determined $MAE \simeq -27\mu\text{eV/atom}$ which have to be compared with $MAE^{bulk} = +0.4\mu\text{eV/atom}$ for the fct Ni [96].

We will first describe the origin of the magnetic anisotropy and its relation to the anisotropy of the orbital moment for $3d$ transition metals. In the second part, since the x-ray magnetic circular dichroism measurements allow us to determine separately the spin and orbital magnetic moments, we will determine for a Ni_2/Pt_2 multilayer, by combining high magnetic field and angular-dependent measurements, the anisotropy of the orbital moment and relate it to the magnetic anisotropy energy. We will show that saturation effects can lead into erroneous conclusions in the determination of the anisotropy of the orbital moment and that they have to be considered in the analysis [153].

5.1   Origin of the anisotropy

The primary property of ferromagnets such as Fe, Co or Ni is the appearance of spontaneous magnetization below the Curie temperature T_c. It is recognized since Heisenberg that the appearance of ferromagnetism is due to the Pauli principle, which prevents two electrons with parallel spins to occupy the same orbital state. As a direct consequence, the effective Coulomb repulsion for a pair of electrons with parallel spins is weaker than for antiparallel spins. This is known as the exchange interaction. This exchange interaction is invariant for a rotation of the magnetization direction. However, the magnetization lies generally in a preferential direction (easy axis), [111] for fcc Ni, [0001] for hcp Co and [100] for bcc Fe. This property is known as the magnetic anisotropy. The magnetic anisotropy energy is the necessary energy to rotate the magnetization from a direction of low energy (easy axis) towards a direction of high energy (hard axis). MAE is typically of order of 10^{-6} to 10^{-3}eV/atom.

The easy axis of magnetization results from a competition between two anisotropy mechanisms:

  i) The shape anisotropy which arises from the dipolar interaction between the spins

  ii) The magnetic anisotropy which arises from the spin-orbit coupling interaction

In thin films or multilayers, shape anisotropy favours always an in-plane orientation of the easy direction whereas the magnetic anisotropy can either favour an in-plane or an out-of-plane easy axis. When the magnetic anisotropy energy favours an out-of-plane easy direction and is higher than the shape anisotropy energy (or shape anisotropy), we observe the so-called perpendicular magnetic anisotropy like ultrathin Ni on Cu(001) [96].

5.1.1 The shape anisotropy

In an itinerant ferromagnet, the magnetization distribution within each atomic cell is not spherical; then its expansion includes various multipoles. The first term in the multipole expansion corresponds to the magnetic spin moment. The monopole term of the spin density gives rise to the so-called dipole-dipole interaction. Since all the moments are parallel due to the strong exchange interaction, the dipolar energy can be written as:

$$E_{dip-dip} = \frac{\mu_0}{4\pi} \sum_{i \neq j} \frac{m_i m_j}{r_{ij}^3} (1 - 3\cos^2\theta_{ij}) \tag{5.1}$$

where i, j are the atomic indices and θ_{ij} the angle between the magnetic moment and the direction $\vec{u}_{ij}$ of the pair (i,j). So, the energy is smallest when the magnetic moments are aligned parallel to the internuclear axis. The quadrupole term in the multipole expansion of the spin density gives rise to the intra-atomic magnetic dipole moment (which corresponds to the T_z term). Since the anisotropy coming from this contribution is smaller than the spin magnetic moment, they can be neglected in a first approximation . We will indeed show later on that the anisotropy of the magnetic dipole term for an anisotropic Ni/Pt multilayer is very small.

For bulk materials, since the summation of the pairs (i,j) converges very slowly (due to r_{ij}^3), the dipolar field depends strongly on the moment localized at the boundary, which results in the shape anisotropy. The most important "macroscopic" contribution of the dipolar field is the demagnetisation field due to the pseudo-charges on the external surface[1] For a uniform magnetized thin film, the shape anisotropy is written as:

$$E_{dip-dip} = -2\pi M_V^2 \tag{5.2}$$

where M_V is the volume magnetization. For bulk Ni, for example, the shape anisotropy energy is $E_{dip-dip} = 11.8\mu eV/atom$ [152]. For thin films and multilayers, the shape anisotropy favours always in-plane orientation of the easy direction. Here, we see first how important it is to know with high accuracy the magnetization in order to determine the shape anisotropy energy for thin films since the magnetic moments for ultrathin Co and Ni films on Cu(001) are not bulklike (see chapter 3).

5.1.2 The magnetic anisotropy

Van Vleck in 1937 was the first who attributed the physical origin of MAE to the spin-orbit coupling [154]. This interaction is interpreted as the coupling between the spin of

---

[1]There are two other terms, the contribution from the dipoles within the volume and the Lorentz field. They contribute to the dipolar crystalline anisotropy but are negligible compared to the shape anisotropy.

	$m_{tot}(\mu_B)$	$\Delta m_{tot}(\mu_B)$	$|\mathrm{MAE}|(\mu\mathrm{eV}/\mathrm{atom})$	easy axis
Fe	2.22	1.7×10^{-4}	1.4	bcc [100]
Co	1.72	77×10^{-4}	65	hcp [0001]
Ni	0.62	1.08×10^{-4}	2.7	fcc [111]

Table 5.1: Anisotropic magnetic moment in bulk Ni, Co and Fe [155].

the electron and the magnetic field created by its own orbital motion around the nucleus. The orbital motion is coupled to the lattice via the electric potential of the ions. It is a localized interaction since the spin-orbit interaction is large in the neighbourhood of the nucleus, where the potential is spherically symmetric in a good approximation. For $3d$ transition metals, the crystal field[2], which is of order of $\approx$ 1eV quenches the orbital moment. However, the spin-orbit coupling lifts partially the quenching of the orbital moment. The spin-orbit constant ξ which is the radial average of $\xi(r)$ over d-orbitals is of the order of 50-100meV. Table 5.1 shows that the anisotropy of the magnetic moments is very small but not zero. The anisotropy can only be measured by applying an external field strong enough to saturate the sample, i.e. to tilt the magnetization $\vec{M}$ away from the easy direction. The magnetic anisotropy can be deduced from the dynamic response of the magnetic system or from the static response. The dynamic response of the magnetic layer can be measured with ferromagnetic resonance (FMR) [156] whereas the static response can be measured with magneto-optic Kerr effect (MOKE), vibrating sample magnetometry (VSM) or superconducting quantum interference device (SQUID). FMR is the most suitable technique for determining all magnetic anisotropy constants via angular-dependent measurements [156, 157]. Since van Vleck, the magnetic anisotropy energy was treated as a phenomenological quantity of the free energy density [158] and described in terms of thermodynamic constants K_i. These anisotropy constants have a surface and a volume contribution which are temperature-dependent [156]. They can be determined with high accuracy as it has been shown for Fe/V multilayers [159]. Since the magnetic anisotropy energy is a small fraction (in the order of μeV/atom) of the total energy per atom in solids (in the order of 10eV/atom), *ab initio* calculations of the magnetic anisotropy energy and microscopic theories were for a long time able to reproduce the experimental values. Only recently, with increasing the accuracy of calculations of MAE [160], and by including the orbital polarisation correction [48], the values obtained for the MAE are comparable to the experimental ones, as it was demonstrated for fct Ni [101].

---

[2]It is given by the band dispersion of the energy levels.

However, a simple model to understand the microscopic origin of the MAE was lacking. Bruno shows that the magnetic anisotropy energy MAE in the $3d$ itinerant "hard" ferromagnetic element is proportional to the anisotropy of the orbital moment Δm_L and to the spin-orbit coupling parameter ξ (MAE$\sim \xi \Delta m_L$) [161] as it is know in the picture of localized magnetism [162]. The beauty of Bruno's model lies in the simplicity to explain that there is only one source of the magnetic anisotropy in the microscopic limit: this is the anisotropy of the orbital moment.

The only technique up to now which allows a precise determination of the orbital moment is the x-ray magnetic circular dichroism and its advantage, on the top of this, is the element specificity. FMR allows to measure with high precision the MAE and the g factor which is proportional to the ratio of the orbital-to-spin moment, but not separately to the orbital moment.

The MAE in perturbation theory

For $3d$ transition ferromagnets, since the spin-orbit coupling parameter ξ is much smaller than the bandwidth W and the exchange splitting Δ_{ex} (few eV), then it is natural to calculate the magnetic anisotropy by using the perturbation theory. For rare earth elements, since the spin-orbit coupling is larger, a different approach has to be used [163]. To calculate an anisotropy constant of order n, one has to use a perturbation theory of order n. For hcp crystals and ultrathin films, a second order perturbation is sufficient, whereas for cubic crystals, the fourth order perturbation is necessary[3]. The anisotropy energy is a very small correction to the total magnetic energy. The change in energy of second order in spin-orbit coupling is given by the well known formula:

$$\Delta E_{s.o.} = \sum_{exc} \frac{\mid \langle exc. \mid H_{s.o.} \mid gr. \rangle \mid^2}{E_{gr.} - E_{exc.}} \tag{5.3}$$

where $\mid gr. \rangle$ and $\mid exc. \rangle$ correspond to the ground and excited state, respectively, and $H_{s.o.}$ to the spin-orbit Hamiltonian $\xi \vec{l} \cdot \vec{s}$. The only excited states one needs to consider here, are those where an electron is raised from an occupied state into an empty state above the Fermi level. A very rough estimate of K_1 for a uniaxial system (hexagonal) yields in:

$$K_1 \sim \frac{\xi^2}{W} \tag{5.4}$$

where W is the d bandwidth. By taking $\xi = 75$meV and $W \approx 5$eV, we obtain an anisotropy constant of 2nd order $K_1 \approx 1$meV/atom which corresponds to the order of magnitude of

---

[3]It is similar to the symmetry consideration in the thermodynamic description for a cubic system where the coefficient of second order is forbidden.

the experimental anisotropy value in ultrathin films, multilayers or uniaxial systems. For cubic system, the fourth order perturbation theory gives for K_1:

$$K_1 \sim \frac{\xi^4}{W^3} \qquad (5.5)$$

By taking the same parameter, we obtain an anisotropy constant of 4th order of about $K_1 \approx 0.3 \mu eV/atom$, as compared to the experimentally determined bulk values for Ni and Fe (see table 5.1).

The expectation value of the orbital moment can be treated in second-order perturbation theory since the spin-orbit coupling is much smaller than the bandwidth and the exchange splitting (few eV). It can be written as:

$$\langle \overrightarrow{L} \rangle = \sum_{exc} \frac{\langle gr. \mid \overrightarrow{L} \mid exc. \rangle \langle exc. \mid H_{s.o.} \mid gr. \rangle}{E_{gr.} - E_{exc.}} \qquad (5.6)$$

If we consider now that the exchange splitting Δ_{ex} is larger than the crystal field parameter Δ_{cf} (correlated to the bandwidth W), then the majority spin band is full and a spin-flip cannot occurs. In this case, Bruno showed that the change in energy (Eq. 1.3) and the orbital moment of the minority spin are related as:

$$\Delta E_{s.o.} \sim -\frac{1}{4} \xi \hat{S} \cdot \overrightarrow{m}_L^{\downarrow} \qquad (5.7)$$

where $\hat{S}$ is the magnetization direction (the direction of the external saturation field), $\overrightarrow{m}_L^{\downarrow}$ is the orbital moment in the minority spin band and ξ the radial part of the spin-orbit interaction.

By using a thermodynamic description, taking into account symmetry considerations, the anisotropy energy (which is given by the Gibb's free energy) for uniaxial or tetragonal systems can be expressed as:

$$\Delta E_{s.o.} = K_0 + K_1 \sin^2\theta \qquad (5.8)$$

where K_1 is the anisotropy of order 2 and θ is taken with respect to the uniaxial axis. It is clear that the anisotropy constant K_1 is thickness- and temperature-dependent [156].

Thus, in the case of a "hard" $3d$ ferromagnet (like Co and Ni), the magnetic anisotropy energy which is the energy difference between two principal crystallographic directions (the direction parallel $\parallel$ and perpendicular $\perp$ to the film plane) for uniaxial systems is given by:

$$MAE = \Delta E_{s.o.}^{\perp} - \Delta E_{s.o.}^{\parallel} = -K_1 \sim -\frac{1}{4} \xi (m_L^{\perp} - m_L^{\parallel})^{\downarrow} \qquad (5.9)$$

where the orbital moment is given in μ_B/atom. We use the convention that $MAE < 0$ for an easy axis perpendicular to the surface. Here, we see directly the enormous advantage to determine directly the magnetic anisotropy energy without calculating explicitly the total energy of the system as a function of the magnetization. However, it doesn't take into account any change of the Fermi surface. Finally, for "hard" $3d$ ferromagnet where the majority spin band is filled, the magnetic anisotropy energy is directly related to the anisotropy of the orbital moment at T=0K.

This model given by Bruno was recently extended by van der Laan by including the majority spin band orbital moment and spin-flip excitations [164]. The MAE can then be expressed as:

$$MAE \sim -\frac{1}{4}\xi\left[(m_L^\perp - m_L^\parallel)^\downarrow - (m_L^\perp - m_L^\parallel)^\uparrow\right] + \frac{21\xi^2}{2\Delta_{ex}}(m_T^\perp - m_T^\parallel) \qquad (5.10)$$

where Δ_{ex} is the $3d$ exchange splitting. In higher order perturbation, we see that the dipole magnetic moment contributes in the magnetic anisotropy. For "hard" $3d$ ferromagnets, we can neglect the term $(m_L^\perp - m_L^\parallel)^\uparrow$ in the Eq. 1.10. For the other ferromagnets, an other difficulty appears, since the XMCD measures the total orbital magnetic moment $(m_L^\downarrow + m_L^\uparrow)$ and not the difference $(m_L^\downarrow - m_L^\uparrow)$. Unfortunately, $m_L^\downarrow$ and $m_L^\uparrow$ cannot be obtain separately. But, their contribution can be estimated using either theoretical models or an analysis of the first spectral moment of the XMCD spectra [165]. The first term in the Eq. 5.10 contains only excitations which conserve the spin. The second term contains both spin conserved and spin-flip terms. We see that the energy will decrease in the presence of excitations that conserve the spin but increases for excitations that reverse the spin. Thus, the easy direction of magnetization will be dictated by the largest contribution and lies not always along the direction where the orbital magnetic moment is the largest. In our case, we will neglect the second term since $\xi^2/\Delta_{ex} \ll 1$ and the dipole magnetic is small compared to the orbital magnetic moment.

Using a tight-binding formalism, Bruno showed a strict relation between the magnetic anisotropy and the anisotropy of the orbital moment [161]. This relation for "hard" ferromagnet is the following:

$$MAE = -K_1 = -\alpha\frac{1}{4}\xi(m_L^\perp - m_L^\parallel)^\downarrow \qquad (5.11)$$

where in the prefactor α enter the bandwidth W and the Coulomb integral U. For the case where the exchange splitting Δ_{ex} is much larger than the bandwidth W, the prefactor $\alpha = 1$. For transition metals, $\Delta_{ex} < W$ so that the prefactor is smaller than 1 [50]. Since the band structure changes as a function of the thickness, W, U and α may not be constant for ultrathin films with variable thickness. First-principle calculations have

indeed shown that a strict proportionality between the MAE and Δm_L $((m_L^\perp - m_L^\parallel)^\downarrow$ in our case) does not exist, which means that the prefactor α is not a simple numeric constant but it is a function of Δm_L as depicted in Fig. 5.13 [101] (see §5.3.4). This means that to each Δm_L corresponds a prefactor α.

Recently, van der Laan demonstrated that for $3d$ itinerant transition metals, the MAE is also directly proportional to the anisotropic angular part of the spin-orbit interaction. The spin-orbit interaction could be obtain trough x-ray magnetic linear dichroism measurements [167].

The anisotropy of the orbital moment

The microscopic origin of the anisotropy of the orbital moment can be attributed to the anisotropy of the lattice [36]. The 5 pure d orbitals (d_{xy}, d_{yz}, d_{xz}, $d_{3z^2-r^2}$ and $d_{x^2-y^2}$) have no orbital moment. All these d orbitals possess a perfect balance of $\pm m_l$ contributions. In presence of the spin-orbit coupling, this balance is destroyed. The spin-orbit interaction mixes different d orbitals (see Eq. 1.6). This leads to new states with unequal $\pm m_l$ contributions and the orbital moment becomes nonzero.

In a $3d$ transition metal, the crystal potential gives rise to a splitting of the d orbitals which reflects the symmetry of the lattice. If the crystal symmetry is high (e.g. cubic symmetry), the d orbital bonding is symmetric, and in this case the orbital moment will be isotropic. Now, in the case of a free standing monolayer or multilayers, the charge distribution (which is correlated to the chemical environment) is anisotropic. This implies that for a free standing monolayer the orbital moment should be larger in the bonding plane than perpendicular to it. This comes from the lack of the out- of-plane neighbours. In the case of multilayers, the orbital would be larger in the out-of-plane direction. However, the enhancement of the orbital moment along one principal crystallographic direction does not necessarily increase the anisotropy.

First-principle band structure calculations indeed provide the basis for anisotropic bonding in monolayers and multilayers [168]. Daalderop *et al.* demonstrate for a free Co monolayer the bandwidth associated with the in-plane d_{xy} and $d_{x^2-y^2}$ orbitals is larger than the bandwidth associated with the out-of-plane d_{xz}, d_{yz} and $d_{3z^2-r^2}$ orbitals. Effectively, the overlap of the in-plane orbitals (σ bonding) leads to a larger bandwidth compared to the less overlapping of the out-of-plane orbitals (π bonding). Based on a ligand field model, Stöhr showed that the magnetic anisotropy energy is written as [166]:

$$MAE = -\frac{1}{4}\xi(m_L^\perp - m_L^\parallel)^\downarrow = \frac{\xi^2}{8V_\parallel}\left(\frac{3}{R} + \frac{2}{R+1} - 4\right) \qquad (5.12)$$

where the in-plane d_{xy} and $d_{x^2-y^2}$ orbitals are separated by $2V_\parallel$ and the out-of-plane d_{xz},

d_{yz} orbitals by $2V_\perp$ and R the ratio $V_\perp/V_\parallel$. It was assumed that the spin-flip between the majority and minority are negligible and that the majority band is full. We see, indeed, that an in-plane easy axis for $V_\parallel > V_\perp$ revealed that $m_L^\parallel > m_L^\perp$ and an out-of-plane easy axis for $V_\perp > V_\parallel$. Similar conclusion are drawn as those expressed in §5.2.1 by taking into account the majority band contribution and spin-flip excitations [166]. This model correlates nicely the difference in the bandwidth with the anisotropy of the orbital moment and allows to predict qualitatively, by knowing the bandwidth from calculations, the anisotropy of the orbital moment [169].

5.2 The longitudinal x-ray magnetic circular dichroism

In this section, we will describe the classical longitudinal geometry where the applied magnetic field is along the incident photon direction [50]. There is an other geometry which is the transverse geometry where the applied magnetic field is perpendicular to the incident photons direction [170]. The advantage of the transverse geometry is its ability to determine directly in only one measurement the anisotropy of the orbital magnetic moment and the anisotropy of the dipole magnetic moment. However, the longitudinal one permits to measure a fully angular-dependent orbital and effective spin magnetic moment using the sum rules. In our case, we choose to use the classical longitudinal geometry.

As presented in §1.1.3, the sum rules link the integrals of the x-ray magnetic circular dichroism to the orbital $\vec{m}_L$ and the effective spin magnetic moment $\vec{m}_S^{eff}$ (Eq. 1.17 and 1.18). For the $L_{3,2}$-edges, the sum rules and their ratio are written as:

$$\vec{m}_L \cdot \hat{\vec{P}} = -\frac{4n_h}{3P_C} \cdot \frac{(\Delta A_3 - \Delta A_2)_\theta}{2A^{iso}} \tag{5.13}$$

$$\vec{m}_S^{eff} \cdot \hat{\vec{P}} = \left(\vec{m}_S - 7\vec{m}_T\right) \cdot \hat{\vec{P}} = -\frac{2n_h}{P_C} \cdot \frac{(\Delta A_3 + 2\Delta A_2)_\theta}{2A^{iso}} \tag{5.14}$$

$$\frac{\vec{m}_L \cdot \hat{\vec{P}}}{\vec{m}_S^{eff} \cdot \hat{\vec{P}}} = \frac{2}{3} \cdot \frac{R+1}{R-2} \qquad R = \frac{\Delta A_3}{\Delta A_2} \tag{5.15}$$

where $\hat{\vec{P}}$ is a unit vector along the incident photon direction which is parallel to the applied magnetic field and θ is the angle between the normal of the film and the incident photon directions as depicted in Fig. 5.1.
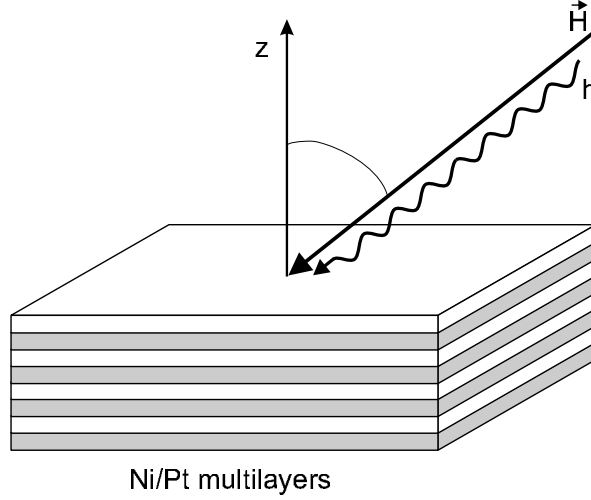
Figure 5.1: Schematic illustration of the incidence angle θ and of the longitudinal geometry

Note that the expectation values of the moments $\overrightarrow{m}$ are vector quantities. The dipole magnetic moment $\overrightarrow{m}_T$ is a product of a second rank tensor, the quadrupole charge moment and the spin moment [36]. So, that we can write it as:

$$\overrightarrow{m_T} = \bar{\bar{Q}} \cdot \hat{\overrightarrow{S}} \tag{5.16}$$

where $\bar{\bar{Q}}$ is a second rank tensor of the quadrupole charge distribution and $\hat{\overrightarrow{S}}$ is a unit vector along the spin magnetic moment.

A similar relation holds for the orbital magnetic moment as illustrated by the Eq. 5.6:

$$\overrightarrow{m_L} = \bar{\bar{R}} \cdot \hat{\overrightarrow{S}} \tag{5.17}$$

where $\bar{\bar{R}}$ is a second rank tensor.

In the case of a uniaxial symmetry and for $3d$ transition metals, the tensor $\bar{\bar{R}}$ (it holds for $\bar{\bar{Q}}$ too) is diagonal and has two independent components R_{zz} and $R_{xx} = R_{yy}$ (z is along the normal of the film plane). In XMCD, we measure the projection of the magnetic moment $\overrightarrow{m_L}$ along the incident photon direction $\hat{\overrightarrow{P}}$. An external magnetic field orients $\hat{\overrightarrow{S}}$ in the $y - z$ plane at an angle γ with respect to the sample normal, and the incident photon has an angle θ. The value observed for the orbital moment is then [171]:

$$\hat{\overrightarrow{P}} \cdot \overrightarrow{m_L} = \hat{\overrightarrow{P}} \cdot \bar{\bar{R}} \cdot \hat{\overrightarrow{S}} \tag{5.18}$$

which can be written as

$$m_L^\theta = R_{xx} sin\gamma sin\theta + R_{zz} cos\gamma cos\theta \tag{5.19}$$

A similar expression is obtained for m_T^θ.

In the case, where the applied field is strong enough to saturate magnetically the sample, the Eq. 5.18 can be written as:

$$m_L^\theta = R_{xx}\,sin^2\theta \,+\, R_{zz}\,cos^2\theta \tag{5.20}$$

Finally, in a longitudinal geometry, for a uniaxial system and for $3d$ transition metals (by assuming that the applied magnetic field saturates magnetically the sample), the anisotropic orbital and effective spin magnetic moments are given:

$$m_L^\theta \;=\; m_L^\parallel\,sin^2\theta \,+\, m_L^\perp\,cos^2\theta \tag{5.21}$$

$$m_S^{eff} \;=\; m_S - 7(m_T^\parallel\,sin^2\theta \,+\, m_T^\perp\,cos^2\theta) \tag{5.22}$$

where the magnetic spin moment is *a priori* isotropic. Since it is impossible to determine the orbital and effective spin magnetic component in the plane of the sample, it is useful to determine their angular dependence and to extrapolate their values for in-plane.

We can see from Eq.s 5.20 and 5.21 that in the case of $3d$ transition metals with uniaxial symmetry the spin magnetic moment obeys a circular angular- dependence by rotating the applied magnetic field from the normal to in-plane direction. Contrary to this, the orbital magnetic moment and the dipole magnetic moment exhibit an ellipsoid angular-dependence. The message is that the orbital and the dipole magnetic moments are only collinear to the spin magnetic moment along a principal crystallographic axis [171].

It is interesting to notice, as presented in §1.1.3 that for $3d$ transition metals and for systems with uniaxial symmetry, the average of the dipole magnetic moment along the x, y and z direction is (with $m_T^x = m_T^y$):

$$m_T^z + 2m_T^x = 0 \tag{5.23}$$

This means that there is an angle where the projection of the dipole magnetic moment is zero. This angle is called the "magic angle", θ^* =arcos(-1/3)/2≃54.7^o from the z axis [36]. This is valid under the assumption that the spin-orbit interaction is much smaller than the exchange interaction and the crystal potential (the crystal field splitting), i.e. when the spin-orbit can be treated by perturbation theory. Measurements done under this angle θ^* give directly the isotropic spin $m_S^{eff,*}$ and orbital m_L^* magnetic moments as:

$$m_S^{eff,*} = m_S \tag{5.24}$$

$$m_L^* = \frac{2m_L^{\parallel} + m_L^{\perp}}{3} \tag{5.25}$$

The anisotropy of the effective spin $m_S^{eff,ani}$ and orbital m_L^{ani} magnetic moment are then given by:

$$m_S^{eff,ani} = -7(m_T^{\parallel} - m_T^{\perp}) = -\frac{21}{2}m_T^{\perp} \tag{5.26}$$

$$m_L^{ani} = m_L^{\perp} - m_L^{\parallel} \tag{5.27}$$

In summary, we show that a longitudinal geometry setup for angular-dependent x-ray magnetic circular dichroic measurements allows us to determine the anisotropic and isotropic part of the orbital and effective spin magnetic moment of $3d$ transition metals with uniaxial symmetry.

5.3   Experimental determination of MAE of Ni in Ni/Pt multilayers

The first experimental support for the simple picture of the microscopic origin of the MAE has been provided by Weller *et al.* for thin Co in Au/Co/Au(111) in 1995 [50]. They have determined separately the macroscopic and microscopic magnetic anisotropy energy (left and right part of the Bruno relation 5.11). Later, Dürr *at al.* have performed similar experiments on Co/Ni ultrathin films, but, unfortunately, they deduce from the measurements unrealistic macroscopic magnetic anisotropy energies (several meV/atom)[172]. In 1999, Anisimov *et al.* using a totally different method (ferromagnetic resonance), checked quantitatively the Bruno relation of anisotropic orbital moments and MAE for Fe in Fe/V superlattices [159]. In continuation of this previous work, we have performed angular-dependent XMCD measurements for Ni in Ni/Pt multilayers. We have determined the anisotropy of the orbital moment of Ni and demonstrated that saturation effects play an important role in the data analysis. They have to be corrected in order to determine the anisotropy of the orbital moment. The saturation effects were previously not always taken into account.

    In the following, we will first describe the sample preparation and characteristion of the Ni/Pt multilayers. Afterwards, we will determine the macroscopic magnetic anisotropy energy (the left part of the Bruno relation 5.11) using a conventional Vibrating Sample Magnetometer. Using high-field and angular-dependent x-ray magnetic circular dichroism at the Ni $L_{3,2}$-edges, the anisotropy of the orbital magnetic moment which is the only

source of anisotropy in the microscopic limit (the right part of the Bruno relation 5.11) will be measured. The prefactor α will then be determined. Few data for the prefactor α are available for Co [50] and Fe [159] layers only. No data are available for Ni up to now.

5.3.1 Sample preparation and characterisation

The Ni/Pt multilayers were prepared and characterised in the Department of Physics, Aristotle University of Thessaloniki (Greece) by M. Angelakeris and P. Poulopoulos from the group of Prof. N.K. Flevaris. The Ni_n/Pt_m multilayers were grown by e-beam evaporation under ultra-high vacuum conditions (base pressure of the chamber $\sim 5 \times 10^{-9}$ mbar). The deposition rates used were 3-18 nm/min. The indices n and m denote numbers of atomic planes of the corresponding constituent in each multilayer period; they were varied between 1 and 13. The individual Pt and Ni thicknesses were determined by using pre-calibrated quartz crystals and x-ray diffraction (XRD) with a precision of about 5% and then were approximated to the closest integer or half-integer number of atomic planes (monolayers). The samples were grown on polyimide (Kapton) substrate. For a better rigidity, a Cu backing foil was used. An other advantage of this, is a better thermal contact with the cold sample holder. The total film thickness was generally between 100-150nm. All the multilayers were deposited on a Pt buffer layer of 150-200ML for better texturing. For the buffer, 1ML corresponds to 2.26Å. The samples were capped with a thin Pt layer ($\sim$10ML thick) for chemical protection (for an example, see Fig. 5.2). We will present here briefly the main structural characteristics of the Ni/Pt multilayers.
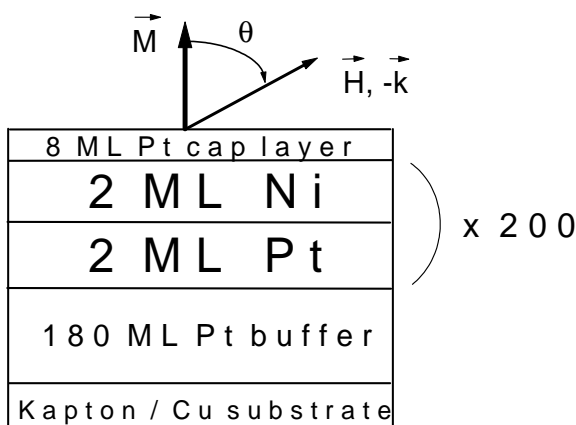

Figure 5.2: Typical representation of the stacking in the Ni_n/Pt_m multilayers. The indices correspond to the number of atomic planes. In this case, $n = 2$ML and $m = 2$ML.

More details concerning sample preparation and structural studies can be found in Ref.
[150, 173]. X-ray diffraction experiments and simulations revealed that all the samples
have polycrystalline fcc (111) structure. Transmission electron microscopy shows that the
samples have a columnar morphology with grains of several tens of nm large (30-250nm
typically). This columnar growth begins just above the Pt buffer layer. Inside the grains,
the interfaces are fairly flat and roughness could be of maximum about 1-2ML. The in-
terfaces between Ni and Pt in evaporated Ni/Pt multilayers are sharp in the monolayer
limit even for extremely thin n and m layers. In Fig. 5.3, the XRD patterns at small
and high angle for a Ni_2/Pt_2 are shown. They demonstrates clearly that a superlattice
structure is present. For such thin layers of both constituents superlattice reflections are
rarely published. Thus, this is the most indicative and direct way to show the sharpness
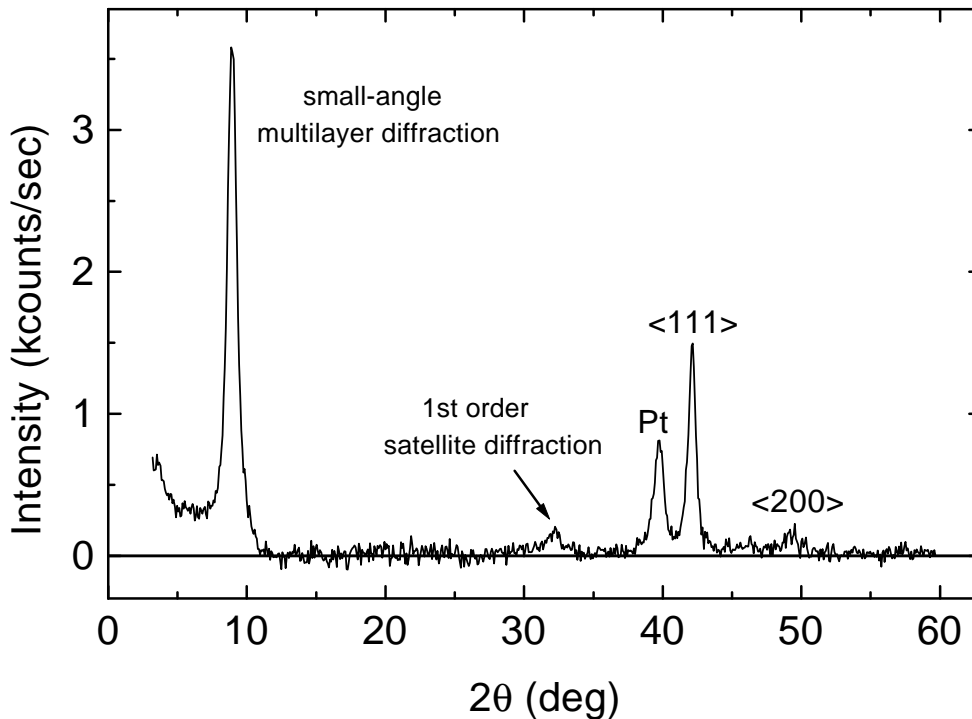of the interfaces of these multilayers. This shows that, if any, interdiffusion is strictly

Figure 5.3: θ-2θ XRD spectrum for a Ni_2/Pt_2 multilayer. Despite the very thin Ni and Pt layers
a small-angle-multilayer- and a high-angle first-order-satellite- diffraction are shown indicative
of sharp interfaces. One may also observe the Pt-buffer-layer diffraction and the solid solution
diffractions (which are the average-interplanar-spacing-multilayer diffractions) from <111> and
<200>. For a detailed analysis of XRD spectra from multilayers see, e.g. [174].
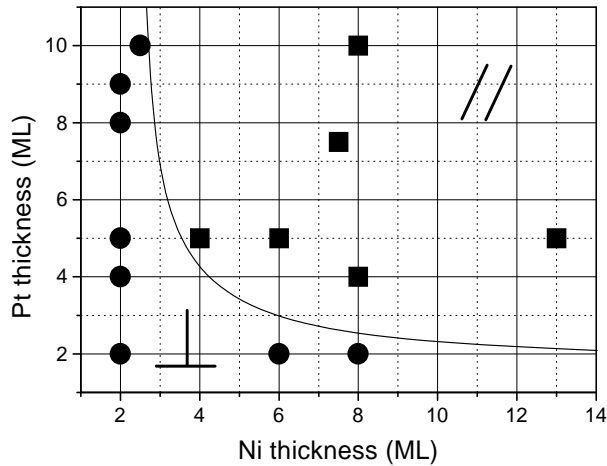
Figure 5.4: Phase diagram showing the easy magnetization direction as a function of the Ni thickness and Pt thickness (in ML). The square (circle) corresponds to an in-plane (out-of-plane) easy magnetization direction. The line showing the boarder between the two phases is a guide to the eyes.

limited at the interfaces.

Independently, the sharpness of the Ni/Pt interfaces have been observed from a detailed structure analysis on similarly prepared samples [175]. The lattice parameter of fcc Pt is 3.96Å and for fcc Ni it is 3.52Å. This makes a lattice misfit of about 10-11%. Since this is fairly large, Ni and Pt develop a structure with considerable strain relief to minimize their elastic energy. Thus, only thin Pt layers are expected to grow coherently on Ni layers. For thicker Pt layers, dislocations will then occur to reduce the elastic energy. For layers thinner than ∼8ML for Pt or Ni, the residual strain should be of about only 0-2% [175]. Similarly, in Pd/Co or Au/Co where the misfit is larger (10-15%), the residual strain was found to be only of about 1.5-2% for individual layers thinner than 10ML in the period [176]. These informations are important to construct a magnetic profile which we will present in the next chapter and to understand the appearance of a perpendicular magnetic anisotropy.

5.3.2 Macroscopic magnetic properties

As it was emphasized in the beginning, a perpendicular anisotropy appears in Ni/Pt multilayers with decreasing the Ni thickness for constant Pt thickness. This behaviour is mostly observed for a lot of multilayer systems, e.g. Co/Pt. Unexpectedly, this behaviour is also observed for thicker Ni layers (8ML) when the Pt layers became considerably thin (2ML)(see Fig. 5.4) [150, 173]. This behaviour could be related to strain relaxation phenomena with increasing the Pt thickness as it is described by Angelakeris *et al.* [150]. As discussed before, very thin Pt layers grow coherently on Ni layers. By increasing the Pt thickness, dislocations will be formed due to lattice misfit. The uniaxial anisotropy is

due to the elastic stress which favours a perpendicular anisotropy. Like for Ni/Cu(001), the negative sign of the magnetostriction favours a perpendicular anisotropy. However, the dislocation formation will reduce the uniaxial anisotropy and favour again an in-plane easy axis. In the case of Ni/Cu(001), the dislocations appear above 20ML and turn back the easy magnetization on the film plane [96].

Most commonly, the magnetic anisotropy is determined from the information provided by field-dependent measurements along two orthogonal directions of the magnetic field relative to the sample plane. Earlier magneto-optic studies performed on Ni/Pt multilayers revealed that the Ni_2/Pt_2 possesses the highest magnetic anisotropy [150, 173]. To determine the macroscopic MAE, we have performed magnetization hysteresis-loops using a Vibrating Sample Magnetometer (VSM). The measurements have been realised by P. Poulopoulos and W. Wisny. All the measurements have been performed parallel and perpendicular to the sample and at the lowest temperature 10K. The values of the MAE can be determined from the area enclosed between the parallel and the perpendicular loops.

The angle-dependent part of the energy E of the magnetization of the thin film can be written as:

$$E = (-K_2 + 2\pi M_s^2)cos^2\theta - 2\pi M_s H cos(\phi - \theta) \qquad (5.28)$$

where θ and ϕ denote the angles between the magnetization or the field, respectively, and the film normal. The coefficient K_2 contains all the second order anisotropies. The area between the perpendicular and parallel curves gives the effective anisotropy, $K_2^{eff} = K_2 - 2\pi M_s^2$. The macroscopic MAE is determined after subtracting the shape anisotropy[4].

As expected, the Ni_2/Pt_2 is the only Ni-based perpendicularly magnetized multilayers with relatively large values of MAE. Fig. 5.5 shows the magnetization hysteresis loops of the Ni_2/Pt_2 recorded by VSM at T=10K with an external field applied in-plane and normal to the sample. The easy-magnetization axis is the film normal. The remanent magnetization is almost equal to the saturation magnetization. The in-plane saturation magnetization is achieved progressively under a field of 25kG. It is very important to reach the saturation field for the determination of the MAE. An underestimation of the saturation field could have dramatic consequences as we will see in the next section for the determination of the anisotropy of the orbital moment. The shape of the hard-axis loop reveals that higher order anisotropies are not negligible. In the absence of higher order anisotropies, the hysteresis-loops with increasing and decreasing the applied field are similar. However, in a first approximation, we stay in a uniaxial approach. The magnetization

---

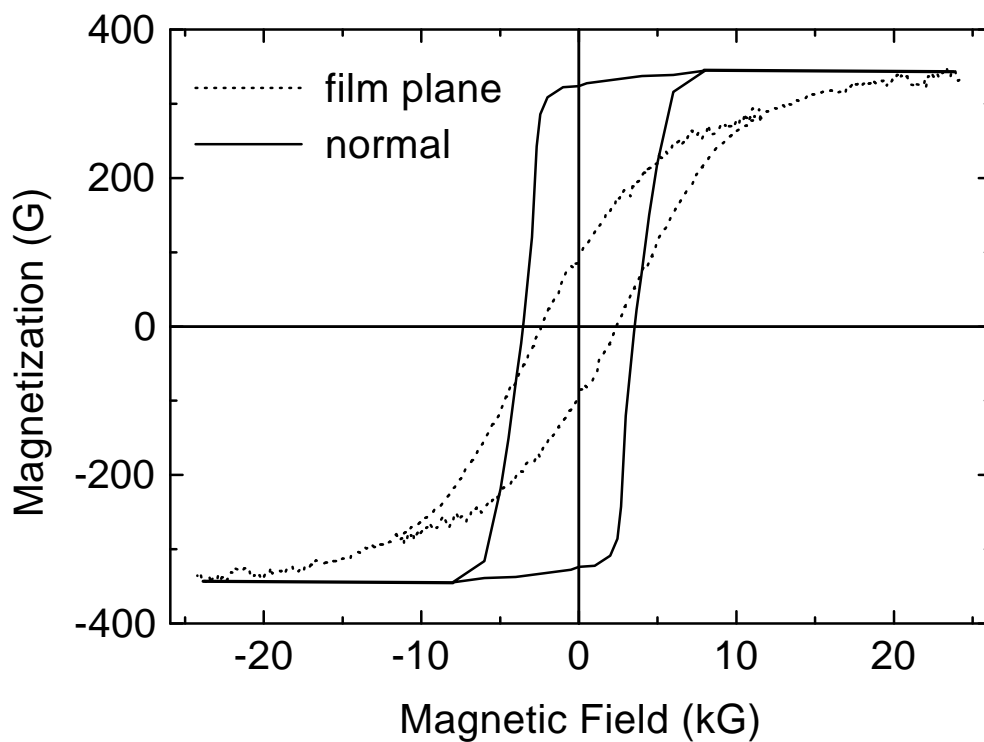[4]A high precision is required to determine the saturation magnetization.

Figure 5.5: VSM-hysteresis loops along the easy-(solid) and hard-(doted-line) magnetization axis for a Ni_2/Pt_2 recorded by VSM at T=10K. The magnetization values have been normalized to Ni using experimental input from XMCD measurements.

axis was originally determined in emu. With the help of the sum rules, the total magnetic moment of Ni was determined by XMCD (see §5.3.4) and scaled in Gauss. The element-specificty of XMCD allows us to determine separately the magnetic contribution coming from Ni and Pt, which is impossible to be done only from the VSM data. The saturation magnetization is found to be $M_s = 345 \pm 10$G. After subtraction of the shape anisotropy, we have estimated MAE$\simeq -20\mu$eV/atom[5]. This slightly smaller than the largest reported values -27μeV/atom for perpendicularly magnetized ultrathin Ni/Cu(001) films [96]. For comparison, for Au/Co(4ML)/Au(111), the magnetic anisotropy energy was estimated $\simeq -160\mu$eV/atom which is higher than for Ni based samples [50].

In summary, we have determined via VSM measurements at 10K the macroscopic magnetic anisotropy energy for Ni_2/Pt_2. It is estimated to be $\simeq -20\mu$eV pro atom. We have then determined the left part of the Bruno relation (5.11).

---

[5]In our convention, a positive value of K means or a negative value of MAE means that the easy magnetization axis is normal to the film plane.

5.3.3 Microscopic magnetic properties

The high-field and angular-dependent XMCD measurements presented in this chapter have been performed at the European synchrotron radiation facility (ESRF) in Grenoble (France) on the ID12B soft x-rays beamline[76] at the Ni $L_{3,2}$-edges using the total electron yield (TEY) detection mode. The degree of polarisation of the circular light was 85%. Large magnetic fields up to 50kG (5 Tesla) were applied for complete magnetic saturation of the samples. The applied magnetic field is always along the incident photon direction in order to obtain the full XMCD signal. As described before, this is the longitudinal setup. All the measurements have been performed at T=10K. The spectra were recorded both by inverting the helicity of the light and reversing the direction of the applied magnetic
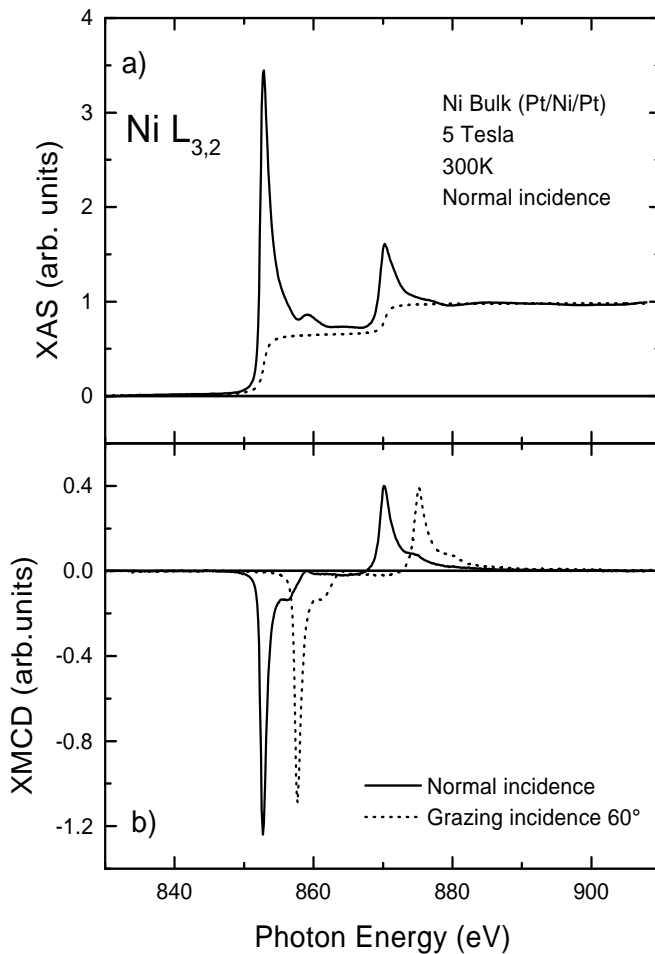

Figure 5.6: a) Isotropic absorption spectra (solid line) for bulk fcc Ni measured at 300K and at normal incidence under an applied magnetic field of 5T. The bulk Ni film is 20nm thick. The film was grown on a Pt buffer and capped with Pt. The continuum has been fitted by a double step function with a ratio 2:1. b) The corresponding x-ray magnetic circular dichroism spectra taken at normal incidence (solid) and at grazing incidence (60° from the normal) (dotted, the spectra was artificially shifted by 5eV for a better view). The applied field was 5T. The saturation effects can be clearly observed.

field. This is a great advantage because it allows us to check the reproduction of the measurements since we are looking for small effects. The orbital moment in bulk fcc Ni is $0.06\mu_B$/atom which is small compared to bulk bcc Fe ($0.086\mu_B$/atom) or bulk hcp Co ($0.153\mu_B$/atom) experimental values [41]. So, high photon intensity and resolution are required to carry out such experiments. In combination we had the possibility to have a superconducting magnet which allows to produce fields up to 7T in order to saturate magnetically the samples in all directions.

Influence of saturation effects

In Fig. 5.6, we show the average of the absorption spectra measured for right and left circularly polarized light[6] and the corresponding XMCD spectra (solid line) measured at the $L_{3,2}$-edges in normal incidence for a bulk fcc Ni. The XAS spectra were normalized in a way that the Ni edge jump above the L_2-edge is equal to 1. This sample is taken as a reference sample for all our measurements. This sample is 20nm thick and has been grown on a Pt buffer on Kapton and capped with 10ML Pt as protective layers. First, we may notice that the white line is much higher compared to the one of the 15ML Ni/Cu(001) measured in Bessy I (synchrotron of second generation). We see that in comparison the full width half maximum (FWHM) is, in contrast, much smaller. This occurs because the resolution is increased. The higher resolution allows us to resolve much better the satellite and the continuum features in the XMCD spectra compared to the XMCD spectra recorded for the 15ML Ni/Cu(001)(see §3.2.). Also, it is shown the XMCD spectra taken at grazing incidence (60° from the normal, dotted line). First, the two XMCD spectra taken at normal and grazing incidence have the same shape. However, we can notice that the maximum of the L_3-edge and in a minor way the L_2-edge of the XMCD spectra taken at grazing incidence are reduced compared to the XMCD spectra taken at normal incidence. The same observation can be done for the XAS spectra but the difference is less obvious. These are clearly the saturation effects, as expected for such film thickness. Application of the sum rules may directly determine the ratio of the orbital to the effective spin magnetic moment $m_L^{\theta}/m_S^{eff,\theta}$ with $m_S^{eff,\theta} = m_S - 7m_T^{\theta}$, m_T^{θ} is the magnetic dipole contribution. According the sum rules, this ratio depends exclusively on the ratio of the integrated XMCD signal ΔA_3 and ΔA_2 at the L_3 and L_2 edges (Eq. 5.15). This ratio does not dependent on the number of $3d$ holes n_h, the polarisation degree P_c and normalisation factor A^{iso}. The ratio m_L^0/m_S^0 and $m_L^{65^o}/m_S^{eff,65^o}$ are respectively 0.105 ± 0.005 and 0.854 ± 0.005. For a spin magnetic moment of $0.6\mu_B$/atom, we would deduce the existence of an anisotropy of the orbital moment of

---

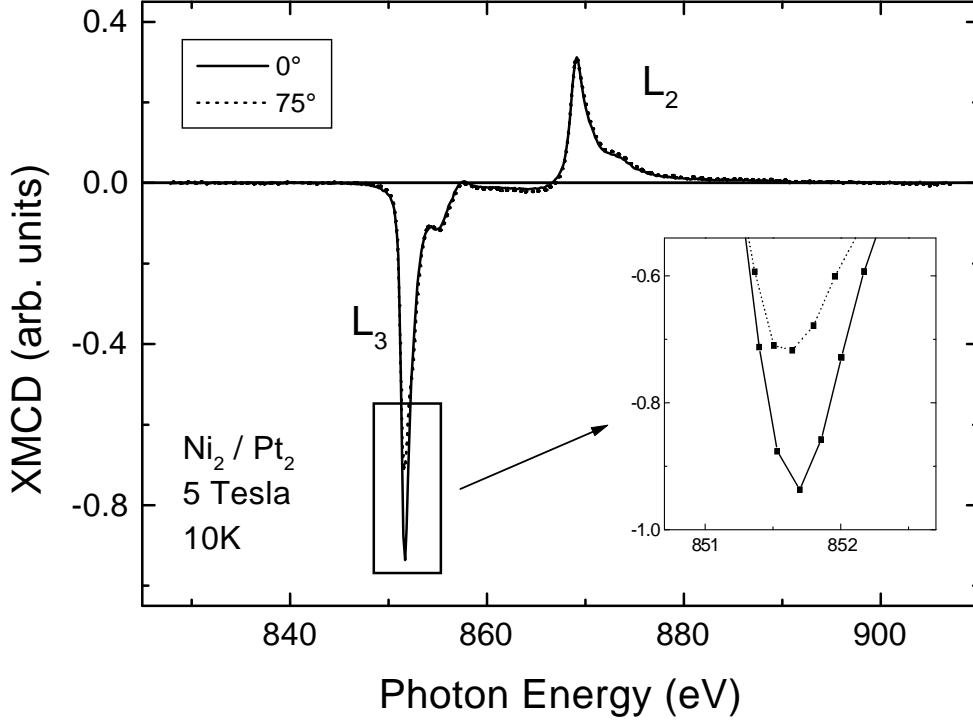[6]This corresponds in a first approximation to the isotropic absorption spectra.

Figure 5.7: XMCD spectra at the Ni $L_{3,2}$-edges of the Ni_2/Pt_2 multilayer measured at two different angles of incidence. The inset shows an enlargement of the L_3-edges maximum where the main differences of the two spectra are located.

about $\Delta m_L = m_L^\perp - m_L^\parallel \approx 0.012 \mu_B/$atom. This is unrealistic since the anisotropy of the orbital magnetic moment is of about $10^{-4} \mu_B/$atom (see table 5.1). We see here a nice example to demonstrate the necessity to correct for the saturation effects.

Figure 5.7 shows the XMCD spectra at the $L_{3,2}$-edges of Ni for the Ni_2/Pt_2 multilayer recorded at $\theta = 0^o$ and 75° with respect to the film normal. From the spectra, we see clearly again that the main difference between the two measurements is located at the L_3-edge maximum. Again, one may conclude that $m_L^\theta/m_S^{eff,\theta}$ changes from $\theta = 0^o$ to 75°. However, as shown, the saturation correction has to be taken into account in the analysis of the angular-dependent XMCD measurements. As illustrated in the chapter §2.2, the orbital magnetic moment is more affected from the saturation effects than the spin magnetic moment.

In Fig. 5.8, the integrated XMCD spectra for different angles θ with respect to the film normal are shown. We observe a strong dependence of the integrated XMCD signal as a function of the angle θ. The orbital magnetic moment seems to decrease strongly
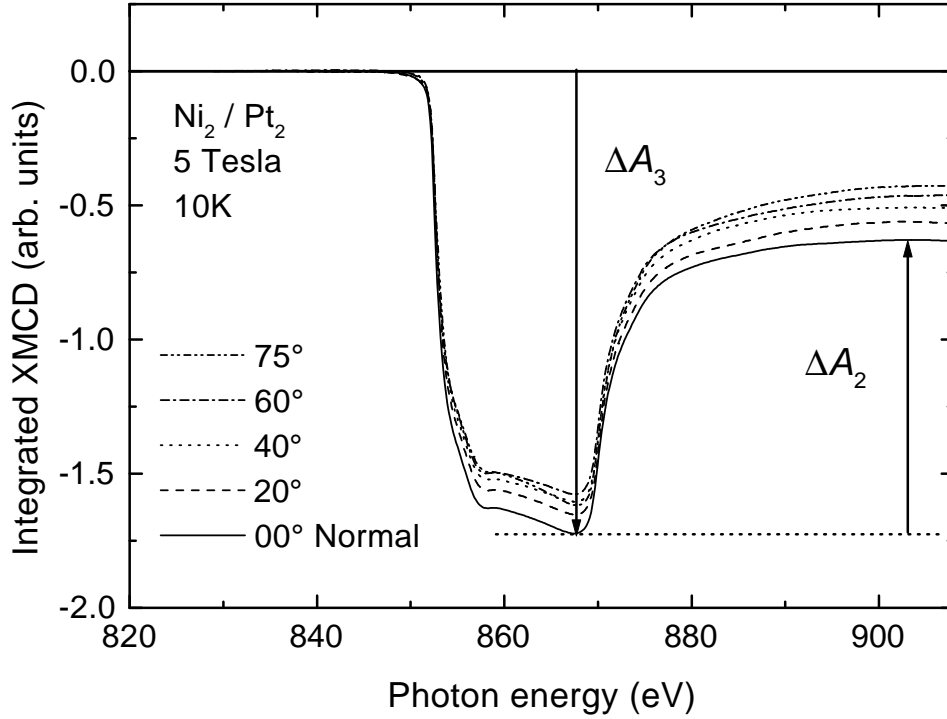
Figure 5.8: Integrated XMCD signal measured at the Ni $L_{3,2}$-edges for the Ni_2/Pt_2 multilayer (with H=5T and T=10K). The angle θ with respect to the film normal is given by the photon incident direction and the applied magnetic field. The measurements have been done at 5 different angles as indicated. The integrated XMCD spectra have not been corrected for saturation effects. The integrals ΔA_3 and ΔA_2 are the integrals which appear in the sum rules (5.13 and 5.14). With increasing angle, we see clearly that the orbital magnetic moment ($\sim \Delta A_3 + \Delta A_2$) decreases. This shows a possible anisotropy of the orbital magnetic moment.

with increasing the angle θ. However, before drawing any conclusion, the spectra have to be corrected for saturation effects.

In Fig. 5.9 is shown the angular dependence of the ratio m_L/m_S^{eff} before applying the saturation effect corrections to our experimental spectra using the model described in §2.3 for three different samples: the Ni_2/Pt_2 multilayer (open circles), Ni_6/Pt_5 multilayer (open squares) and the thick Ni film (open triangles) which is used as a reference for bulk Ni. At first glance, all samples show an angular dependent m_L/m_S^{eff} ratio. After correction for the saturation effects (solid symbol), only the Ni_2/Pt_2 multilayer shows an angular dependent m_L/m_S^{eff} ratio. For the correction of saturation effects, we have used for the escape electron depth 25Å for Ni in the range 800-900eV and the exact construction
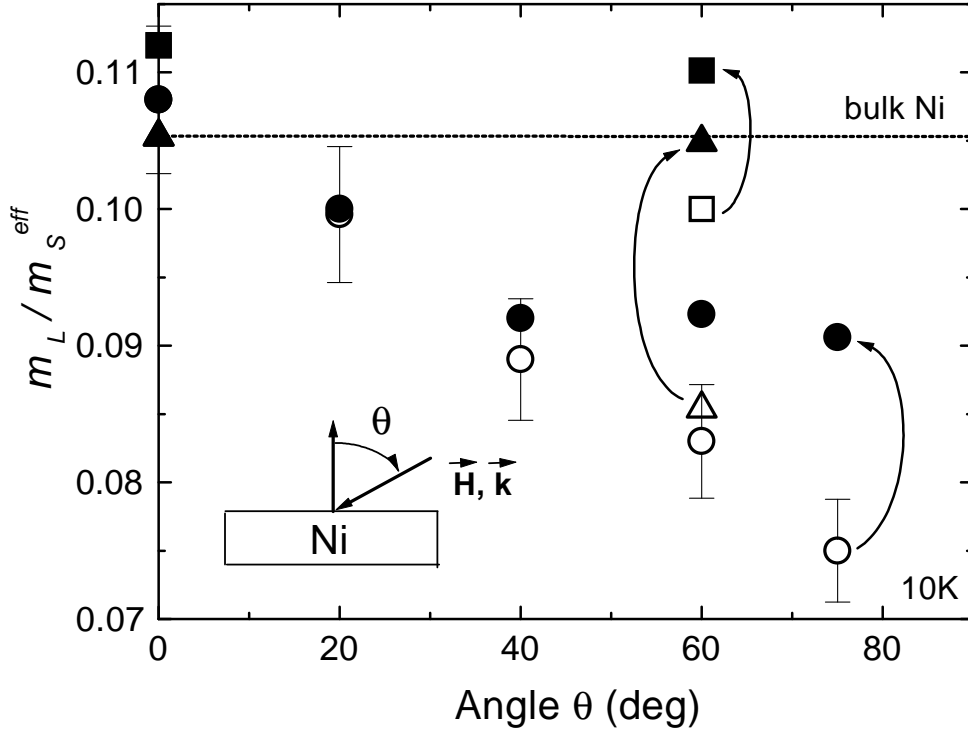
Figure 5.9: The ratio m_L/m_S^{eff} determined from the XMCD spectra as a function of the incident angle (depicted in the sketch) before (open) and after (solid) the correction for saturation effects for Ni_2/Pt_2 (circles), Ni_6/Pt_5 (squares) and the 20nm thick bulk Ni film (triangles). After the correction for saturation effects, only the Ni_2/Pt_2 multilayer shows a true angular dependence of the ratio m_L/m_S^{eff}. The measurements have been performed at 10K. The curved arrows are guides to the eyes.

of the multilayer (n, m, the number of multilayer periods, and the Pt capping and buffer layer thickness). As expected, we see clearly that the saturation effects increase from the normal to grazing incidence (see the angular dependence of the Ni_2/Pt_2 multilayer). This increase is not linear but in a first approximation exponential-like. For the same angle (60°), the saturation effects are stronger for the Ni bulk than for the multilayers. Indeed, the saturation effects are thickness-dependent. For an angle of 60°, the saturation effect corrections for the ratio m_L/m_S^{eff} are for the three samples 10% (Ni_2/Pt_2, 200 repetitions), 9.6% (Ni_6/Pt_5, 63 repetitions) and 18.6% (Ni bulk) with respect to the corrected values. We call that the thickness calibration was about 5%. If now, we assume a variation of 16% for n in the case of a Ni_6/Pt_5 multilayer ($\pm 1ML$), the influences of the saturation effects correction were only less than 1% with respect to the corrected values. In a first

approximation, for thick multilayers, the saturation effect correction at a constant angle seems to be proportional to the ratio $n/(n+m)$. We see in Fig. 5.9, that after saturation effect corrections, the bulk Ni and the Ni_6/Pt_5 which have the easy magnetization axis in the film plane do not show any angular dependence of the ratio m_L/m_S^{eff}. Only the Ni_2/Pt_2 multilayer shows a true angular dependence of the ratio m_L/m_S^{eff} after correction for the saturation effects. The true ratio m_L/m_S^{eff} varies smoothly from 0.108 to 0.0906 by rotating the spin magnetic moment direction (the applied magnetic field which saturates magnetically the sample) from the normal (0°) to 75°.

The anisotropy of the orbital magnetic moment

Figure 5.10 shows the orbital moment m_L of Ni in the Ni_2/Pt_2 multilayer as a function of the angle θ. As discussed before, it is impossible to determine the orbital magnetic moment in the plane of the sample. However, in $3d$ transition metals with uniaxial symmetry, the orbital magnetic moment varies as (see Eq. 5.21):

$$m_L^\theta = m_L^\perp + (m_L^\| - m_L^\perp) \, sin^2\theta \qquad (5.29)$$

where $m_L^\perp$ and $m_L^\|$ denote, respectively, the orbital magnetic moment measured perpendicular and along the film plane. The easy axis of magnetization is perpendicular to the film plane as it was determined using VSM measurements. To determine to orbital magnetic moment, we have used the Ni bulk sample as a reference with the number of $3d$ holes n_h =1.43 [78]. By using the sum rules and the fit of our experimental data according to the theoretical prediction (Eq. 5.29), we found that the orbital magnetic moment along the easy magnetization axis (which is perpendicular to the film plane) is $m_L^\perp = 0.037 \pm 0.002 \mu_B$/atom. We find that the anisotropy of the orbital magnetic moment is $\Delta m_L = m_L^\perp - m_L^\| = 0.008 \pm 0.004 \mu_B$/atom. The orbital moment is smaller compared to the $0.06 \mu_B$/atom of bulk like Ni. As we will see in the next chapter §6, this is due to the hybridization between the 2ML Ni and 2ML Pt. The absolute value of the anisotropy of the orbital magnetic moment is small, however it is out of the errors bars. It represents a significant amount $\approx 22\%$ of $m_L^\perp$. The isotropic orbital magnetic moment deduced from Eq. 5.25 gives $m_L^* = 0.032 \pm 0.002 \mu_B$/atom. The Δm_L found in our multilayer film is comparable to the one determined by Transverse-XMCD for a Cu/33ML Ni/Cu/Si(100) film which is about $\Delta m_L = 0.014 \mu_B$/atom [172]. Interestingly, concerning the last case, no saturation effect corrections were taken into account.
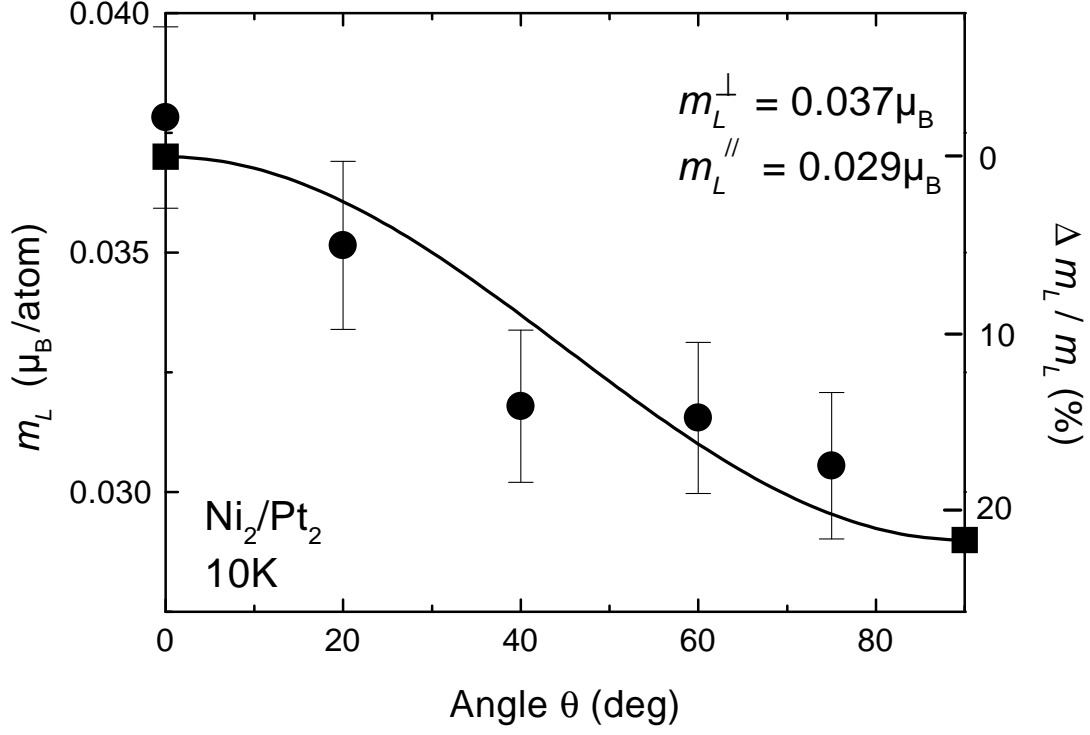
Figure 5.10: Orbital moment of Ni measured in Ni_2/Pt_2 multilayer (circles) as a function of the angle θ between the applied magnetic field and the normal to the surface (which is the easy magnetization axis). The solid line is the yield of the fit according to Eq. 5.29. From this, we determine the orbital magnetic moment along the easy and hard magnetization axis (squares).

The anisotropy of the dipole magnetic moment

By using the sum rules, we can determine the effective spin magnetic moment. For $3d$ transition metals with uniaxial symmetry, it is possible to determine separately the spin magnetic moment which is *a priori* isotropic from the dipole magnetic moment which is angular dependent. The effective spin magnetic moment as a function of the angle θ is written (Eq. 5.22):

$$m_S^{eff,\theta} = (m_S - 7m_T^\perp) + \frac{21}{2}m_T^\perp \sin^2\theta \qquad (5.30)$$

Figure 5.11 shows the effective spin magnetic moment m_S^{eff} of Ni in the Ni_2/Pt_2 multilayer. A fit of our experimental data according the Eq. 5.30 is shown with the solid line. From this analysis, we find that the isotropic spin magnetic moment is equal to $m_S^* = 0.34 \pm 0.01\mu_B$/atom. The dipole magnetic moment which is angular dependent is found

to be $m_T^\perp = -0.001 \pm 0.001 \mu_B$/atom for the perpendicular contribution and $m_T^\parallel = m_T^\perp/2$ for the in-plane contribution. As expected, the dipole magnetic contribution is very small and negligible compared to the spin magnetic moment m_S^* [32]. We see here that the spin moment is reduced by a factor of $\approx$ 1.7 compared to the bulk Ni moment ($m_S = 0.60 \mu_B$/atom). This reduction will be the subject of the next chapter. The anisotropy of the dipole magnetic moment which represents the spin-flip anisotropy energy (Eq. 5.10) is about $m_T^\perp - m_T^\parallel \simeq -0.001 \mu_B$/atom. As for the orbital magnetic moment, the effective spin moment is larger along the easy magnetization axis (perpendicular to the sample). The same tendency was found in ultrathin Co films in Au/Co/Au(111) [50] and (111) CoPt$_3$ thin films [51].
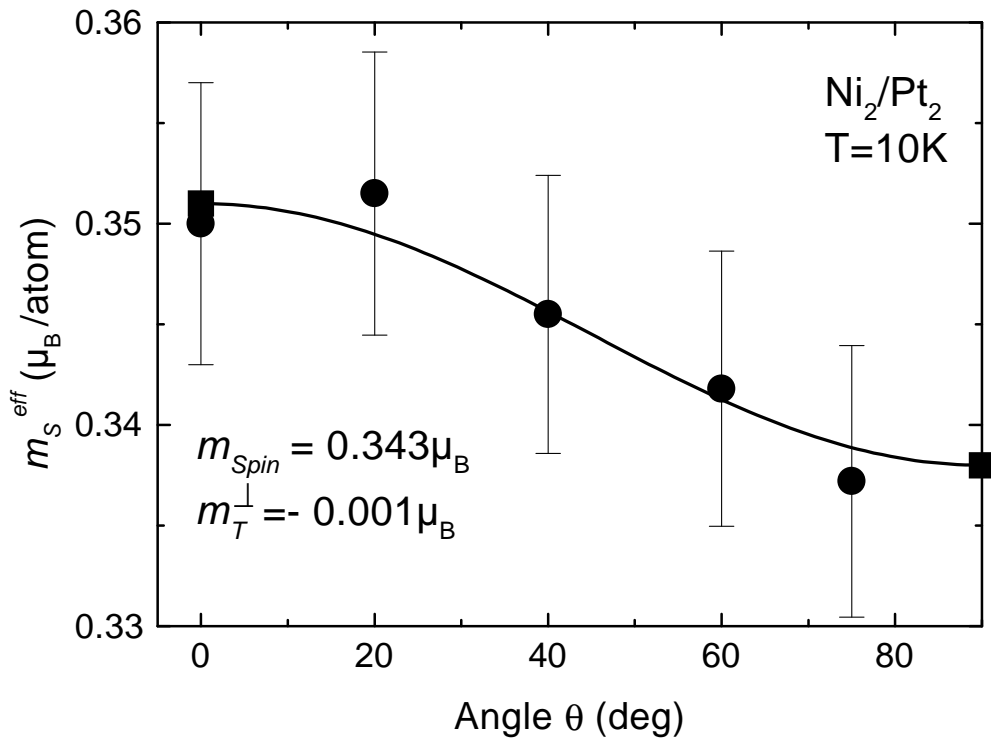

Figure 5.11: Effective spin magnetic moment of Ni measured in Ni$_2$/Pt$_2$ multilayer (circles) as a function of the angle θ between the applied magnetic field and the normal to the surface (which is the easy magnetization axis). The solid line is the yield of the fit according to Eq. 5.30. From this, we determine the dipole magnetic moment along the easy and hard magnetization axis (squares).

5.3.4   Discussion

As discussed in section § 5.1.2, there is *a priori* no simple relation between the magnetic anisotropy and the anisotropy of the orbital moment. However, in the case of Ni, where the spin majority band is totally filled, in a first approximation MAE is proportional to Δm_L. Now, we have determined the right and the left part of the Bruno relation (Eq. 5.11), so we may evaluate the prefactor α. The anisotropy of the orbital magnetic moment $\Delta m_L = 0.008 \pm 0.004 \mu_B$/atom was determined with angular-dependent XMCD measurements and the macroscopic magnetic anisotropy $MAE \simeq -20 \mu eV$/atom via VSM measurements. Using the spin-orbit coupling parameter from Ni bulk, $\xi = 0.105$meV, we find a parameter $\alpha \simeq 0.1$ for Ni. In comparison, from Weller *et al.*, we can evaluate for 4ML Co in Au/Co/Au(111) a prefactor $\alpha \approx 0.1$ [50]. Recently, on the same system but for 3ML Co, Stöhr has found a prefactor $\alpha \approx 0.05$ [166] which is similar to that obtain for Co in Co/Pd multilayers from Dürr *et al.* [177]. Recently, Anisimov *et al.* have determined a prefactor $\alpha \approx 0.05$ for bct Fe in a $Fe_2/V_5(001)$ superlattice [159]. The actual value of the prefactor α for all the $3d$ ferromagnetic elements Fe, Co and Ni are tabulated in table 5.2.

The microscopic origin of the magnetic anisotropy energy is clearly the anisotropy of the orbital moment. The origin of the perpendicular magnetic anisotropy is the distortion of the cubic symmetry due to strain as for ultrathin Ni/Cu(001) films [96]. As we have discussed in §5.3.1, a residual strain of about only (0-2)% exists for thin Pt or Ni layers. For a Ni_2/Pt_2, the strain should be maximum (2%) and it responsible for an magnetization axis normal to the film plane.

Using first principles calculation, Hjortstam *et al.* have shown that the orbital magnetic moment for Ni crystal varies as a function of the ratio c/a (Fig. 5.12). For an fcc structure, the orbital magnetic moment along the [001]-axis and [110]-axis are practically equivalent. For distorted fct structure ($c/a <$1), the orbital magnetic moment is found to

	MAE(μeV/atom)	$\Delta m_L (\mu_B)$	α	Method
Fe in $Fe_2/V_5(001)$	-2	0.003	0.05	FMR
Co in Au/Co/Au(111)	-160,-180	0.12, 0.22	0.10*, 0.05	XMCD
Ni in $Ni_2/Pt_2(111)$	-20	0.008	0.10	XMCD

Table 5.2: Experimental results for the MAE, Δm_L and α for $3d$ ferromagnetic elements Fe (Ref. [159]), Co (Ref. [50], [166]) and Ni (this work). α for Ni and Fe were determined for T close to 0K, whereas for Co it was determined at room temperature. The value denoted (*) can be estimated by using MAE and Δm_L from Ref. [50].

be larger along the [001]-axis than the [110]-axis. For Ni_2/Pt_2, due to the residual strain, we found indeed that the orbital magnetic moment is larger out-of-plane than in-plane [101]. Also they show that for tetragonally distorted Ni on Cu(001), the prefactor α, which is the slope plotted in Fig. 5.13, varies from 0.05 to 1 as a function of the anisotropy of the orbital magnetic moment. The magnetic anisotropy energy of $-20\mu eV/atom$ for a ratio $c/a = 0.79$ corresponds to a prefactor $\alpha =0.38$ and to an anisotropy of the orbital magnetic moment $\Delta m_L = 0.0025\mu_B/atom$. This obtained value of the anisotropy of the orbital moment is 3 times lower than the experimentally determined one. However, these values were determined for tetragonal (001) system. For trigonal distortion (i. e. a length change in the [111] direction), no calculation is available for Ni(111). If we assume that α depends more on the element than the crystallographic direction, the experimental value is in agreement with the theoretical predicted one. The discrepancy could come from neglecting the anisotropy of the magnetic dipole contribution (second term in Eq. 5.10). Using for Ni bulk the spin-orbit coupling parameter $\xi = 0.105meV/atom$ and the exchange splitting $\Delta_{ex} = 1eV$, the energy coming from the anisotropy of the dipole magnetic moment is about $\simeq 1 \times 10^{-4}eV/atom$. This is two times smaller and positive compared to the magnetic energy coming from the anisotropy of the orbital magnetic
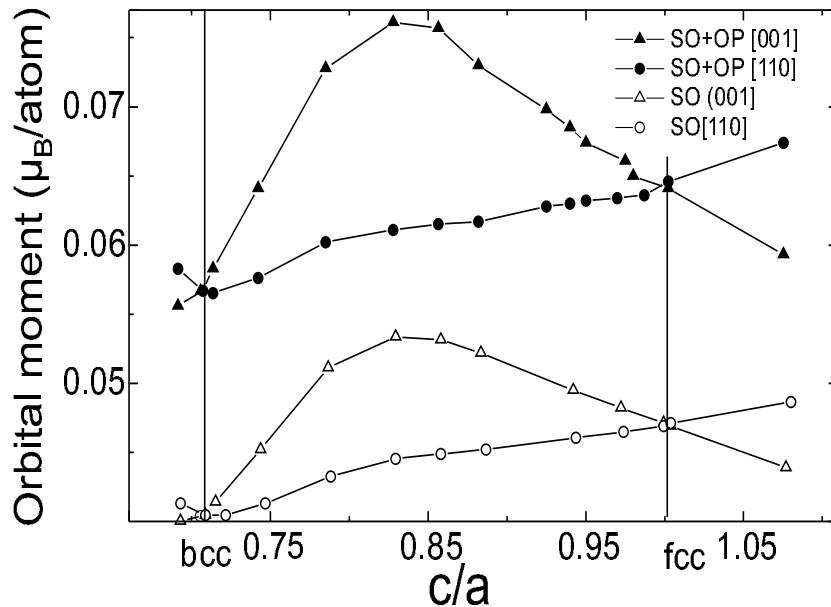

Figure 5.12: Calculated orbital moments for Ni crystal versus the ratio c/a for the magnetization direction [001] and [110] (c is the out-of plane lattice constant and a the in-plane lattice constant). The volume is conserved during the variation of c/a. Results are presented for spin-orbit only (circles) and spin-orbit in combination with orbital polarisation (triangles) [101].
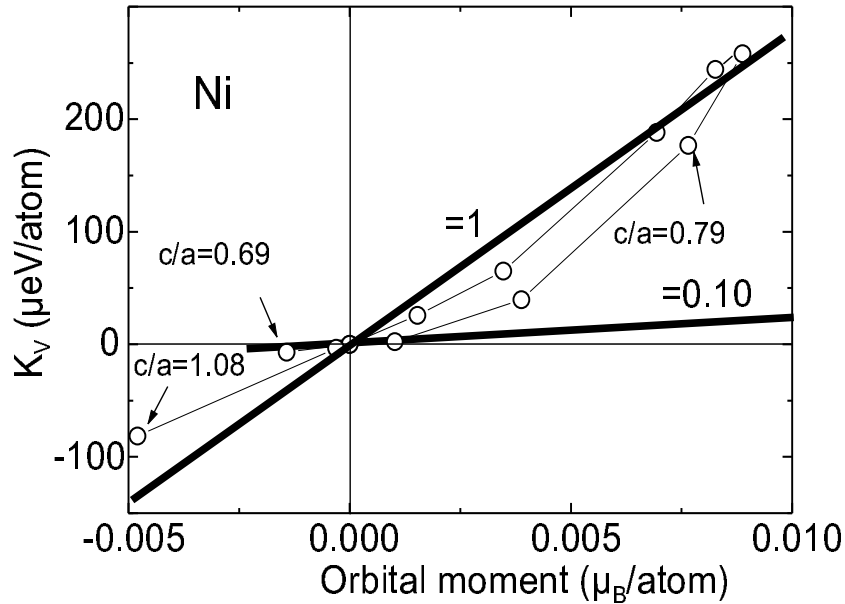
Figure 5.13: Calculated volume anisotropy K^v for Ni crystal, using only spin-orbit, as a function of the anisotropy of the orbital magnetic moment. The solid line connects the volume anisotropy for different c/a ratios. The lines corresponds to the values obtained for prefactors $\alpha = 0$, 0.10 [101].

moment which was $\simeq -2.1 \times 10^{-4}$ev/atom.

It comes out, by taking into account the anisotropy of the orbital and dipole magnetic moment using Eq. 5.10, that the prefactor $\alpha \simeq 0.2$. This is in better agreement to the theoretical predicted one. An other source of small discrepancies could come from the fact that the macroscopic magnetic anisotropy measured via VSM contains the contributions from the magnetically polarized Pt atoms at the interface. Indeed, XMCD measurements done on $CoPt_3$ thin film at the Pt $L_{3,2}$-edges revealed in parallel to Co an anisotropy of the orbital magnetic moment carried by Pt [51]. This anisotropy is much smaller but due to the stronger spin-orbit coupling parameter ($\sim$500meV), the anisotropy of the orbital magnetic moment of Pt could be contributed to the magnetic anisotropy energy. However, in this case, the Bruno relation (Eq. 5.11) does not hold since the spin-orbit coupling parameter is comparable to the exchange splitting.

In summary, we showed first that the saturation effect corrections play an important role in the determination of the anisotropy of the orbital moment from the XMCD spectra and they must be taken into account in the data analysis. We show that the magnetic anisotropy is directly correlated to the anisotropy of the orbital moment and to a smaller degree to the anisotropy of the dipole magnetic moment. We have probed a small abso-

lute value ($0.008\mu_B$ pro atom) although large in a relative scale (22%) anisotropy of the orbital moment of Ni in Ni_2/Pt_2 with considerable MAE ($\simeq -20\mu_B$/atom). The magnetic anisotropy energy was scaled to the anisotropy of the orbital magnetic moment with a prefactor $\alpha \approx 0.1$. The orbital moment perpendicular to the film plane is larger than the one in-plane which is consistent with the sign and magnitude of the intrinsic MAE at T=0K.

Chapter 6

Induced magnetism in $3d/5d$ multilayer systems

It is well known that atoms which are nonmagnetic acquire an induced magnetic moment when they are brought in a ferromagnetic environment. This induced moment may couple ferromagnetically or antiferromagnetically to the moment of the host material. These results have been experimentally proved since more than 30 years by Campbell [178]. The same observation was done for alloys, e.g. for NiPt [99, 179]. The strong hybridization with the orbitals of the ferromagnet is directly responsible for the induced spin polarization in the $3d$, $4d$ and $5d$ elements which are nonmagnetic in bulk. Due to the spin-orbit interaction, a small orbital moment is then induced by the spin polarization. The $5d$ elements are of particular interest due to the large spin-orbit interaction. The XMCD method, because of its element selectivity and sensitivity, is an appropriate technique to investigate multi-component systems combining $3d$ and $5d$ elements. Up to now, there are very few XMCD studies concerning induced magnetism in $5d$ transition metals. The first experiments were done by Schütz *et al.* at the $L_{3,2}$-edges of $5d$ impurities in Fe where the local magnetic moment were qualitatively determined [180, 181]. The discovery of multilayer systems has attracted a lot of attention due to their interesting magnetic and magneto-optical properties. A lot of efforts was concentrated on the study of interlayer coupling and the magnetoresistance phenomenon. Multilayers composed of alternating layers with magnetic and nonmagnetic transition metals like $3d/5d$ were considered as very good candidates for technological applications. Despite the discovery of a rich variety of novel effects related to the artificial structure, very few work has been concentrated on the inducting (the $3d$ elements) and induced (the $5d$ elements) magnetic moments in these multilayers. In order to elucidate the influence of the $3d$ and $5d$ elements on the magnetic properties, it is important to determine the magnetic contribution of each layer in these

127

multilayers.

In the first section, we will construct a full magnetic moment profile for the Ni/Pt multilayer system. We will show that the hybridization effects between Ni and Pt are essentially localized at the interface. They result in a reduction of Ni moment (stronger for thick Pt layers) and spin polarization of Pt (stronger for thicker Ni layers). In the second section, we will show the existence of an induced magnetic moment on W and Ir in W/Fe and Ir/Fe multilayers. Up to now, no induced magnetic moment has been detected in these two systems. The main interest is to start to study the induced magnetism in $3d/5d$ multilayers. This will have as direct consequence to understand more from theoretical point of view the hybridization effects which take place in the $5d$ transition metals.

6.1   The Ni/Pt multilayer system

Schütz and coworkers were the first in 1993 to investigate a magnetic profile for a $5d$ transition metal, in this case Pt and Ir, in Pt/Co and Co/Pt/Ir/Pt/Co multilayers using the advantage of the element-specificity of the XMCD technique [182]. Later on, after the establishing of the sum rules, Vogel *et al.* have determined the magnetic profile of Pd in Fe/Pd multilayers [183]. These two studies show clearly that the induced magnetic moments decrease from the interface to the inner layers. More recently, XMCD measurements performed at the $N_{4,5}$-edges of Pt in Pt/Fe multilayers reported a constant magnetic profile up to 5ML for Pt [184]. This does not support the two previous studies. Unfortunately, all the studies concerning the induced magnetic profile in the $3d/4d$ or $3d/5d$ multilayers have never considered the magnetic moment profile of the $3d$ ferromagnetic transition metal. This is however an important point to draw conclusions about the magnetic properties of the polarisable material.

The Ni/Pt multilayer system has been the subject of conflicting results these last years. Classic magnetometry techniques, like SQUID or VSM, have measured from slightly enhanced ($\approx 15\%$) [151] to slightly reduced ($\approx$-10%) [185] or even strongly reduced [186, 187] magnetizations for Ni/Pt multilayers. These effects were either attributed to a possible Pt polarization [151] or to a number of dead Ni layers at the Ni/Pt interface [185, 186, 187].

In order to elucidate this problem, we will study here the magnetic moments in Ni/Pt multilayers and provide a layer-resolved magnetic moment profile for the whole system. This will be done via a combination between SQUID magnetometry and XMCD spectroscopy. The element-specific XMCD method allows us to separate the magnetic contributions of Ni and Pt. Using the sum rules, the spin and orbital magnetic moments will

be determined. A comparison with *ab initio* theoretical calculations will be carried out. We find that the Ni magnetic moment is reduced at the interface and that the Pt acquires an induced magnetic moment up to $0.3\mu_B$/atom [188].

The Ni_n/Pt_m multilayers with n and m ranged between 2 and 13 monolayers were prepared by e-beam evaporation and characterized wit respect to their structural, magnetic and magneto-optic properties as it is described elsewhere (see section §5.3.1) [150, 151]. The individual Pt and Ni thicknesses were determined by precalibrated quartz crystals and XRD with a precision of about 5%. The atomic planes (n and m) were approximated to the closest integer or half-integer numbers. The samples were grown on glass and on polyimide (Kapton) with an diamagnetic Cu backing foil. No substrate influence was found on the magneto-optic properties [150]. To summarize, the samples have polycristalline fcc (111) structure and a columnar morphology with grains of several tens on nm large. The roughness could be of about 1-2ML in the grains. The interface between Ni and Pt in evaporated Ni/Pt multilayers are sharp in the monolayer limit. Limited alloyed NiPt regions are formed at the grain boundaries [175]. The easy magnetization direction is either perpendicular or parallel to the surface plane (see Fig. 5.4). To avoid to correct all the data for saturation effects (total electron yield) or self-absorption (fluorescence yield), we have chosen to measure all the XMCD spectra along the out-of-plane direction. A strong magnetic field was applied in order to saturate magnetically all the samples.

6.1.1   The Ni $L_{3,2}$-edges

The XMCD experiments have been performed at the European Synchrotron Radiation Facility (ESRF) at Grenoble (France) on the ID12B soft x-rays beam line at the $L_{3,2}$-edges using the total electron yield mode detection [76]. The degree of polarization of the circular light was 85%. To saturate the samples magnetically, large magnetic fields (2 to 5T) were applied along the x-ray beam direction. All the samples were measured at low temperatures T=10K. All the spectra were recorded either by changing the helicity of the incoming x-ray light or by inverting the magnetic field. The magnetic saturation was verified by tracing element-specific hysteresis curves. Figure 6.1 shows the XMCD spectra recorded at the Ni $L_{3,2}$-edges for the Ni_2/Pt_5 (dotted line), Ni_6/Pt_5 (dashed line) and the Ni bulk reference (a 20nm thick sample) (solid line). We can clearly see that the XMCD intensity decreases as the thickness of Ni decreases for a constant Pt interlayer thickness. A first comment is that no dead layer of Ni is observed since 2ML Ni (2 interfaces) in the Ni_2/Pt_5 multilayers are still magnetic. With the help of the sum rules, we are able to determine the spin and orbital magnetic moments as described in the section §1.2. We will suppose that the dipole magnetic contribution is negligible. As we saw, in the section
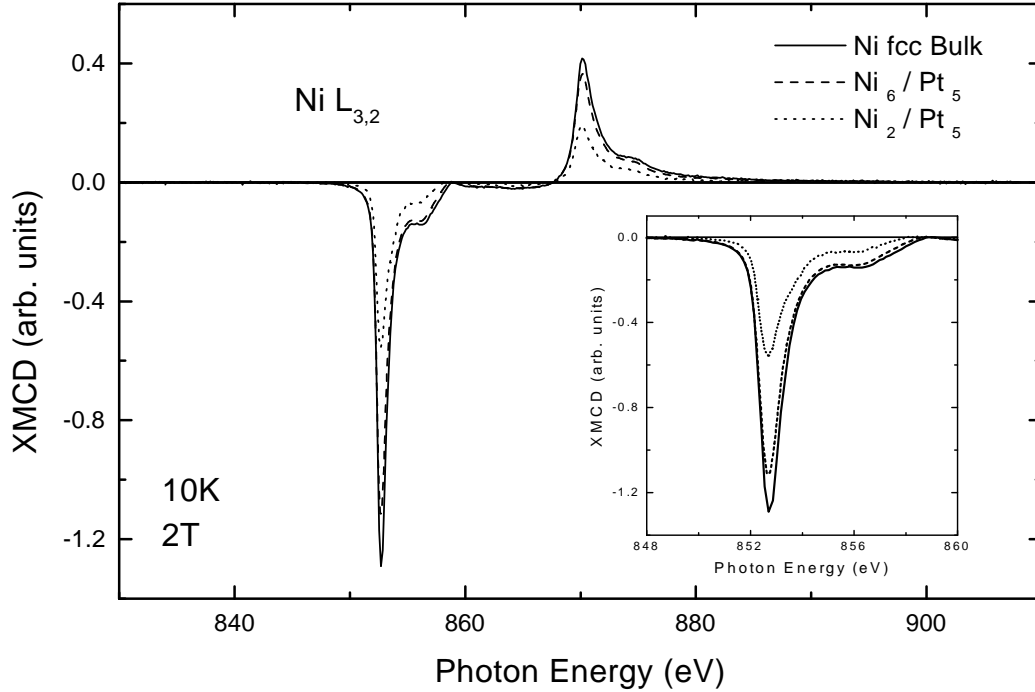
Figure 6.1: XMCD signal measured at the Ni $L_{3,2}$-edges for the Ni_2/Pt_5 (dotted line), the Ni_6/Pt_5 (dashed line) and the Ni bulk reference (a 20nm thick sample) (solid line). The spectra were recorded in the normal to the film plane under 2 T field and at 10K. The inset shows an enlargement of the L_3-edge for better view.

§5.3.3, its contribution is only 2% for the most anisotropic sample. Then, for the others samples which are less anisotropic it should be even smaller. As a reference sample, we have taken a 20nm thick Ni sample (grown on a Pf buffer and capped with Pt). The number of holes taken into account was $n_h = 1.45$. The Ni average magnetic moments determined for all our samples are summarized in the table 6.1. The thick Ni reference sample (see last row) has been taken from the reference [189]. We see directly that even in films with only 2ML Ni, the Ni carries a magnetic moment which is not negligible. Its value depends on the Pt thickness. It goes from $0.2\pm0.02\mu_B$/atom for 9ML Pt to $0.4\pm0.04\mu_B$/atom for only 2ML Pt. Contrary to this, Shin *et al.* [186] and Coyle *et al.* [190] have reported about 2ML or more, respectively, dead Ni layers at each interface for Ni/Pt multilayers which were prepared by sputtering. Krishnan *et al.* came to the same conclusion that 1ML dead Ni layer exists at each Ni/Pt interface for multilayers prepared by e-beam evaporation (like in our case). This would directly mean that Ni_2/Pt_2

multilayers should not carry any magnetic moment. However, we measured for Ni_2/Pt_2 multilayers a Ni magnetic moment which is $\approx 35\%$ reduced compared to Ni bulk. By increasing the Ni thickness an keeping constant the Pt thickness, the Ni average magnetic moment increases towards the Ni bulk value. Only for 13ML, the Ni magnetic moment is nearly bulk. This is expected since the Ni magnetic moment is reduced by $\approx 50\%$ at the interface. The XMCD technique probes the average magnetic moments of Ni and Pt separately, but is not layer-resolved. Concerning the spin and orbital magnetic moment contributions, the ratio m_L/m_S is $\simeq$ 0.100-0.110 regardless of the Ni or Pt thickness. The ratio is in a first approximation bulke-like. Contrary to this, 4ML Ni/Cu(001) have an enhanced orbital-to-spin ratio of 0.14. Recently, the hybridization between Co and Pt has been considered to be responsible for enhanced Co orbital moments for very small Co thicknesses [191]. In (111) $CoPt_3$ thin films , the enhancement of the orbital-to-spin ratio was attributed to the existence of anisotropic chemical local order [51]. It is interesting

n (ML)	m (ML)	m_{tot}^{Ni} (μ_B/atom)	m_S^{Ni} (μ_B/atom)	m_L^{Ni} (μ_B/atom)	m_L^{Ni}/ m_S^{Ni}
2	9	0.253 *	-	-	-
2	5	0.246	0.222	0.024	0.108
2	2	0.388	0.350	0.038	0.108
2.5	9.5	0.195 *	-	-	-
4	5	0.379	0.345	0.034	0.098
6	5	0.470	0.423	0.047	0.111
6	2	0.489	0.441	0.048	0.108
7.5	7.5	0.455	0.414	0.041	0.099
13	5	0.547	0.495	0.052	0.105
Ni bulk		0.61 [1]	0.554	0.055	0.100 [2]

[1] Reference [189]

[2] Reference [5]

Table 6.1: Total, spin and orbital Ni average magnetic moment in μ_B/atom provided from XMCD measurements for different Ni_n/Pt_m multilayers. The value with an (*) have been determined using the total magnetization of the sample from SQUID [173] and subtracting the total magnetic moment of Pt from XMCD (see section §6.1.2). The error bars are typically of about 10%.

to notice that by decreasing the Pt (spacer) thickness for a given Ni thickness, the Ni average magnetic moment increases. It may be seen for the Ni_2/Pt_m multilayers where the Ni magnetic moment increases from 0.25 to $0.4\mu_B$/atom. A similar observation was reported for the Ni moment in Co/Cu/Ni trilayers with ultrathin 2-3 ML Cu spacers (see section §4.3.4). These effects could come from interlayer exchange coupling and proximity effects.

6.1.2   The Pt $L_{3,2}$-edges

Concerning Pt, the XMCD measurements have been performed at the ID12A hard x-rays beam line at the ESRF at the $L_{3,2}$-edges of Pt (11 564 and 13 273eV respectively) using the fluorescence detection yield [75]. The degree of polarisation of the circular light was 84%. As previously, large magnetic fields (2 to 5T) were applied along the x-ray beam direction. The incident angle of the light was normal to the sample plane. The same setup was used as for the Ni XMCD measurements. The spectra were taken at 10K. As before, all the spectra were recorded either by changing the helicity of the incoming x-ray light or by inverting the magnetic field. The correction for self-absorption are not required here for several reasons: the detection geometry, the very small white line intensity and the relative small total thickness of the samples ($\sim$ 1000-1500Å). This was confirmed by the fact that no difference in the XMCD signal compared to the white line was observed for grazing (60°) and normal incidence. Another essential point was checked, if the field itself does induced a magnetic moment on Pt. No difference between 2 and 4 Tesla was detected on the XMCD spectra. In Fig. 6.2 is shown the isotropic absorption spectra (the average of left and right circularly polarized x-ray absorption spectra) at the Pt $L_{3,2}$-edges for a Ni_2/Pt_9 multilayer. Unlike Ni, the normalisation process of the Pt spectra at $L_{3,2}$-edges is not obvious due to a very large spin-orbit coupling in the $2p$ core states (more than 1keV) and a very small white line intensity. We will follow the same procedure suggested by Grange *et al.* [51]. We will describe here briefly this normalisation method.

   For small $2p$ spin-orbit coupling, e.g. the $3d$ transition metals, the proportionality factor between the absorption coefficient at the L_3 and L_2-edge is equal in a first approximation to the ratio of the degeneracy of the core states $2p_{3/2}$ and $2p_{1/2}$. Then, it corresponds to the statistical ratio 2:1. For larger $2p$ spin-orbit coupling, the radial part of the transition elements $< 5d \mid r \mid 2p_{3/2} >$ and $< 5d \mid r \mid 2p_{1/2} >$ are not any more identical [192]. In the case of Pt, the measurement of the absorption coefficient in transmission revealed that the ratio of the L_3 and L_2 edge jump ratio is equal to 2.22 [192]. So, the step height of the absorption spectra recorded in total fluorescence yield has to be adjusted to a ratio 2.22:1 as shown in Fig. 6.2. It is very important that this process
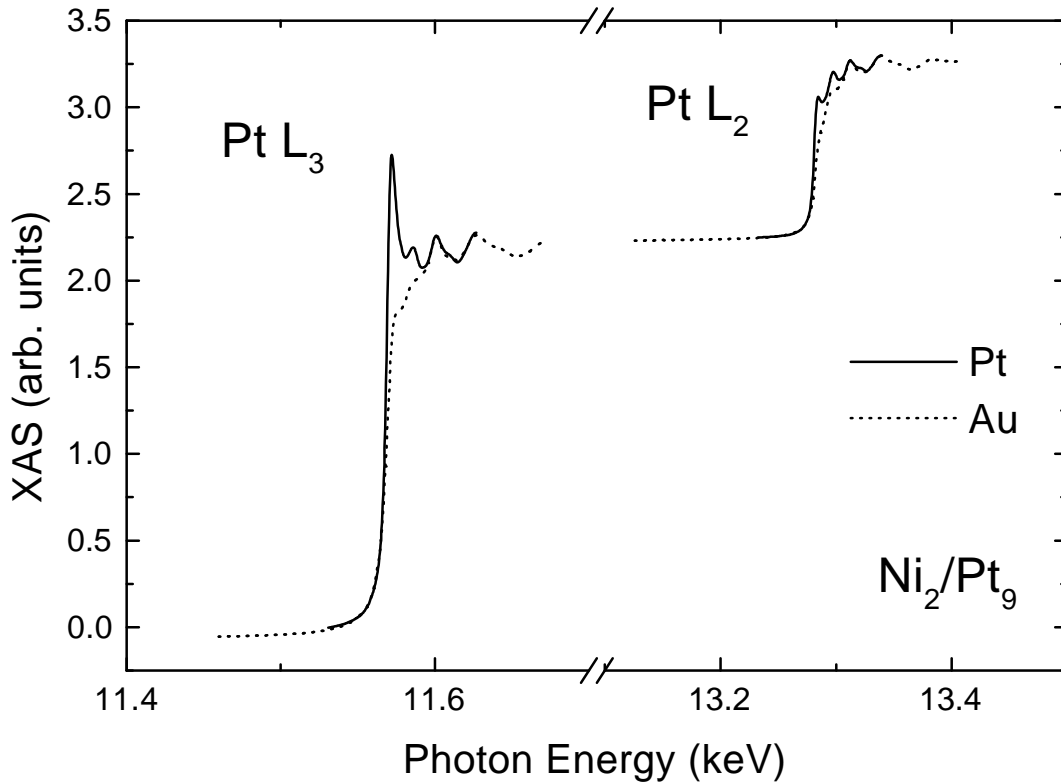
Figure 6.2: Isotropic absorption spectra measured at the Pt $L_{3,2}$-edges for the Ni_2/Pt_9 (solid line) and these of Au (dotted line). The spectra were recorded in the normal to the film plane and normalized as described in detail in reference [51].

is done properly since the ratio of the XMCD intensity at the L_3 and L_2-edges depends strongly on it.

After this normalisation procedure, we can extract the XMCD signal which is now correctly adjusted. Figure 6.3 shows the XMCD signal at the Pt $L_{3,2}$-edges for Ni_6/Pt_2 and Ni_2/Pt_2 multilayers. The dichroic spectra were corrected in order to take into account the non polarized buffer and overlayer contributions. Since the photon penetration depth is for the $5d$ transition metal at the $L_{3,2}$-edges in the order of magnitude of the μm, we can assume than the buffer contributes linearly to the signal. Then, all the XMCD spectra were multiplied by a factor R which is equal to the total thickness of Pt divided by the total thickness of magnetic Pt. The difference is less than 5% by taking into account the decay in intensity of the deeply lying Pt layers which can be modelled using the effective photon escape depth $\lambda \approx 1000 Å$ (see reference [6]). By taking into account the degree of polarisation, the XMCD signal for the Ni_6/Pt_2 is 8.6% of the L_3-edge jump. This is comparable to the Pt XMCD signal for (111) $CoPt_3$. By decreasing the Ni thickness down

to 2ML, a magnetic induced moment is still induced in Pt even if the magnetic moment of Ni is reduced by a factor ≈ 2 compared to bulk Ni. By comparing the Fig. 6.1 and 6.3, the signals at the L_3 and L_2 of Pt and Ni have the same sign. This indicates directly that the Pt moments couple ferromagnetically to the one of Ni. Indeed, this is expected for the two transitions metals which are hybridized and have d bands more than half-filled. In Fig. 6.4 is plotted the Pt XMCD signal at the $L_{3,2}$-edges for a Ni_n/Pt_m series with $n = 2$ML and $m = 2,5$ and 9 ML. We see clearly that with increasing the Pt thickness the XMCD signal decreases. This means that the Pt induced magnetic moment is mostly located at the interface and decreases towards the inner layers. No sizeable change was observed in the white line of Pt for different thicknesses.

Van Veenedaal *et al.* have calculated that in most cases, the sum rules are still applicable on fluorescence yield spectra [193]. The multiplet effects as reported in [194] should be small at the Pt $L_{3,2}$-edges since the fluorescence process ($3d \longrightarrow 2p$) is not
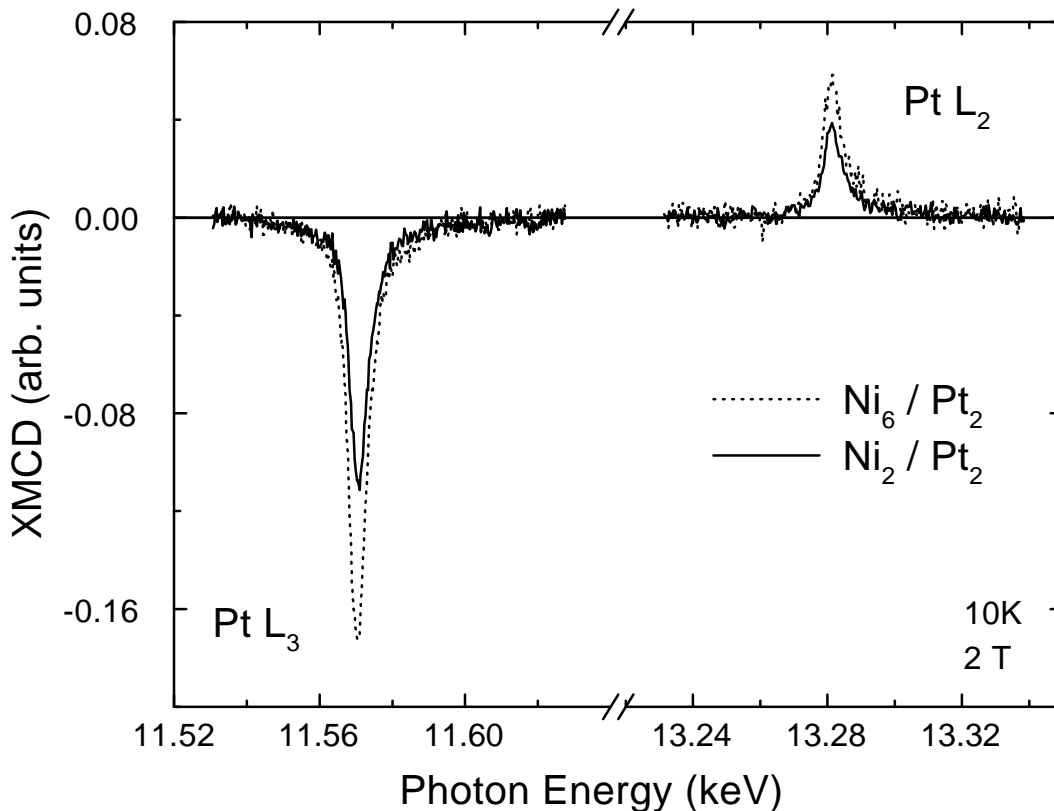

Figure 6.3: XMCD signal at the $L_{3,2}$-edges of Pt for Ni_6/Pt_2 (dotted line), Ni_2/Pt_2 (solid line) multilayers. The spectra were taken at normal incidence at 10K and under a magnetic field of 2 Tesla. The spectra were corrected for the Pt buffer and overlayer contributions. Even for a 2ML Ni, a Pt induced average magnetic moment is observed.

resonant with the absorption process ($2p \longrightarrow 5d$) [194]. The application of the sum rules request the knowledge of the number of n_h^{5d} holes and the isotropic absorption cross section. In order to determine them, we will follow the same procedure suggested by Vogel *et al.* [183] and extended later for Pt by Grange *et al.* [51].

For the late $3d$ transitions metals, in order to separate the transitions to unoccupied $3d$ states from other allowed $2p \longrightarrow nd, s$ dipole transitions (the continuum), a double step like function was subtracted from the isotropic absorption spectra. In this case where the number of holes is important (the white line is very intense), the process is in a first approximation justified. However, for the late $5d$ transition metals, e.g. Pt, the $L_{3,2}$-edges does not present a strong white line. Then, the errors in the determination of a step-like continuum can be as large as 40% [51]. In order to minimize these errors, the continuum is modelled by the $L_{3,2}$-edges of a pure Au sample measured at normal incidence. The energy scale of the Au spectra has been expanded by a factor 1.14 in order to get the
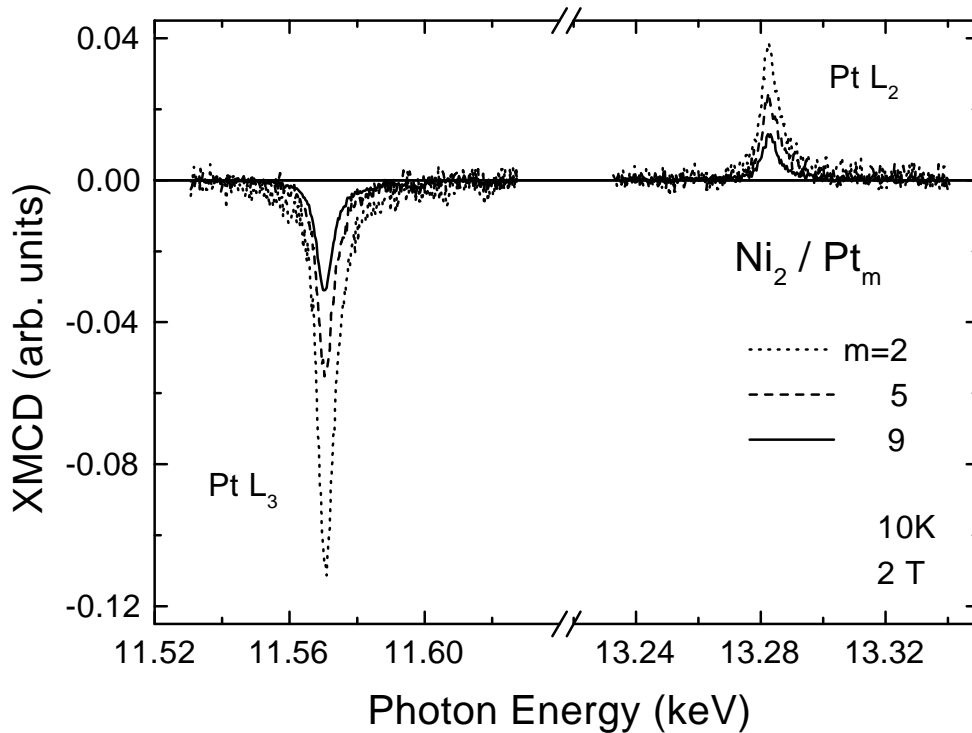

Figure 6.4: XMCD signal at the $L_{3,2}$-edges of Pt for Ni$_2$/Pt$_m$ (m=2, 5 and 9) multilayers. The spectra were taken at normal incidence at 10K and under a magnetic filed of 2 Tesla. The spectra were corrected for the Pt buffer and overlayer contributions. All the samples of constant Ni thickness show a Pt average induced magnetic moment.

same energy separation between the different features in the fine structure [183]. This factor reflects the larger lattice constant of Au compared to this of Pt. Then, the Pt and Au spectra were aligned in energy on the fine structure as we can see in Fig. 6.2. and normalized to the edge jump.

Then, the isotropic absorption cross section per $5d$ hole (see Eq. 1.17 and 1.18) is given by [51]:

$$\frac{A^{iso}}{n_h^{5d}} = \int_{L_{3,2}} \frac{d\omega}{\omega} \left(\frac{I_{Pt}^{Iso}(\omega) - I_{Au}^{Iso}(\omega)}{n_{Pt}^{5d} - n_{Au}^{5d}} \right) \tag{6.1}$$

where $\int_{L_{3,2}} (d\omega/\omega)[I_{Pt}^{Iso}(\omega) - I_{Au}^{Iso}(\omega)]$ is the integrated intensity between the isotropic normalized absorption cross section of Pt and Au spectra. For $n_{Pt}^{5d} - n_{Au}^{5d}$, we took 1.06 which is the difference between the calculated number of $5d$ hole in the various multilayers (1.80 Ref. [195]) and Au (0.74 Ref. [51]).

The results for the average Pt induced magnetic moments determined for all samples are presented in Table 6.2. We have assumed in this case that the magnetic dipole term contribution to the effective spin magnetic moment is negligible. For the samples, a Pt induced average magnetic moment is detected even for small Ni layer thickness. The magnetic moment of Pt at the interface may be as large as $0.29\mu_B/$atom for 2ML Pt in Ni_6/Pt_2 multilayer. For comparison, this value is in agreement within 5% to the higher induced Pt moments for Ni-rich NiPt alloys [196]. The ratio orbital-to-spin magnetic

n (ML)	m (ML)	m_{tot}^{Pt} (μ_B/atom)	m_S^{Pt} (μ_B/atom)	m_L^{Pt} (μ_B/atom)	m_L^{Pt}/m_S^{Pt}
2	9	0.056	0.047	0.009	0.191
2	5	0.089	0.075	0.014	0.186
2	2	0.169	0.138	0.031	0.224
2.5	9.5	0.065	0.055	0.010	0.181
4	5	-	-	-	-
6	5	0.168	0.125	0.043	0.344
6	2	0.293	0.237	0.056	0.236
7.5	7.5	-	-	-	-
13	5	0.212	0.168	0.044	0.262
Pt bulk		0	0	0	-

Table 6.2: Total, spin and orbital Pt average magnetic moment in μ_B/atom provided from XMCD measurements for different Ni_n/Pt_m multilayers. The error bars are typically of about 10%.

moment is ≈ 0.20 for 2ML Ni thickness and ≈ 0.26 for larger Ni thickness. This ratio is in good agreement with those determined experimentally in (111) $CoPt_3$ alloys (0.23)[51]. In this case, a Pt average induced magnetic moment is found of about $0.29\mu_B$/atom. For Co_2/Pt_13 multilayers, the Pt magnetic moment at the interface was estimated to be $0.15\mu_B$/atom [182]. In the case of Co/Pt multilayer, the determination of the magnetic moment were done using a simplified model (this work were done before the derivation of the sum rules). Recently, Antel *et al.* found a constant Pt magnetic moment 0.4-$0.5\mu_B$/atom up to 5ML in Fe/Pt multilayers [184].

6.1.3 The full Ni/Pt magnetic moment profile

From the XMCD measurements performed at the $L_{3,2}$-edges of Ni and Pt for various Ni_n/Pt_m multilayers, we are now able to construct the magnetic moment profile for the whole system. Before, we will first compare our results with SQUID magnetometry.

Comparison with SQUID measurements

The SQUID measurements have been performed at the Institute of Materials Science, NCSR-Demokritos in Athena (Greece). The measurements were done at 10K and under an applied magnetic field of 2 Tesla. In Fig. 6.5 the total magnetization of Ni_n/Pt_m multilayers as a function of n (top axis) or $1/n$ (bottom axis) is shown. The total magnetization was normalized with respect to the Ni volume. Since SQUID magnetometry measures the total magnetization, it is not possible to separate the contributions coming from Ni and Pt contrary, to XMCD magnetometry. Then, we assume, as it is common in the literature that the total magnetization determined by SQUID comes only from the Ni layers. We denote such data by squares in Fig. 6.5. For comparison, we plot by circles the data of XMCD when for each multilayer the contributions of Ni and Pt are added and divided only by the Ni volume. An excellent agreement is shown between SQUID and XMCD measurements. For technical reasons, the same samples could not be measured with SQUID and XMCD. For the optimisation of the SQUID and XMCD measuremnts, we measure in some cases samples with approximately the same m and n grown on Kapton/Cu and glass, respectively. In a previous publication (Ref. [150], Fig. 7), it was demonstrated that such samples from one evaporation run prepared on glass and Kapton give identical hysteresis loops and magneto-optic spectroscopic response[1].

---

[1]In the determination of the magnetization by SQUID it enters the film area. So, for SQUID measurements we used mainly the samples on Kapton (with a Cu backing foil) because, contrary to glass, they can be cut very accurately and then the area of the film is precisely determined. XMCD, contrary to SQUID, has spatial resolution. However, the Cu backing foil gives an enormous background in the
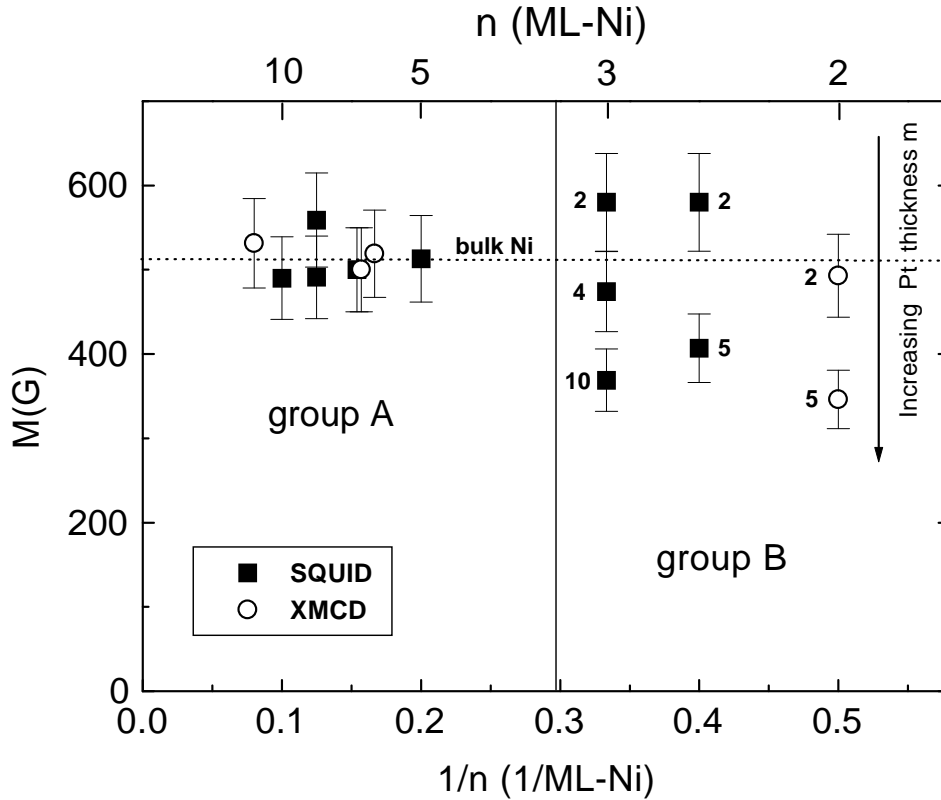
Figure 6.5: Total magnetization of Ni_n/Pt_m multilayers normalized to the Ni volume with n (top) or 1/n (bottom). SQUID (squares) and XMCD (circles) measurements are shown. The dotted line represents the magnetization of bulk Ni [189]. Note that the films of group B show a decrease of the magnetization with increasing Pt thickness m (arrow). The m values for each sample are also indicated. All the samples were measured at T=10 K and under an applied magnetic field of 2 Tesla.

We can distinguish clearly two groups of samples:

i) the first, group A, for 4< n <12 ML shows no dependence of the total magnetization on n. If we would not have the possibility to separate the Ni and Pt moments we could ascribe this finding to a purely bulk-like behaviour.

ii) the second, group B, for n <4ML shows decreasing magnetization with m. Interestingly, samples with very thin Pt layers (m =2 ML) show a small increase in the total magnetization which was not found in NiPt alloys. Contrary to Ref. [186, 187], no evidence for a strongly reduced total magnetization is found.

hard x-ray regime and then samples on glass or Kapton without a backing foil are more suitable. All the samples on glass were not always available on Kapton.

We can see that a common $1/n$ analysis of the total magnetization coming from the non element-specific measurements is not appropriate for Ni_n/Pt_m multilayers. The groups A and B have non-comparable $1/n$ magnetization dependence. For the group B, by increasing the Pt thickness, the total magnetization decreases which reflects the decrease of the Ni average magnetic moment. Contrary to this, Shin *et al.* [186] and Kim *et al.* [187] have reported an $1/n$ dependence of the total magnetization done at room temperature, which for many samples is close to or higher than the Curie temperature. This was then interpreted as the existence of 'dead' Ni layers at the each interface. Our work done at 10K, excludes clearly this possibility. If 2ML of Ni at each interface were non-magnetic, our Ni_2/Pt_m multilayers would not be magnetic at all. Here, we have a nice example which shows how erroneous conclusion are drawn when the Curie temperature is not taken into account.

The full magnetic moment profile

The results reported in table 6.1 and table 6.2 give the average magnetic moments per Ni atom and Pt atom over the whole layer. By combining the results, we can obtain the average moment per Ni and Pt as a function of the distance to the interface using the same construction process as for Pd in Fe/Pd multilayers [183]. The method is the following: for example, by subtracting the average magnetic moment (multiplied by the number of layers) of a 2ML sample from the one of a 4ML sample, we will get the average magnetic moment of the two additional layers. This process can be done for more layers. This process gives a simple picture of the magnetic profile since we suppose that the magnetic moments at the interface layers do not change by adding more Pt in the inner layers.

The XMCD data allow us to construct a layer-dependent magnetic moment profile for a Ni_6/Pt_5 multilayer, shown in Fig. 6.6(a). Two series of Ni_n/Pt_m samples, one with constant Pt $m =5$ and Ni $n =2$, 4, 6 and another with constant Ni $n = 6$ and Pt $m =2,5$ were used in order to construct the profile. The profile construction assumes that the magnetic moment of Ni is constant with m. However, Table 6.1 and Fig. 6.5 reveal that this does not hold well for films with $n =2$ ML. Thus, for the evaluation of the interface Ni moment we considered the average value for Ni_2/Pt_5 and Ni_2/Pt_2. We estimate that this gives an error bar of $\approx 0.1 \mu_B$/atom as indicated. The Ni/Pt multilayer are suitable to construct a magnetic moment profile since the constituents retain almost their bulk lattice parameters and the residual strain is very small (0-2%) [175, 176] despite that the lattice misfit is very large ($\sim 10\%$). As an evidence, no sizeable changes in the fine structure after the $L_{3,2}$-edges of Pt are observed for all the multilayers. Figure 6.7 shows the x-ray isotropic absorption spectra at the L_2-edge of Pt for two extreme multilayers
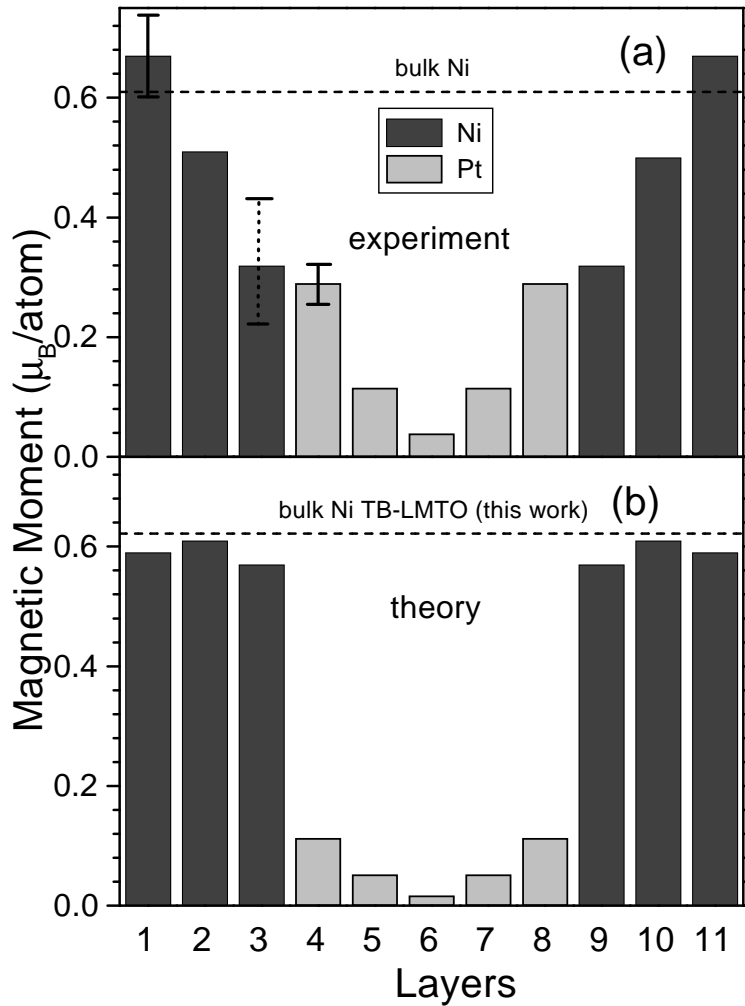
Figure 6.6: (a) Experimentally determined magnetic moment profile for a Ni_6/Pt_5 multilayer. The total magnetization per Ni volume of this sample is equal to the one of bulk Ni (Fig. 6.5). It is only via an element-specific method like the XMCD that layer-resolved information on the magnetic moments may be obtained. The error bars indicated with solid lines ($\pm 10\%$) are typical for all the moments except the one of the Ni at the interface (dotted line)(see text). For the separation of the contribution of the second- to the third-from-the-interface Pt layer we used the ratio of the Pt moments predicted by the TB-LMTO. The Ni-bulk magnetization was taken from Ref.[189]. (b) Theoretical result for the spin magnetic moments of the same multilayer. The trends between experiment and theory are the same. However, the calculated effects at the interface are smaller than the experimental ones.

considered in the profile construction, i.e. the Ni_6/Pt_2 and the Ni_2/Pt_5. The positions of the fine-structure wiggles after the L_2-edge of Pt, which are very sensitive to the electronic and lattice structure, are identical. It can be assumed that the Ni lattice structure does not also change because then, it could have affected the Pt one.

Let us now see if the small residual strains affect the magnetic moments. As it is known, changes in the volume affect the magnetization [197]. However, usually, distortions of the cubic symmetry due to small strains are volume-conserving. In Ni/Pt multilayers, where possible strains could be up to 2%, even by assuming that the volume is not conserved, its change would be of about 5% or less. This would result in a small magnetic moment modification ($\sim$10%). This is supported, e.g. by Moruzzi *et al.*, showing that fcc Ni is a stable ferromagnetic system and the magnetic moment varies smoothly with the lattice
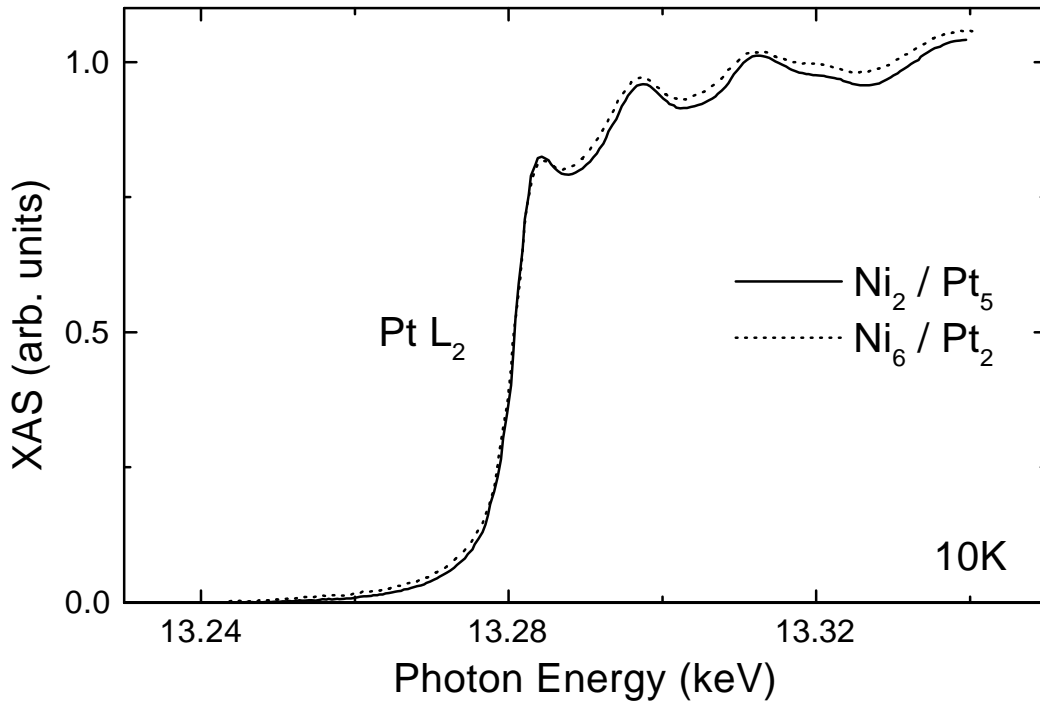

Figure 6.7: Isotropic absorption spectra measured at the Pt L_2-edges for the Ni_2/Pt_5 (solid line) and Ni_6/Pt_2 (dotted line). The spectra were recorded in the normal to the film plane and at 10K. These two spectra, and especially the fine-structure features, are almost identical showing that the electronic and lattice configuration of Pt for both samples are practically the same despite the fact that the intensity of the corresponding XMCD signals which carry the magnetic information (seen in Fig. 6.3 and Fig. 6.4) are quite different.

parameter [197]. These arguments show that one may use samples of different m and n to construct a layer-resolved magnetic profile keeping the error bars as small as $\sim 10\%$ as we indicate in Fig. 6.6(a). The only larger error bar is given for the interface-Ni layer for reasons that we have already explained above.

While similar profiles have been published for the non-magnetic polarisable constituent [182, 199, 183, 200], here it is the first time that such a profile for both constituents of the multilayer is constructed. Figure 6.6a reveals that Pt acquires a large induced magnetic moment up to $0.29\mu_B$/atom at the interface, while the Ni magnetic moment at the interface is strongly reduced (by a factor ~ 2 compared to Ni bulk). These effects may be attributed to hybridization at the Ni/Pt interface. They are much less pronounced in the second from the interface Ni and Pt layers indicating, thus, a sharp interface between Ni and Pt in agreement with the structural studies [150, 175, 151].

Comparison with *ab initio* calculations

In order to complete the study of the monolayer-resolved magnetic moments in Ni/Pt multilayers, we will compare our results to band-structure calculations carried out by the linearized muffin-tin orbital method. The calculations were performed by D. Benea, from the group of Prof. H. Ebert, Institut für Physikalische Chemie, Ludwig Maximilians Universität München (Germany). The electronic structure of the multilayers was calculated self-consistently by means of the tight-binding linearized muffin-tin orbital (TB-LMTO) method in the combined correction ASA mode [201]. Exchange and correlation effects were treated within the framework of local density functional theory, using the parametrization of von Barth and Hedin [202]. Relativistic effects were included through the well known scalar-relativistic approximation, i.e. the effects of the spin-orbit coupling were not taken into account. For the calculations an fcc(111) layered structure was assumed. Thus, a hexagonal unit cell was used according to the multilayer periodicity. The lattice parameters used in the unit cell as well as the interlayer distances were estimated using elastic theory and experimental data for the pure elements.

The calculations were carried out to see how the experimental profile is compared to theory. One of the interesting point is if we could expect an enhanced total magnetization for very thin Ni and Pt layers (for example for Ni_2/Pt_2) and a reduction of the Ni magnetic moment for samples with small n values as m increases.

In Fig. 6.6b is presented the theoretically predicted profile of the spin magnetic moments for the Ni_6/Pt_5 sample. A comparison with the experimental results can be done even if the orbital magnetic moment was not calculated. Its contribution is $\sim 10\%$ for Ni and $\sim 20\text{-}25\%$ for Pt compared to the spin magnetic moment. The consideration of the

n	m	m_{tot}^{Ni}	m_{tot}^{Pt}
(ML)	(ML)	(μ_B/atom)	(μ_B/atom)
2	2	0.39	0.17
2	5	0.24	0.09
6	2	0.49	0.29
6	5	0.47	0.17
13	5	0.54	0.21
Ni bulk[1]		0.61	

[1] Reference [189]

Table 6.3: XMCD tabulated data for the average total magnetic moment of Ni and Pt from table 6.1 and table 6.2. The error bars are typically of about 10%.

spin-orbit coupling affects generally less than 5% the spin magnetic moment [203]. The calculations predict only a small (>8%) reduction of the interface Ni moment compared to the bulk. Note that the experimental profile of Fig. 6.6a shows that this reduction should be of about 50%. The predicted interface Pt magnetic moment of about 0.11 μ_B/atom is of about 2-3 times smaller than the experimental one. Nevertheless, the trend predicted by the calculations is in full accordance with that deduced from the XMCD data. In Table 6.3, we have tabulated some values of Ni and Pt average magnetic moments which are relevant for the comparison.

In Table 6.4, the results for a series of multilayers with n =2 ML and variable m are

m	m^{Ni}	m^{Pt}	m^{Pt}	m^{Pt}	m^{Pt}
(ML)	(μ_B/atom)	(μ_B/atom)	(μ_B/atom)	(μ_B/atom)	(μ_B/atom)
		at interface	at interface-1	at interface-2	average
1	0.66	0.16	-	-	0.16
4	0.51	0.12	0.05	-	0.09
6	0.42	0.10	0.02	0.02	0.05
Ni bulk	0.62				

Table 6.4: Theoretical results for the Ni and Pt spin magnetic moment of three multilayers with n =2 and m =1,4,6 and for bulk Ni. Ni magnetic moments larger than the bulk one are predicted for very thin Pt layers. The Ni moment decreases with m justifying the data of Fig. 6.5 (group B). Note that the average Pt moments are in excellent agreement with the XMCD data of table 6.3.

presented . An increased Ni moment compared to Ni bulk for very small m values is found. This decreases below the bulk-Ni value with increasing m. The calculated Ni moments are larger than the experimental ones of Table 6.3. On the other hand, the average Pt moments are in very good agreement with the ones for the n =2 series of Table 6.3. Note that the calculated moments should result in an enhanced magnetization per Ni volume for very thin Ni and Pt layers. This effect was not observed for bulk NiPt alloys [99, 179]. However, in contrast to the alloys, multilayers with n =2 have all Ni atoms at the interface where a narrowing of the d band width and enhanced magnetic moments are expected [204]. In addition, when m is very small (1-2 ML) interlayer exchange coupling and proximity effects become stronger.

In summary, we show that theory and experiment give a similar variation of the magnetic moments in Ni_n/Pt_m as a function of m and n while giving different absolute values. However, one has to note the following: (i) Slightly different lattice constants compared to the real ones may have been used in the theoretical calculations. These might have resulted in small changes in the volume ($\sim$1-5%) and affected the magnetic moments (up to about 10% for fcc Ni [197]). (ii) In real samples interface exchange processes between Pt and Ni could occur. These would form some alloyed regions at the interface. If the alloying would be through all the Ni thickness, a constant average Ni magnetic moments would be observed. Analysis of our element-specific experimental data with respect to the ones recorded for alloys [99, 179] shows that the Ni moment is reduced by alloying, while the Pt moment is almost unaffected [205].

Effects of interface alloying

We have constructed in the previous paragraph a layer-resolved full magnetic moment profile for Ni/Pt multilayers and compare our experimental results to theoretical calculations. We have seen that experiment and theory show the same trends for the magnetic moments. The hybridization effects between Ni and Pt are mostly localized at the interface and result in a reduction of the Ni magnetic moment and spin polarization of Pt. Experimentally, a reduction of the Ni magnetic moment by a factor $\sim$2 is observed whereas the theory predicts only $\sim$10% reduction. Concerning the Pt induced magnetic moments, the agreement is found to be better. We suggest that the difference in the absolute values of the magnetic moments of Ni at the interface could come from the presence of limited alloying at the interface. We estimate that this is only of about 20-30% , however we will show how it can reduce the Ni magnetic moment [205].

To demonstrate this we will start by comparing data between multilayers and alloys of the same at.% composition. In Fig. 6.8, it is represented the magnetic moment of Ni

(squares) and Pt (circles) for a series of Ni_n/Pt_5 multilayers (solid symbols) determined with XMCD and corresponding magnetic moments for NiPt alloys (open symbols) determined by diffuse neutron scattering [179]. The bottom axis is calibrated in monolayers of Ni in each period of the multilayers. It refers only to the multilayers. The top axis is calibrated in an approximate average Ni composition (in at.% units) and it refers to both alloys and multilayers (e.g. a Ni_6/Pt_5 corresponds to $\sim 55\%$ Ni atoms in NiPt alloys). First, we see that the onset of ferromagnetism in NiPt alloys is $\sim 40\%/$at. concentration of Ni [179]. Second, in multilayers with lower Ni concentration magnetic response in observed. Moreover, in all the multilayers, the Ni magnetic moments are 20-30% enhanced compare to the NiPt alloys of the same composition. However, the induced magnetic moment in Pt is approximately the same for the multilayers and the alloys. The total
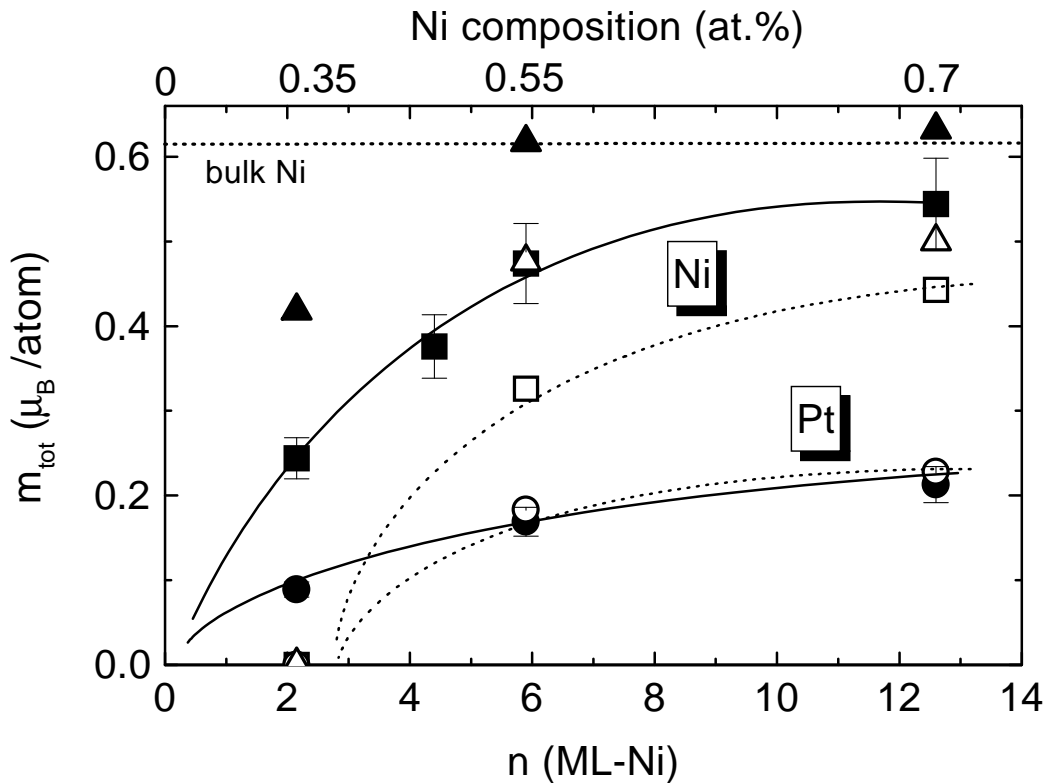
Figure 6.8: Magnetic moment of Ni (squares) and Pt (circles) for Ni_n/Pt_5 multilayer (solid symbols) determined with XMCD and for NiPt alloys (open symbols) [179]. For better illustration, all the points for the NiPt alloys from [179] were represented by dotted lines. The solid lines are guide to the eyes. The triangles represent the sum of the magnetic moments of Pt and Ni normalized per Ni atom. The Ni bulk magnetic moment is given as a reference [189]. All the measurements were done at very low temperatures.

magnetic moment of Ni and Pt normalized to Ni per atom (solid triangles) is found to be Ni bulk-like for the multilayers with thick Ni layers (as found using SQUID magnetometry). In NiPt alloys, a decreased total magnetization (open triangles) has been found even for large Ni concentrations. Therefore, we conclude that a transition from a multilayer to an alloy of the same composition introduces reduction of the Ni magnetic moment while the Pt moment is practically the same. This change of the Ni moment would result in a reduction of the total magnetization detected for example by a SQUID. Now that we have understand the difference between Ni/Pt multilayers and alloys, we are ready to bridge the difference between experiment and theory.

In Fig. 6.9, the average Ni (squares) and Pt (circles) total magnetic moment is plotted for a Ni_2/Pt_m with variable Pt thickness m. The spin magnetic moments deduced from the calculations have been scaled to the total magnetic moments with the help of the experimentally determined orbital-to-spin ratio m_L/m_S (10% for Ni and 20% for Pt).
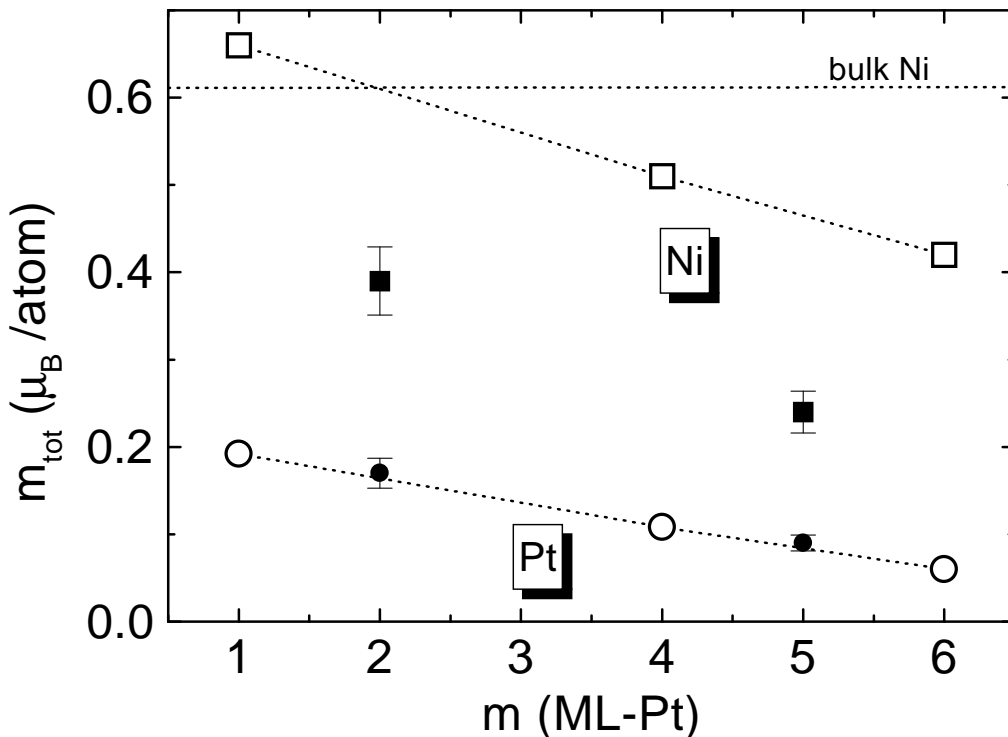

Figure 6.9: Average Ni (squares) and Pt (circles) total magnetic moment determined experimentally (solid symbols) and calculated theoretically (open symbols) for Ni_2/Pt_m with m variable between 1-6ML. The dotted lines are guides to the eyes. The Ni bulk total magnetic moment is also shown [189].

We observe an excellent agreement for Pt between theory and experiment. For Ni, the same trend is observed as a function of the Pt thickness but the experimental values (closed symbols) are $\sim 35\%$ lower than the theoretical ones (open symbols). This could be explained if we consider a limited alloyed at the interfaces (the alloying areas at the grain boundaries contribute certainly, but to a smaller degree. Indeed the size of the grains are $\sim 30 - 250$nm, so their contribution to the volume is less than 5%). While the difference of the surface energy between Ni and Pt atoms is very small [175], which means that intermixing between Ni and Pt is not expected, the considerable difference in the size of Ni and Pt atoms would render atomic interface exchange process energetically favourable [206]. This could lead to limited alloying areas at the Ni/Pt interface.

If we consider that 20-30% alloy is present at the interface, then this, according to Fig. 6.8, would have reduced the Ni moments but not affected the Pt moments. Then, the results of Fig. 6.9 are justified. This small alloying effect should only have some influence on the Ni magnetic moments in Ni/Pt multilayers with very thin Ni layers. This could explain a stronger reduction of the Ni magnetic moments at the Ni/Pt interface as expected by theory. We have to stress once more that the alloyed effect is limited as even a multilayer with all Ni and Pt layers at the interface (Ni_2/Pt_2) gives superlattice XRD.

6.2 The Fe/T (T=Ir, W) multilayer system

Interlayer coupling and giant magnetoresistance (GMR) effects have brought magnetic multilayers on the top of scientific interest the last decade [138]. Almost all combinations between non-magnetic spacers separating ferromagnetic layers in multilayer form have been tested in order to improve properties with technological importance [133]. In parallel, there is a significant effort to understand the physics governing such phenomena. In a simple RKKY-like picture the non-magnetic atoms are considered as the mediators of the interlayer coupling, see e.g. Ref. [136]. Based on these ideas one expects to find a small polarization of the non-magnetic spacer induced by the magnetic layers. XMCD is an ideal technique for investigating such effects because of its element-specificity and its high sensitivity. Indeed, for example, recent XMCD experiments in Co/Cu multilayers [207] have revealed an induced moment for Cu of the order $0.01\text{-}0.05\mu_B$/atom in good agreement with theoretical predictions [54].

The observation of antiferromagnetic coupling in Fe/W and ferromagnetic coupling Fe/Ir multilayers [133] is promising for detecting small induced magnetic moments on the non-magnetic elements. Up to now, very few work has been concentrated on the induced magnetic moments in Ir and W. In 1991, Wienke *et al.* have studied the change between

ferro- and antiferromagnetic coupling and estimated roughly the total magnetic moments of the $5d$ impurities in Fe [181]. This transition should occur between Os and Ir and was confirmed theoretically [39]. Later, an induced Ir polarisation was even found in Co/Pt/Ir/Pt/Co. However, there is no measurement concerning the polarisation of W in multilayers. Usually, the induced magnetic moments of $5d$ elements are determined as a function of the non-magnetic layers in the same multilayers [183] or in different ferromagnetic environments [198]. However, there is not a meaningful comparison between induced moments of various $5d$ elements in multilayers. We start here to work with multilayers of the same compositional profile, this is to keep the thickness of magnetic and non-magnetic layers constant, and vary the kind of the non magnetic element itself. By taking advantage of XMCD, we will present here the beginning of a systematic classification of the $5d$ non magnetic elements of the Periodic Table with respect to their magnetic polarisability. We will present here the first results on the induced magnetic moments at the Ir and W layers in Fe/T (T=Ir, W) multilayers.

These two different multilayer systems have been prepared in collaboration with M. Angelakeris in the group of Prof. N. K. Flevaris. The samples were prepared by e-beam evaporation on Kapton and glass substrates and characterized via x-ray diffraction and electron microscopy. The Fe_5/Ir_2 and Fe_5/W_2 were respectively grown on an Ir and W buffer (60ML). The samples were capped to be prevented from oxidation. The total thickness of the samples are of about 1000Å. The samples have polycrystalline bcc(110) structure with typical grain size of 20-50nm [209]. The easy magnetization direction was found via VSM to be in the surface plane for the two specimens. An external magnetic field of 7 Tesla was found to be sufficient to saturate magnetically the samples in the hard direction (normal to the film plane).

The XMCD measurements have been performed at the ID12A hard x-rays beam line at the ESRF at the $L_{3,2}$-edges of W (10 197 and 11 273eV respectively) and Ir (11 215 and 12 824ev respectively) using the fluorescence detection yield [75]. The degree of polarisation of the circular light was 84%. As previously, large magnetic fields (2 to 5T) were applied along the x-ray beam direction. The spectra were taken either at 10K or 200K. The incidence angle of the light was normal to the sample plane. As before, all the spectra were recorded either by changing the helicity of the incoming x-ray light or by inverting the magnetic field. This was indeed very useful since the signal at the W $L_{3,2}$, as we will see, are rather small. No correction for self-absorption is required since measurements done at different incidence angle revealed identical absorption and XMCD spectra. The measurements were mostly performed along the hard axis.

6.2.1 The Fe/Ir multilayer system

In Fig. 6.10 is shown the isotropic absorption (polarization average absorption)(top) and XMCD (bottom) spectra at the Ir $L_{3,2}$-edges in the Fe_5/Ir_2 multilayer system. As for Pt, the step height of the isotropic absorption spectra recorded in total fluorescence yield were adjusted in a ratio R. The absorption jump calculated for an Ir atom is $121.5cm^2.g^{-1}$ at the L_3 and $54.1cm^2.g^{-1}$ at the L_2 which results in a ratio 2.24:1 [74]. The results show that the Ir layer is significantly spin-polarized by the neighbouring Fe layers. As in the case of Pt, the continuum is modelled by the $L_{3,2}$-edges of a pure Au sample measured at normal incidence. The errors by using a step-like continuum is found to be smaller than in the case of Pt since Ir shows a stronger white line intensity. We will follow here the same procedure as describe before for Pt for the determination of the isotropic absorption cross section per $5d$ holes (Eq. 6.1). For n_{Ir}^{5d}, we took 2.7 coming from fully relativistic *ab*
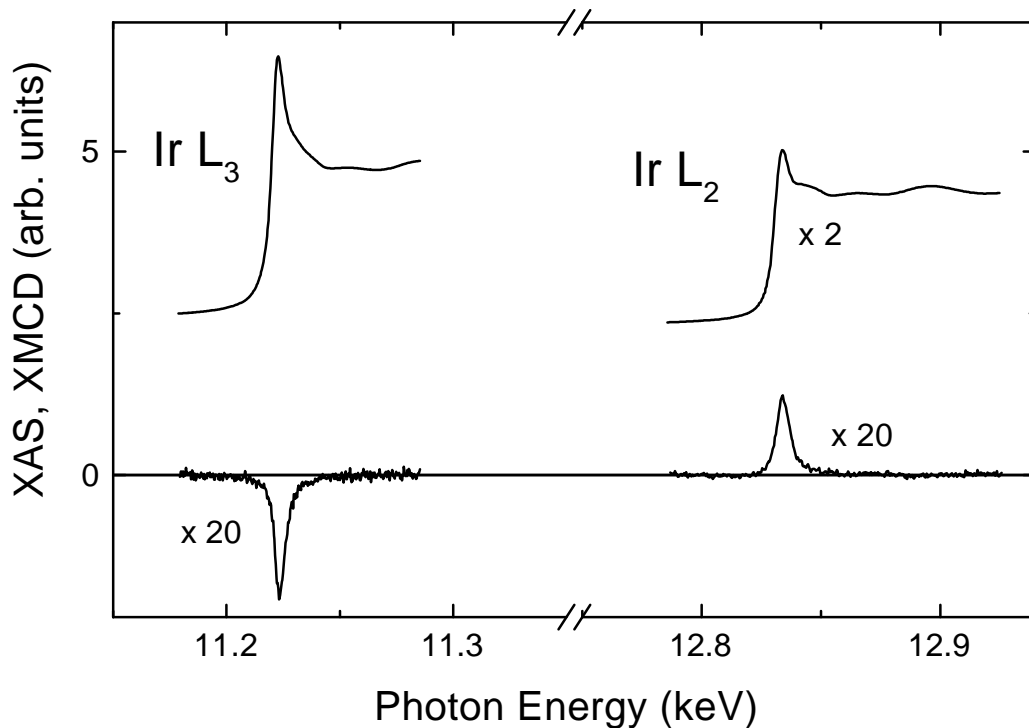

Figure 6.10: Isotropic absorption spectra (top) and corresponding XMCD (bottom) spectra at the Ir $L_{3,2}$-edges in Fe_5/Ir_2 multilayers. The absorption signals L_3 and L_2 have been normalized to a ratio 2.24:1 as explained in the text. Ir was found to be coupled ferromagnetic to Fe. The spectra were taken at normal incidence under an applied magnetic field of 5T and at 10K.

initio calculations [210]. Using the sum rules and assuming that the magnetic dipole term contribution to the effective spin magnetic moment is negligible, we found an average Ir induced total magnetic moment of about $\sim 0.2 \pm 0.1\mu_B$/atom. The induced magnetic moment of Ir is coupled ferromagnetically to Fe. For comparison, the magnetic moment of Ir impurities (3%) in Fe was found to be $\sim 0.51 \pm 0.1\mu_B$/atom (this was determined before the derivation of the sum rules) [181]. Calculations have predicted an induced total local moment of Ir impurities in Fe of $0.2\mu_B$/atom [208]. This is in good agreement with our results for Ir in Fe_5/Ir_2 multilayers. In the case of $Co_2/Pt_5/Ir_4/Pt_5/Co_2$ multilayers, an average induced Ir total magnetic moment was estimated to be $\sim 0.03\mu_B$/atom [182]. This is explain from the fact that the Pt carries a small induced magnetic moment too. Here, we show for the first time a realistic evaluation of the induced magnetic moment of Ir in Fe/Ir multilayer. To complete the study, it should be necessary to determine the Fe magnetic moment at the interface as it was done for Ni/Pt. This would be the next step.

6.2.2   The Fe/W multilayer system

Figure 6.11 shows the isotropic absorption (polarization average absorption) and XMCD spectra at the W $L_{3,2}$-edges in the Fe_5/W_2 multilayer system. As for Ir, the step height of the isotropic absorption spectra has to be adjusted. The absorption jump calculated for a W atom is $138.2 cm^2.g^{-1}$ at the L_3 and $63.1 cm^2.g^{-1}$ at the L_2 which results in a ratio 2.19:1 [74]. We see again that the W layers are spin-polarized be the Fe layers. We can directly see that the sign of the XMCD signal at the $L_{3,2}$-edges are inverted compare to the Ir ones (Fig. 6.10). This means directly that W is coupled antiferromagnetically to Fe as it is expected. In order to determine the magnetic moment, we have modelled the continuum with a step function. Contrary to Pt or Ir , the white line intensity is much larger. In this case, by using the Au $L_{3,2}$ edges or the step function, the final results have a difference of less than 10%. The number of $5d$ holes which enters directly in the sum rules was 5.7 [210]. Using the sum rules and assuming that the magnetic dipole term contribution to the effective spin magnetic moment is negligible, we found an average W induced total magnetic moment of about $\sim -0.2 \pm 0.1\mu_B$/atom. In comparison, the only data available up to now are the magnetic moment of W impurities (3%) in Fe which was found to be $\sim -0.40 \pm 0.1\mu_B$/atom (this was determined before the derivation of the sum rules) [181]. Calculation have predicted an induced total local moment of W impurities in Fe of $-0.45\mu_B$/atom [208]. We found in our multilayers a smaller W induced magnetic moment. Here, we have determined the total W induced magnetic moment in Fe/W multilayers. It is found to be coupled antiferromagnetically to the Fe layers.

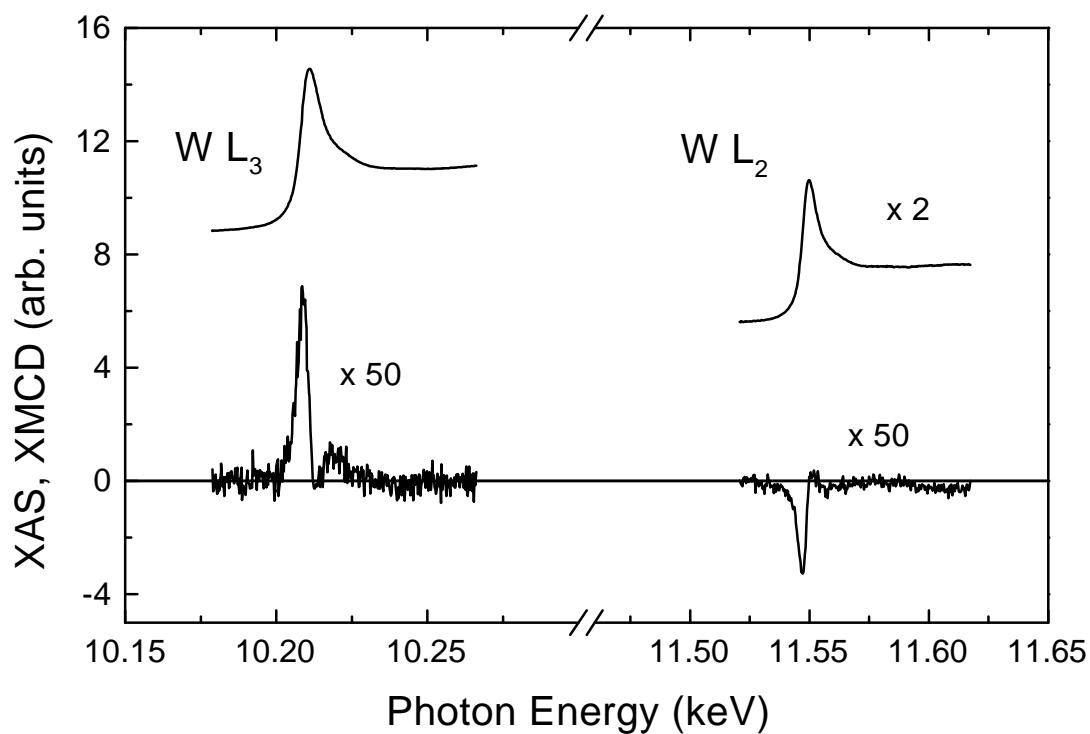In the future, XMCD measurements will be done for Fe at the interface in order to

Figure 6.11: Isotropic absorption spectra (top) and corresponding XMCD (bottom) spectra at the W $L_{3,2}$-edges in Fe_5/W_2 multilayers. The absorption signals L_3 and L_2 have been normalized to a ratio 2.19:1 as explained in the text. W was found to be coupled antiferromagnetic to Fe. The spectra were taken at normal incidence under an applied magnetic field of 5T and at 10K.

compare the hybridization effects between the Fe/Ir and Fe/W.

Conclusion

In this work, we have demonstrated the power of the newly developed x-ray magnetic circular dichroism (XMCD) to solve fundamental problems of thin film magnetism. XMCD measurements at low temperatures allow for the determination of element-specific magnetic moments and the separation into orbital and spin contributions. Temperature-dependent measurements reveal ordering temperatures for single films and layered structure. The anisotropy of the orbital moment, which is the origin of magnetic anisotropy energy, is determined via high-field angular-dependent XMCD.

XMCD measurements at low temperatures on ultrathin Co and Ni films on Cu substrates were performed. An experimental proof of the predicted enhanced orbital moment of ultrathin Co is reported. The orbital-to-spin magnetic moment ratio is found to be enhanced for ultrathin Co films. We show that 2ML Co on Cu(001) and Cu(1 1 21) carry an orbital magnetic moment of 0.22 and $0.26\mu_B$/atom, respectively. They are enhanced compare to the $0.14\mu_B$/atom of the orbital magnetic moment of Co bulk. Moreover, a small enhanced spin magnetic moment was found for the ultrathin Co films compared to the bulk. On the other hand, 4ML Ni on Cu(001) show a reduced magnetic moment of about $0.28\mu_B$/atom compared to $0.64\mu_B$/atom for Ni bulk. As for ultrathin Co films, an enhanced orbital-to-spin ratio is also found. In a simple picture, the narrowing effect of the d-bands of Co at the surface is larger than the Co-d-Cu-d hybridization at the interface to observe enhanced magnetic moment in this system contrary to Ni/Cu(001). By Cu-capping the Co and Ni ultrathin films, a reduction of the magnetic moments and the Curie temperature is found. Within the framework of a mean-field model, the reduction of the magnetic moment and the Curie temperature are correlated.

By use of temperature-dependent XMCD measurements, we show that it possible to enhance the ordering temperature of Cu/Ni/Cu(001) to higher temperature by the addition of another ferromagnetic layer, i.e. Co, which possess an intrinsic different Curie temperature. Thanks to the element-specificity of the XMCD method, two different magnetization curves which vanish at different ordering temperatures were recorded. The interlayer exchange coupling between the two ferromagnetic layers was found to oscillate

between ferro- and anti-ferromagnetic depending on the Cu-spacer thickness. Antiferromagnetic coupling was observed down to 2ML Cu-spacers showing the high structural quality of the epitaxial trilayers. It is demonstrated that this interlayer exchange coupling in the trilayer is responsible for the positive temperature shift ΔT of the lowest magnetization compared to the bilayer case. This ΔT shift is found to oscillate like the interlayer exchange coupling as a function of the Cu-thickness. The oscillation periods are in good agreement with the simple RKKY theoretical predicted ones. The ΔT shift is ascribed to the suppression of the spin fluctuations caused by the interlayer exchange interaction which acts as an external field. This results in an increase of the lower magnetization for two-dimensional systems. By decreasing the thickness of the higher-moment element, the two different magnetization curves were found to cross each other. At lower temperatures, the magnetization of the element with the lowest magnetic moment is found to be increased. Their origin could be attributed to the interlayer exchange coupling.

The magnetic properties of $3d/5d$ multilayers were investigated by means of XMCD. In the case of Ni/Pt multilayers, high-field angular-dependent XMCD measurements were performed. An anisotropy of the Ni orbital magnetic moment in Ni_2/Pt_2 multilayer of $0.008\mu_B$/atom was measured. The anisotropy of the orbital moment is directly linked to the magnetic anisotropy since it is its origin. The spin and orbital magnetic moment were determined for Ni/Pt multilayers with several thicknesses. The measurements at both $L_{3,2}$-edges of Ni and Pt, allow to construct a full magnetic profile of a multilayer. No dead Ni layers at the interface of Ni/Pt was found, contrary to literature. Sharp interfaces are the origin of this observation. Induced magnetic moment on Pt up to $0.3\mu_B$/atom are observed. The Ni magnetic moment at the interfaces are found to be reduced by $\sim 50\%$ compared to Ni bulk value. Theoretical calculations predicted the same trends. However, at the interfaces, the Ni magnetic moments should only be slightly reduced ($\sim8\%$) whereas the magnetic moment contribution is found to be 2 to 3 times smaller compared to the experimentally determined one. Induced magnetic moments for W and Ir in Fe/T(T=W,Ir) multilayers were probed. As predicted, W is coupled antiferromagnetically to Fe, while Ir ferromagnetically.

In summary, by using a unique experimental tool, the XMCD technique, we were able to bring new light in the understanding of thin film magnetism starting from single overlayers and going step-by-step to novel multilayers with technological importance. We studied the single magnetic overlyers demonstrating the effects of the hybridization with the substrate and the reduced coordination number at surface/interfaces on the magnetic moments. In a next step, we showed the modification of the magnetic moments and the Curie temperature by capping. We entered the miraculous world of multilayer magnetism by evaporating an other magnetic material on the top of the bilayer. We demonstrated

that it is the interlayer exchange coupling and the reduce dimensionality that tune the ordering temperature to higher values. Using our prototype trilayers to understand the physics of multilayer magnetism, we proceed to thick multilayer systems with potential technological applications as perpendicular magneto-optic recording media. We probed the microscopic origin of this perpendicular anisotropy and induced magnetic moments, ending up with a novel, world-wide, magnetic moment profile of a magnetic multilayer.

Bibliography

[1] P. Grünberg, R. Schreiber, Y. Pang, M. B. Brodsky and H. Sower, *Phys. Rev. Lett.* **57**, 2442 (1986).

[2] D. Weller and A. Moser, *IEEE Transactions on Magnetics* **35**, 4423 (1999).

[3] P. Poulopoulos and K. Baberschke, *J. Phys. :Condens. Matter* **11**, 9495 (1999) and references therein.

[4] G. Schütz, W. Wagner, W. Wilhelm, P. Kienle, R. Zeller, R. Frahm and G. Materlik, *Phys. Rev. Lett.* **58**, 737 (1987).

[5] O. Hjortstam, J. Trygg, J. M. Wills, B. Johansson and O. Eriksson, *Phys. Rev. B* **53**, 9204 (1996).

[6] M. Tischer, O. Hjortstam, D. Arvanitis, J. Hunter Dunn, F. May, K. Baberschke, J. Trygg, J. M. Wills, B. Johansson and O. Ericksson, *Phys. Rev. Lett.* **75**, 1602 (1995).

[7] M. Faraday, *Phil. Trans. R. Soc.* **136**, 1 (1846).

[8] J. Kerr, *Phil. Mag.* **3**, 321 (1877).

[9] M. J. Freiser, *IEEE trans. Mag.* **4** (1968).

[10] J. C. Chapman, *Phil. Mag.* **25**, 792 (1913).

[11] A. H. Forman, *Phys. Rev.* **3**, 306 (1914).

[12] J. L. Erskine and E. A. Stern, *Phys. Rev. B* **12**, 5016 (1975).

[13] B. T. Thole, G. van der Laan and G. A. Sawatzky, *Phys, Rev. Lett.* **55**, 2086 (1985).

[14] G. Van der Laan, B. T. Thole, G. A. Sawatzky , J. B. Goedkoop, J. C. Fuggle, J. M. Esteva, R. Karnatak, J. P. Remaika and H. Dabkowska, *Phys. Rev. B* **34**, 6529 (1986).

[15] D. P. Siddons , M. Hart, Y. Amemiya and J. B. Hastings, *Phys. Rev. Lett.* **64**, 1967 (1990).

[16] K. Mori, K. Namikawa, Y. Koyama and M. Ando, *Japan J. Appl. Phys.* **32**, 323 (1992).

[17] P. Strange, P. J. Durham and B. L. Gyorffy, *Phys. Rev. Lett.* **67**, 3590 (1991).

[18] D. Gibbs, D. R. Harshman, E. D. Isaacs, D. B. McWhan, D. Mills and C. Vettier, *Phys. Rev. Lett.* **61**, 1241 (1988).

[19] L. Alagna, T. Prosperi, S. Turchini, J. Goulon, A. Rogalev, C. Goulon-Ginet, C. R. Natoli, R. D. Peacock and B. Stewart, *Phys. Rev. Lett.* **80**, 4799 (1998).

[20] J. B. Kortright, D. D. Awschalom, J. Stöhr, S. D. Bader, Y. U. Ydzerda, S. S. P. Parkin, I. K. Schuller and H.-C. Siegmann, *J. Magn. Magn. Mater.* **207**,7 (1999).

[21] M. Born and E. Wolf, *Principles of Optics*, Pergamon Press, Oxford, sixth edition, (1980).

[22] J. H. Hubbel, *J. Phys. C4* **32**, 4 (1971).

[23] A. Fontaine, *Neutron and synchrotron radiation for condensed matter studies*, edited by J. Baruchel, J. L. Hodeau, M. S. Lehmann, J. R. Regnard and C. Schlenker, Vol. 1, pp. 323-361 (Les editions de physique, Springer Verlag, 1993).

[24] J. Stöhr and Y. Wu, *Proccedings Nato Advanced Study Institute "New Directions in Research with 3rd Generation Soft X-ray Synchrotron Radiation Sources"*, edited by A.S. Slachter and F. J. Wuilleumier (Kluwer Academic Publishers, Dordrecht, 1994).

[25] B. T. Thole, P. Carra, F. Sette and G. van der Laan, *Phys. Rev. Lett.* **68**, 1943 (1992).

[26] P. Carra, B. T. Thole, M. Altarelli and X. Wang, *Phys. Rev. Lett.* **70**, 694 (1993).

[27] P. Carra, H. König, B. T. Thole and M. Altarelli, *Physica B* **192**, 182 (1993).

[28] G. van der Laan, *Phys. Rev. B* **57**, 5250 (1998).

[29] B. K. Teo, *EXAFS: Basic Principles and Data Analysis*, (Springer-Verlag, Berlin, 1986)

[30] A. Ankudinov and J. J. Rehr, *Phys. Rev. B* **56**, R1712 (1997).

[31] R. Wu, D. Wang and A. J. Freeman, *Phys. Rev. Lett.* **71**, 3581 (1993).

[32] R. Wu and A. J. Freeman, *Phys. Rev. Lett.* **73**, 1994 (1994).

[33] A. I. Nesvizhskii, A. L. ankudinov and J. J. Rehr, (unpublished).

[34] J. Schwitalla and H. Ebert, *Phys. Rev. Lett.* **80**, 4586 (1998).

[35] J. Kanamori, in *Anisotropy and Magnetostriction of Ferromagnetic and Antiferro-magnetic Materials*, Magnetism Vol. I, edited by G. T. Rado and H. Suhl (Academic, New York, 1963).

[36] J. Stöhr and H. König, *Phys. Rev. Lett.* **95**, 3748 (1995).

[37] P. Sainctavit, M.-A. Arrio and C. Brouder, *Phys. Rev.* B**52**, 12766 (1995).

[38] A. Ankudinov and J. J. Rehr, *Phys. Rev.* B**51**, 1282 (1995).

[39] H. Ebert, *Rep. Prog. Phys.* **59**, 1665 (1996).

[40] G. Y. Guo, *Phys. Rev.* B**57**, 10295 (1998).

[41] C. T. Chen, Y. U. Idzerda, H.-J. Lin, N. V. Smith, G. Meigs, E. Chaban, G. H. Ho, E. Pellegrin and F. Sette, *Phys. Rev. Lett.* **75**, 152 (1995).

[42] C. Brouder and J.-P. Kappler, in *Magnetism and Synchrotron Radiation*, edited by E. Beaurepaire, B. Carrière and J.-P. Kappler, pp. 19-32 (Les editions de physique, Les Ulis, 1997).

[43] W. L. O'Brien, B. P. Tonner, G. R. Harp and S. S. P. Parkin, *J. Appl. Phys.* **76**, 6462 (1994).

[44] F. May, M. Tischer, D. Arvanitis, M. Russo, J. Hunter Dunn, H. Henneken, H. Wende, R. Chauvistré, N. Mårtensson and K. Baberschke, *Phys. Rev.* B**53**, 1076 (1996).

[45] S. S. Dhesi, H. A. Dürr, G. Van der Laan, E. Dudzik and N. B. Brookes, *Phys. Rev.* B**60**, 12852 (1999) and references therein.

[46] M. B. Stearns, *in Numerical Data and Functional Relationships in Science and technology*, edited by H. P. J. Wijn, Landolt-Börnstein, New Series, Group 3, Vol.19, Pt. A (Springer-Verlag, Berlin, 1986).

[47] M. Tischer, *PhD Thesis*, FU Berlin (1995)(unpublished).

[48] O. Eriksson, A. M. Boring, R. C. Albers, G. W. Fernando and B. R. Cooper, *Phys. Rev. B***45**, 2868 (1992).

[49] W. L. O'Brien and B. P. Tonner, *Phys. Rev. B***50**, 12672 (1994).

[50] D. Weller, J. Stöhr, R. Nakajima, A. Carl, M. G. Samant, C. Chappert, R. Mégy, P. Beauvillain, P. Veillet and G. A. Held, *Phys. Rev. Lett.* **75**, 3752 (1995).

[51] W. Grange, M. Maret, J.-P. Kappler, J. Vogel, A. Fontaine, F. Petroff, G. Krill, A. Rogalev, J. Goulon, M. Finazzi and N. B. Brookes, *Phys. Rev. B***58**, 6298 (1998).

[52] K. Baberschke, *Appl. Phys. A* **62**, 417 (1996) and references therein.

[53] J. Fink, Th. Müller-Heinzerling, B. Scheerer, W. Speier, F. U. Hillebrecht, J. C. Fuggle, J. Zaanen and G. A. Sawatzky, *Phys. Rev. B***32**, 4899 (1985).

[54] G. Y. Guo, H. Ebert, W. M. Temmerman and P. J. Durham, *Phys. Rev. B***50**, 3861 (1994).

[55] H. Petersen, M. Willmann, F. Schäfers and W. Gudat, *Nucl. Instr. and Meth. in Phys. Res. A***333**, 594 (1993).

[56] D. Arvanitis (private communication).

[57] J. L. Rodríguez-López, J. Dorantes-Dávila and G. M. Pastor, *Phys. Rev. B***57**, 1040 (1998).

[58] H. Wende, *Extended X-ray Absorption Fine Structure Spectroscopy of Surfaces and Thin Films: Local Structure, Dynamic and Magnetic Properties, PhD Thesis*, Fu-Berlin (Verlag Dr. Köster, Berlin, 1999).

[59] A. Aspelmeier, M. Tischer, M. Farle, M. Russo, K. Baberschke and D. Arvanitis, *J. Magn. Magn. Mater.* **146**, 256 (1995).

[60] J. M. Tonnerre, L. Sève, D. Raoux, G. Soullié, B. Rodmacq and P. Wolfers, *Phys. Rev. Lett.* **75**, 740 (1995).

[61] Y. U. Idzerda, V. Chakarian and J. W. Freeland, *Phys. Rev. Lett.* **82**, 1562 (1999).

[62] P. Fischer, T. Eimüller, G. Schütz, P. Guttmann, G. Schmahl, K. Pruegl and G. Bayreuther, *J. Phys. D: Appl. Phys.* **31**, 649 (1998).

[63] J. Stöhr, A. Scholl, T. J. Regan, S. Anders, J. Lüning, M. R. Scheinfein, H. A. Padmore and R. L. White, *Phys. Rev. Lett.* **83**, 1862 (1999).

[64] J. Hunter Dunn, D. Arvanitis, N. Mårtensson, M. Tischer, F. May, M. Russo and K. Baberschke, *J. Phys.: Condens. Matter* **7**, 1111 (1995).

[65] J. Stöhr, in *NEXAFS Spectroscopy*, Vol. 25 of Springer Series in Surface Sciences (Springer-Verlag, Heidelberg, 1992).

[66] N. Haack, *PhD Thesis*, FU Berlin (1999)(unpublished).

[67] A. Scherz, *Diplomarbeit*, FU Berlin (2000)(unpublished).

[68] J. Stöhr, C. Noguera and T. Kendelewicz, *Phys. Rev. B* **30**, 5571 (1984).

[69] W. Gudat and C. Kunz, *Phys. Rev. Lett.* **29**, 169 (1972).

[70] H. Henneken, *PhD Thesis*, FU Berlin (1999)(unpublished).

[71] L. Tröger, *PhD Thesis*, FU Berlin (1993)(unpublished).

[72] L. Tröger, D. Arvanitis, K. Baberschke, H. Michaelis, U. Grimm and E. Zschech, *Phys. Rev. B* **46**, 3283 (1992).

[73] R. Nakajima, J. Stöhr and Y. U. Idzerda, *Phys. Rev. B* **59**, 6421 (1999) and references therein.

[74] B. L. Henke, E. M. Gullikson and J. C. Davis,in *X-ray interactions: photoabsorption, scattering, transmission, and reflection*, Atomic Data and Nuclear Data Tables **54**(no.2) pp. 181-342 (July 1993). See for example www-cxro.lbl.gov.

[75] J. Goulon, N. B. Brookes, C. Gauthier, J. B. Goedkoop, C. Goulon-Ginet, M. Hagelstein and A. Rogalev, *Physica B* **208-209**, 199 (1995).

[76] N. Drescher, G. Snell, U. Kleinberg, H.-J. Stock, N. Müller, U. Heinzmann and N. B. Brookes, *Rev. Sci. Instrum.* **68**, 1939 (1997).

[77] ESRf web-pages, www.esrf.fr.

[78] P. Srivastava, N. Haack, H. Wende, R. Chauvistré and K. Baberschke, *Phys. Rev. B* **56**, R4398 (1997).

[79] H. A. Dürr, G. van der Laan, J. Vogel, G. Panccione, N. B. Brookes, E. Dudzik and R. McGrath, *Phys. Rev. B* **58**, R11853 (1998).

[80] J.J. de Miguel, A. Cebollada, J. M. Gallego, S. Ferrer, M. Miranda, C. M. Schneider, P. Schuster, J. Garbe, K. Bethke and J. Kirschner, *Surf. Sci.* **211-212**, 732 (1989).

[81] A. K. Schmid, A. Atlan, H. Itoh, B. Heinrich, T. Ichinokawa and J. Kirschner, *Phys. Rev. B* **48**, 2855 (1993).

[82] R. Pentcheva and M. Scheffler, *Phys. Rev. B* **61**, 2211 (2000).

[83] F. Nouvertné, U. May, M. Bamming, A. Rampe, U. Korte, G. Güntherodt, R. Pentcheva and M. Scheffler, *Phys. Rev. B* **60**, 14382 (1999).

[84] O. Heckmann, H. Magnan, P. le Fevre, D. Chandesris and J. J. Rehr, *Surf. Sci.* **312**, 62 (1994).

[85] E. Navas, P. Schuster, C.M. Schneider, J. Kirschner, A. Cebollada, C. Ocal, R. Miranda, J. Cerdá and P. de Andrés, *J. Magn. Magn. Mater.* **121**, 65 (1993).

[86] J. Lindner, *Diplomarbeit*, FU Berlin (1999)(unpublished).

[87] P. Poulopoulos, J. Lindner, M. Farle and K. Baberschke, *Surf. Sc.* **437**, 277 (1999).

[88] P. Srivastava, F. Wilhelm, A. Ney, N. Haack, H. Wende and K. Baberschke, *Surf. Sci.* **402-404**, 818 (1998).

[89] D. Wang, A. J. Freeman and H. Krakauer, *Phys. Rev. B* **26**, 1340 (1982).

[90] F. Wilhelm, P. Srivastava, A. Ney, N. Haack, G. Ceballos, M. Farle and K. Baberschke, *J. Synchrotron Rad.* **6**, 699 (1999).

[91] A. B. Schick, A. J. Freeman and A. I. Liechtenstein, *J. Appl. Phys.* **81**, 7022 (1998).

[92] A. Berger, U. Linke and H. P. Oepen, *Phys. Rev. Lett.* **68**, 839 (1992).

[93] A. V. Smirnov and A. M. Bratkovsky, *Phys. Rev. B* **54**, R17371 (1996).

[94] W. Platow, U. Bovensiepen, P. Poulopoulos, M. Farle, K. Baberschke, L. Hammer, S. Walter, S. Müller and K. Heinz, *Phys. Rev. B* **59**, 12641 (1999).

[95] J. Lindner, P. Poulopoulos, F. Wilhelm, M. Farle and K. Baberschke, (to be submitted).

[96] B. Schulz and K. Baberschke, *Phys. Rev. B* **50**, 13467 (1994).

[97] J. Hunter Dunn, D. Arvanitis and N. Mårtensson, *Phys. Rev. B* **54**, R11157 (1996).

[98] M. Tischer, D. Arvanitis, T. Yokoyama, T. Lederer, L. Tröger and K. Baberschke, *Surf. Sci.* **307-309**, 1096 (1994).

[99] R. E Parra and R. Medina, *Phys. Rev. B* **22**, 5460 (1980) and references therein.

[100] B. Hernnäs, M. Karolewski, H. Tillborg, A. Nilson and N. Mårtensson, *Surf. Sci.* **302**, 64 (1994).

[101] O. Hjortstam, K. Baberschke, J. M. Wills, B. Johansson and O. Eriksson, *Phys. Rev. B* **55**, 15026 (1997).

[102] T. Herrmann, M. Potthoff and W. Nolting, *Phys. Rev. B* **58**, 831 (1998).

[103] L. P. Kadanoff, W. Götze, D. Hemblen, R. Hecht, E. A. S. Lewis, V. V. Palciankas, M. Rayl and J. Swift, *Rev. Mod. Phys.* **39**, 395 (1967).

[104] K. S. Wilson, *Phys. Rev. B* **4**, 3174 (1971).

[105] N. D. Mermin and H. Wagner, *Phys. Rev. Lett.* **17**, 1133 (1966).

[106] M. Tischer, D. Arvanitis, A. Aspelmeier, M. Russo, T. Lederer and K. Baberschke, *J. Magn. Magn. Mater.* **135**, L1 (1994).

[107] U. Bovensiepen, P. Poulopoulos, M. Farle and K. Baberschke, *Surf. Sci.* **402-404**, 396 (1998) and references therein.

[108] B. Schulz, R. Schwarzwald and K. Baberschke, *Surf. Sci.* **307-309**, 1102 (1994).

[109] Y. Li and K. Baberschke, *Phys. Rev. Lett.* **68**, 1208 (1992).

[110] R. P. Erickson and D. L. Mills, *Phys. Rev. B* **43**, 11527 (1991).

[111] H. J. Elmers, *Int. J. Mod. Phys. B* **9**, 3115 (1995).

[112] K. Wagner, N. Weber, H. J. Elmers and U. Gradmann, *J. Magn. Magn. Mater.* **167**, 21 (1997).

[113] C. M. Schneider, P. Bressler, P. Schuster, J. Kirschner, J. J. de Miguel and R. Miranda, *Phys. Rev. Lett.* **64**, 1059 (1990).

[114] M. E. Buckley, F. O. Schumann and J. A. C. Bland, *Phys. Rev. B* **52**, 6596 (1995).

[115] P. J. Jensen, H. Dreyssé and K. H. Bennemann, *Surf. Sci.* **269-270**, 627 (1992).

[116] W. Platow, U. Bovensiepen, P. Poulopoulos, M. Farle, K. Baberschke, L. Hammer, S. Walter, S. Mller and K. Heinz, *Phys. Rev. B* **59**, 12641 (1999).

[117] J. Shen, M.-T. Lin, J. Giergiel, C. Schmidthals, M. Zharnikov, C. M. Schneider and J. Kirschner, *J. Magn. Magn. Mater.***156**, 104 (1996).

[118] F. Wilhelm, U. Bovensiepen, A. Scherz, P. Poulopoulos, A. Ney, H. Wende, G. Ceballos and K. Baberschke, *J. Magn. Magn. Mater.* , (accepted) (2000).

[119] B. Schulz, *PhD Thesis*, FU Berlin (1995)(unpublished).

[120] F. May, M. Tischer, D. Arvanitis, J. Hunter Dunn, H. Henneken, H. Wende, R. Chauvistré and K. Baberschke, *J. Phys. IV France***7**, C2-389 (1997).

[121] P. Srivastava, F. Wilhelm, A. Ney, M. Farle, H. Wende, N. Haack, G. Ceballos and K. Baberschke, *Phys. Rev. B***58**, 5701 (1998).

[122] F. Wilhelm, P. Srivastava, A. Ney, N. Haack, G. Ceballos, M. Farle and K. Baberschke, *J. Magn. Magn. Mater.* **198-199**, 458 (1999).

[123] C. A. Ramos, D. Lederman, A. R. King and V. Jaccarino, *Phys. Rev. Lett.* **65**, 2913 (1990).

[124] A. S. Carriço and R. E. Camley, *Phys. Rev. B***45**, R13117 (1992).

[125] E. N. Abarra, K. Takeno, F. Hellman and A. E. Berkowitz, *Phys. Rev. Lett.* **77**, 3451 (1996).

[126] R. W. Wang and D. L. Mills, *Phys. Rev. B***46**, 11681 (1992).

[127] U. Bovensiepen, F. Wilhelm, P. Srivastava, P. Poulopoulos, M. Farle, A. Ney and K. Baberschke, *Phys. Rev. Lett.* **81**, 2368 (1998).

[128] U. Bovensiepen, *PhD Thesis*, FU Berlin (2000)(unpublished).

[129] P. Jensen, K. H. Bennemann, P. Poulopoulos, M. Farle, F. Wilhelm and K. Baberschke, *Phys. Rev. B***60**, R14994 (1999).

[130] P. Jensen, K. H. Bennemann, P. Poulopoulos, M. Farle and K. Baberschke, *J. Appl. Phys.* (in press).

[131] J. H. Wu, T. Herrmann, M. Potthoff and W. Nolting, *J. Phys.: Condens. Matter* **12**, 2847 (1999).

[132] Z. Celinski, B. Heinrich and J. F. Cochran, *J. Magn. Magn. Mater.***145**, L1 (1995).

[133] S. S. Parkin, *Phys. Rev. Lett.* **67**, 3598 (1991).

[134] P. Bruno and C. Chappert, *Phys. Rev. Lett.* **67**, 1602 (1991).

[135] A. Ney, F. Wilhelm, M. Farle, P. Poulopoulos, P. Srivastava and K. Baberschke, *Phys. Rev. B* **59**, R3938 (1999).

[136] K. B. Hathaway, *Ultrathin Magnetic Structures*, edited by J. A. Bland and B. Heinrich, Vol. II, pp. 45-81 (Springer-Verlag, Berlin, 1994) and references therein.

[137] P. Poulopoulos, U. Bovensiepen, M. Farle and K. Baberschke, *Phys. Rev. B* **57**, R14036 (1998).

[138] A. Fert, P. Grünberg, A. Barthelemy, F. Petroff and W. Zinn, *J. Magn. Magn. Mater.* **140-144**, 1 (1995) and references therein.

[139] S. S. Parkin, N. More and K. P. Roche, *Phys. Rev. Lett.* **64**, 2304 (1990).

[140] A. Fert and P. Bruno, *Ultrathin Magnetic Structures*, edited by J. A. Bland and B. Heinrich, Vol. II, pp. 82-117 (Springer-Verlag, Berlin, 1994).

[141] P. Bruno, *Phys. Rev. B* **52**, 411 (1995) and references therein.

[142] C. H. Back, W. Weber, Ch. Würsch, A. Bischof, D. Pescia, R. Allenspach, *J. Appl. Phys.* **81**, 5054 (1997).

[143] P. J. H. Bloemen, M. T. Johnson, M. T. H. van de Vorst, R. Coehoorn, J. J. de Vries, R. Jungblut, J. aan de Stegge, A. Reiders and J. J. de Jonge, *Phys. Rev. Lett.* **72**, 764 (1994).

[144] S. N. Okuno and K. Inomata, *Phys. Rev. Lett.* **72**, 1553 (1994).

[145] W. Weber, R. Allenspach and A. Bischof, *Europhys. Lett.* **31**, 491 (1995).

[146] G. Bayreuther, F. Bensch and V. Kottler, *J. Appl. Phys.* **79**, 4509 (1996).

[147] P. Segovia, E. G. Michel and J. E. Ortega, *Phys. Rev. Lett.* **77**, 3455 (1996).

[148] A. Vega, L. C. Balbas, A. Chouairi, C. Demangeat and H. Dreyssé, *Phys. Rev. B* **49**, 12797 (1994).

[149] D. Weller, W. Reim, K. Spörl and H. Brandle, *J. Magn. Magn. Mater.* **93**, 183 (1991).

[150] M. Angelakeris, P. Poulopoulos, N. Vouroutzis, M. Nyvlt, V. Prosser, S. Visnovsky, R. Krishnan and N. K. Flevaris, *J. Appl. Phys.* **82**, 5640 (1997).

[151] P. Poulopoulos, M. Angelakeris, D. Niarchos and N. K. Flevaris, *J. Magn. Magn. Mater.* **140-144**, 613 (1995).

[152] P. Bruno, in *Magnetismus in Festkörpern und Grenzflächen*, 24. IFF-Ferienkurs (KFA Jülich, Jülich, 1993).

[153] F. Wilhelm, P. Poulopoulos, P. Srivastava, H. Wende, M. Farle, K. Baberschke, M. Angelakeris, N. K. Flevaris, W. Grange, J.-P. Kappler, G. Ghiringhelli and N. B. Brookes, *Phys. Rev. B* **61**, 8647 (2000).

[154] J. H. van Vleck, *Phys. Rev.* **52**, 1178 (1937).

[155] Landolt-Börnstein, Vol. III/19a, edited by H. P. J. Wijn (Springer-Verlag, Berlin, 1986).

[156] M. Farle, *Rep. Prog. Phys.* **61**, 755 (1998) and references therein.

[157] B. Heinrich and J. F. Cochran, *Adv. Phys.* **42**, 523 (1993).

[158] H. B. Callen and E. R. Callen, *J. Phys. Chem. Solids* **27**, 1271 (1966).

[159] A. N. Anisimov, M. Farle, P. Poulopoulos, W. Platow, K. Baberschke, P. Isberg, R. Wäppling, A. M. N. Niklasson and O. Ericksson, *Phys. Rev. Lett.* **82**, 2390 (1999).

[160] J. Trygg, B. Johansson, O. Ericksson and J. M. Wills, *Phys. Rev. Lett.* **75**, 2871 (1995).

[161] P. Bruno, *Phys. Rev. B* **39**, 865 (1989).

[162] A. Abragam and B. Bleaney, in *Electron Paramagnetic Resonance of Transitions Ions*, (Oxford: Clarendon, 1970).

[163] J. Jensen and A. R. Mackintosch, in *Rare Earth Magnetism*, (New York: Oxford University press, 1991).

[164] G. van der Laan, *J. Phys.: Condens. Matter* **10**, 3239 (1998).

[165] G. van der Laan, *Phys. Rev. B* **55**, 8086 (1997).

[166] J. Stöhr, *J. Magn. Magn. Mater.* **200**, 470 (1999).

[167] G. van der Laan, *Phys. Rev. Lett.* **82**, 640 (1999).

[168] G. H. O. Daalderop, P. J. Kelly and M. F. H. Schuurmanns, *Phys. Rev. B* **50**, 9989 (1994).

[169] B. Újfalussy, L. Szunyogh, P. Bruno and P. Weinberger, *Phys. Rev. Lett.* **77**, 1805 (1996).

[170] H. A. Dürr and G. van der Laan, *Phys. Rev. B***54**, R760 (1996).

[171] H. A. Dürr, G. van der Laan and B. T. Thole, *Phys. Rev. Lett.* **76**, 3464 (1996).

[172] H. A. Dürr, G. Y. Guo, G. van der Laan, J. Lee, G. Lauhoff and J. A. C. Bland, *Science* **277**, 213 (1997).

[173] P. Poulopoulos, *PhD Thesis*, Aristotle Univ. of Thessaloniki (1996)(unpublished).

[174] B.Y. Jin and J.B. Ketterson, *Adv. in Phys.* **38**, 189 (1989).

[175] W. Staiger, A. Michel, V. Pierron-Bohnes, N. Hermann amd M. C. Cadeville, *J. Mater. Res.* **12**, 161 (1997).

[176] F. Hakkens, A. De Veirman, W. Coene and F. J. A. den Broeder, *J. Mater. Res.* **8**, 1019 (1993).

[177] H. A. Dürr, G. van der Laan, J. Vogel, M. Finazzi and J. B. Goedkoop, *IEEE Trans. Magn.* **34**, 1201 (1998).

[178] I. A. Campbell, *Proc. R. Soc. London* **89**, 71 (1966).

[179] R. E. Parra and J. W. Cable, *Phys. Rev. B***21**, 5494 (1980).

[180] G. Schütz, R. Wienke, W. Wilhelm, W. Wagner, P. Kienle, R. Zeller and R. Frahm, *Z. Phys. B***73**, 495 (1989).

[181] R. Wienke, G. Schütz and H. Ebert, *J. Appl. Phys.* **69**, 6147 (1991).

[182] G. Schütz, S. Stähler, M. Knülle, P. Fischer, S. Parkin and H. Ebert, *J. Appl. Phys.* **73**, 6430 (1993).

[183] J. Vogel, A. Fontaine, V. Cros, F. Petroff, J.-P. Kappler, G. Krill, A. Rogalev and J. Goulon, *Phys. Rev. B***55**, 3663 (1997).

[184] W. J. Antel Jr., M. M. Schwickert, T. Lin, W. L. O'Brien and G. R. Harp, *Phys. Rev. B***60**, 12933 (1999).

[185] R. Krishnan, H. Lassri, S. Prasad, M. Porte and M. Tessier, *J. Appl. Phys.* **73**, 6433 (1993).

[186] S.-C. Shin, G. Srinivas, Y.-S. Kim and M.-G. Kim, *Appl. Phys. Lett.* **73**, 383 (1998).

[187] Y.-S. Kim and S.-C. Shin, *Phys. Rev. B***59**, R6597 (1999).

[188] F. Wilhelm, P. Poulopoulos, G. Ceballos, H. Wende, K. Baberschke, P. Srivastava, D. Benea, H. Ebert, M. Angelakeris, N. K. Flevaris, D. Niarchos, A. Rogalev and N. B. Brookes, (to be submitted).

[189] C. Kittel, *Introduction to Solid State Physics*, pp. 465 (Wiley & Sons, New York, 1976).

[190] J. W. Coyle, J. G. Booth, J. A. Cowen, A. D. Boardman, K. M. Booth and R. Krishnan, *J. Magn. Magn. Mater.* **156**, 33 (1996).

[191] N. Nakajima, T. Koide, T. Shidara, H. Miyauchi, H. Fukutani, A. Fujimori, K. Iio, T. Katayama, M. Nývlt and Y. Suzuki, *Phys. Rev. Lett.* **81**, 5229 (1998).

[192] L. F. Mattheiss and R. E. Dietz, *Phys. Rev. B***20**, 1663 (1980).

[193] M. Van Veenedaal, J. B. Goedkoop and B. T. Thole, *Phys. Rev. Lett.* **77**, 1508 (1996).

[194] F. M. F. Groot, M. A. Arrio, Ph. Sainctavit, Ch. Cartier and C. T. Chen, *Solid State Commun.* **92**, 991 (1994).

[195] D. Benea (private communication).

[196] R. E. Parra and J. W. Cable, *J. Appl. Phys.* **50**, 7522 (1979).

[197] V. L. Moruzzi, P. M. Marcus, K. Schwartz and P. Mohn, *Phys. Rev. B***34**, 1784 (1986).

[198] W. Grange, J.-P. Kappler, M. Maret, A. Rogalev and J. Goulon, *J. Synchrotron Rad.* **6**, 679 (1999).

[199] M. A. Tomaz, W. J. Antel Jr., W. L. O'Brien and G. R. Harp, *J. Phys. Condens. Matter***9**, L179 (1997).

[200] L. Sève, N. Jaouen, J. M. Tonnerre, D. Raoux, F. Bartolomé, M. Arend, W. Felsch, A. Rogalev, J. Goulon, C. Gautier, and J. F. Berar, *Phys. Rev. B***60**, 9662 (1999).

[201] O. K. Andersen, O. Jepsen and M. Sob, *in Lecture Notes in Physics No. 283, Electronic Band Structure and Its Applications*, edited by M. Yussouff, pp. 1 (Springer-Verlag, Berlin, 1987).

[202] U. von Barth and L. Hedin, *J. Phys. C:Solid State Physics* **5**, 1629 (1972).

[203] O. Eriksson, B. Johansson, R. C. Albers, A. M. Boring and M. S.S. Brooks, *Phys. Rev. B* **42**, R2707 (1990).

[204] H. Krakauer, A. J. Freeman and E. Wimmer, *Phys. Rev. B* **28**, 610 (1983).

[205] P. Poulopoulos, F. Wilhelm, H. Wende, G. Ceballos, K. Baberschke, D. Benea, H. Ebert, M. Angelakeris, N. K. Flevaris, A. Rogalev and N. B. Brookes, (to be submitted).

[206] J. Tersoff, *Phys. Rev. Lett.* **74**, 434 (1995).

[207] M. G. Samant, J. Stöhr, S. S. P. Parkin, G. A. Held, B. D. Hermsmeier, F. Hermann, M. van Schilfgaarde, L. C. duda, D. C. Mancini, N. Wassdahl and R. Nakajima, *Phys. Rev. Lett.* **72**, 1112 (1994).

[208] H. Ebert, R. Zeller, B. Drittler and P. H. Dederichs, *J. Appl. Phys.* **67**, 4576 (1990).

[209] N. Vouroutzis (private communication).

[210] V. Popescu and H. Ebert, (unpublished).

List of publications

1. P. Srivastava, F. Wilhelm, A. Ney, N. Haack, H. Wende and K. Baberschke

   Modifications in the electronic structure of 3d single-, bi- and tri-layers on Cu(001)

   Surf. Sci. **402-404**, 818 (1998).

2. P. Srivastava, F. Wilhelm, A. Ney, M. Farle, H. Wende, N. Haack, G. Ceballos and K. Baberschke

   Magnetic moments and Curie temperatures of Ni and Co thin films and coupled trilayers

   Phys. Rev. B**58**, 5701 (1998).

3. U. Bovensiepen, F. Wilhelm, P. Srivastava, P. Poulopoulos, M. Farle, A. Ney and K. Baberschke

   Two susceptibility maxima and element specific magnetizations in indirectly coupled ferromagnetic layers

   Phys. Rev. Lett. **81**, 2368 (1998).

4. F. Wilhelm, P. Srivastava, A. Ney, N. Haack, G. Ceballos, M. Farle and K. Baberschke

   Influence of exchange coupling on the Ni magnetization in Co/Cu/Ni trilayers

   J. Magn. Magn. Mat. **198-199**, 458 (1999).

5. A. Ney, F. Wilhelm, M. Farle, P. Poulopoulos, P. Srivastava and K. Baberschke

   Oscillation of the Curie temperature and interlayer exchange coupling in magnetic trilayers

   Phys. Rev. B**59**, R 3938 (1999).

6. F. Wilhelm, P. Srivastava, H. Wende, A. Ney, N. Haack, G. Ceballos, M. Farle and K. Baberschke

Magnetism of thin films and in Fe/Ni, Co/Fe bilayers on Cu(001)

J. Syn. Rad. **6**, 699 (1999).

7. H. Wende, P. Srivastava, D. Arvanitis, F. Wilhelm, L. Lemke, A. Ankudinov, J. J. Rehr, J. W. Freeland, Y. U. Idzerda and K. Baberschke

Magnetic L-edge EXAFS of 3d elements: Multiple scattering analysis and spin dynamics

J. Syn. Rad. **6**, 696 (1999).

8. U. Bovensiepen, F. Wilhelm, P. Srivastava, P. Poulopoulos, M. Farle and K. Baberschke

Do exchange coupled ferromagnetic monolayers show different Curie temperatures?

Physica Status Solidi (a) **173**, 153 (1999).

9. M. E. Dãvila, D. Arvanitis, J. Hunter Dunn, N. Mårtensson, P. Srivastava, F. Wilhelm and K. Baberschke

In situ MCXD measurements: an epitaxial Fe wedge on Cu(100)

Mat. Res. Soc. **24**, 41 (1999).

10. M. E. Dãvila, D. Arvanitis, J. Hunter Dunn, N. Mårtensson, P. Srivastava, F. Wilhelm and K. Baberschke

Magnetic circular x-ray dichroism of metastable epitaxial Fe on Cu(100)

J. Magn. Magn. Mat. **196-197**, 120 (1999).

11. F. Wilhelm, U. Bovensiepen, A. Scherz, P. Poulopoulos, A. Ney, H. Wende, G. Ceballos and K. Baberschke

Manipulation of the Curie temperature and the magnetic moments of ultrathin Ni and Co films by Cu-capping

J. Magn. Magn. Mater., accepted (2000).

12. P. J. Jensen, K. H. Bennemann, P. Poulopoulos, M. Farle, F. Wilhelm and K. Baberschke

Enhanced induced magnetization in coupled magnetic trilayers in the presence of spin fluctuations

Phys. Rev. B**60**, R14994 (1999).

13. F. Wilhelm, P. Poulopoulos, P. Srivastava, H. Wende, M. Farle, K. Baberschke, M. Angelakeris, N. K. Flevaris, W. Grange, J.-P. Kappler, G. Ghiringhelli and N. B. Brookes

Magnetic anisotropy and the anisotropy of the orbital moment of Ni in Ni/Pt multilayers

Phys. Rev. B**61**, 8647 (2000).

14. F. Wilhelm, P. Poulopoulos, G. Ceballos, P. Srivastava, H. Wende, K. Baberschke, D. Benea, H. Ebert, M. Angelakeris, N. K. Flevaris, D. Niarchos, A. Rogalev and N. B. Brookes

Layer-resolved magnetic moments in Ni/Pt multilayers

Phys. Rev. Lett., accepted (2000).

15. H. Wende, F. Wilhelm, P. Poulopoulos, K. Baberschke, J. W. Freeland, Y. U. Idzerda, A. Rogalev, D. L. Schlagel, T. A. Lograsso and D. Arvanitis

On the Temperature Dependence of Multiple- and Single-Scattering Contributions in Magnetic EXAFS

subm. to AIP Proceedings SSRT NET 99 Work shop (Frascati).

16. J. Lindner, P. Poulopoulos, F. Wilhelm, M. Farle and K. Baberschke

The Role of Intermixing on the magnetic Properties of ultrathin Ni/Cu (001)-Films

subm. to Phys. Rev. B (2000).

17. P. Poulopoulos, F. Wilhelm, H. Wende, G. Ceballos, K. Baberschke, D. Benea, H. Ebert, M. Angelakeris, N. K. Flevaris, A. Rogalev and N. B. Brookes

X-ray magnetic circular dichroic magnetometry on Ni/Pt multilayers

subm. to J. Magn. Magn. Mat. (2000).

18. A. Scherz, F. Wilhelm, U. Bovensiepen, P. Poulopoulos, H. Wende and K. Baberschke

Separate Curie temperatures in magnetic trilayers and the effect of spin fluctuations

subm. to J. Magn. Magn. Mat. (ICM2000).

19. A. Ney, P. Poulopoulos, F. Wilhelm, A. Scherz, M. Farle and K. Baberschke

Absolute determination of the magnetic moments of co monolayers: A combination of UHV magnetometry

subm. to J. Magn. Magn. Mat. (ICM2000).

Acknowledgements

A PhD is never a result coming from one person alone. I would like to thank all the persons which have contributed in the realization of this work.

First of all, I want to thank and to express all my gratitude to Prof. Dr. Klaus Baberschke which has successfully supervised this work. His competence, knowledge and continuous interest in this work were for me precious. I am very thankful that he gave me the opportunity to work in his group and introduced me in the world of the ultrathin film physics. Merci Klaus.

I would like to thank Prof. Dr. Nikolaus Schwentner for his willingness to co-asses this thesis.

I address my recognition to Prof. Dr. Michael Farle for stimulating my interest on other magnetic techniques.

I want here, especially, to thank Dr. Panagiotis Poulopoulos. His broad knowledge in magnetism on ultrathin films and multilayer systems is very impressive. Thanks for his help during all the stage in this work. His opinion and comments on physics are full of right meaning. From his experience to approach and interpret experimental results, I learned a lot. Together, we have measured so many things. Together, our imagination has no limit. Measuring until the machine dies, this is our leitmotiv. Like the L_3- and L_2-edges of $3d$ metals, we are inseparable friends in life. $Eu\chi\alpha\rho\iota\sigma\tau\omega$.

Dr. Pankaj Srivastava showed me the right way to attack quietly problems. He was a real magician, from experimental and theoretical point of view, all the problems were solved.

The grateful knowledge in x-ray absorption spectroscopy of Dr. Dimitri Arvanitis were very appreciable. No doubt about his enthusiasm in physic.

I want now to thank all the Bessy crew, Dr. Heiko Wende, Andreas Scherz, Dr. Gustavo

Curriculum vitae

I. Personal Data

Name: Fabrice WILHELM

Nationality:	French
Place and Date of Birth:	Haguenau (France), May 19th, 1973
Address:	Freie Universität Berlin
	Institut für Experimentalphysik
	Arnimallee 14
	D-14195 Berlin
	Germany
	Tel.: 49-30-838 5 6144
	Fax: 49-30-838 5 3647
	email: fwilhelm@zedat.fu-berlin.de

II. Educational Qualifications / Research Experience:

1979 to 1984	Elementary school "Ecole des filles et des garçons" in Roeschwoog (France).
1984 to 1991	High school "Seminaire des Jeunes de Walbourg" in Walbourg (France).
May, 1991	Baccalaureat.
1991 to 1992	Diplôme d'etudes universitaire general en Physique $1^{ière}$ année (DEUG I) Université Louis Pasteur, Strasbourg (France).
1992 to 1993	Diplôme d'etudes universitaire general en Physique $2^{ième}$ année (DEUG II) Université Louis Pasteur, Strasbourg (France).
1993 to 1994	Licence de Physique Université Louis Pasteur, Strasbourg (France) .
1994 to 1995	Maîtrise de Physique Université Louis Pasteur, Strasbourg (France) .
1995 to 1996	Diplôme d'etudes approfondies (DEA) de Physique Université Louis Pasteur, Strasbourg (France) . Stage de DEA:"Magnetisme induit dans les systèmes Pd/3d, etude par dichroisme magnetique circulaire" IPCMS- Strasbourg Supervisor: Dr. J.-P. Kappler
March 1997 to April 2000	Ph.D. work in Prof. Dr. K. Baberschke's group Freie Universität Berlin.

III International conferences attended:

- The 10th International Conference on X-ray Absorption Fine Structure (Chicago, USA, 1998).

- The Annual Greek Conference (Patras, Greece, 1999).

- The 44th Annual Conference on Magnetism & Magnetic Materials (San José, USA, 1999).

Zusammenfassung

In dieser Arbeit wurde die Fähigkeit des neuentwickelten Röntgenzirkulardichroismus (XMCD) demonstriert, fundamentale Probleme des Dünnfilmmagnetismus zu lösen. X-MCD Messungen bei tiefen Temperaturen ermöglichen die elementspezifische Bestimmung von magnetischen Momenten und die Trennung von Spin- und Bahnmoment. Aus temperaturabhängigen Messungen erhält man die Ordnungstemperaturen von einzelnen Filmen und Viellagensystemen. Die Anisotropie des Bahnmoments, welche der Ursprung der magnetischen Anisotopie ist, wird mittels winkelabhängigen Hochfeldmessungen des XMCD bestimmt.

Es wurden XMCD Messungen bei tiefen Temperaturen von ultradünnen Co- und Ni-Filmen auf Cu-Substraten durchgeführt. Die vorhergesagte Erhöhung des Bahnmomentes wurde für ultradünnes Co experimentell nachgewiesen. Ebenso wird eine Erhöhung des Verhältnis von Bahn- zu Spinmoment gefunden. Es wird gezeigt, daß 2 ML Co auf Cu(001) bzw. Cu (1 1 21) ein Bahnmoment von 0.22 bzw. 0.26 μ_B/Atom haben. Dies ist eine deutliche Erhöhung verglichen mit dem Wert für den Co-Volumenkristall von 0.14 μ_B/Atom. Darüberhinaus wurde auch eine leichte Erhöhung des Spinmoments für ultradünne Filme verglichen mit dem Volumenkristall gefunden. Anders als Co zeigen 4 ML Ni auf Cu(001) ein auf $0.28\mu_B$/Atom reduziertes Moment verglichen mit dem Wert für den Volumenkristall von $0.64\mu_B$/Atom. Dagegen ist wie für Co das Verhältnis von Bahn- zu Spinmoment erhöht. In einem einfachen Bild ist bei Co im Gegensatz zu Ni auf Cu(001) der Effekt des kontrahierten d-Bands an der Oberfläche größer als die Hybridisierung von Co-d-Cu-d Zuständen an der Grenzschicht, was zu einem erhöhten Moment für Co führt. Durch Cu-Bedeckung der ultradünnen Co- und Ni-Filme wird die Curietemperatur und das magnetische Moment reduziert. Im Bild der Mean-Field Theorie sind die Reduktion von Curietemperatur und magnetischem Moment verknüpft.

Mittels temperaturabhängigen XMCD Messungen wird gezeigt, daß es möglich ist, die Ordungstemperatur von Cu/Ni/Cu(001) zu höheren Temperaturen zu verschieben, indem man eine weitere ferromagnetische Lage mit unterschiedlicher intrinsischer Curietemperatur aufbringt. Dank der Elementspezifität des XMCD können zwei getrennte

Magnetisierungskurven gemessen werden, die bei unterschiedlichen Temperaturen verschwinden. Die indirekte Austauschkopplung zwischen den ferromagnetischen Lagen oszilliert in Abhängigkeit von der Cu-Zwischenschichtdicke zwischen ferro- und antiferromagnetisch. Antiferromagnetische Kopplung wurde bis hin zu 2 ML Cu-Zwischenschichtdicke gefunden, was die hohe strukturelle Qualität der epitaktischen Dreilagensysteme zeigt. Es wird gezeigt, daß die Interlagenaustauschkopplung mit der Erhöhung der Ordungstemperatur ΔT der ferromagnetischen Lage mit der geringeren intrinsischen Curietemperatur korreliert ist und wie diese mit der Cu-Zwischenschichtdicke oszilliert. Die gefundene Periode is in guter Übereinstimmung mit den Vorhersagen eines einfachen RKKY-Modells. Die Ursache von ΔT kann in einer Unterdrückung von Spinfluktuationen gesehen werden, da die Interlagenaustauschkopplung wie ein äußeres Feld wirkt. Dies führt auch zu einer Erhöhung der Magnetisierung für zweidimensionale Systeme. Reduziert man die Dicke – und damit die Curietemperatur – des Elements mit dem höheren Moment, kann erreicht werden, daß sich die beiden Magnetisierungskurven kreuzen. Die relative Erhöhung der Magnetisierung des Elements mit dem geringeren Moment bei tiefen Temperaturen konnte wiederum der Interlagenaustauschkopplung zugeschrieben werden.

Die magnetischen Eigenschafen von $3d/5d$ Multilagen wurden mittels XMCD untersucht. Im Falle der Ni/Pt Multilagen wurden winkelabhängige Hochfeldmessungen mit XMCD durchgeführt. Eine Anisotropie des Bahnmoments von Ni in Ni_2/Pt_2 Multilagen von $0.008\mu_B/Atom$ wurde gemessen. Diese kann direkt mit der magnetischen Anisotropie verbunden werden, da sie den mikroskopischen Ursprung der Anisotropie darstellt. Spin- und Bahnmoment wurden für verschiedene Ni/Pt Multilagen bestimmt. Die Messungen sowohl an den Ni, wie auch an den Pt $L_{2,3}$-Kanten erlauben die Konstruktion eines vollständigen magnetischen Profils. Im Gegensatz zur Literatur wurden keine "toten" Ni-Lagen an der Grenzschicht von Ni und Pt gefunden was auf die scharfen Grenzflächen der gemessenen Multilagen zurückzuführen ist. Ein induziertes Pt-Moment bis zu $0.3\mu_B/Atom$ wurde beobachtet. Das Ni-Moment an der Grenzfläche ist um $\sim 50\%$ reduziert verglichen mit dem Wert des Volumenkristalls. Theoretische Rechnungen bestätigen diesen Trend, wenn auch eine Reduktion von lediglich 8% vorhergesagt wird und das experimentell gefundene, induzierte Pt-Moment zwei bis dreimal größer ist. Induzierte Momente wurden auch für W und Ir in Fe/T (T=W,Ir) gemessen. Wie vorhergesagt ist W antiferromagnetisch und Ir ferromagnetisch an das Fe gekoppelt.

Zusammenfassend ist es gelungen, mit einer einzigartigen experimentellen Technik, dem XMCD, neues Licht auf das Verständnis des Dünnfilmmagnetismus zu werfen, beginnend von einzelnen Lagen, Schritt für Schritt hin zu neuen Multilagen von technologischem Interesse. An einzelnen Lagen wurden Effekte der Hybridisierung mit dem Substrat und der Einfluß der geringeren Koordination an der Oberfläche bzw. Grenzfläche

auf das magnetische Moment untersucht. Im nächsten Schritt wurde die Modifikation von Curietemperatur und magnetischem Moment durch eine Deckschicht gezeigt. Der Schritt in die wundervolle Welt des Multilagenmagnetismus' wurde mit dem Aufbringen einer weiteren ferromagnetischen Schicht auf das Zweilagensystem vollzogen. Es wurde gezeigt, daß es die Interlagenaustauschkopplung und die reduzierte Dimensionalität sind, die die Ordnungstemperatur zu höheren Werten verschieben. Mit Kenntnis der Dreilagensysteme als Prototyp für die Physik des Multilagenmagnetismus, konnten dann dicke Systeme mit technologischem Potential – wie senkrechter magnetischer Anisotropie für magnetooptische Speicher – untersucht werden. Es wurden der mikroskopische Ursprung der senkrechten Anisotropie und die induzierten magnetischen Momente studiert, was in einem weltweit einzigartigen magnetischen Profil einer Multilage resultierte.